THE UNIVERSITY *of* EDINBURGH

Coupled Analyses of Multi-Unit Floating Offshore Wind Turbines in Combined Wave-Current Environments

Mujahid Elobeid

A thesis submitted in partial fulfilment of the requirements for the award of an Engineering Doctorate

THE UNIVERSITY OF EDINBURGH

2024

♡ ♡ ♡

To my awesome grandma, ***Sittana****,*
and my dearest parents, ***Sumaya*** *&* ***Omer***

I'm forever indebted for your unwavering sacrifices!

IDCORE

This thesis is submitted in partial fulfilment of the requirements for the award of an Engineering Doctorate (EngD), jointly awarded by the University of Edinburgh, the University of Strathclyde, the University of Exeter, and the Scottish Association for Marine Science (SAMS). The work presented herein has been conducted under the industrial supervision of EnerOcean S.L. as a research project within the EPSRC and NERC Industrial Centre for Doctoral Training in Offshore Renewable Energy (IDCORE).

THE UNIVERSITY *of* EDINBURGH

University *of* Exeter

Abstract

Deployments of offshore wind have focused primarily on shallow seas using bottom-fixed foundations. However, much of the world's offshore wind resource lies in deeper waters where bottom-fixed foundations are not suitable, and floating platforms must be utilised. However, these Floating Offshore Wind Turbines (FOWTs) encounter economic and technical hurdles. Economically, most of the developed floating foundations support a single Wind Turbine Generator (WTG), resulting in high Capital Expenditures (CapEx). Technically, these FOWTs are subject to environmental loads, and their dynamic responses are complex and not thoroughly understood.

Driven by these challenges, this research presented an innovative twin-turbine semi-submersible platform as an alternative solution for reducing the CapEx and Levelised Cost of Energy (LCoE), thereby facilitating the commercialisation of floating offshore wind farms. This platform is called W2Power, developed by EnerOcean S.L., and is engineered to support a pair of generic WTGs. The present work aims to investigate the implications of Wave-Current Interaction (WCI) on the dynamics of multi-unit FOWTs by means of coupled numerical analyses and physical model experiments.

Numerical analyses are performed at full-scale of the W2Power FOWT; herein, the floater model is first developed. A new mooring system is first designed, and a numerical model of the floater-mooring-towers-nacelles-turbines is established. Equipped with two 5 MW WTGs, the developed model incorporates structural hydrostatic and dynamics, hydrodynamic effects, mooring loads, and aerodynamics.

Based on Airy wave theory, two numerical WCI models are developed to analyse the effects of a uniform current interacting with regular and irregular waves. WCI models are integrated with the OrcaFlex programme for the coupled aero-hydro-servo-elastic analysis. Experiments are also conducted in the FloWave Ocean Energy Research Facility on a 1:40-scale physical model of W2Power under multi-directional waves combined with currents. Furthermore, the numerical simulations are validated against the tank trails.

The results revealed that the current's presence significantly modified the wave profiles and the system's static equilibrium. Wave directionality impacted the platform motions and mooring forces. Also, WCI influenced the dynamics of the platform motions and the mooring and nacelles of the FOWT. WCI particularly influences translational platform motions, mooring loads, and nacelles accelerations. Remarkably, WCI can lead to differences of up to $\pm 22\%$ and $\pm 26\%$, respectively, in the line's maximum tension and surge response, depending on the current direction and mooring layout. In turn, these variations have significant implications for fatigue loads, operational maintenance (O&M), and CapEx costs of the mooring systems.

In addition, comparative benchmarks of validations between measurements and simulations, with and without WCI, demonstrated the reliability of the WCI models in accurately capturing system dynamics. Thus, the frameworks established can serve as a foundation for other studies exploring the applications of WCI in the dynamic responses of FOWTs. This will contribute to the advancements of FOWT technologies, thereby facilitating the commercialisation of floating wind farms.

Lay Summary

Offshore wind energy holds immense promise for clean power generation. It has been predominantly harnessed in shallow waters using bottom-fixed foundations to support the turbines. However, the untapped potential of offshore wind resources in deeper waters necessitates the utilisation of floating platforms due to the impracticality of bottom-fixed solutions. Floating platforms offer a solution but entail technical and economic challenges.

To reduce capital costs and enhance bankability, multi-unit floating platforms have emerged as innovative solutions that accommodate more than a turbine on the same floater.

On a technical front, these floating wind turbines are subject to diverse environmental loads, such as wind, waves, and currents. In combined wave-current environments, waves interacting with currents lead to changes in wave characteristics. This wave-current interaction can impact the platform's responses and fatigue the superstructures of the entire system.

This work, therefore, considered a twin-turbine floating offshore wind system, W2Power, developed by EnerOcean S.L. It further investigated how wave-current interaction impacts the dynamic responses of floating wind turbines using experimental and numerical modelling.

In the numerical phase, a new single-point mooring system was proposed and coupled with the floater-towers-nacelles. The platform was equipped with two 5 MW wind turbines, giving a total capacity power of 10 MW per platform. Furthermore, two models were developed to account for the interaction with regular and irregular waves. Then, a framework was established by integrating these models with a commercial industry-standard tool to carry out coupled aero-hydro-servo-elastic analyses incorporating wave-current interaction.

In the experimental phase, extensive tests were conducted at the cutting-edge FloWave Ocean Energy Research Facility employing a 1:40 physical model of the W2Power under multi-directional waves combined with currents to simulate real-world conditions.

Findings showed that current alters wave profiles and affects the equilibrium point of the floating system. Wave-current interaction was found to impact platform motions, mooring dynamics and nacelles' accelerations. Novel validations also demonstrated the capabilities of the developed wave-current models in capturing system dynamics. Therefore, the numerical and experimental frameworks developed can be the basis for the applications of advanced wave-current interaction in analysing floating wind turbines.

Acknowledgements

Funding from the Engineering and Physical Sciences Research Council (EPSRC) and the Natural Environment Research Council (NERC) Industrial Centre for Doctoral Training in Offshore Renewable Energy (Grant number EP/S023933/1) is gratefully acknowledged.

This EngD research would not have been possible without the help of my IDCORE academic supervisory team. In particular, I would like to thank my academic supervisors, Prof Longbin Tao, Prof David Ingram and Dr Ajit Pillai, for their guidance throughout the project. They were reliable and unfailing sources of advice and support throughout the research. Many thanks for your kindness, motivation, and recharging my batteries when needed; I owe each of you a debt of thankfulness.

I would like to thank EnerOcean S.L., specifically Dr Pedro Mayorga, for their collaboration and industrial support. A shout-out goes to the dedicated team at the FloWave Facility for their guidance and collaborative efforts, which were instrumental in accomplishing the experimental phase of this study. I also thank the National and Kapodistrian University of Athens for providing the hindcast data.

Acknowledgement, with gratitude, is also due to my examiners, Prof Zhiqiang Hu (Newcastle University), Dr Richard Wakefield (Flotation Energy), and Dr Saishuai (David) Dai (University of Strathclyde), whose thorough examination of my thesis and insightful discussions during the viva enhanced the quality of my work.

I would also like to express my appreciation to the IDCORE programme itself for offering me the opportunity to develop my personal and professional skills. Thanks to everyone who has contributed to making this programme nothing short of phenomenal. A special thank you goes to the hero behind the scenes, Dr Katrina Tait, for her tireless work.

The camaraderie and encouragement from the 2019 IDCORE cohort were indispensable and truly appreciated. Thanks to each of you for making these past years enjoyable.

Heartfelt thanks are extended to my parents, family, and friends for their unwavering support throughout this journey and every other path I have chosen to pursue. Lastly, a big thank you is owed to Mohaned Fargali, Abdelhameed Terayo and Mohammed Bashir for making my studies and everything else manageable.

Declaration

I declare that this work has not been submitted for any other degree or professional qualification. Furthermore, I declare that this thesis was composed by myself and that the material presented herein is entirely my own work. Except where explicitly stated in the text, otherwise by reference or acknowledgement. Further details on the contributions are as follows:

- Parts of the work presented in this thesis have been published:
  - ◇ The experimental model developed in Chapter 4 is based on the hydrodynamic outcomes in Elobeid, M., Tao, L., Ingram, D., Pillai, A.C., Mayorga, P. and Hanssen, J.E., (2022), June. Hydrodynamic performance of an innovative semi-submersible platform with twin wind turbines. In International Conference on Offshore Mechanics and Arctic Engineering (Vol. 85932, p. V008T09A032). American Society of Mechanical Engineers.
  - ◇ Chapters 6 and 8 are based on Elobeid, M., Pillai, A.C., Tao, L., Ingram, D., Hanssen, J.E. and Mayorga, P., (2024). Implications of wave-current interaction on the dynamic responses of a floating offshore wind turbine. Ocean Engineering Journal, 292, p.116571.
- The characteristics of the W2Power floating offshore wind turbine in Chapters 4 and 6 are provided by EnerOcean S.L. (EnerOcean S.L., 2007).
- The physical model at a scale of 1:40 was manufactured by EnerOcean S.L. Málaga, Spain, and shipped to FloWave tank for testing (EnerOcean S.L., 2007).

Mujahid Elobeid

List of Figures

List of Tables

Nomenclature

Acronyms and Abbreviations

2D, 3D	2, 3-Dimensional
BEM	Blade Element Momentum
CAGR	Compound Annual Growth Rate
CALM	Catenary Anchor Leg Mooring
CapEx	Capital Expenditures
CFD	Computer Fluid Dynamics
DAQ	Data Acquisition
DLLs	Dynamic Link Library
DNV	Det Norske Veritas
DoF	Degree of Freedom
EMEC	European Marine Energy Centre
EPSRC	Engineering and Physical Sciences Research Council
EU	European Union
FEM	Finite Element Method
FIM	Flow-Induced Motions
FPSO	Floating Production Storage and Offloading
FOWT	Floating Offshore Wind Turbine
FPP	Floating Power Plant
GHG	Emissions of Greenhouse Gases
GWEC	Global Wind Energy Council
IEC	International Electrotechnical Commission
IDCORE	Industrial Doctoral Centre for Offshore Renewable Energy
IFORM	Inverse First-Order Reliability Method
IPCC	Intergovernmental Panel on Climate Change
IRENA	International Renewable Energy Agency
ISORM	Inverse Second-Order Reliability Method
JONSWAP	JOint North-Sea WAve Project
KRISO	Korea Research Institute of Ships and Ocean Engineering
LC	Load Case or Load Cell (context-dependent)
LCoE	Levelised Cost of Energy
LDV	Laser Doppler Velocimetry
Lir NOTF	Lir National Ocean Test Facility
MARINET	Marine Renewables Infrastructure Network for emerging Energy Technologies

MBL	Minimum breaking load
MoCap	Motion Capturing System
MUFOWP	Multi-Unit Floating Offshore Wind Platform
MUFOWT	Multi-Unit Floating Offshore Wind Turbine
MWL	Mean Water Level
NERL	National Renewable Energy Laboratory
NERC	Natural Environment Research Council
NKUA	National and Kapodistrian University of Athens
NWT	Numerical Wave Tank
OEM	Original Equipment Manufacturer
OpEx	Operating Expenditures
ORE	Offshore Renewable Energy
PIV	Particle Imaging Velocimetry
PM	Pierson–Moskowitz
PSD	Power Spectral Density
PTV	Particle Tracking Velocimetry
QTF	Quadratic Transfer Function
RAO	Response Amplitude Operator
RANS	Reynolds Averaged Navier-Stokes
RC	Rated Capacity
R&D	Research and Development
RNA	Rotor-Nacelle Assembly
RMS	Root Mean Square
SAMS	Scottish Association for Marine Science
SCD	Super Compact Drive
SPM	Single Point Mooring
StDev	Standard Deviation
TLP	Tension Leg Platform
TRL	Technology readiness levels
UKCRF	UK Coastal Research Facility
ULS	Ultimate Limit State
VIM	Vortex-Induced Motions
VIV	Vortex-Induced Vibration
WD	Water depth
WEC	Wave Energy Converter
WG	Wave Gauge
WCI	Wave-Current Interaction
WTG	Wind Turbine Generator

Greek Symbols

γ	Peak enhancement factor [-]	η	Water surface elevation [m]
θ	Angle [°]	λ	Scale factor [–]
ν	Kinematic viscosity [m^2/s]	ρ	Seawater density [kg/m^3]
ω	Angular frequency [rad/s]	ω_r	Relevant frequency [rad/s]
Ω	Intrinsic frequency [rad/s]	Δx	Mesh characteristic length
Δt	Time step		

Roman Symbols

A	Wave amplitude [m]	$\mathbf{C}$	Stiffness matrix
C_h	Hydrostatic stiffness	C_g	Wave group velocity [m/s]
C_m	Mooring stiffness	E	Modulus of Elasticity [–]
F	Force [N]	Fr	Froude scale ratio [–]
g	Gravitational acceleration [m/s^2]	h, h_w	Water depth [m]
H	Wave height [m]	H_s	Significant wave height [m]
κ	Wavenumber [1/m]	L	Wavelength [m]
$\mathbf{M}$	Mass matrix [kg]	R	Radius [m]
Re	Reynolds scale ratio [–]	S	Wave steepness [–]
$S(f)$	Wave spectrum [m^2s]	t	Time [s]
T	Wave period [s]	T_d	Design tension [N, kN]
T_{dyn}	Dynamic tension [N, kN]	T_{mean}	Mean tension [N, kN]
T_r	Return period [year]	T_s	Sea state duration [s]
f, f_p	Frequency, peak frequency [Hz]	γ	Peak enhancement factor [-]
u, v, w	Fluid velocities in streamwise, transverse, and vertical directions [m/s]	U_c	Current velocity [m/s]
U_w	Wind speed [m/s]	x, y, z	Spatial dimensions [m]
X, Y, Z	Tank coordinates [m]	$\mathbf{A}_\infty$	Added mass matrix at infinite frequency [kg]
$\mathbf{B}$	Damping matrix	S_c	Characteristic mooring line strength [N, kN]

Subscripts

a, c	Regions in the absence and presence of current
Exp	Experimental or measured value
i	i-th component
Num	Numerical or calculated value

Key Definitions and Terminologies

- ◇ **Surge, Sway and Heave** are the translational motions of a floating platform in x, y and z directions, whereas **Pitch, Roll, and Yaw** are rotations about the x, y, and z axes.
- ◇ **Following current** refers to a current that flows in the same direction as the waves. **Opposing current** refers to a current that flows in the opposite direction as the waves.
- ◇ **Following waves** refer to waves propagating at 0° and in the same current direction. **Crossing waves** refer to waves propagating at 90° and in the cross direction to the current. **Opposing waves** refer to waves propagating at 180° and in the opposite direction to the current.
- ◇ **W2Power** is a terminology for a win-turbine floating wind platform developed by Ener-Ocean S.L.
- ◇ **FloWave** is a term for the FloWave Ocean Energy Research Facility based in Edinburgh, United Kingdom.

Contents

Chapter 1

Introduction

1.1 Overview

Climate change is a serious global concern that threatens human lives and ecosystems, and its implications are evident, such as extreme weather events. About two-thirds of the world's emissions of Greenhouse Gases (GHGs) are attributed to the burning of depleting fossil fuels for energy (Meinshausen et al., 2022). According to the Intergovernmental Panel on Climate Change (IPCC) report, if global warming is to be confined to 1.5°C, GHG emissions must be cut by almost half by 2030 (IPCC, 2023).

Limiting global warming to 1.5°C above pre-industrial levels is essential and requires substantial, rapid, and sustainable reductions in GHGs across all sectors. The energy supply sector (e.g. electricity, heat, and other forms of energy) is the largest contributor to global GHG emissions, accounting for approximately 30-35% of the total emissions; thus, it plays a key role in achieving these reductions (Bogdanov et al., 2021). Thereby, renewable energy resources are being utilised instead of conventional ones (e.g., coal, oil, and natural gas) due to their falling costs and sustainable and environmental characteristics. This transition also allows emerging economies to grow while reducing GHG emissions.

1.2 Offshore Wind Power

Wind power has emerged as a viable alternative to fossil fuels due to recent advancements in technology. These developments have resulted in the maturation of the wind energy industry, providing investors with a reliable and consistent rate of return. Globally, cumulative wind power capacity is currently 837 GW, preventing over 1.2 billion tonnes of CO_2 per year (i.e. equal to South America's annual carbon emissions), with 93.6 GW of this capacity installed in 2021, of which 72.5 GW are onshore. In the next five years, onshore wind power is expected to increase at a Compound Annual Growth Rate (CAGR) of 6.1%, with an annual average installation rate of 93.3 GW, resulting in 466 GW of total added capacity between 2022 and 2026 (GWEC, 2022).

Despite the advantages of wind power, the development of wind farms usually faces barriers during the consultation phase with local communities. Concerns about health, quality of life, and property values are frequently at the heart of uneasiness triggered by wind turbines' visual impact and noise constraints. This opposition to wind farm development, sometimes known as NIMBY-ism (Not In My Back Yard), has emerged as a barrier to deploying wind farms in areas with high populations (E. Smith & Klick, 2007). Consequently, wind energy developers have considered coastal regions a plausible alternative in light of these constraints. Offshore wind projects have the advantage of being constructed close to densely populated communities without the same level of NIMBY-ism that might occur with onshore installations. In addition, offshore sites often have higher and more consistent wind speeds, allowing for the development of gigawatt-scale projects. Hence, offshore wind has the potential to become an option for the future growth of wind power.

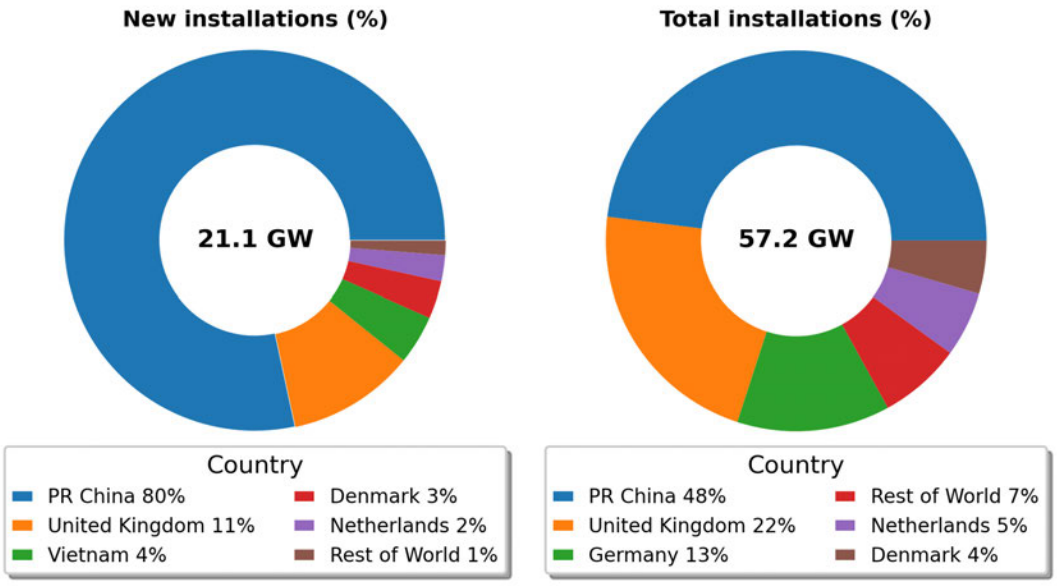

Figure 1.1: Breakdowns of cumulative and new installations for global offshore wind power in 2021 (GWEC, 2022).

In 2021, the offshore wind market achieved a record-breaking year with 21.1 GW commissioned, despite the ongoing COVID-19 outbreak. Thereby bringing the cumulative offshore capacity to 57.2 GW (see Figure 1.1). In line with the existing regulations, offshore wind capacity is likely to grow at a higher CAGR of 8.3%. By 2026, it is expected to increase from 21.1 GW to 31.4 GW, bringing the total installations to over 90 GW (GWEC, 2022). Around 240 GW of offshore wind energy in Europe is expected to be operational by 2050 (WILSON, 2020). At the time of writing, the United Kingdom is a key player, with an accumulated installed capacity of over 10 GW over 38 locations. In addition to the 5 GW currently under the pre-

construction phase, there are plans for an additional 11 GW. Furthermore, the UK is a leader in floating offshore wind with a total capacity of 80 MW, including 50 MW from the Kincardine farm installed in 2021 (UK-DBT, 2023). This addition brought the global floating offshore wind capacity to 139 MW (GWEC, 2022).

1.3 Floating Wind Power

The deployment of offshore wind turbines has focused primarily on shallow seas (e.g. the North Sea, Chinese coastal waters, and the New England coast) of soft seabeds (i.e. made of sand, gravel or mud), which makes bottom-fixed foundations the most cost-effective and optimal option. As depicted in Figure 1.2, the most common bottom-fixed foundation designs (i.e. for water depths up to 50 m) are gravity-base, suction caissons, monopiles, tripods, and jackets (Byrne & Houlsby, 2003).

On the other hand, some regions (e.g. the Mediterranean Sea) lack favourable seabed conditions for bottom-fixed foundations. Moreover, 80% of offshore wind potential is in waters deeper than 60 m, which is the limit for bottom-fixed foundations, thereby making them problematic in such depths (WindEurope, 2018). Hence, floating offshore foundations are emerging as potential revolutionary solutions that offer broader wind resource exploitation and alleviate problems associated with bottom-fixed designs. In 2017, Equinor's 30 MW Hywind Scotland project was the world's first floating wind farm, deployed off the coast of Peterhead, Scotland (Duarte et al., 2022; Durakovic, 2021).

1.4 Floating Wind Design Concepts

In its most basic form, a floating offshore wind turbine system comprises a floating platform, a mooring system, and a wind turbine superstructure (tower and Rotor-Nacelle Assembly, RNA) (Robertson & Jonkman, 2011; Edwards et al., 2023). Conceptually, floating offshore wind platforms be categorised as follows (see Figure 1.2):

1.4.1 Spar-Buoy Platform

Spar buoy design is a cylindrical floater typically containing heavy ballast (e,g. water and gravel) in its large draft (Skaare, 2017). The ballast is attached at the bottom of the draft to ensure the floater's stability and mitigates motions (Breton & Moe, 2009; Arapogianni et al., 2013). Moreover, a conventional mooring system of catenary lines holds the floater in place (C. Wang et al., 2010).

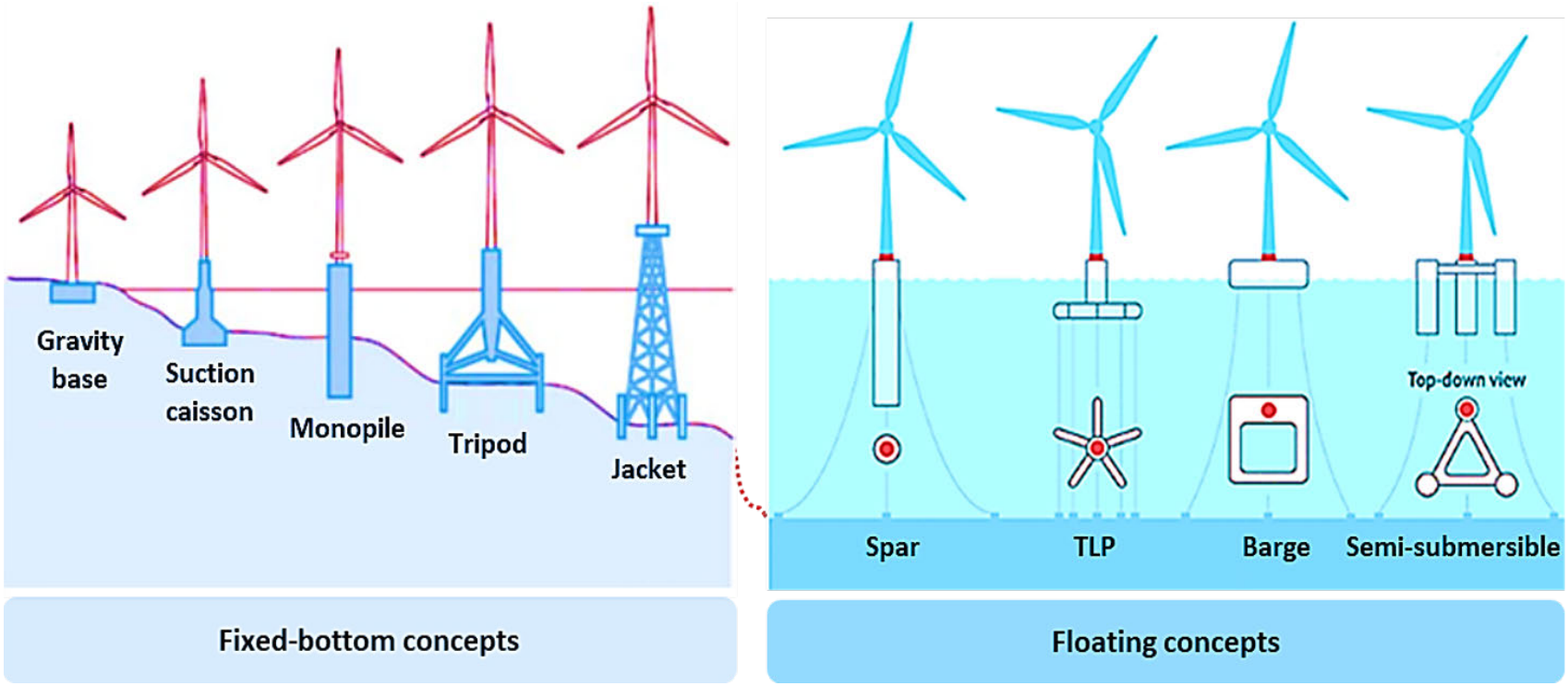

Figure 1.2: Different design concepts of offshore wind turbines; after (Moulas et al., 2017; Mei & Xiong, 2021).

1.4.2 Tension Leg Platform

Tension Leg Platforms (TLPs) are extensively employed in the oil and gas industry and were initially conceived for drilling in ultra-deep waters surpassing 1500 m. They consist of a buoyant semi-submersible floater anchored to the seabed via taut vertical mooring lines (i.e. tendons) that offer superior stability. TLPs feature a central column connecting the submerged floater to the wind turbine tower above the water surface (Edwards et al., 2023). Conversely, the vertically tensioned lines exert uplifting loads on the anchors, requiring a more robust anchoring system (C. Wang et al., 2010; Butterfield et al., 2007).

1.4.3 Barge Platform

This foundation design achieves stability using its distributed buoyancy and large water-plane area. Barges are commonly characterised by rectangular, annular-shaped designs featuring a centralised pool (i.e. moon pool) that absorbs wave loads, thereby reducing the floater motions (Van Kessel, 2010). Catenary mooring systems are utilised to prevent barges from drifting (Jonkman & Buhl, 2007), as adopted in the most common floating barge platform in the floating wind sector, Ideol.

1.4.4 Semi-Submersible Platform

Semi-submersible platforms employ a combination of strategies for stability. Their pontoons and columns offer substantial buoyancy volume compared to the spar and TLP. Unlike barges, the waterplane areas of the semi-submersibles are relatively small in comparison to their buoyancy volume, resulting in lesser susceptibility to environmental loads. Typically, their mooring systems utilise catenary lines (Pegalajar-Jurado et al., 2018).

1.5 Floating Wind Power Optimisation

The recent development of spar buoy and semi-submersible designs has brought the floating offshore wind industry towards commercial readiness. For instance, over its five years of operation, Hywind Scotland has achieved a remarkable average capacity factor of 54% compared to a UK offshore wind average of about 40% (Equinor, 2023). The International Renewable Energy Agency (IRENA) expects offshore wind farms to make even more significant leaps, with projected capacity factors ranging from 36% to 58% by 2030 and 43% to 60% by 2050, compared to an average of 43% in 2018. Furthermore, industry experts expect that 5 GW to 30 GW of floating offshore capacity could be deployed globally by 2030, and by 2050, floating wind projects could constitute 5% to 15% of the worldwide offshore wind installations (nearly 1000 GW) (IRENA, 2019).

Efforts are being implemented to minimise the levelised cost of energy for offshore wind, such as wind farm scaling. Gigawatt-scale fixed-bottom offshore wind parks are being installed (e.g., UK's Seagreen and Dogger Bank, New Zealand's Waikato). Additionally, floating offshore wind farms are being developed to access deeper waters, allowing for economies of scale and expanding potential sites for offshore wind energy farms (Hall et al., 2014).

A key difference between floating and bottom-fixed turbines lies in the mooring systems. These subsystems are a significant cost driver, potentially accounting for 5-15% of the capital cost of a floating wind farm (Myhr et al., 2014). Ensuring the cost-efficiency of this subsystem is vital for the deployment of FOWTs. Thus, shared mooring lines and anchors are being explored to reduce costs, particularly for deeper-water deployments (Sloan et al., 2022).

Offshore wind trends indicate that FOWTs of 10-20 MW will be operational (Bauer, 2020). Deploying such large turbines at commercial scales using conventional single platforms is both technically challenging and, so far, has proven very expensive. Hence, Multi-Unit Floating Offshore Wind Platforms (MUFOWPs) are being developed as viable innovations for higher installed wind capacity. The concept pertains to an offshore floating platform that supports more than a single wind turbine, hereafter referred to as MUFOWPs. These platforms utilise weathervaning systems to minimise the platform's height and unfavourable loads and ensure alignment with the wind direction. They are designed with the turbines in close position without significant wake losses. Thus leading to more cost-efficient wind energy capture compared to single-turbine floaters of comparable power (Barltrop, 1993).

1.6 Motivation

The successful deployment of conventional FOWTs faces challenges, such as the high CapEx per individual platform and the higher LCoE; hence, it is imperative to accelerate the development of MUFOWPs. Therefore, the W2Power FOWT has been explicitly developed as an innovative solution to reduce the CaPex and LCoE of the single-unit floating platforms (see Figure 1.3).

Furthermore, the assessment of dynamic behaviours for these coupled systems in sophisticated oceanic environments adds another layer of complexity. As such, FOWTs are subjected to various loads, such as wind, waves, and currents. In deep waters, where FOWTs are deployed (Atcheson et al., 2016), the effects of the currents on their mooring lines are pronounced due to the larger submerged length of these lines, and these effects become more prominent when currents interact with waves (Hall et al., 2014; L. Chen & Basu, 2019).

As waves propagate on currents, their interaction results in frequency shifts (i.e. Doppler effect) and influences the wave-related parameters (e.g. wavelength, amplitude, and spectral energy density); thus, higher-velocity currents substantially impact such interaction (Janssen, 1989; J. Smith, 1997).

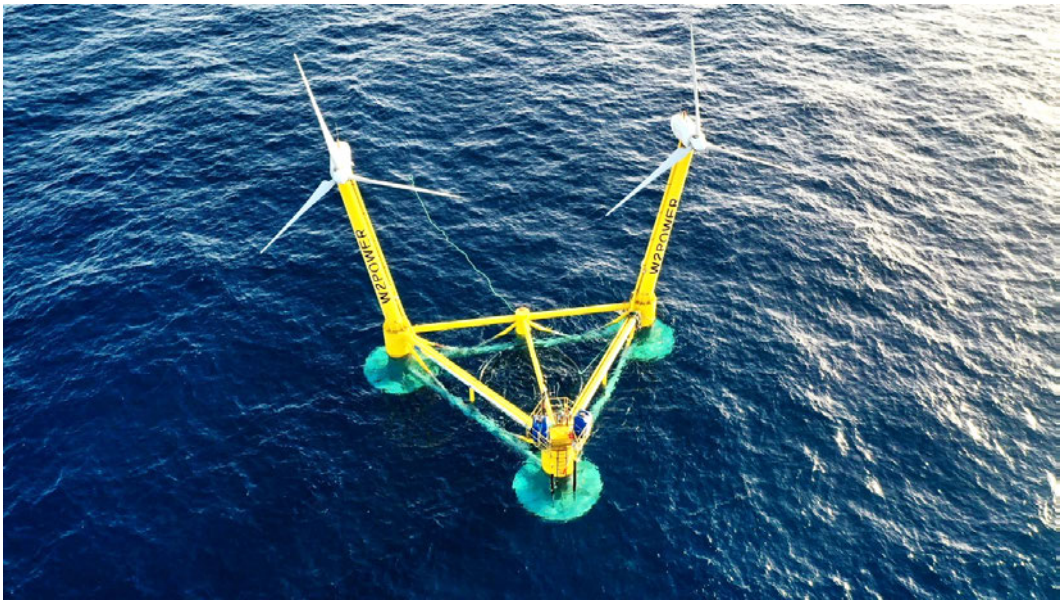

Figure 1.3: The W2Power prototype (i.e. at a scale of 1:6) in the open sea at Plocan in Gran Canaria, November 2022. Photo courtesy of EnerOcean S.L.

Wave-current interaction has not yet been extensively addressed in the coupled analysis of FOWTs, and that is due to two key challenges that must be handled: (i) a fully nonlinear mooring model capable of incorporating current, and (ii) an appropriate WCI model. The recent development of non-linear mooring models has addressed the first challenge (Palm et al., 2016; Davidson & Ringwood, 2017; A. C. Pillai et al., 2018b). However, the latter challenge has not yet been overcome and is still an ongoing research topic.

Moreover, most commercial engineering tools (e.g. FAST, Sima, OrcaFlex) rely on the linear dispersion relationship when specifying the properties of waves (J. M. Jonkman & Jonkman, 2016; OrcaFlex, 2023; Sima, 2023), such as JONSWAP (Joint North Sea Wave Project) waves (Hasselmann et al., 1973). However, these tools typically neglect the Doppler shift modification of the linear dispersion relationship in the presence of currents. The Doppler shift alters the frequency of waves due to the relative motion between the observer (e.g. a floating structure) and the waves, making it crucial for accurately modelling the encounter wave frequency and the shape of the wave spectrum. Without accounting for this, the wave-structure interaction under current conditions can be misrepresented, potentially leading to inaccurate predictions of loads and responses.

To overcome this limitation, new formulations and derivations for the total fluid particle velocity, the vector sum of the current velocity and wave-induced fluid particle velocity, are needed to incorporate Doppler shift appropriately. The motivation behind addressing WCI in the coupled analysis of FOWTs stems from the need for a deeper understanding of how such interaction

influences their dynamic behaviours, shedding light on aspects that were previously not fully explored. By developing models that can accurately capture WCI, this work contributes to the design and operation of floating platforms and mooring systems, ultimately advancing the deployment of FOWTs in deep waters.

1.7 Thesis Aims and Objectives

The overall aim of this research is to investigate the dynamic responses of multi-unit FOWTs and their mooring systems in combined wave and current environments. Thus, this project attempts to answer the following research questions:

I) How does the utilisation of a MUFOWP concept influence the platform motion responses and the dynamics of mooring system loads?

II) To what extent do currents impact the design process of FOWTs, and how can they be accurately considered in this design process?

III) How does wave-current interaction impact the dynamic behaviour of the mooring systems and/or the entire floating system?

In order to answer these questions, a range of objectives have been established. Firstly, the innovative W2Power FOWT model is developed (Figure 1.3). This included the development of the W2Power floater model and the conduction of hydrodynamic analysis in the frequency domain. A new mooring system is designed, and coupled analyses are performed for the floater-mooring model. Then, the coupled floater-mooring-towers-nacelles-rotors model is developed.

Secondly, wave-current interaction models are established based on linear Airy theory, which comprises the development of two analytical models: a regular wave-current model and an irregular wave-current model.

Thirdly, the effects of wave-current interaction on the structural responses and mooring system dynamics of FOWTs are investigated through both numerical and experimental analyses. This involves incorporating the developed WCI models in the coupled aero-hydro-servo-elastic simulations for the floater-mooring-towers-nacelles-turbines model. Additionally, comprehensive experiments are conducted at the FloWave Ocean Energy Research Facility under combined wave and current conditions to validate the numerical simulations (D. Ingram et al., 2014). These test campaigns utilised a 1:40 scale model of the W2Power concept.

1.8 Thesis Overview and Outline

The remainder of this thesis is divided into eight chapters, organised into three overarching parts and a standalone chapter. These parts encompass (I) Background and Literature Review, (II) Experimental Modelling of FOWTs in Combined Wave-Current Environments, and (III) Numerical Modelling of FOWTs in Combined Wave-Current Environments; with Chapter 9 dedicated to Overall Thesis Conclusions. Below is an outline of the structure of the research components. Figure 1.4 provides an overview of how the parts and elements within the thesis are interconnected.

Part I: Background and Literature Review

- **Chapter 2** provides an in-depth review of the current state of development of the **multi-unit floating offshore wind platforms** and their structural and dynamic, as well as addresses both technical and commercialisation constraints. Thus, it introduces the twin-turbine floating offshore wind platforms as innovative technologies designed to overcome the limitations of MUFOWPs accommodating more than two wind turbine units. The chapter further explores the core of this thesis, the W2Power platform, outlining its development path and discussing its multi-use solutions and versatile applications beyond power generation.
- **Chapter 3** offers an overview of **wave-current interaction** and its impact on the dynamics of **offshore structures**, including analytical, numerical, and experimental studies. Then, it evaluates existing research on offshore wind turbines in combined wave-current environments. Afterwards, it identifies key challenges and knowledge gaps regarding the implications of wave-current interaction on the dynamics of FOWTs and mooring systems, laying the groundwork for the next chapters of this thesis.

Part II: Experimental Modelling of MUFOWTs in Combined Wave-Current Environments

- **Chapter 4** describes the **experimental methods** to explore the dynamic responses of FOWTs when tested in simultaneous wave and current conditions. A theoretical framework is outlined, accompanied by a detailed description of both the test facility and the physical model. Then, environmental modelling of metocean conditions and the generation of various load cases are presented. Experiments are carried out under current, waves and different wave-structure scenarios interacting with current. This serves as the foundation for the subsequent chapter.
- **Chapter 5** discusses the **experimental findings** obtained from tank testing at scale mode; these include the dynamics of motion responses and the mooring system. Investigations delve into the effects of wave directionality under both regular and irregular waves propagating from different directions. It presents diverse structure-wave-current interaction scenarios and their impacts on mooring loads and platform motion responses.

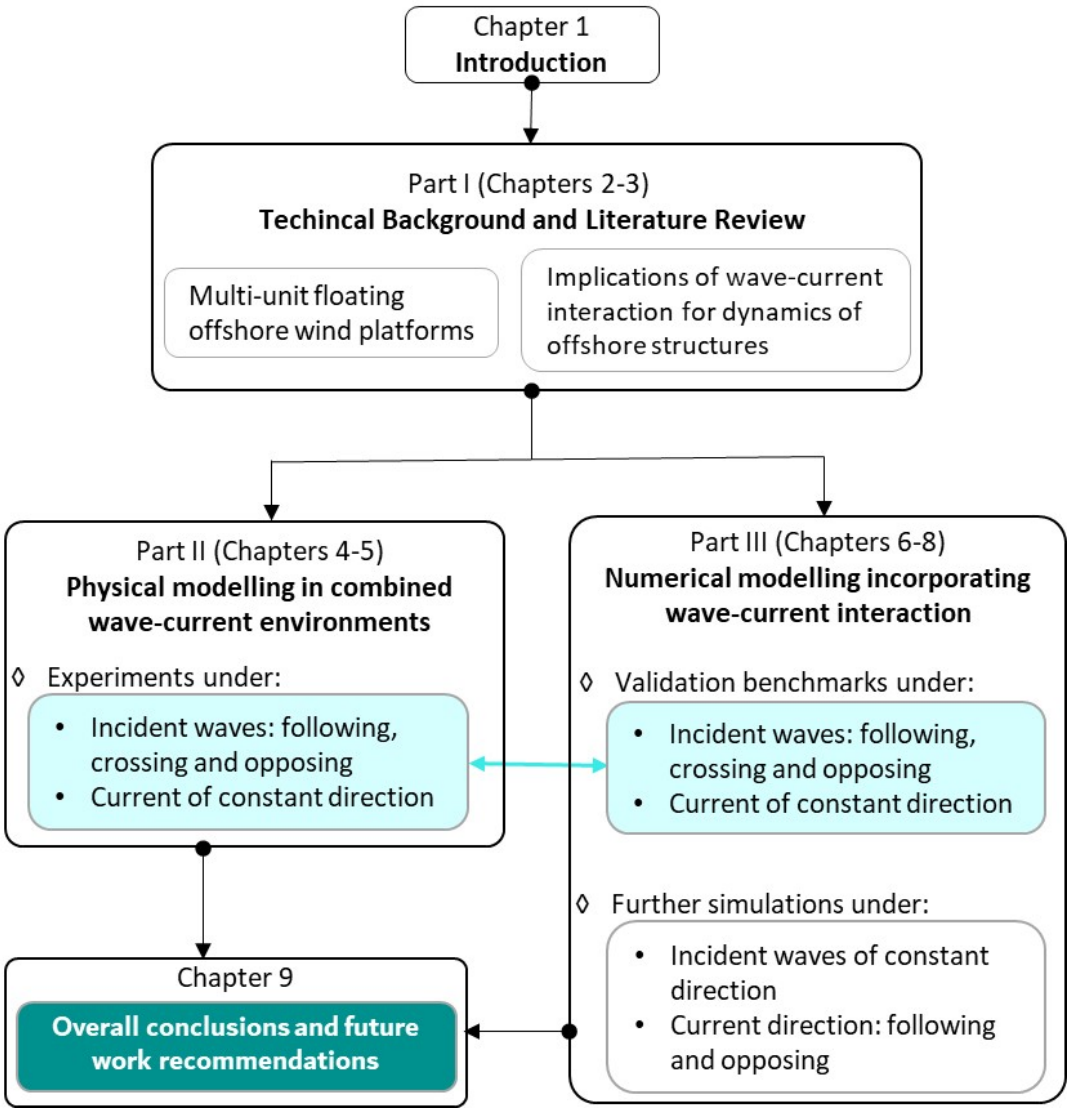

Figure 1.4: Overview of the project structure and chapters, illustrating the interconnections between main parts and chapters and their contributions to the analysis flow.

Part III: Numerical Modelling of MUFOWTs in Combined Wave-Current Environments

- **Chapter 6** introduces comprehensive **analytical and numerical analyses** to explore the effects of wave-current interaction on the structural responses of FOWTs. It begins by developing the W2Power floating platform and evaluating its hydrodynamic performance. The chapter further proposes a new mooring system and delineates the development of a coupled model encompassing floater-towers-nacelles-rotors. Then, simulations are performed under different environmental loads for the coupled analyses of aero-hydro-servo-elastic-mooring. These simulated loads include current, waves, and different wave-structure scenarios interacting with current.

- **Chapter 7** conducts comprehensive **validation benchmarks**, comparing the experimental findings from the tank tests against the numerical simulations. Firstly, the experimental measurements presented in Part II are up-scaled to full scale, and the numerical models developed in Chapter 6 are employed to simulate these tested conditions. Validations are then carried out to assess the accuracy and reliability of the coupled model of the W2Power FOWT, as well as the developed wave-current interaction models.
- **Chapter 8** offers a thorough discussion of the **numerical results** of the developed models of the W2Power FOWT and WCI introduced in Chapter 6. Firstly, it analyses the effects of following and opposing currents on regular and stochastic wave fields. Then, it presents the implications of wave-current interaction on FOWT dynamics. These encompassed the dynamic responses of platform motion, mooring system, and nacelles.

Chapter 9: Overall Thesis Conclusions

This chapter summarises the overall **conclusions** and contributions made about the presented research. Furthermore, it provides **recommendations** for future work that could be carried out to build upon the current findings.

1.9 Main Research Outcomes

1.9.1 Contribution to Knowledge

1. Two numerical models have been developed to investigate the implications of wave-current interaction on the dynamic responses of FOWTs and their mooring systems.
2. Established a framework that accounts for wave-current interaction in the coupled aero-hydro-servo-elastic analyses of FOWTs.
3. Demonstrated the importance of incorporating wave-current interaction in the numerical simulations of FOWTs and mooring systems.
4. Developed a model of a twin-turbine floating wind platform and developed its coupled floater-mooring-towers-nacelles-turbines model.
5. Designed a new single-point mooring system for FOWTs.
6. Showed to what extent wave directionality influences mooring loads and platform motions.
7. Developed an experimental model and provided validation data for testing FOWTs in combined wave-current conditions.
8. Proved the peculiarity of the developed FOWT model and showcased its capabilities to weathervane and dynamically respond to the dominant sea load.

PART I

Background and Literature Review

Chapter 2

Multi-Unit Floating Offshore Wind Platforms

2.1 Introduction

Given the scope of this EngD project, which explores the dynamic response of multi-unit floating offshore wind turbines and the implications of wave-current interaction on the dynamic behaviours of FOWTs by utilising the W2Power twin-turbine platform (EnerOcean S.L., 2007). Thus, it is imperative to scrutinise previous studies and developments of multi-unit floating offshore wind platforms. Specifically, the chapter reviews the work done so far on MUFOWPs and their mooring systems, highlighting the technical barriers hindering their commercialisation. In turn, this review provides the foundational understanding required to address the aims and objectives outlined in Section 1.7.

Offshore wind energy is growing rapidly and has significant potential to play a major role in future energy systems, especially if it can be harnessed with technologies that deliver it at a low LCoE. It is projected that by 2030, the LCoE for fixed-bottom offshore wind will decrease by an average of 30%, compared to a 2014 median-expert baseline value of $169/MWh, with a further 41% reduction by 2050. In contrast, early commercialisation of floating offshore wind is anticipated to yield a 25% cost reduction by 2030 and a 38% reduction by 2050, relative to the 2014 fixed-bottom baseline (see Figure 2.1). Floating offshore wind is expected to experience more rapid cost reductions through industrialisation compared to fixed-bottom, with cost parity expected in the long term (Wiser et al., 2021).

One of the key cost-reduction drivers is the turbine size of turbines. By 2030, turbines are expected to have an average capacity of 20 MW, with tower heights of 125 m and rotor diameters of 190 m. Market trends in the floating offshore wind industry indicate that 10-20 MW turbines will shortly be operational (see Figure 2.2) (Bauer, 2020).

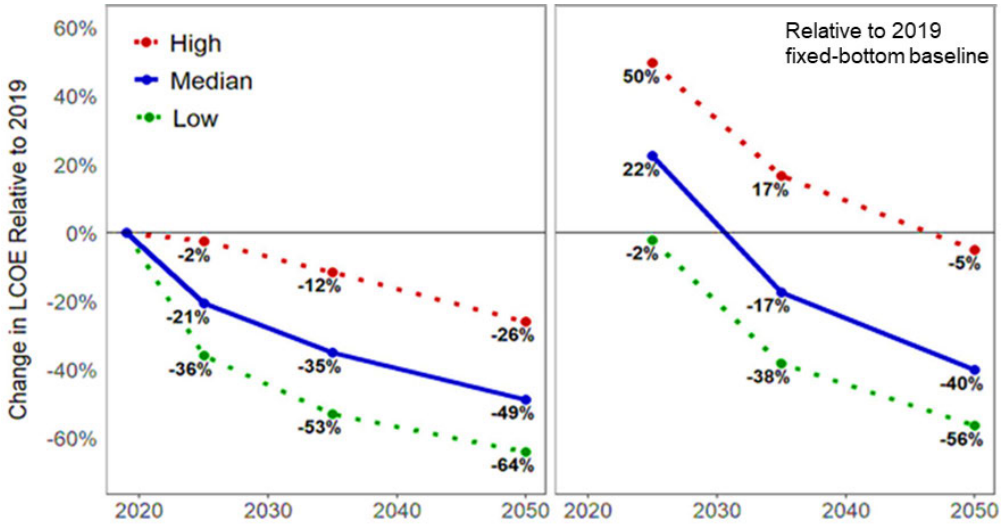

Figure 2.1: Estimated changes in LCoE for typical offshore wind projects in 2025, 2035, and 2050, under three scenarios: low (with only a 10% probability of lower LCoE), median (with equal chances of higher or lower LCoE)and high (with only a 10% probability of higher LCoE). These scenarios are expressed as percentages relative to the 2019 baseline values. Subplots show results for (left) fixed-bottom offshore wind and (right) floating offshore wind against the 2019 fixed-bottom offshore baseline; adopted from Wiser et al. (2021).

Furthermore, several factors influence lower costs for floating wind, with foundation and support structure design being the most crucial driver. Thus leading to reductions in CapEx and Operating Expenditures (OpEx), ultimately contributing to a lower LCoE. However, mounting such large turbines on conventional floating platforms as a single unit poses technical complexities and high costs.

In addition, given the infancy of floating wind, experts anticipate that its LCoE in 2025 will be higher than that of fixed-bottom installations from 2019 (Wiser et al., 2021), as evident in Figure 2.1. Thereby, MUFOWPs are being developed as viable innovations for boosting installed wind capacity per floating platform. Fundamentally, more than a single wind turbine will be mounted on the same structure, hence reducing costs per unit of generated power, such as CapEx, installation, and maintenance expenses. Therefore, the development of a MUFOWP model is inherently among the core objectives of this research outlined in Section 1.7.

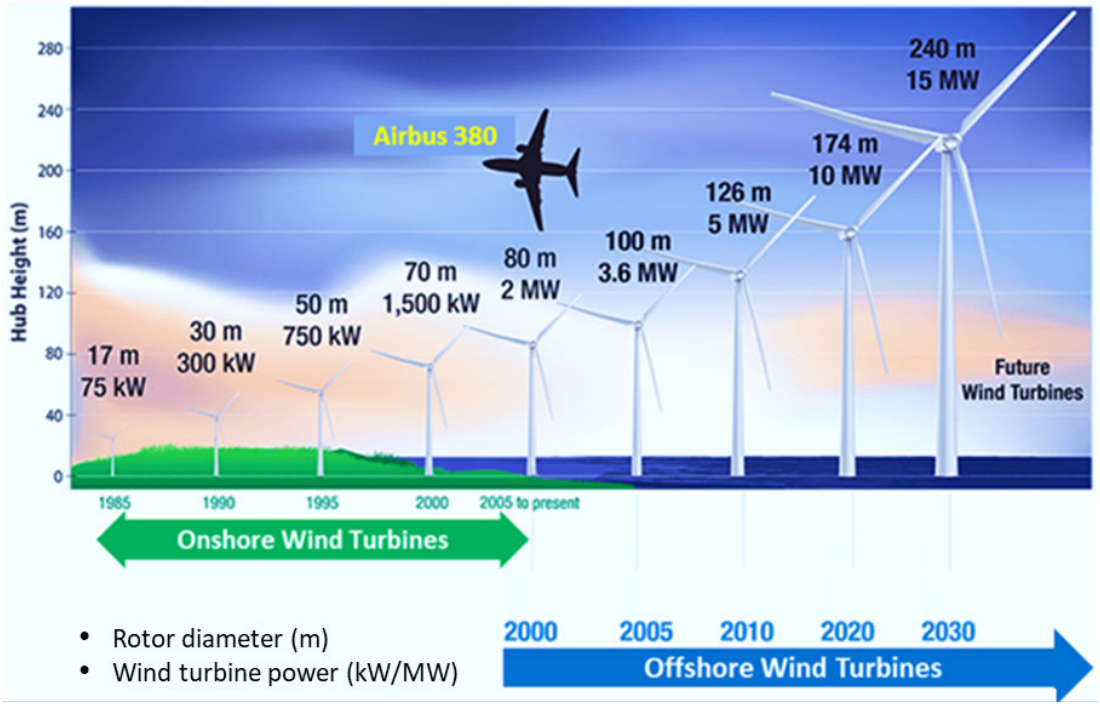

Figure 2.2: Evolution of wind turbine size and power output since 1980. Green grass at the bottom left half of the chart indicates land-based projects. Diagram illustrated by Bauer at NREL webinar - April 2020 (Bauer, 2020).

2.2 Advantages and Disadvantages of MUFOWPs

In 1993, Barltrop introduced the concept of MUFOWPs, which offer a range of advantages and disadvantages, though the following lists are not exhaustive (Barltrop, 1993).

Advantages

- **Cost-efficiency and transformers integration:** Up-scaling results in cost reduction, both in terms of cheaper installation per unit and lower production costs compared to conventional single units (A. Henderson et al., 2000), but also due to fewer anchors required for the same capacity (Pillai et al., 2022, 2022b). Moreover, transformers, essential in every wind farm, can be conveniently integrated into the platforms instead of constructing separate structures in single-unit wind farms. This approach streamlines the costs of logistics and marine operations while optimising functionality.
- **Improved stability and motion characteristics:** Larger structures can accommodate taller turbines, aligning with the growing trends in turbine height, weight, and power output; Figure 2.2. Thus, achieving static stability (i.e. anti-capsize) is more attainable on giant structures than on the smaller ones of single wind turbines (Bashetty & Ozcelik, 2020). As such, the next generation floating wind platforms are anticipated to be 100 m

wide and weigh around 5-7 thousand tonnes [†]. Furthermore, MUFOWPs effectively mitigate the chaotic and non-linear behaviours often seen in conventional FOWPs, particularly in extreme sea conditions (H.-K. Jang et al., 2019). The enhanced stability is attributed to the greater mass and dimensions of the platforms, which provide better resistance and resilience against turbulent conditions.

- **Enhanced accessibility, navigational advantages, and versatility:** MUFOWPs provide easier access to larger platforms, reduce travel requirements, and enhance wind farm visibility for nearby ships. Helicopter platform integration is also conceivable for rapid and dependable wind farm access. Moreover, deploying platforms further offshore creates additional navigation space, reducing the risk of collision and enhancing accessibility for maritime activities (A. R. Henderson, 2000).

Disadvantages

On the other hand, deploying MUFOWPs comes with several challenges (Barltrop, 1993):

- **Turbine spacing challenges:** Due to the imperative to minimise foundation size for cost-efficiency and mitigation of loads, aerodynamic wake interaction and turbulence issues, spacing between turbines is inherently challenging.
- **Unsuitability for shallow waters:** MUFOWPs are not applicable for shallow waters because their mooring systems require water depths that are over 70 m (A. Henderson et al., 2002).

2.3 Structural and Dynamic Aspects

To meet the demands of challenging environmental conditions, alternative concepts of MUFOWPs are being developed to ensure both reliability and cost-effectiveness. Research within the INNWIND.EU framework concluded that by keeping production costs constant and constructing larger turbine rotors, energy costs could be reduced by 20% (Natarajan et al., 2014; Chaviaropoulos et al., 2014; INNWIND.EU, 2020).

Typical MUFOWP designs accommodate two turbines, prioritising potential upscaling and modelling simplicity. MUFOWPs that support three wind turbines were conceptualised (Ishihara et al., 2007). Numerical and experimental assessments highlight the pivotal role of hydrodynamic of their hydrodynamic damping. While wind effects were evident on peak surge during operational drafts, they became negligible during survival drafts due to increased hydrodynamic damping (T. Ishihara et al., 2007; Van Phuc & Ishihara, 2007).

[†]. This information is obtained from a discussion with Dr Richard Wakefield (Flotation Energy) during the viva examination of this EngD thesis.

2.3.1 MUFOWP Concepts of Multi-Turbine Rows

2.3.1.1 Steel-Based MUFOWPs

The Korea Research Institute of Ships and Ocean Engineering (KRISO) introduced multiple MUFOWP models. KRISO's concept features a square frame structure with slender bracing elements and utilises a spread mooring system, with two mooring lines at each corner for station-keeping. The design accommodates four 3 M.W. wind turbines at the corners and incorporates six point-absorber-type WECs along each side. These models have been extensively studied.

For instance, H. Jang et al. (2015) employed Kane's dynamic theory to create coupled dynamic equations for analysing overall system motion and kinetics in the time domain (Kane, 1961). The rotor's rotation induced a gyroscopic effect in sway, roll, and yaw, particularly under maximum operational conditions. Heave motion and phase differences between the front and rear tower tops of upwind turbines exhibit significant accelerations, which increase the axial forces at the tower bases, an effect that should be considered in structural fatigue assessments.

Y. H. Bae & Kim (2015) used the KRISO platform to assess the impact of asymmetric aerodynamic loading on the overall performance and mooring line tensions of MUFOWPs. This was achieved by simulating a scenario where one turbine failed with a fully feathered blade pitch angle without accounting for aerodynamic interaction between turbines (e.g. wake effects). Results revealed that unbalanced aerodynamic loading from a single turbine in a MUFOWP significantly influenced both the platform and mooring dynamics (Y. H. Bae & Kim, 2015).

Additionally, Kang et al. (2017) conducted coupled hydroelastic analysis and assessed resonance risk and its impact on global and structural responses on the KRISO floating system. Resonance and non-resonance deformations were identified. Wind loads indirectly triggered resonant deformations by increasing mooring tension, which, in turn, influenced non-resonance deformations. Current and wave loads, in the absence of wind loads, induced strong drift and dominant low-frequency horizontal motion, leading to a reduction in most high-frequency hydroelastic responses (Kang et al., 2017).

On the other hand, Campagnolo et al. (2016) conducted wind tunnel tests on a KRISO model to validate two control strategies applied to MUFOWPs with closely spaced wind turbines. Results indicated that yawing turbines out of the wind direction could increase the produced power by up to 7%, depending on the power plant layout and wind speed. However, layouts with fully waked downstream wind turbines showed no power gains. Experiments also demonstrated that derating did not generally result in power gains.

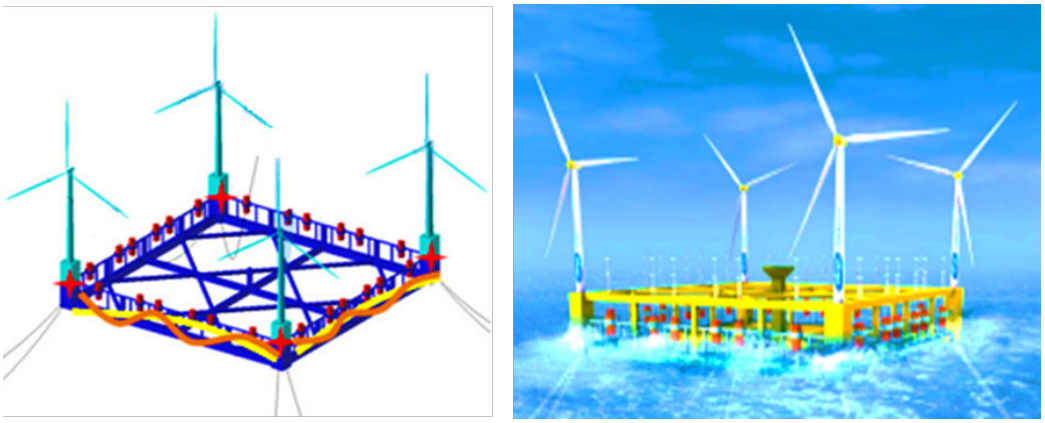

Figure 2.3: Rendered images of the 10 MW wind-wave hybrid platform, KRISO concept, developed by the Korea Research Institute of Ships and Ocean Engineering by the (Kang et al., 2017; H.-C. Kim et al., 2017).

H.-C. Kim et al. (2017) conducted numerical simulations and experiments using the same 1:50 Froude scale model employed by K. H. Kim et al. (2016) for systematic verification and validation (see Figure 2.3). The results demonstrated reasonable agreements between numerical simulations and measurements, especially in terms of surge, pitch, top mooring tension, and the mean horizontal offset. Wake effects on downstream turbines resulted in pitch asymmetry (H.-C. Kim et al., 2017).

To assess the impact of heave plates on MUFOWPs, H.-K. Jang et al. (2019) conducted extensive numerical simulations with and without heave plates. Subsequently, the simulations were rigorously compared with physical tests using the KRISO model. Heave plates effectively reduced both heave and pitch motions and altered their natural frequencies, all achieved with a minimal increase in platform mass. Conversely, platforms without heave plates exhibited more significant heave and pitch motions, with a maximum increase of 35% and 72%, respectively, than those with plates. Notably, there was almost no change in surge motion (H.-K. Jang et al., 2019).

2.3.1.2 Concrete-Based MUFOWPs

Concrete rafts have emerged as economical alternatives to steel MUFOWPs (Wong, 2015; S. Li et al., 2019; Lamei et al., 2023). As shown in Figure 2.4, these rafts come in two configurations: triangular, accommodating three turbines, or trapezoidal, hosting five turbines. Their capabilities in accurately tracking wind directions have been rigorously examined, both numerically and experimentally. The system flexibility was found to have a significant role in the surge and yaw responses of the floating structure (S. Li et al., 2019). The weathervaning mechanism was observed to influence the overall system dynamics. Changing the mooring system configuration can substantially alter the structure's motion under combined wind and wave loads (Lamei et al., 2023).

If engineered to endure over 100 years, following concrete bridge specifications, these rafts could serve four successive generations of turbine replacements. This extended serviceability, combined with the cost-effective prestressed concrete and the ability to support multiple turbines, significantly reduces construction costs. This, in turn, paves the way for capturing deep-water offshore wind resources (Wong, 2015).

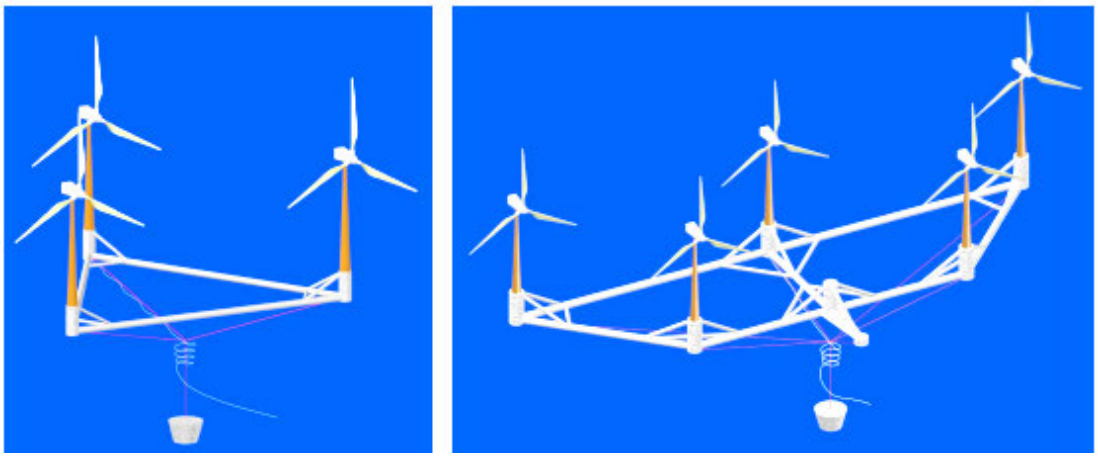

Figure 2.4: Semisubmerged concrete rafts as cost-effective alternatives to steel MUFOWPs. Left: triangular rafts designed to accommodate three wind turbines. Right: trapezoidal rafts engineered to host up to five wind turbines (Wong, 2015).

Likewise, in conceptualising raft designs, the National Maritime Research Institute (NMRI) has conducted studies on pontoon-type MUFOWPs to accommodate multiple wind turbines (NMRI, 2006). Experimental and numerical analyses by YAGO et al. (2006) affirmed the feasibility of these concepts for future deployments. Building on collaborative research by the Massachusetts Institute of Technology (MIT) and the National Renewable Energy Laboratory (NREL) (Wayman et al., 2006; Jonkman & Buhl, 2007), Iijima et al. (2010) performed further fully-coupled analysis and observed an interesting gyroscopic effect due to yaw motion, which remains not entirely understood. Furthermore, pontoon MUFOWPs were found to be susceptible to roll and pitch motions in extreme wave conditions, hence, limiting their deployments in calm seas, such as harbours, sheltered coves, or lagoons (Iijima et al., 2010).

2.3.2 Tension-Leg MUFOWPs

Applications of TLPs to support multi-turbine have been explored by Ren et al. (2010). Compared to the conventional single-turbine TLPs, multi-turbine TLPs were found to experience smaller yaw responses due to their large yaw inertia. This, in turn, effectively mitigated the acceleration responses of the top nacelles. However, the extended connecting cylinders of the multi-turbine TLP introduced significant additional hydrodynamic loads, resulting in larger sway, heave, pitch, and roll responses compared to the single-unit TLPs.

2.4 Multi-Purpose and Hybrid MUFOWP Concepts

To optimise the return on investment for large offshore wind farms, researchers have explored integrating additional revenue sources and maximising MUFOWPs utilisation. This pursuit has gained widespread interest due to the substantial costs of manufacturing, installing, and maintaining these large offshore wind farms.

The EU-funded "Modular Multi-use Deep Water Offshore Platform Harnessing and Servicing Mediterranean, Subtropical and Tropical Marine and Maritime Resources" (TROPOS) project investigates ambitious synergy implementations (TROPOS, 2012; Papandroulakis et al., 2017). It emphasises the advantages of deep-water installations for the aquaculture industry, with reduced pollutants and pathogens due to increased distance from the shore, ultimately benefiting aquaculture product quality (Papandroulakis et al., 2017).

Several MUFOWP concepts explore the integration of various energy sources, such as solar and wave power, into floating wind systems. For instance, C. Hu et al. (2013) introduce a triangular-shaped hybrid MUFOWP featuring three wind turbines at each corner and solar panels positioned between them. Additionally, H.-K. Jang et al. (2019) propose a large-scale square hybrid design holding four wind turbines and 24 wave energy converters on frames. Note that these designs are still in the conceptual phase.

In demonstrating the world's first operating floating combined wave and wind hybrid plant within the Poseidon project developed by Floating Power Plant, Kallesoe et al. (2011) analyse platform motion and turbine loading. This hybrid MUFOWP features three wind turbines and multiple Wave Energy Converters (WECs). Results reveal the platform's high stability, confirming its suitability for wind turbines. Turbines are also seen to enhance the platform's stability in high waves. Although the platform's motion increases the load on the towers, it does not affect blade loading.

2.5 Turret and Single-Point Mooring Systems

The design of MUFOWPs frequently overlooks the thorough analysis of mooring systems, which are critical for maintaining stability and ensuring correct positioning. Unlike single-turbine FOWTs, MUFOWPs can not rely on turbine nacelle yaw drives to align with the wind direction due to the potential risk of turbine blade clashing. Instead, the entire platform must be designed to yaw or weathervane to face the wind and ensure safe and efficient operation (A. Y. Liu et al., 2023).

Therefore, the use of rotating-turret systems has emerged as a viable solution for MUFOWTs, drawing from extensive experience in the oil and gas industry, where these systems have been employed for decades (Zanganeh & Thiagarajan, 2018). For instance, various offshore Floating Production Storage and Offloading (FPSO) vessels have been anchored via rotating-turrets mooring systems. Tests on scale turret models demonstrated effective heading stability and alignment with environmental forces (Zanganeh & Thiagarajan, 2018).

The application of turret and Single-Point Mooring (SPM) systems to FOWTs has resulted in innovative concepts utilising advanced mooring designs for improved performance (A. Y. Liu et al., 2023). As such, TetraFloat (TetraFloat, 2014), Scotstream's Spintral (Scotstream Generation Limited, 2023), the SelfAligner developed by DNV and Hamburg University (Netzband et al., 2020), and the BRUNEL concept (Brunel, 2023).

Floater developers have also focused on designing weathervaning turret and SPM systems tailored for FOWTs. Some of these developments are depicted in Figure 2.5 and include:

- EOLINK adapted the CALM concept for a four-column semi-submersible connected to a single-point mooring system using hawsers, tested in France (EOLINK, 2023).
- X1-Wind introduced the PivotBuoy® concept with a weathervaning turret mooring system and downwind turbine (X1-Wind, 2023), successfully demonstrated in the Canary Islands (Cahay & Milde, 2023).
- SAITEC designed a turret-moored concept with twin hulls and a turbine installed between them, deploying a 2 MW prototype in Spain (SAITEC, 2023).
- Aerodyn Engineering GmbH developed the SCD (Super Compact Drive)-Technology based on single-point moored FOWT concepts, including single and twin-turbine configurations tested in Japan (Aerodyn, 2023).
- Aerodyn also initiated the OPTIFLOW concept, a turret-moored FOWT with a guy wire-supported tower, tested in Japan (Schnepf, 2019; Aerodyn, 2023).

Weathervaning turret and SPM systems have proven to be highly effective in MUFOWPs. For instance, Floating Power Plant's (FPP) Poseidon concept, a hybrid wind-wave platform, utilises an SPM for passive rotation to align with waves, optimising wave energy absorption by up to 60-80% (FPP, 2023; Yde et al., 2014). The SCD-Nezzy^2 2×7.5 model underwent testing in the Baltic Sea, demonstrating its easily detachable turret system (SCD-Nezzy^2, 2014). EnerOcean is also advancing the commercialisation of the W2Power floating system, which incorporates weathervaning through a pivot point located at one vertex of the triangular-shaped platform (EnerOcean S.L., 2007).

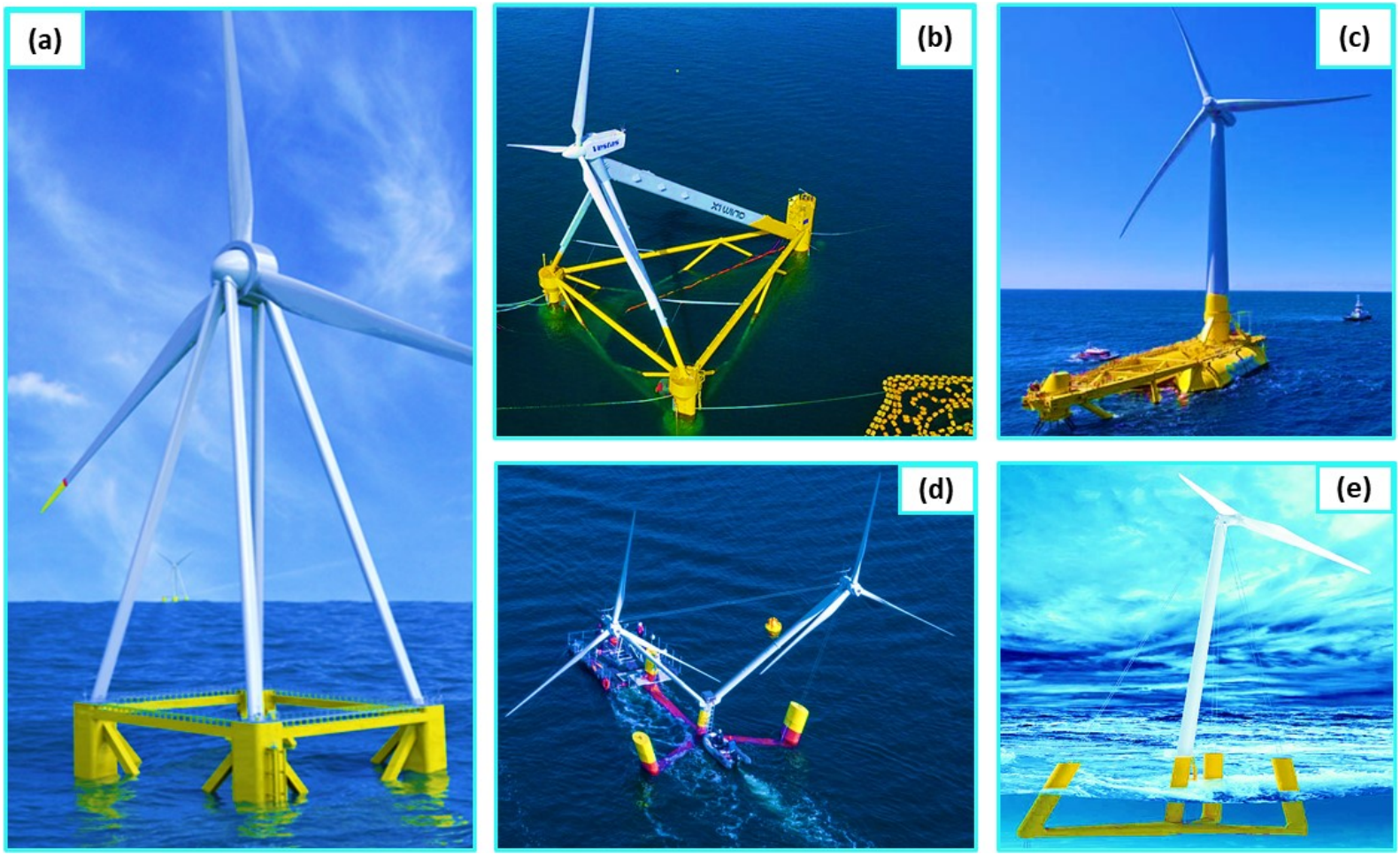

Figure 2.5: Artistic depictions visualising various FOWT concepts that utilise weathervaning turret and SPM systems: (a) EOLINK concept (EOLINK, 2023), (b) PivotBuoy® design (X1-Wind, 2023), (c) SAITEC concept (SAITEC, 2023), (d) SCD-Nezzy^2 concept (Aerodyn, 2023), and (e) PTIFLOW concept (Schnepf, 2019).

2.6 Twin-Turbine Floating Offshore Wind Platforms

Designing MUFOWPs capable of accommodating turbines in the same alignment is imperative to eliminate shading effects between upwind and downwind turbines. Consequently, developing turret-bearing systems for platforms that support more than two turbines is highly challenging and extremely costly. Moreover, mooring such platforms with non-weathervaning systems deprives them of the ability to orient towards the wind automatically, rendering them susceptible to wake interference from aligned turbines. This, in turn, results in increased dynamic loads on critical superstructure components, such as mooring systems and power dynamic cables (Y. H. Bae, 2013).

To obtain an ideal configuration for a twin-turbine platform, it is crucial to strike a balance between minimising wake interactions, ensuring acceptable tower base loads, and maintaining tolerable nacelle and platform accelerations and motions. This requires a comprehensive evaluation of platform weight, motion characteristics, tower loads, and nacelle accelerations across a spectrum of operational and extreme load scenarios that are typically known to drive FOWT designs (Hanssen et al., 2015; Udoh & Zou, 2020).

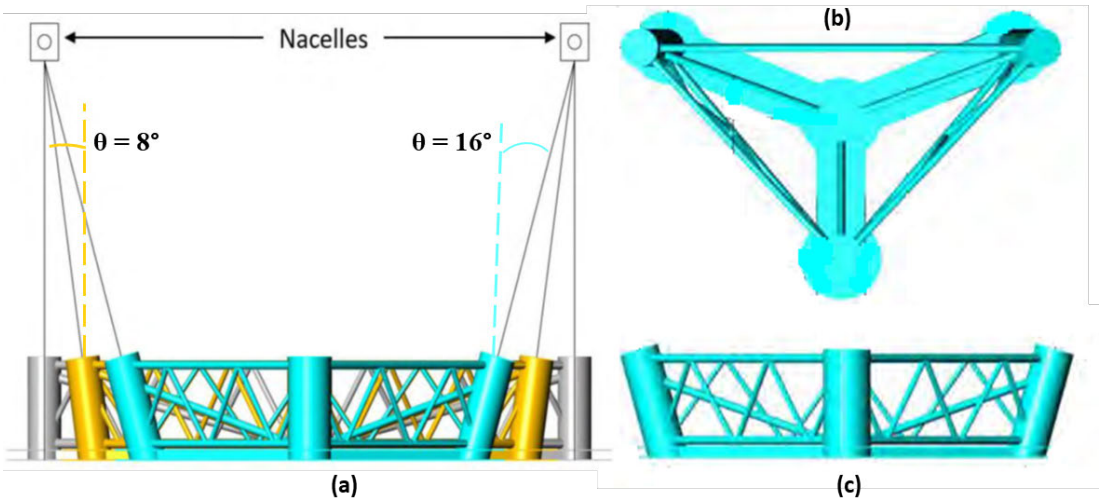

Figure 2.6: Visualisation of a twin-turbine floating offshore wind platform with a central-turret mooring system. (a) Combined elevation view of three configurations with optimised columns and towers: (grey) vertical, (yellow) inclined towers at 8°, and (turquoise) inclined towers at 16°. Views of the 16° inclined-towers configuration: (b) elevation, (c) plan. After Udoh & Zou (2020).

For instance, Udoh & Zou (2020) performed a parametric design analysis on a twin-turbine floating offshore wind platform featuring a central turret mooring system, see Figure 2.6. They assessed three configurations: a base case with vertical columns and towers, inclined towers at 8°, and inclined towers at 16°. Findings indicated that a reduction in platform length combined with outwardly inclined turbine towers resulted in favourable motion characteristics, thus demonstrating the feasibility of an optimal tower inclination (Udoh & Zou, 2020).

W2Power is also a successful pilot of a twin-turbine floating offshore wind platform (W2Power, 2010; EnerOcean S.L., 2007). Given that one of the objectives of this thesis is the development of a multi-unit FOWT, considering the W2Power concept as a case study, the TRL (Technology Readiness Levels) development trajectory and multi-use solutions of the platform are further detailed in Appendix A.

2.7 Chapter Summary

This chapter comprehensively reviewed various MUFOWP designs, such as steel-based, concrete-based, and pontoon-type platforms, and explored their hydrodynamic behaviours and stability under different environmental conditions. However, there remains a gap in how these MUFOWPs influence structural responses and mooring system dynamics of FOWTs under combined wave-current conditions. For instance, detailed investigations on how MUFOWPs mitigate dynamic loads or enhance operational efficiency in the presence of currents are underrepresented. In turn, Research Question 1 in Section 1.7 aims to explore the influence of a specific MUFOWP concept, W2Power, on structural responses of the floating system under wave-current loads.

Moreover, while existing literature underscored the necessity of integrating current effects into the design of FOWTs, there remains limited explicit detail on the methodologies and numerical models to be employed for accurate simulation of current-wave interaction. Thus, Research Question 2, Section 1.7, seeks to address this gap by examining the extent to which currents impact the design process of FOWTs and by investigating approaches to incorporate current effects into coupled analyses. This critical exploration will be further developed in Chapter 3, where an in-depth review will be explored on the implications of current and its interaction with waves on the motion responses of MUFOWPs and the dynamics of their mooring systems. Addressing these challenges and advancing robust analysis techniques are crucial for the successful commercialisation of floating wind technologies.

Chapter 3

Wave-Current Interaction and Its Implications for Offshore Structures

3.1 Introduction

The chapter aims to delve into the dynamic responses of FOWTs and their mooring systems in combined wave and current environments. It further identifies key challenges and knowledge gaps by critically evaluating existing research on FOWTs, wave-current interaction, and numerical simulations while suggesting potential areas for future research. This review lays the groundwork for subsequent chapters that will present original research aimed at exploring the extent to which tides and their interaction with waves impact the structural responses of FOWTs and the dynamics of mooring systems when deployed in wave-current environments.

3.2 Chronological Overview

The literature on theoretical approaches toward wave-current interaction has been extensively studied since the work of Barber (1949). Subsequent important contributions include the papers by Longuet-Higgins & Stewart (1960), Bretherton & Garret (1970), and Dalrymple (1973). Then the highly illuminating work by Peregrine (1976), Phillips (1977), Thomas (1979) and Jonsson (1990). These studies have laid the foundation for most investigations in this field and are the basis for the widely used spectral wave models crucial for forecasting in oceanic and coastal environments.

Waves are typically driven by wind, gravity, and tidal forces. Predicting the changes that random waves undergo when interacting with currents is relatively straightforward when the currents align with the waves. However, the effects become more complex when an opposing current exists due to increased wave-breaking events (T. S. Hedges et al., 1985). Additionally, when currents are oblique to the wave direction, the interaction can lead to wave refraction and diffraction, further complicating the wave dynamics and potentially increasing the variability and unpredictability of the wave field (Pascal et al., 2009; S. Draycott et al., 2021).

When waves and currents interact with each other, leading to the following mutual effects:

- **Effects of currents on waves:**
  - The interaction between waves and currents alters the wavenumber and frequency due to phenomena such as shoaling and refraction, where the depths and currents influence the dispersion relation of the waves. The Doppler shift theory explains these alterations by describing how the relative motion of currents to waves affects their characteristics. The Doppler shift theory explains how variations in wavelength occur, with following currents lengthening waves and opposing currents shortening waves (Jonsson et al., 1970; Jonsson, 1990; Masson, 1996; J. Smith, 1997).
  - Wave dynamics: Currents can modulate wave amplitudes, which affect the energy and height of the waves. These changes can impact the conservation of wave action, which is the principle that wave energy in a system remains constant unless acted upon by external forces (Jonsson et al., 1970; Moreira & Peregrine, 2012). For example, the interaction of waves with a current of a speed of 2 m/s can increase both their wavelengths and phase speeds by up to 26% under following currents and decrease them by up to 31% under opposing currents (Jonsson et al., 1970).
- **Effects of waves on currents:**
  - Induction of longshore currents: Waves generate longshore currents due to radiation stress, which is the force exerted by waves on the water column. This effect is particularly significant near shorelines, where it can shape coastal processes and sediment transport (Longuet-Higgins & Stewart, 1964).
  - Alteration of bottom friction coefficient: Waves modify the bottom friction coefficient for currents, impacting the vertical structure of current profiles and the overall energy dissipation in the boundary layer near the seafloor (Prandle, 1982).

3.3 Theoretical Framework

Novel frameworks developed to calculate the current and current-modified wave parameters have shown how the resulting combination largely determines the loading on offshore structures and floating buoys (A. C. Pillai et al., 2021). The dynamics of a coupled wave-current flow are governed by the Navier-Stokes (N-S) equations. These fundamental equations describe how the velocity field of a fluid evolves over time and space, taking into account various forces and fluid properties.

By solving the N-S equations, we can predict the interaction between waves and currents, which is key for addressing the research questions and objectives of the research project; refer to Section 1.7. The N-S equations consist of the energy, momentum, and continuity equations. The equation of continuity is given as:

$$\frac{\partial u}{\partial x} + \frac{\partial v}{\partial y} + \frac{\partial w}{\partial z} = 0 \tag{3.1}$$

and in a Cartesian coordinate system of x represents the streamwise direction and z represents the vertical, the momentum equations for an incompressible fluid with respective velocity components (u, v, w) are given as follows:

$$\frac{\partial u}{\partial t} + u\frac{\partial u}{\partial x} + v\frac{\partial u}{\partial y} + w\frac{\partial u}{\partial z} = -\frac{1}{\rho}\frac{\partial p}{\partial x} + \nu\nabla^2 u + f_x \tag{3.2}$$

$$\frac{\partial v}{\partial t} + u\frac{\partial v}{\partial x} + v\frac{\partial v}{\partial y} + w\frac{\partial v}{\partial z} = -\frac{1}{\rho}\frac{\partial p}{\partial y} + \nu\nabla^2 v + f_y \tag{3.3}$$

$$\frac{\partial w}{\partial t} + u\frac{\partial w}{\partial x} + v\frac{\partial w}{\partial y} + w\frac{\partial w}{\partial z} = -\frac{1}{\rho}\frac{\partial p}{\partial z} + \nu\nabla^2 w + f_z \tag{3.4}$$

where p, ρ, t and ν are the static pressure, density, time and kinematic viscosity, respectively. ∇^2 depicts the Laplacian operator in three dimensions; f_x, f_y, and f_z are the forces per unit mass acting on the body.

In a combined wave-current environment, the velocity and pressure components can be expressed as:

$$u = \overline{u} + \tilde{u} + \acute{u} \tag{3.5}$$

$$v = \overline{v} + \tilde{v} + \acute{v} \tag{3.6}$$

$$w = \overline{w} + \tilde{w} + \acute{w} \tag{3.7}$$

$$p = \overline{p} + \tilde{p} + \acute{p} \tag{3.8}$$

Substituting these equations, Equations (3.5) to (3.8), into the fundamental N-S equations, Equations (3.1) to (3.4), gives the corresponding equations for a combined wave-current motion. Note that the velocity component in each direction of the combined flow contains a periodic component in addition to the steady and random ones, which is also true for the pressure component. For a quantity N, its time-average over the samples is $\overline{N}$, $\widetilde{N}$ is its periodic component, $\langle N \rangle$ is its ensemble-average, and $\acute{N}$ is its turbulent component. For a wave with a period T and f cycles for ensemble-averaging, $\langle N \rangle$ and $\tilde{N}$ can be expressed by:

$$\langle N \rangle = \frac{1}{f}\sum_{j=0}^{f-1} N(t + jT), \quad 0 \le t \le T \tag{3.9}$$

$$\widetilde{N}(t) = \langle N \rangle - \overline{N}, \quad 0 \le t \le T \tag{3.10}$$

Scientists have employed various wave-current interaction models to solve these equations. These models can be categorised into two main types: numerical models and analytical approaches. The latter is thoroughly reviewed and accompanied by mathematical formulae involving simplified N-S equations based on specific assumptions to fulfil the objectives of this EngD thesis; refer to Section 6.8 for further details.

3.4 Numerical Models

Numerical models are computational tools used to simulate physical processes by solving mathematical equations that describe these processes. In the realm of WCI, numerical models solve the N-S equations to predict how waves and currents interact in various marine environments.

Early studies of wave-current interaction were conducted in laboratory-based wave tanks. However, with the advancements in computing, Computational Fluid Dynamics (CFD) numerical wave tanks emerged as an alternative, significantly reducing the associated experimental costs. Many researchers have investigated the combined wave-current interaction using the N-S equations by employing various CFD solver approaches and numerical wave tank simulations (X. Zhang, Simons, et al., 2022). Open-source and commercial CFD programmes, such as ANSYS's Fluent (ANSYS, 2016), are available for simulating flow dynamics.

The accuracy of such simulations is assessed by comparing experimental data with model validation results. Due to cost limitations, spatial constraints, and measurement capabilities, extensive experimental investigations on the wave and current interaction have been limited. In such cases, verifying the results of one CFD technique with another becomes conceivable.

Wave modelling employs two main methods: phase-resolved and phase-averaged models. Phase-resolved models are deterministic models that excel at depicting abrupt changes in waves (Fritts & Alexander, 2003). These models resolve individual wave phases, capturing rapid variations in wave characteristics over distances relative to the wavelength (X. Zhang, Simons, et al., 2022).

In contrast, phase-averaged models are spectral models that average wave phases over time and space. These models describe statistical properties such as significant wave height and wave period without resolving individual phases. The spectral nature of these models makes them particularly useful for long-term and large-scale simulations, providing valuable insights into wave climate dynamics and their applicability in climatology (Fritts & Alexander, 2003; X. Zhang, Simons, et al., 2022).

3.5 Theoretical and Numerical Studies

Extensive numerical and theoretical research have examined wave-current interaction and its impact on ocean dynamics. Numerical studies utilise computer models to simulate and analyse the effects of various factors, such as the currents' strength and direction and the waves' characteristics, on the ocean's dynamics. On the other hand, theoretical studies em-

ploy mathematical equations to analyse and comprehend the fundamental physics and underlying mechanisms governing this interaction using mathematical equations. In turn, theoretical investigations contributed to developing robust models that can accurately predict such interaction behaviour.

Longuet-Higgins & Stewart (1961) focused on wave-current interaction for regular waves, while N. E. Huang et al. (1972) examined random waves. In the case of linear regular waves, when the current is in the direction of wave propagation, the wave amplitude decreases and the wavelength increases. Conversely, when the current opposes the wave direction, the wave amplitude increases and the wavelength decreases, as depicted in Figure 3.1.

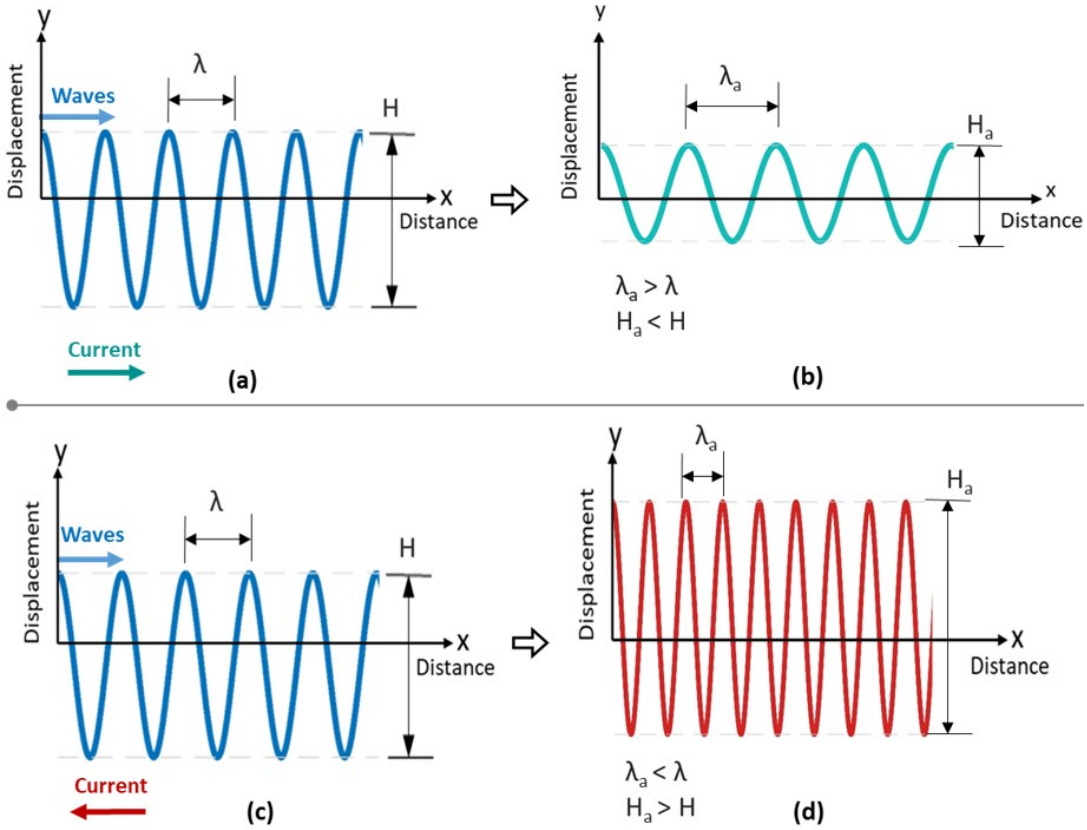

Figure 3.1: Diagram illustrating the interaction of pure waves with uniform currents. Changes are indicated in wave heights (H) and wavelengths (λ) due to interaction with current fields. Examples show waves interacting with a following current (a-b), where the wave height decreases and the wavelength increases. Also, waves interacting with an opposing current (c-d), where the wave height increases and the wavelength decreases. Subscript 'a' denotes the presence of current.

Similar behaviour, as observed by Longuet-Higgins & Stewart (1961), was encountered in random wave fields, leading to modifications in both the amplitude and position of the energy peak in the spectrum. Furthermore, the wave spectrum's root mean square (RMS) surface slope exhibits high sensitivity to changes in current conditions, particularly in opposing current scenarios. Integrating surface slope data with a generalised dispersion relation offers a potential current measuring approach for applications of current measurements (e.g. stereoscopic photography and radar scattering) (N. E. Huang et al., 1972).

Tung & Huang (1974) investigate the effect and sensitivity of current on many statistical features of irregular waves (such as the amplitude of maxima, number of zero crossings and specular peaks). It was found that the presence of the current moderately influences the statistical features of sea surface maxima, whereas the zero velocity, specular point, and point of inflexion are significantly influenced.

These parameters are crucial for assessing the impact of waves on marine and offshore structures (Faltinsen, 1993). For example, the amplitude of maxima affects the design loads on structures, influencing their stability and safety. The number of zero crossings relates to the frequency of wave loading, which impacts fatigue life. Specular peaks and points of inflexion are critical for understanding wave-structure interactions, affecting how forces are distributed along the structure (Clemens et al., 2008). Therefore, understanding these influences is essential for designing resilient and efficient marine structures.

In line with N. E. Huang et al. (1972), incorporating these characteristics can help extract current measurements effectively from wave records by employing remote sensing devices. Burrows & Hedges (1985) demonstrated the influence of currents on the characteristics of an integrated wave. T. Hedges (1987) Hedges (1987) states that including wave-current interaction is critical in studying bottom pressure data for waves and calculating energy spectra, refraction and loads on offshore structures, particularly under extreme waves.

Jonsson (1990) provided an overview of wave-current interaction and explored the impacts of depth-varying currents and their consequences when waves propagate into tidal-driven flows. Hedges & Lee (1992) provided a set of formulas for predicting a uniform equivalent current in wave-current analysis. Soulsby et al. (1993) investigated WCI in a transverse plane, covering wave kinematics and dynamics, bottom shear stresses, and wave-induced mass transfer. They demonstrated that a mean current estimation can accurately predict the wavelength and bottom orbital velocities. It was shown that currents on the North-western European continental shelves (i.e. the North Sea) influence wave models and must be considered unsteady (Tolman, 1990, 1991b,a).

Wolf & Prandle (1999) explored potential interaction mechanisms between waves, tides, and surges. Based on SCAWVEX project data (Wyatt et al., 1998), they examined the effects of depth and current variations on waves and the reciprocal effects of waves on tidal currents. Their findings revealed that wave-induced changes in tidal currents predominantly occur in water depths below 50 m, whereas, in shallower water with a depth of fewer than 20 m, a dramatic effect manifests as dispersive point wave velocities for waves with periods longer than 6 s. The apparent amplitude of tidal currents decreased as wave height increased; they also recommended concurrent monitoring of waves and currents in shallow waters.

Researchers have widely utilised singularities to model free-surface flows, providing valuable insights into various natural phenomena' fundamental aspects and complexities. The pioneering work of Lamb (1932) highlighted the importance of singularities in free-surface flow modelling. In fluid mechanics, singularities have found applications in studying nonlinear effects caused by underlying currents and understanding disturbances on the free surface induced by vortex and sink flows (Tuck & Vanden-Broeck, 1984; Vanden-Broeck & Keller, 1987; Mekias & Vanden-Broeck, 1989; Mekias & Vanden-Broeck, 1991). Contributions in modelling underlying flows employing singularities have been made by Tyvand (1991, 1992), Hocking & Forbes (1992), Miloh & Tyvand (1993), Barnes et al. (1996), Xue & Yue (1998), (Moreira, 2001), Stokes et al. (2003, 2008) and Suastika & Battjes (2009).

Moreira & Peregrine (2010) developed a fully nonlinear model to investigate the interaction between a free-surface flow with surface tension and a submerged cylinder. Once the waves have dissipated, it was found that unsteady flows tend to converge towards a steady solution, whereas a steady solution was not attained in some cases. Intriguing phenomena were also observed close to the free surface, including the emergence of "parasitic capillaries" and the formation of capillary-gravity waves upstream of the submerged cylinder. Inspired by the experimental investigations of Chawla & Kirby (1998) and Suastika et al. (2001), Moreira & Peregrine (2012) further modelled the interaction between wave groups and currents numerically. The analysis involved identifying the number of waves within each group by calculating the frequency difference between two monochromatic waves with similar amplitudes but slight frequency variations. They addressed the initial constraints by superimposing two uniform wave-train components, focusing on the cleanest wave groups (i.e. bichromatic waves with zero energy transmitted to the sidebands).
Q. Yang & Liu (2018) simulated wave-current interaction in the Yellow Sea using a RANS (Reynolds-Averaged Navier-Stokes) model. His observations revealed a significant reduction in wave height and an increase in wave period due to the presence of currents. This has significant consequences on coastal and offshore structures as they are designed to withstand certain wave heights and periods that may not withstand the actual wave conditions in the presence of currents.

3.6 Experimental and Validation Studies

Experimental investigations have been conducted to validate the accuracy of the theoretical frameworks. Brevik & Bjørn (1979) and Brevik (1980) performed wave-current experiments in large-scale flumes with rippled and smooth beds, respectively. In all tests, the average velocity was measured by adopting a micro-propeller and was found to decrease as the wave propagated with the flow. The friction factor was estimated by the wave-attenuation method and was found to be more accurate when using a seabed with ripples (Brevik, 1980). The results of the rippled bed tests were reasonably consistent with the findings of Jonsson (1966) and Van Hoften & Karaki (1976), yet in contrast with those of Jonsson & Carlsen (1976). Similarly, the results from the smooth bed experiments were in reasonable agreement with the predictions of linear wave theory.

The Airy wave theory and Stokes wave theory are some of the wave theories used to calculate wave forces on offshore structures (Thomas, 1981). The former is the foundation for the commonly used models for linear wave-current interactions. These models consider the changed wave frequency and wave dispersion relation due to an underlying current.

Thomas (1981, 1990) developed two numerical models for the interaction of currents of arbitrary vorticity with linear and nonlinear regular-wavetrains. The linear wave model was based on the Airy theory, whereas the second model was extended from the work of Dalrymple (1973, 1977). Furthermore, experiments were undertaken to provide validation data, and a good agreement was obtained between the models and tests regarding the predictions of the wavelengths and velocities of the particles travelling through the waves (Thomas, 1981, 1990).

Experiments have investigated how wave superposition changes turbulence properties, such as boundary layer thickness and velocity profile. Bakker & Van Doorn (1978) researched wave paths where waves propagate with the current over a rocky bed. They employed Laser Doppler Velocimetry (LDV) to derive velocity distributions and compared them with theoretical solutions using mixed-length theory. The experiments focused on horizontal oscillating flow, particularly relevant to oscillating water tunnel data. The measured instantaneous mean velocities agreed with the predictions of Bakker's first developed model Bakker (1974) and the improved one Bakker & Van Doorn (1978), thereby validating the hypothesis.

Utilising a LDV, Umeyama measured Reynolds stress and velocity components in a combined wave-current environment (Umeyama, 2005, 2009). Wave characteristics (e.g. height and period) were found to be related to the mean velocity and logarithmic profile differences. Flow reversal near the bottom was detected, indicated by the average phase of horizontal velocity. Consequently, a lagging behaviour in the velocity profile was observed. He further employed Particle Imaging Velocimetry (PIV) and Particle Tracking Velocimetry (PTV) to track water

particle trajectories and capture instantaneous velocity fields. In the presence of a current, the periodic circulations (i.e. made up of clockwise and counterclockwise vortices) lost their structure, although they should be distinguished from horseshoe vortices within the turbulent boundary layer (Umeyama, 2011).

In a laboratory flume, Singh & Debnath (2016) experimented then combined wave-current effects in a free-surface turbulent flow. An ADV was utilised to measure velocities and then analyse the turbulent characteristics of the complex wave flow. They observed changes in the mean velocities, Reynolds shear stress, and turbulence intensities due to the interaction between waves of varying frequencies and a current-only flow.

Furthermore, the average velocity profile exhibited a distinct dip in the upper zone and increased near the bed. This is crucial as it indicates potential issues for marine structures: reduced flow in the upper zone could affect sediment transport and scour, while increased velocities near the bed imply higher shear forces that can increase erosion and structural loading. Deviations from the known turbulent boundary layer behaviour were also observed, hence, emphasising the need for reliable experimental data to understand the quadrant contribution to Reynolds shear stress (Singh & Debnath, 2016).

Sleath (1993) looked at the velocity field and flow kinematics in complex flows where waves propagate perpendicular to the flow. Different bed designs were tested using a vibrating bed flow flume to simulate a mixed wave boundary layer. LDV was employed to quantify velocity, revealing that the average velocity distribution aligns qualitatively with the flow field when the flow carries the wave. Building upon this technique, Ranasoma & Sleath (1994) extended the experimentation to include the effect of bed ripples. It was found that a logarithmic distribution was applicable in the outer region but not near the bed, attributed to the formation and shedding of eddies near the ground.

In addition to the contributions of Bakker & Van Doorn (1978), Brevik & Bjørn (1979) and Brevik (1980), Kemp & Simons (1982, 1983) conducted experiments to investigate the turbulence characteristics of the wave boundary layer and wave-current interaction near the seafloor. All experiments were then validated against the theoretical models developed by Davies et al. (1988) and Fredsøe (1984), and reasonable agreements were obtained, particularly with the measurements of Bakker & Van Doorn (1978). Based on experimental data obtained from the UKCRF (Simons et al., 1995, 1997), Myrhaug et al. (2001) extended the approach proposed by Myrhaug (1995) to investigate bottom friction under combined random waves and both orthogonal and near-orthogonal currents. Fernando et al. (2011) measured the velocity across the uneven seabed using an ADV in a wave pool (i.e. length 24 m, width 10 m, depth 0.9 m. The orthogonal regular waves were found to slow down near-bed velocities.

Lim & Madsen (2016) employed an ADV in the National University of Singapore Hydraulic Engineering Laboratory to experiment periodic waves interacting with near-orthogonal currents over smooth and uniform fixed roughness beds. A linear interaction was observed in the smooth bed scenario. As a result, they found that the perception of roughness predicted by Grant & Madsen (1979) is overestimated for large angles of WCI. Faraci et al. (2018) conducted comprehensive experiments on the velocity distribution and turbulent variability of orthogonal waves and currents over a bed with varying roughness elements, in which velocity was measured by a MicroADV. It was revealed that the probability density functions of the total velocity close to the bed can be described by Gaussian and double-peak distributions for the stream-only and coupled wave-current flux scenarios, respectively. Thus providing new perspectives on the statistical properties of near-bed velocities. In a larger tank, Faraci et al. (2021) further examined how the current-to-wave velocity ratio and bed roughness affect the apparent roughness. Regardless of the bed roughness type, it was discovered that adding waves to a current-dominated flow increases the flow resistance, whereas the contrary occurs when the flow is wave-dominated.

Inspired by their numerical simulations using the cutting-edge spectrum model, SWAN (Rusu & Guedes Soares, 2007), Rusu & Soares (2011) conducted large-scale experiments on a vertical U-tube at the Danish Hydraulic Institute's 3D offshore wave basin. The analysis of the wave frequency spectrum indicated that the following (adverse) current resulted in a substantial decrease (increase) in wave height, and the experiments and simulations agreed well and were consistent with those published by (Nwogu, 1993; Suh et al., 1994; S. K. Chakrabarti, 1996; Soares & De Pablo, 2006).

Hashemi et al. (2016) developed a simplified method based on the linear wave theory. After validation with data from two energetic UK shelves with strong wave/current interaction (i.e., Pentland Firth and Bristol Channel), the method demonstrated high accuracy. As a result, it can be utilised to effectively predict the impacts of tidal currents on the wave energy resource. Utilising the state-of-the-art FloWave of the University of Edinburgh (D. Ingram et al., 2014), comprehensive investigations have been carried out to assess the impact of currents on waves in basins and to isolate incident and reflected wave spectra in the presence of current, as well as several tools and frameworks were developed for testing physical scale models in combined wave-current environments (Noble et al., 2015; Sutherland et al., 2017; Noble, 2018; S. Draycott, Steynor, et al., 2018; S. Draycott, Noble, et al., 2018; S. Draycott et al., 2019; Noble et al., 2020; A. C. Pillai et al., 2021; S. Draycott et al., 2021; Gabl et al., 2021).

3.7 Offshore Structures and Wave-Current Interaction

Waves and currents coincide in oceans and coastal regions, making them the most significant factors governing the hydrodynamic behaviours of coastal and offshore structures (e.g. floating breakwaters, oil rigs, and renewable energy devices). Since currents influence wave-related parameters (e.g. wavelength, amplitude, direction of propagation, and energy density spectrum), thus, higher-velocity ocean currents significantly impact the wave-current interaction (Wolf & Prandle, 1999; Tayfun et al., 1976). Moreover, low-velocity ocean currents have a considerable impact on these wave parameters. In real-world engineering settings, the wave and the current typically coexist. Therefore, it is crucial to estimate the velocity movements that may induce extremely significant horizontal excursions caused by synchronisation between floating structures and wave-current loading.

Utilising the Airy wave theory, Tung & Huang (1973) investigated the influence of WCI on the response of slender structures by employing the Morison equation Morison et al. (1950). Iwagaki & Asano (1984) conducted flow visualisation tests to analyse the vortex characteristic around a slender cylinder in a wave-current coexisting environment, and the hydrodynamic forces acting on the cylinder were also examined.

Using a time-domain approach, (Isaacson & Cheung, 1993) examined the impact of current throughout a two-dimensional body (i.e. semi-submerged circular cylinder) while considering wave radiation and diffraction. It was demonstrated that the significance of current or forward speed influences large offshore structures in wave environments. In contrast, three-dimensional floating structures exhibited distinct behaviours when subjected to the combined effects of wave-current diffraction and radiation, in contrast to pure wave action. A higher-order time-domain boundary element method was developed by Zhen et al. (2010) to simulate the interaction of these structures with wave-current conditions. Compared to frequency domain techniques, the method showed excellent agreement in predicting the body's response, wave run-up, and wave-induced forces.

From 20 to 25 years ago, several research projects focused on investigating the effects of wave-current interaction and calculating wave drift damping on offshore structures (Pan et al., 2016). New methods have been introduced to assess wave drift damping in which the frequency domain zero speed velocity potentials are rectified by including the first-order disturbed components resulting from the sluggish forward speed (Nossen et al., 1991; Finne & Grue, 1998; Finne et al., 2000).

For large structures, using the diffraction theory (Chakrabarti, 1987), Watanabe (1982) assessed the wave-current forces resulting from the interaction of plane waves with currents. They found that the wave dispersion relation in the flow field around the structure varies with position coordinates but reduces to the dispersion relation for waves on still water at stagnation points.

Jian et al. (2008) researched the wave-current forces exerted on a bigger-size cylinder by interacting short-crested waves with ocean currents. Wave-current interactions were found to have a relatively small effect on the structural response of the large-size rigid structures, which can be attributed to the fact that these structures are fundamentally designed at frequencies considerably higher than the frequency of the predominant waves (Wu, 1976).

Saruwatari et al. (2013) investigated the effects on marine energy converters and found that strong currents of up to 3 m/s when interacting with large waves can increase or decrease wave energy by up to 60% at maximum. Furthermore, local effects can increase considerable wave height by 150-200% when these large waves oppose the current. Therefore, an in-depth understanding of the WCI at such locations is required during both the development and operational phases of marine energy projects. Particularly for a wind farm at a typical site with strong tidal currents and sheltered wave conditions. (Saruwatari et al., 2013; D. M. Ingram, 2011).

Based on the Boundary Element Method (BEM), Ryu et al. (2003) developed a numerical wave tank (NWT) to investigate nonlinear wave-wave and wave-current interaction and the subsequent kinematics. It was found that the implications of such nonlinear interaction effects are crucial for the design of coastal and offshore structures. Employing ANSYS Fluent Solver (ANSYS, 2016), CFD simulations in a viscous numerical wave tank were done by S.-Y. Kim et al. (2016) to further investigate the loads of wave-wave and wave-current interaction on fixed offshore substructures. The numerical results demonstrated that wave loads in conditions with wave-current interaction exceed those predicted by a linear combination of wave and current loads due to non-linear wave deformation effects.

These simulations were then rigorously validated against experimental data from Chakrabarti & Tam (1975) and the Morison et al. equation (Morison et al., 1950). S.-J. Kim & Kim (2022) developed a three-dimensional, fully nonlinear potential-flow-based NWT to examine wave-current-body interaction on fixed and floating structures. It was demonstrated that WCI affects second-order wave loads (mean drift force) more than first-order wave loads, particularly near the resonance region. The model accurately predicted the wave frequency, mean-drift wave loads and wave drift damping when verified against Kinoshita & Bao (1996) and D. Kim & Kim (1997). Among various CFD codes like REEF3D, OpenFOAM and CFX, ANSYS-Fluent was found to be the most reliable and user-friendly software for modelling fluid-structure interaction near the free surface in offshore environments, particularly for complex multi-component structures (Ahmed et al., 2020).

Systematic experiments were conducted by L. Chen et al. (2022) to explore the effects of WCI on the pore-water pressures around a monopile in a two-dimensional wave flume. Around the monopile, the hydrodynamic and seafloor responses induced by irregular WCI were stronger than those brought by regular WCI. For CALM (Catenary Anchor Leg Mooring) buoy structures, WCI was found to considerably affect their stability, hydrodynamic characteristics, and deformation. Therefore, buoy manufacturers must consider WCI when constructing these buoys (Amaechi et al., 2022c,b,a; Ju et al., 2023).

WCI is a key optimisation factor for marine current turbines, alongside parameters like underwater positioning and blockage effects (Rotor, 2023). Ongoing research highlights substantial velocity variations throughout the water column, even in relatively sheltered sites (Sellar et al., 2017). Since wave direction relative to current determines the level of wave-current interaction, high currents at certain angles to the incident wave potential can significantly impact the turbine's efficiency and health. Hence, for resource characterisation and assessing implications on turbine performance and its control system, WCI must be thoroughly considered when evaluating potential deployment locations (de Jesus Henriques et al., 2014; Tatum et al., 2016; Rotor, 2023).

Floating wave buoys were tested in combined wave-current environments by S. Draycott et al. (2022). Large pitch and heave motions are observed in high-frequency opposing WCI conditions due to higher wave heights and increased wavenumbers caused by current. Yaw motions are insignificant, very low-frequency, and unrelated to wave forcing in wave-only conditions. Following currents reduce heave motion while opposing currents increase them, a phenomenon induced by additional restoring forces due to the nonlinear coupling effect of heave and pitch. Furthermore, currents and their interaction with waves induced large vortex-induced motions (VIM) exceeding the buoy diameter.

3.8 WCI Implications on Bottom-Fixed Offshore Wind Turbines

Offshore wind turbines (OWTs) are subjected to various environmental loads, such as wind, waves, currents, earthquakes, and ice loadings (Van Der Tempel et al., 2011), Figure 3.2. Several investigations have been carried out to determine their dynamic behaviours. Bottom-fixed offshore wind turbines mostly dominate offshore wind installations today. Despite the importance of wave-current interaction on the dynamic responses of offshore wind turbines, there have been relatively limited studies in this area. In shallow and intermediate water depths, the potential impacts of the WCI on fatigue loading of bottom-fixed wind turbines were identified physically (i.e., using in-situ measurements) (Peters & Boonstra, 1988) and emphasised numerically by methods of spectral fatigue analysis (Peeringa, 2014). Including

WCI in the calculation of design loads for these structures leads to an increase in fatigue load by 11% and a reduction in the 20-year fatigue life by 5% compared to scenarios where WCI effects are not considered (Peeringa, 2014). Thus, integrating WCI considerations is crucial in the design of offshore wind turbine structures (Peters & Boonstra, 1988; Peeringa, 2014).

Santo et al. (2017) experimentally validated the application of simple porous blocks to mimic complex space-frame structures (e.g. truss offshore wind platforms) under combined large waves and in-line currents. Flow behaviour shows significant similarity between regular waves with in-line sheared and uniform current: the wake downstream of the tower is strongly influenced by the waves, while flow within the tower remains relatively straightforward. The diagonal loading configuration attracts higher forces, emphasising the structural orientation's role in the structure's survivability. Comparisons with the analytical current blockage models of Taylor et al. (2013a) and Taylor et al. (2013b) for steady uniform current, as well as Santo et al. (2015)'s CFD numerical simulations, demonstrate overall good agreement in terms of peak forces and force time history shapes.

X. Chen et al. (2014) modelled the effects of WCI on a single-pile OWT (Rogers & Still, 1999). WCI resulted in a 17.6% relative error in the free surface elevation and up to 26.88% differences in wave-current loads. The turbine subsequently has experienced substantial and irregular dynamic responses. In locations of strong currents of the same order of magnitude as the wave kinematics (e.g. South China Sea), WCI can raise average loads on fixed structures by 15%. Thus, accounting for WCI is important when calculating the ultimate base shear and overturning moments for these structures (Latheef et al., 2018).

The impact of WCI on sediment scouring around fixed wind turbine structures has been a topic of recent research (Lin et al., 2023). The scour depth was found to increase with the incident wave height at the turbine pile. Considering WCI is crucial for accurately estimating and predicting the scour pit's shape and depth (Aminoroayaie Yamini et al., 2018). Installing OWTs in seismic regions requires accurate simulation of dynamic soil-pile interaction, which is challenging. The complexity arises from soil nonlinearity due to wind-wave loads and pile scour induced by WCI (Liang et al., 2022, n.d.). WCI was also discovered to impact seabed instability near a jacket foundation, with a notable effect with a following current. This interaction tends to liquefy the seabed more significantly around downstream piles than upstream piles (Wei et al., 2022).

P. Wang et al. (2019) analysed short-crested wave diffraction interacting with uniform currents on an axisymmetric composite bucket structure. The wave's incident angle relative to the current velocity notably influences wave run-up, wave forces, and inertia and drag coefficients, particularly when waves and currents are aligned. WCI's effects increased with increased total wave numbers and decreased water depths. Thus, WCI-induced loads should be meticulously considered in the design of the composite bucket foundations for OWTs.

Y. Hu et al. (2020) pioneered experimental research on the influence of wind-wave-current interaction on the towers' dynamic responses of monopile offshore turbines. Compared to wave effects, the current field has a pronounced effect on the monopile dynamics, particularly under WCI events.

Integrated offshore wind and aquaculture applications are important because they represent innovative approaches to maximising ocean space utilisation. Studies have shown that WCI has minimal impacts on system dynamics in such integrated setups (H.-Y. Wang et al., 2021). These limited impacts can be attributed to the effectiveness of the circular cages in wave resistance (Beveridge, 2008). Compared to the traditional solid-floating structures, P. Wang et al. (2021) found that air-floating structures significantly reduce structural responses when subjected to combined wave-current loads, indicating their practical feasibility to support wind turbines.

3.9 WCI Implications on Floating Offshore Wind Turbines

For the design and lifetime safety of FOWTs, the dynamic response in storm conditions, as well as the static stability and coupled dynamic response under operation conditions, are of paramount importance and, hence, have been an ongoing research focus. Analyses of FOWTs must consider complex external loading conditions caused by wind, waves and currents, along with structural loads such as hydrostatic pressure and ballast loads. Therefore, understanding the dynamic behaviours of FOWTs, such as platform motions and mooring dynamics, is essential for designing an optimal floating system that withstands harsh offshore conditions (J. M. Jonkman & Matha, 2011; Butterfield et al., 2007; A. C. Pillai et al., 2018a).

Sea currents are a potentially significant loading source for FOWTs that act as a constant lateral drag force on the platform, dynamic export cables, and mooring lines (Matha et al., 2011). Marine growth should also be considered in these assessments since it impacts flow and surface roughness, directly influencing the drag coefficient of the system elements. The flow characteristics and drag increase due to marine growth are crucial factors to account for in these simulations (Wright et al., 2016; Spraul et al., 2017). DNV offshore standard recommends that they should be accounted for in mooring simulations (DNV-OS-E301, 2010).

Nevertheless, previous investigations utilising linearised or quasi-static cable models disregarded the current effects on mooring lines (J. M. Jonkman, 2007). These currents affect the operating point of the mooring system of FOWTs and result in the mooring lines' static, dynamic, and damping responses (Hall et al., 2014). Moreover, for the overall floating system, currents can cause floater VIM, static offset, and augmented wave drift forces (Gon†calves et al., 2021). These currents can be triggered by winds, tides, or density changes, as illustrated in Figure 3.2.

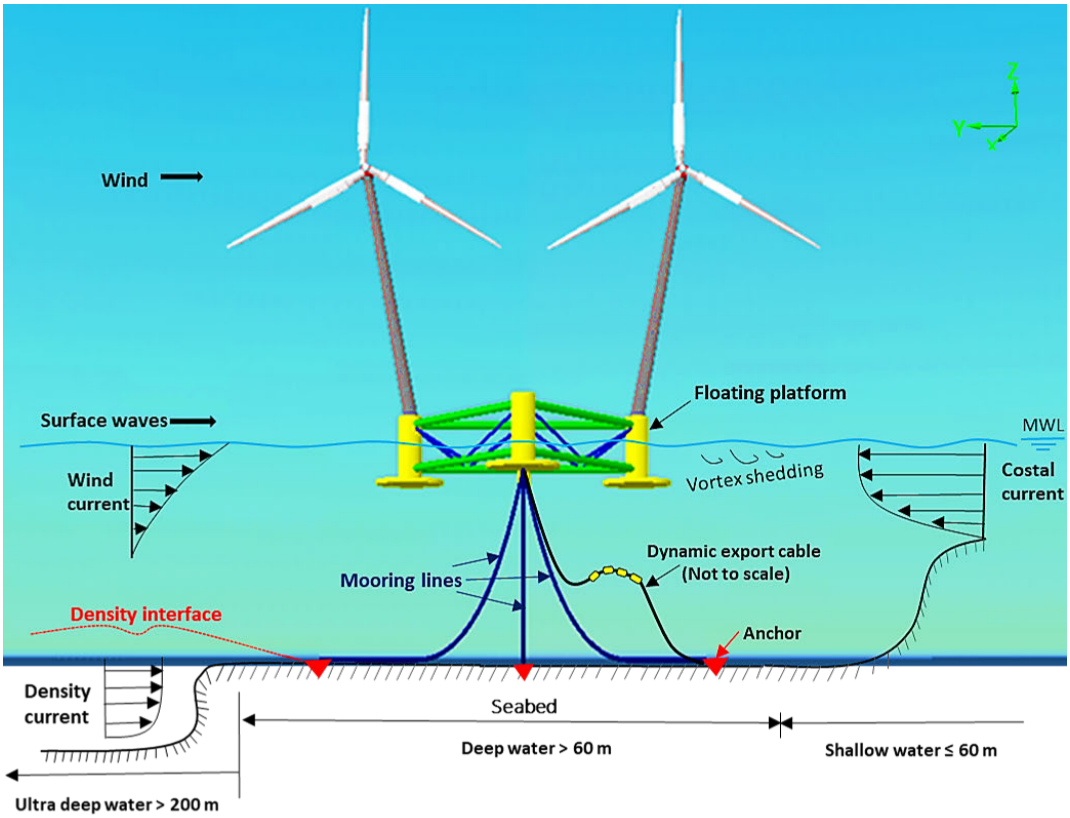

Figure 3.2: Schematic diagram of the environmental loads and fluid-structure interfaces experienced by a FOWT. It also shows the influence of wind-driven and near-shore currents on a floating platform moored in deep water (dynamic export cable not to scale).

Early FOWT installations were in low-current locations. However, future deployments move into deeper waters, including potentially high-current locations such as the Gulf of Mexico, the North Sea, and offshore Japan. Consequently, dynamic excitation of FOWTs becomes an increasingly critical challenge (Matha et al., 2011). When ocean currents are present, wave-induced drift forces, also known as wave drift damping, tend to increase (R. Zhao & Faltinsen, 1988; Stansberg et al., 2013). Applying the potential theory developed by R. Zhao & Faltinsen (1989), wave drift damping has been estimated by Aanesland et al. (1990) for different combinations of wave frequencies and current velocities for a TLP; full-scale results are shown in Figure 3.3.

For spar FOWTs, Qu et al. (2020) explored the impact of the interaction between freak waves and constant currents on their dynamic responses. Following currents were observed to have more pronounced effects on second-order wave loads than opposing ones. Understanding the physics of WCI is important in identifying the severest wave conditions that, in turn, are key for the dynamics of FOWTs and their fatigue and ultimate design considerations.

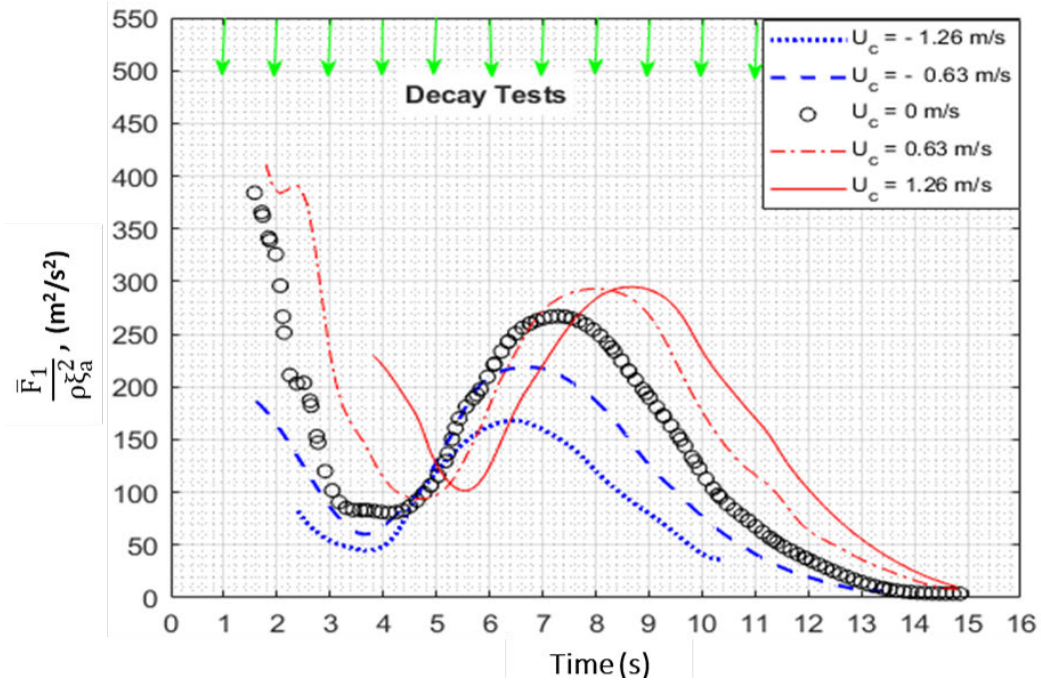

Figure 3.3: Impacts of wave-current interaction on the mean wave-drift force in the surge ($\overline{F}_1$) for a full-scale TLP structure as a function of wave period (T), current velocity (U_c), wave amplitude (ζ_a), and water density (ρ); reproduced from R. Zhao & Faltinsen (1989).

Zheng et al. (2020) examined WCI effects on a 6 MW spar FOWT under park conditions using a cubic BEM in the time domain. Current significantly influenced low-frequency motions and mean wave-drift forces, while second-order sum-frequency responses are insignificant. Viscous drag loads have a notable impact on wave-drift forces, particularly with increasing wave steepness, but do not strongly affect motion responses.

In order to determine the “pseudo” quadratic transfer functions of surge wave drift forces in varying sea states, Fonseca et al. (2022) conducted systematic wave-current tests on a 1:36 scale model of a SAITEC 10 MW FOWT. They used a second-order signal analysis method and found that wave drift force coefficients decrease as sea state severity increases. Wave-current effects amplify wave drift forces when waves and currents coincide, with a more pronounced impact in small sea states than in large ones.

When floating platforms are placed in combined wave-current environments, current often induces flow-induced motions (FIM), while waves generate large inertia forces. These FIM phenomena, particularly in the transverse direction of the flow, are characterised by significant cyclic resonance motions. In single bluff bodies like spar and mono-column platforms, this is known as VIM and has been extensively researched in Mehernosh & Lyle (2005); Roddier et al. (2009); Duan et al. (2016); Carlson & Modarres-Sadeghi (2018).

WCI theoretically augments FIM and, hence, poses challenges for floating structures like multi-column platforms, potentially reducing the fatigue life of mooring and power cable systems. While FIM has been studied for oil and gas platforms in deep waters, its impact on FOWTs with multi-column platforms (e.g. semi-submersibles, TLPs) has been insufficiently explored (Gon†calves et al., 2021).

The impact of collinear wave-current interaction on multi-column FOWTs has been experimentally examined by Gon†calves et al. (2013, 2020). Results vary, with some cases showing little impact on FIM when waves are added, while in other cases, waves mitigate FIM entirely. This phenomenon was also noted by Maximiano et al. (2017) and X. Li et al. (2022). Analysis of the fluid flow vorticity field reveals reduced FIM amplitudes due to wave-current-platform interaction altering vortex shedding patterns and frequencies. It is worth noting that these amplitudes are greater for floating structures with circular columns than those with square columns (Gon†calves et al., 2021). Interestingly, unlike prior studies where waves tend to mitigate VIM in collinear WCI, Li et al. X. Li et al. (2023) found that waves could enhance VIM when there is a non-zero wave-current angle. Furthermore, it has been observed that the largest platform motion does not necessarily result from the largest wave height in the lock-in region; a smaller wave height with a larger wave period can induce even greater motion.

3.9.1 Impacts on Motion Responses

Wave-current interaction is one of the nonlinear forces that could lead to significant second-order loads, yet its impact on FOWTs remains insufficiently investigated. As demonstrated by Robertson et al. (2013), it is essential to consider second-order loads when analysing different FOWT concepts. These second-order forces generate both low-frequency and high-frequency loads based on the difference and sum of frequency components, respectively. For instance, the natural frequency for TLP FOWTs in the vertical plane often exceeds the dominant wave frequency, meaning that difference frequencies can trigger resonant motion in pitch and heave. In contrast, second-order motions for semi-submersible FOWTs can be comparable to first-order ones. This results in substantial horizontal excursions, with surge RAO (Response Amplitude Operator) displacements reaching up to 10 m/m. These high RAOs are particularly pronounced at frequency peaks below the wave frequency range (0.05–0.2 Hz) of the investigated sea states. Such consideration is crucial for the mooring system (Robertson et al., 2013).

Using the OC3-Hywind Spar FOWT (J. Jonkman, 2010a), L. Silva et al. (2021) observed that WCI induces notable horizontal excursions on the platform, with the surge motion showing particularly pronounced effects. Following currents, augmented by the subsequent flows, reduce the minimum, mean, and maximum values of surge motion due to current-induced drag

while opposing currents increase them (L. Silva et al., 2021). Similarly, an opposing current was found to increase the mean values of heave motion, while a following current decreases them. This effect can be attributed to the nonlinear coupling between heave and pitch motions induced by an additional restoring force in the heave direction (P. Wang et al., 2021).

Otter, Flannery, et al. (2022) invented a novel hybrid approach to simulate wave-current interaction without requiring a physical current in basins. They tested a 1:50 scale model of the INNWIND.EU semi-submersible FOWT (Sandner et al., 2015) at the Lir National Ocean Test Facility (NOTF) (Lir NOTF, 2009). Results demonstrated changes in the heave and pitch responses due to WCI, underscoring the importance of considering WCI when conducting coupled simulations involving currents. It was also discovered that wind significantly enhances the platform's pitch response while it has a minor dampening effect on heave motion in wave-current scenarios compared to wave-only conditions (Otter, Flannery, et al., 2022; Otter, Desmond, et al., 2022).

Different numerical methods were benchmarked to address the consequences of wave-current interaction on semi-submersible platforms and mono-hull tankers. Currents were found to alter the air gap below the topsides of the floating platforms, and WCI prominently influenced pitch motions and horizontal drift forces (Pan et al., 2016).

The interaction of surface waves with currents, especially in the presence of multi-directional current profiles, introduces vortex-induced loads that significantly complicate motion responses of FOWTs (Yin et al., 2022). For spar FOWTs, sway and roll motions are mainly governed by the lift forces induced by vortex shedding due to WCI, as well as the heave motion. Whilst the mean positions in pitch and the oscillations in pitch and surge were less impacted (Y. Li et al., 2018). For semi-submersible FOWTs, WCI induces more complex vortex loads due to the wake interference between hull substructures (e.g. columns and pontoons) and the combined effect of waves and currents. This complexity becomes particularly pronounced when there are different headings of waves and currents; hence, in-depth investigations are needed (Yin et al., 2022).

To investigate the implications of wave-current interaction on vibration control of FOWTs, Sarkar et al. (2020) introduced a wavelet multi-resolution-based individual pitch control strategy. They evaluated its performance under combined wind-wave-current conditions, accounting for WCI. The underlying current was found to have an insignificant effect on the wind turbine DoFs. WCI significantly impacts platform surge motion, increasing it with the following current, as well as the tower fore-aft and platform pitch motions. Nevertheless, it does not have a substantial impact on the performance of the controller.

3.9.2 Impacts on Mooring Dynamics

Mooring lines are critical components of FOWTs, and accurately predicting the system's slowly varying motions is essential for safe design. Various factors contribute to slow drift damping, such as viscous hull damping, mooring line damping, wave drift damping, aerodynamic damping, and wave radiation damping (Matha et al., 2011). A current velocity of about 1 m/s can increase the mean drift force by 25-30% and the gradient of the surge drift force by up to 3.2 N/s, impacting wave drift force and wave-drift damping for a moored FOWT (Pan et al., 2016).

The layout of mooring lines can significantly influence their response to currents, impacting the restoring forces of the mooring system and, consequently, the responses of the FOWTs and cables. Thus, proper accounting for the combined effects of waves and currents on mooring cables is crucial in coupled analyses. Wave-only cases focus on wave-induced forces, while current-only cases examine how the steady flow affects mooring tensions. However, the interaction between waves and currents introduces more complex dynamics, as waves modulate the flow around the mooring lines, and currents affect the wave-induced motions of the FOWT and moorings. Ignoring these wave-current interaction effects can lead to overestimating cable fatigue life, as currents tend to increase cable tension (A. C. Pillai et al., 2018a).

Therefore, understanding the physics behind both the individual and combined effects of waves and currents is essential to accurately assess their impacts on FOWTs (L. Chen et al., 2018). Coupled CFD-FEM approaches were implemented to assess the influence of mooring-induced damping on FOWT vortex-induced motions in wave-current environments. In-line horizontal offsets were found to increase due to mooring system drag loads, accompanied by significant reductions in VIM transverse amplitudes within both the lock-in and post-lock-in ranges (H. Huang & Chen, 2020).

The layout of mooring lines can significantly influence their response to currents, impacting the restoring forces of the mooring system and, consequently, the responses of the FOWTs and cables. Thus, proper accounting for the current effect on mooring cables is crucial in the coupled analyses. Ignoring wave-current interaction effects can lead to overestimating cable fatigue life, as currents tend to increase cable tension. Therefore, it is essential to understand the physics behind this interaction to estimate their impacts on FOWTs (L. Chen et al., 2018). Coupled CFD-FEM approaches were implemented to assess the influence of mooring-induced damping on FOWT vortex-induced motions in wave-current environments. In-line horizontal offsets were found to increase due to mooring system drag loads, accompanied by significant reductions in VIM transverse amplitudes within both the lock-in and post-lock-in ranges (H. Huang & Chen, 2020).

Hassan et al. (2009) investigated the effects of current and its interaction with waves on mooring line damping and low-frequency surge motion for semi-submersible FOWTs moored by two systems: horizontal springs and catenary mooring lines. Results showed that current increased damping for both mooring systems. WCI effects on the horizontal springs system were negligible in moderate seas but became prominent in extreme ones, leading to augmented responses (Hassan et al., 2009; Mohamed, 2011). Using a 1:50 Froude-scale model of a semi-submersible FOWT, Hsu et al. (2016) conducted a series of drift and drag tests in a wave-wind-current flume. Currents were found to induce large drag forces when interacting with long waves, consequently altering the motion responses and the mooring tensions.

Employing Airy wave theory-based models (Thomas, 1981), the impact of wave-current interaction on the fatigue life and dynamic structural responses of Spar FOWTs has been assessed by L. Chen & Basu (2018, 2019). Quantitatively, the incorporation of wave-current interaction resulted in up to 10% differences in the dynamic responses of this FOWT and up to 15% increases in its cable fairlead tension (L. Chen & Basu, 2018, 2019).

Additionally, H. X. Nguyen (2022) looked into the interaction effect of long-amplitude waves and currents on the same spar FOWTs, finding that the FOWT drifted 15 m downstream in the presence of a following current. In contrast, when the current opposes the waves, the line fairlead tension can increase by up to 20%. The current was found to significantly impact the horizontal and vertical displacements of the FOWT and modify the cable forces, particularly when it is aligned with the wave direction. However, these contributions from the current alone were not quantified (H. X. Nguyen, 2022).

3.10 Chapter Summary

FOWTs are fully nonlinear systems encompassing aerodynamics, hydrodynamics, structural dynamics, electrical dynamics, mechanical systems, and control mechanisms. This chapter reviewed existing literature on current and its interaction with waves and their implications for FOWTs and mooring systems. It underscored the necessity of a thorough understanding and accurate modelling of fluid-structure interactions to ensure the reliable and safe operation of FOWTs. At the time of writing, current engineering tools for modelling FOWTs, such as OrcaFlex and OpenFAST, cannot adequately handle WCI (OrcaFlex, 2023; J. M. Jonkman & Jonkman, 2016).

The review highlighted significant gaps in current engineering tools for adequately simulating WCI in FOWTs. Specifically, while extensive research has examined the theoretical and numerical aspects of WCI, practical applications and integrated models for FOWTs remain limited. Existing studies predominantly focus on bottom-fixed offshore wind turbines, with relatively few investigations into the dynamic responses of floating systems under combined wave-current conditions. This gap is particularly pertinent given the increasing deployment of FOWTs in high-current environments.

Furthermore, the review identified a need for more comprehensive studies on the impact of WCI on the dynamic responses of MUFOWPs. Current literature primarily addresses single-unit floating structures, leaving a gap in understanding how WCI affects these systems and their mooring dynamics. Such knowledge is critical for optimising the design and operational strategies of MUFOWPs, especially in terms of structural integrity, power generation efficiency, and maintenance planning.

Therefore, this research aims to address the identified gaps and answer the second and third research questions outlined in Section 1.7. Specifically, it seeks to quantify the influence of currents on the design process of FOWTs and investigate how WCI impacts the dynamic behaviour of MUFOWPs, mooring systems, and the overall floating FOWT system. Building upon these insights, the next chapters introduce experiments and novel models that account for WCI in coupled analyses of FOWTs.

PART II

Experimental Modelling of MUFOWTs in Combined Wave-Current Environments

Chapter 4

Experimental Modelling of FOWTs: Methodology and Analysis Approach

4.1 Introduction

This chapter presents comprehensive experimental investigations to explore the dynamic responses of floating offshore wind turbines when subjected to concurrent wave and current conditions. Test campaigns were conducted at the state-of-the-art FloWave Ocean Energy Research Facility, employing a 1:40 scale model of the W2Power floating platform.

To achieve the main aims and objectives of this thesis and to address the research questions defined in Section 1.7, the scaled physical model of the multi-unit FOWT system is first developed. Moreover, to understand the dynamics of FOWT systems in combined wave-current environments, experiments are specifically designed to observe and quantify the impact of currents and their simultaneous influence when combined with waves on the dynamic responses of mooring systems and platform motions.

4.2 Theoretical Framework

Wave-current interaction is a complex and nonlinear phenomenon that presents significant challenges for accurate modelling and analysis (A. C. Pillai et al., 2021). Hence, simplifications are made to approximate the complexity of modelling and allow for more manageable mathematical formulations and computations. As such, waves are assumed to be of small amplitudes, allowing the use of linear wave theory. Also, the current is assumed to be horizontally and vertically uniform, which helps in reducing the complexity of varying current profiles, making it easier to integrate into the modelling framework (J. Smith, 1997; S. Draycott et al., 2021).

Additionally, two reference coordinate systems (i.e., fixed and moving) are defined to better understand wave-current modelling, as shown in Figure 4.1. The reference frame moving at the current velocity aids in separating the effects of the current from the wave dynamics, facilitating a clearer understanding of their individual contributions to the overall interaction (Peeringa, 2014).

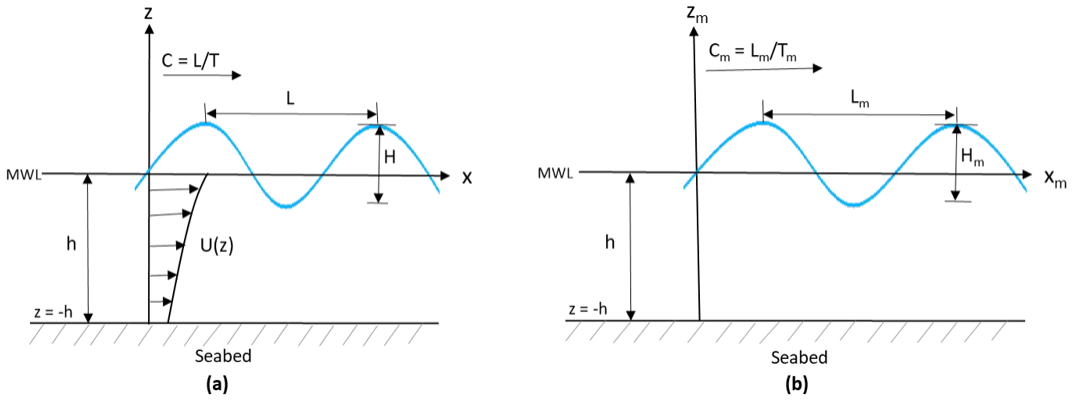

Figure 4.1: Schematic diagram of two reference frames: (a) fixed with waves and current, (b) moving with current speed, $U(z)$, and waves only.

In the absence of a current, wave characteristics in this moving reference frame can be determined using the following dispersion relationship:

$$\omega_r = [g\kappa \tanh(\kappa h)]^{\frac{1}{2}} \tag{4.1}$$

where ω_r denotes the relevant (intrinsic) wave frequency, g and h are the gravitational acceleration and water depth, respectively, and κ is the wave number in the direction of wave propagation.

In the presence of a current of velocity U, wave characteristics can be calculated in a fixed reference frame using the Doppler-shifted dispersion relationship:

$$\omega - \kappa_c U \cos\alpha = \pm\omega_r = \pm[g\kappa_c \tanh(\kappa_c h)]^{\frac{1}{2}} \tag{4.2}$$

in which ω is the wave frequency in the fixed reference frame, the subscript c refers to a region with a current, and α is the angle between the propagation directions of the wave and current.

Subsequently and based on the conservation of 'wave action' (Jonsson, 1990), the modified wave amplitude (A_c) in the presence of current can be represented as (J. Smith, 1997; S. Draycott, Steynor, et al., 2018):

$$A_c = A\left[\left(\frac{C_g}{C_{g,c}}\right)\left(\frac{1}{1+\frac{U\cos\alpha}{C_{g,c}}}\right)\right]^{\frac{1}{2}} \tag{4.3}$$

where C_g is the wave group velocity (i.e. velocity of energy propagation), and its quantity relative to a reference frame moving at the same velocity as the current can be expressed as:

$$C_{g,c} = \frac{\partial \omega_r}{\partial \kappa_c} = \frac{1}{2}\frac{\omega_r}{\kappa_c}\left(1 + \frac{2\kappa_c h}{\sinh(2\kappa_c h)}\right) \tag{4.4}$$

These above formulas account for the interaction of regular waves and currents and are based on the linear Airy wave theory (Thomas, 1981).

For irregular waves, N. E. Huang et al. (1972) and Tung & Huang (1974) proposed analytical spectral models based on the solution of the regular waves model, and these models account for the impacts of the current on the wave spectrum $S(\omega)$ as:

$$S(\omega, U) = \frac{4S(\omega)}{\left[1 + \frac{4U\omega}{g}\right]^{\frac{1}{2}}\left[1 + \left(1 + \frac{4U\omega}{g}\right)^{\frac{1}{2}}\right]^2} \tag{4.5}$$

The spectral energy will decrease with a following current, and the opposite is true with an opposing current. Thomas (1981) and T. S. Hedges et al. (1985) then extended the models to account for wave breaking induced by opposing currents.

4.3 WCI Implications for Dynamic Responses of FOWTs

Emphasising the need to assess the hydrodynamic responses of floating wind turbines, Zhai et al. (2022) integrated a barge-type FOWT with an aquaculture cage under various environmental loads, including dynamic wave-structure interaction, resulting in dynamic amplification of motion responses. Scientists also analysed the dynamic responses and structural dynamics of FOWTs in different sea states, highlighting the coupling effects between various motion modes of FOWTs due to such an interaction (Qu et al., 2020; Sarkar et al., 2020; L. Silva et al., 2021; Zhai et al., 2022).

Under operational conditions, the responses of a FOWT are dominated by wind actions, whereas under storm (parked) conditions, they are dominated mainly by wave and current actions (Qu et al., 2020). Thus, the majority of documented experiments on FOWTs were conducted under combined wave and wind loads (Utsunomiya et al., 2009; Coulling et al., 2013; Y.-s. Zhao et al., 2018).

The impact of wave-current interaction on the fatigue life and dynamic structural responses of a Spar FOWT. Quantitatively, the incorporation of wave-current interaction resulted in up to 10% differences in the dynamic responses of this FOWT and up to 15% increases in its cable fairlead tension (L. Chen et al., 2018; L. Chen & Basu, 2019). The interaction between long-amplitude waves and following currents was found to drift a FOWT up to 15 m downstream. Whereas when opposing currents interact with such waves can increase its mooring load by up to 20% (H. X. Nguyen, 2022).

Moreover, experiments and numerical analyses at the KRISO basin revealed the impact of wave-current interaction on wave drift force in a moving vessel, highlighting practical implications (Seo et al., 2021). Since wind turbine thrust loads significantly amplify mooring tension, with larger turbines, the combined effect of wind and current-driven forces on mooring systems becomes more pronounced. Therefore, stronger design considerations are required for safe operation (A. C. Pillai et al., 2018a).

Under storm conditions, wave-current interaction can substantially impact the motion responses of FOWTs. For example, it can surge a semi-submersible FOWT by up to 8 m and lead to fatigue in their superstructures, such as the mooring lines and towers (L. Chen & Basu, 2018; L. Silva et al., 2021). The interaction between constant currents and extreme waves was found to strongly impact the structural responses of Spar FOWTs (Qu et al., 2020; Sarkar et al., 2020).

Numerical investigations further emphasised the importance of incorporating wave-current interaction in the couple analyses of FOWTs (Utsunomiya et al., 2014). Although it has been numerically demonstrated that wave-current interactions considerably affect platform response, mooring tensions, and the fatigue life of FOWTs. However, the WCI-induced loading is usually disregarded during parked conditions in physical experiments. Hence, more conceptual understanding and experimental analysis are much needed.

Numerical investigations further demonstrated that wave-current interaction significantly impacts platform response, mooring tensions, and the fatigue life of FOWTs (Utsunomiya et al., 2014). However, despite the importance of incorporating wave-current interaction in the couple analyses of FOWTs, the loading induced by this interaction is often overlooked during parked conditions in physical experiments. Therefore, there is a need for further conceptual understanding and experimental analysis to bridge this gap.

Subsequently, the current tests aim to examine the impacts of currents and their combined effects with waves on the mooring loads and platform motions, particularly under realistic extreme conditions at potential deployment sites. The objective is to develop an experimental model for FOWTs in shallow water deployments (i.e., up to 80 m depth) based on long-term metocean data. This experimental data can then be utilised to integrate these effects into numerical simulations and analysis processes, enabling precise assessments and design considerations for mooring and FOWT systems.

4.4 Model Scaling

Hydrodynamic models are often scaled using the Froude scaling principles of similitude, where the inertial and gravity forces remain consistent at both prototype and laboratory scales (Froude, 1868). The Froude scaling laws have been extensively used in the offshore industry to investigate fluid-structure interactions (DNV-RP-C205, 2017). Froude scaling is particularly appropriate when gravity forces dominate, such as in wave loading. However, for flow-related phenomena, such as current-induced drag or aerodynamic forces on turbine blades, Reynolds number scaling may be more suitable because it accounts for the influence of viscosity (De Graaff & Eaton, 2000). For instance, the aerodynamics of the turbine blades should be scaled based on the Reynolds number rather than the Froude number, as viscosity plays a critical role in determining flow separation and drag characteristics.

Therefore, when scaling current loads, while Froude scaling ensures consistency with wave loads, care must be taken to consider potential discrepancies due to the contribution of viscosity and the limitations of Froude similitude in capturing viscous effects. This is particularly relevant for systems with significant aerodynamic or viscous flow effects, which are aspects beyond this thesis's scope. The Froude conversion factors used to convert prototype scale data to model scale for the physical testing are listed in Table 4.1 (Edition et al., 2001).

Since hydrodynamic forces affect signals containing a force or mass term, a density correction is required when testing in freshwater tanks. Note that the present tests were conducted in freshwater. Therefore, all forces and masses are multiplied by the specific gravity factor (i.e., $\gamma = 1.025$), which is the ratio of the seawater density for full scale (1025 kg/m^3) to the freshwater density used for model scale testing (1000 kg/m^3). However, for tests conducted in saltwater tanks, this correction is not necessary, as the densities of the fluid at model and prototype scales are equivalent.

Table 4.1: Conversion factors for Froude scaling similarity.

Variable	Unit	Scale factor
Time	[s]	$\lambda^{0.5}$
Mass	[kg]	$1.025\lambda^{3}$
Length	[m]	λ^{1}
Density	[kg/m^3]	λ^{0}
Velocity	[m/s]	$\lambda^{0.5}$
Frequency	[Hz]	$\lambda^{-0.5}$
Force (tension)	[N]	$1.025\lambda^{3}$

4.5 Materials

4.5.1 FloWave Ocean Energy Research Facility

The experiments were conducted at the FloWave Ocean Energy Research Facility, so-called FloWave, at The University of Edinburgh in Edinburgh, United Kingdom (FloWave, 2014). The basin is circular with a 25 m diameter and a 2 m water depth, with a 15-meter-diameter buoyant floor in the basin's centre, representing the test area. FloWave provides full 360° capabilities for waves and currents with reliable and reproducible characteristics that reflect actual coastal waters. As shown in Figure 4.2, the tank has two volumes: upper and lower. The former volume has a constant water depth of 2 m and is divided by a 1 m thick floor from the lower one (i.e., the testing area). For the present study, no wind was considered, varied wave and current directions were examined, and the following sections explain how they were generated.

4.5.1.1 Waves Generation

The tank's perimeter is surrounded by 168 hinged paddles, which generate waves. Waves produced by these paddles are deterministic, meaning they can be reproduced accurately (D. Ingram et al., 2014). There is full control over the direction of all waves, which can emerge concurrently from multiple angles. The tank can be programmed to mimic any desired sea state for both regular and stochastic seas. It is also possible to produce customised sea states, such as ones with standing, concentric, or spike waves. FloWave is optimised to produce waves with a height of 0.45 m and a period of approximately 2 s. Moreover, it is conceivable to produce waves with large heights (i.e., $\approx$ 0.7 m) and smaller periods (i.e., more than 1 wave per second).

4.5.1.2 Currents Generation

A subset of the 28 current-drive units generates currents across the tank. Each current unit has a single 1.7 m-diameter, 5-bladed, low-solidity, symmetrical impeller housed in a flow diffuser and powered by a 48 kW motor. The facility can generate currents of up to 1.6 m/s in any direction, regardless of the direction of the waves.

4.5.2 FloWave Limits and Constraints

FloWave achieves uniform wave and current direction in its circular basin through precise control of individual impellers and wave-makers (Robinson et al., 2015b). Its unique design features enable the generation of complex wave-current scenarios with minimal spatial variability in flow (S. T. Draycott, 2017a). Although a perfectly uniform current in all directions is challenging to maintain in a circular tank, the tank manages to create a central test region where both wave and current directions remain relatively straight and uniform. Furthermore, FloWave practices demonstrated that a variation of $\pm$10%in flow velocity and $\pm$10$\circ$ in direction is acceptable (Noble, 2018). This allows for accurate creations of real-world wave-current interactions, thus ensuring consistent test conditions for reliable test results despite the basin's circular geometry.

4.5.3 W2Power Floating Offshore Wind Solution

Experimental investigations utilised the innovative W2Power floating wind system, which is being developed by EnerOcean S.L., Spain (EnerOcean S.L., 2007). This model is specifically chosen as a case study due to its twin-turbine design and unique mooring system, making it an ideal candidate for investigating the dynamic responses of multi-unit FOWTs and their mooring systems in combined wave and current conditions. Thus, addressing the core research questions and the thesis's objectives, Section 1.7.

W2Power is a triangular semisubmersible platform with two out-leaning towers mounted on the backside columns to support a pair of original equipment manufacturer (OME) WTGs; refer to Appendix A. It is designed with an operational water daft of 15 m and will be anchored to the seafloor by a SPM system comprising three lines to be attached underneath the front column (W2Power, 2010; EnerOcean S.L., 2007).

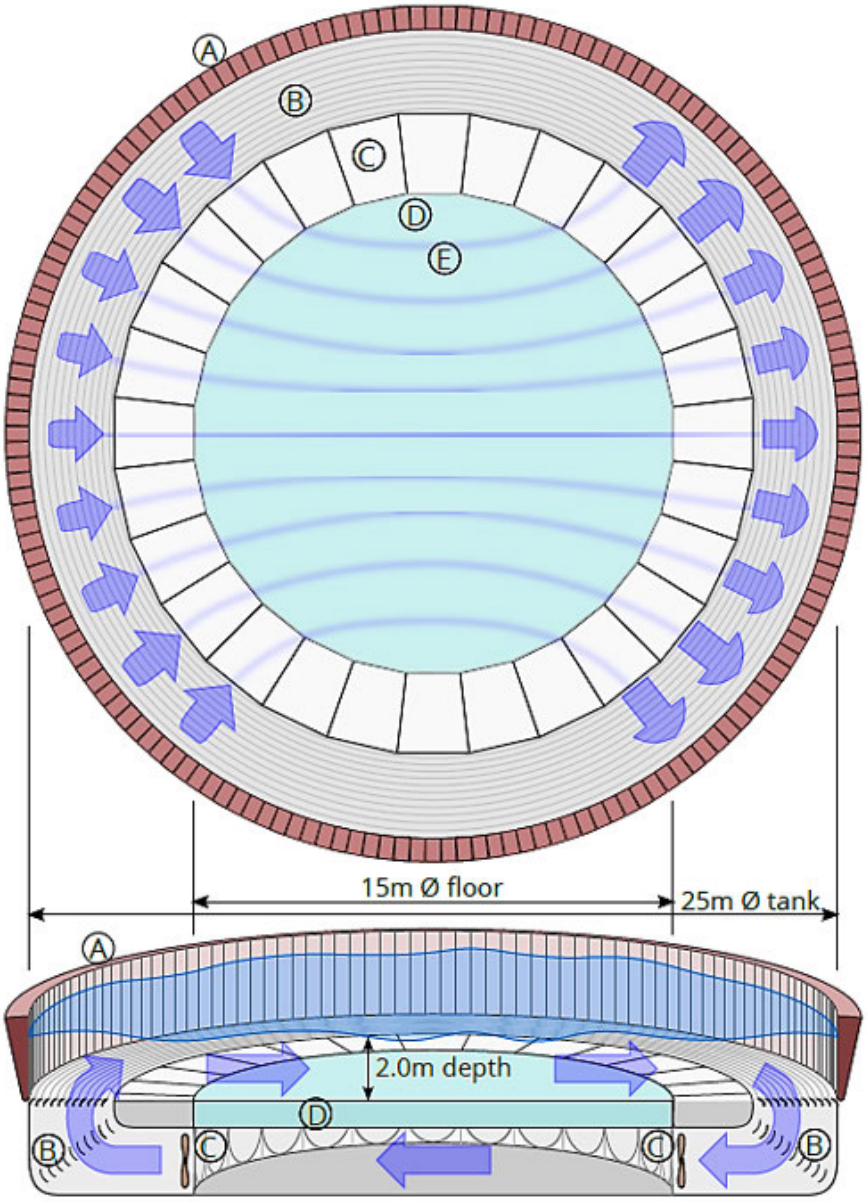

Figure 4.2: A schematic representation of FloWave, detailing both plan and oblique sections. Blue arrows denote indicative flow recirculation and key components: (A) circumferentially arranged wavemakers (168 paddles), (B) turning vanes and flow conditioning filters, (C) current drivers(28 impellers,) (D) the buoyant movable floor, and (E) idealised streamlines portraying the flow pattern across the tank floor. Adopted from Noble (2018).

4.5.3.1 Physical Model Characteristics

Based on the platform prototype's size and the characteristics of the FloWave facility (i.e. tank's wave envelope), a 1:40 scale model of the W2Power design was employed to investigate the dynamic of FOWTs under a variety of loading conditions: currents, waves, and combined wave-current. The physical model utilised in this study was manufactured seven years ago by EnerOcean in Málaga, Spain, and does not represent the current design of the platform (see Figure 4.3).

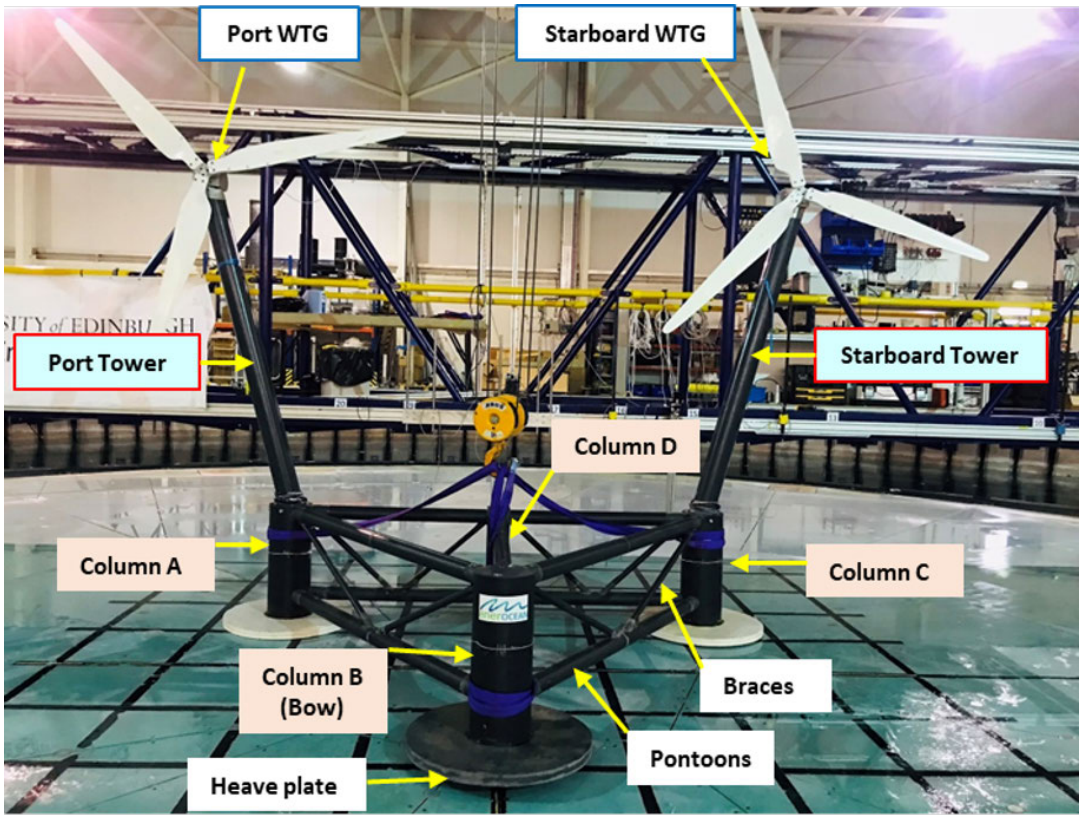

Figure 4.3: Photograph of the 1:40 scale model of the W2Power platform positioned on the FloWave floor, displayed the WTGs, towers and components of the hull.

This model was made of PVC pipes whose dimensions and wall thicknesses were determined by the corresponding scale weights of each component (EnerOcean S.L., 2007; W2Power, 2010; Enerocean-S.L. and Pelagic-Power, 2015; Mayorga, 2016). Scaling similarity was done based on the conversion factors in Table 4.1, and the main particulars of the physical model and prototype of the platform are given in Table 4.2.

Table 4.2: Particulars of the prototype and model scale of the W2Power platform.

Description	Unit	Prototype	Scale model (1:40)
Draft	[m]	15	0.375
Water depth	[m]	80	2
Outward leaning angle	[°]	15	15
Corner columns diameter	[m]	9	0.225
Corner columns height	[m]	25	0.59
Column D diameter	[m]	5	0.125
Column D height	[m]	25	0.59
Towers bases separation	[m]	90	2.250
Heave plates height	[m]	1.5	0.038
Heave plates diameter	[m]	27	0.675
Pontoons diameters	[m]	3	0.075
Braces diameter	[m]	1.32	0.033

4.5.3.2 Mooring System Characteristics

Employing the same scale model, Elobeid et al. (2022) proposed two scaled mooring systems for deep and moderated water depths of 5 and 2 m, corresponding to full-scale water depths of 200 and 80 m. Given the size of the tank, the latter system of 80 m was first scaled down and optimised, and then utilised in the current test campaigns.

The configuration of this mooring system is a typical catenary concept, comprising three lines symmetrically placed along the platform's z-axis and spread by 120° (see Figure 4.4). These mooring cables are made of stud-less chains; their properties are detailed in Table 4.3.

Table 4.3: Mooring system characteristics for the physical model.

Description	Unit	Scale Model (1:40)
Water depth	[m]	2
Line grade and type	[-]	R4 – Stud-less Chains
Weight per meter	[kg/m]	0.76
Nominal chain diameter	[mm]	6
Minimum breaking load (MBL)	[kN]	44.8
Axial stiffness	[kN]	3.21×10^3
Fairlead pretension	[N]	18
Total line length	[m]	6.505
Fairlead depth	[m]	0.375
Anchor radius (R)	[m]	5.7
Anchor depth	[m]	2

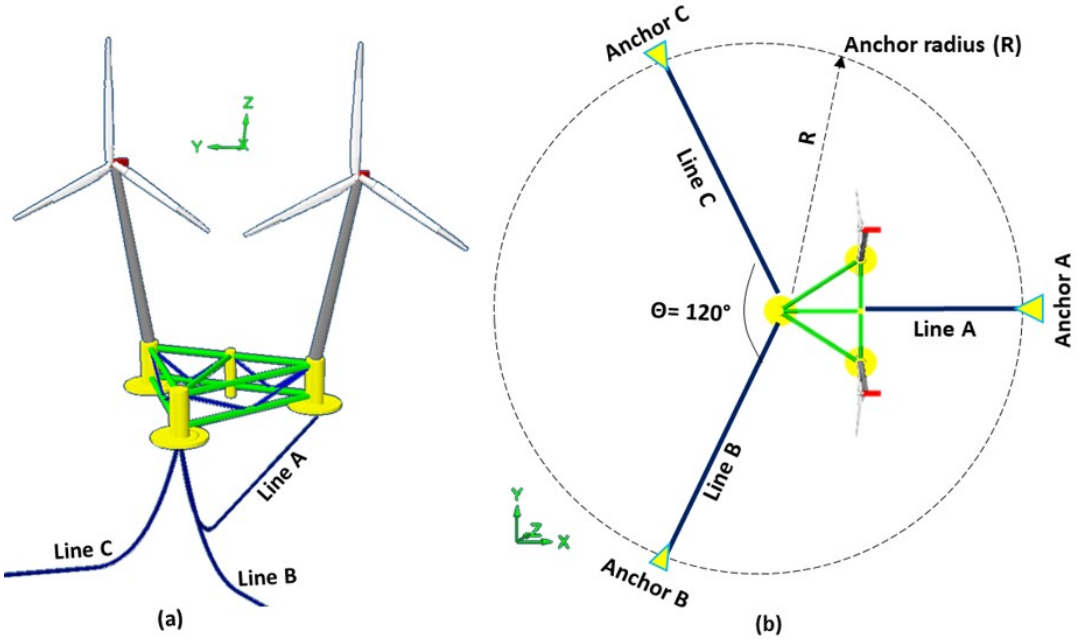

Figure 4.4: Illustrations of side (a) and top (b) views showing the arrangement of catenary mooring lines and anchors (not to scale) of the W2Power physical model.

4.5.4 Instrumentation and Data Acquisition

The present research utilises a range of instrumentation and data acquisition systems to measure the free surface elevations, mooring loads at fairleads of the three lines and platform motion displacements in six DoFs. These measurements collectively contribute to addressing the research questions (i.e. Section 1.7), by providing insights into the dynamic responses of the mooring systems and platforms for the FOWTs in combined wave-current environments.

4.5.4.1 Instrumentation

Three different measurement instruments were employed to capture essential data: (i) a motion capturing system to record the motion and rotation of the floating system, (ii) load cells to measure the loads at the three mooing lines fairleads, and (iii) wave gauges for recording free surface elevations at various locations.

Motion Capturing System (MoCap)

The MoCap utilised a combination of cameras provided by Qualisys: five positioned above water and four sub-water. Above-water cameras were affixed to four tripods near the tank protection cantilevered edge, while underwater cameras were mounted near the edge of the rising floor in the tank. As depicted in Figure 4.5, reflective balls were then affixed at predetermined locations, including a set of five reflective balls on a tree installed on the top of the bow (front) column of the platform and two reflective balls on top of the upper stern (aft) pontoon.

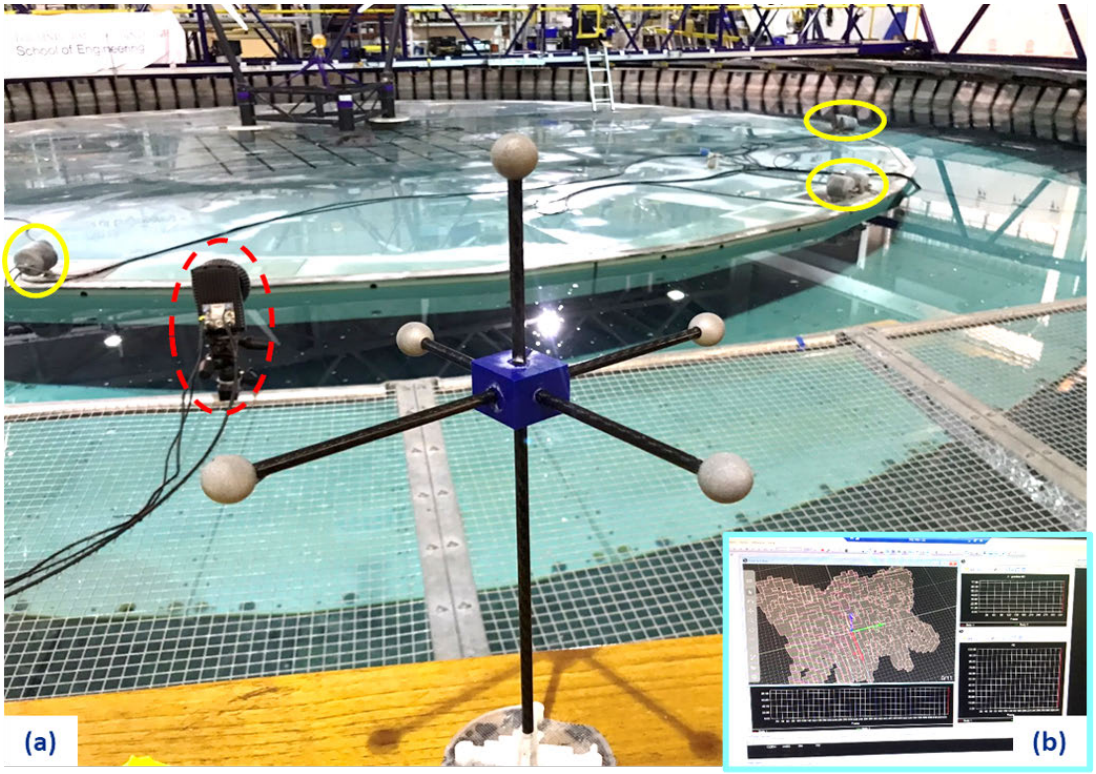

Figure 4.5: Photographs of FloWave with the floor up and the W2Power model in the test area, showing: (a) the Qualisys motion capturing system featuring the tree of reflective balls, a video and underwater cameras (circled in yellow), and an above-water camera (circled in dashed red); (b) the control desk with the MoCap Qualisys system being calibrated.

Additional reflective markers were attached to the towers and rotor blades. This setup of multiple reflective balls and markers defined the rigid body (platform). Thus, it provides measurements in all six degrees of freedom with an accuracy smaller than 1 mm in all coordinate directions. The centre of the body was chosen to be the combined centre of mass of the entire W2Power floating system. Translation and rotation motions were then captured in relation to this local body coordinate system.

Furthermore, extra reflective balls were placed at intervals of 0.5 m along the suspended length of each mooring line, positioned in close proximity to the line's fairlead. This deliberate implementation aimed to acquire reliable data to train the Qualisys MoCap system, specifically to capture the spatial mooring dynamics of floating structures. Note that this aligns with FloWave's ongoing improvement strategies, and it extends beyond the scope of this thesis.

Prior to testing, the MoCap system was calibrated using a wand with reflective markers, which were moved through the measurement volume to define spatial accuracy and alignment. This calibration was repeated until the system's deviation was minimised, ensuring positional accuracy within 1 mm in all coordinate directions.

Load Cells (LCs)

The model installation was executed in a dry environment on the buoyant floor of the tank. In this dry condition, the entire weight of the physical model was supported by a pair of foam blocks beneath each heave plate. Subsequently, three mooring lines were attached to a chain-eye-swivel at the bottom of the front column.

Each mooring line was equipped with an in-line load cell and a turnbuckle. All LCs and turnbuckles are constructed identically. The LCs were positioned at a distance of 0.5 m from the fairlead on each mooring line, see Figure 4.6.a. All three LCs shared the same specifications, each with a rated capacity (RC) of 500 N. The accuracy of the LCs was within $\pm$0.15% of RC, with a typical value of 0.05% (Applied Measurements Ltd, 2020).

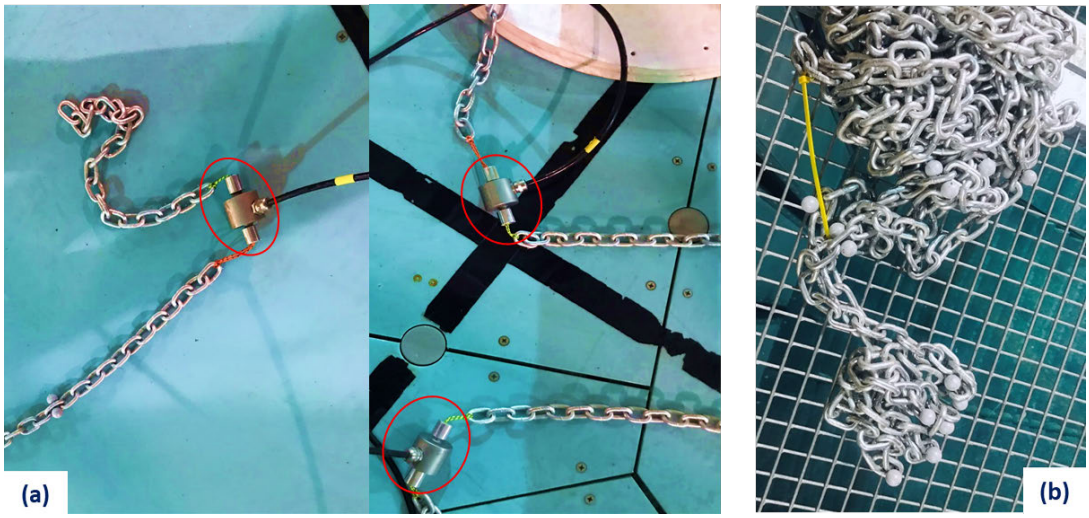

Figure 4.6: Photographs depicting: (a) load cells connected to each mooring line, and (b) the lumped masses of chains on the tank's protection cantilevered edge employed as anchors.

As shown in Figure 4.6.b, anchors in the form of lumped chains were employed at the terminal of each mooring line, and lightweight Dyneema ropes were then used to link these lumped chains to the tank protection cantilevered edge. This selection was made considering safety measures while station-keeping such a relatively bigger model via positioning the anchors at the edge of the movable floor.

Following this configuration, the ropes were precisely tensioned and released to establish a predetermined pretension in each mooring line. The individual pretension could only be corrected with the tensioned lightweight Dyneema ropes. The primary aim during installation was to ensure a uniform value for all three LCs within the targeted range of 18 N while also accepting a reasonable minimum value.

Wave Gauges (WGs)

Free wave surface elevations were measured using multiplexed two-wire resistance-type wave gauges. These WGs, positioned on the tank's instrumentation gantry, offer a straightforward, reliable, and cost-effective solution for wave measurement, and they can provide a suitable resolution of $\pm$0.1 mm (Massel, 1996; S. Draycott, Noble, et al., 2018). Consequently, resistance-type gauges are exclusively employed at FloWave, featuring diverse designs tailored for specific offshore applications.

The initial determination of spacing between the WGs was guided by the expertise of the FloWave staff. However, constraints arose due to the anticipated maximum movement of the FOWT in the dominant flow and wave directions. Despite the stiffness properties of the typical single-point mooring system, the movement, albeit not small, imposed limitations on placing the WGs in close proximity to the model.

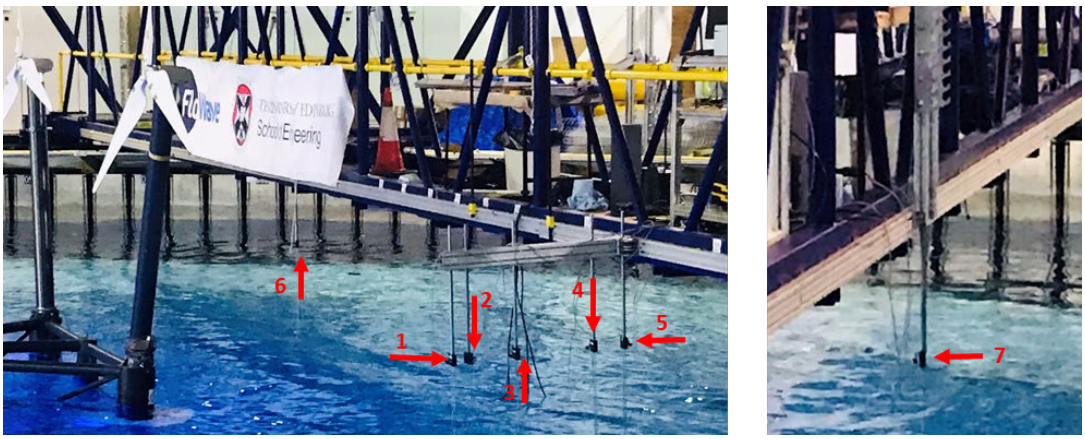

Figure 4.7: Setup of the wave gauges on FloWave's gantry in relation to the W2Power floating system: (left) WG1-WG6 on the test area side, (right) WG7 on the opposite side of the test area.

The first five wave gauges, WG1–WG5, comprised a reflection array structured on the Golomb ruler concept (Bloom & Golomb, 1977). This array was mounted perpendicular to the movable gantry. WG6 was positioned on the same side where the model was tested but with an offset in the y-direction. As a complement, WG7 was installed on the opposite side of the gantry, as depicted in Figure 4.7.

The WGs then encircled the model, which was in its centre. This configuration of WGs allowed for comprehensive documentation of the main flow and incoming waves, incorporating reflections at the floating model. Different scenarios of wave-structure interaction can be examined, considering wave propagation from 0, 90, and 180 degrees.

At the beginning of each testing day, a rigorous calibration routine consisting of five points covering a range of $\pm$100 mm was carried out. This calibration process aimed to ensure the WGs consistently deliver precision in the order of 1 mm. The measurement frequency was set to 128 Hz, identical to the MoCap Qualisys system (Gabl et al., 2019).

4.5.4.2 Data Acquisition (DAQ)

FloWave employs multiple DAQ systems for logging measurements in the tank, including, but not limited to:

(i) The tank control software is utilised for logging wave gauge data.
(ii) A National Instruments DAQ system is employed for logging current or voltage output from load cells.
(iii) Qualisys motion capture cameras for recording data independently through a proprietary software interface.

Given the diversity of the DAQ systems, synchronisation of these instruments is imperative. Consequently, all instruments yield measurements at a frequency of 128 Hz (20.24 Hz full-scale) and are synchronised via a transistor-transistor logic (TTL) pulse output by the tank control system. This synchronisation mechanism ensures alignment in MoCap and LC data acquisition. This comprehensive approach ensures the acquisition of high-quality data synchronised with wave generation processes (Noble, 2018).

To accurately measure the tension forces at the fiarleads, the load cells were calibrated before installing them on the mooring lines. This pre-campaign calibration involved applying known loads to verify the accuracy of each load cell across its full range. This ensures that the measured forces align with the rated capacity of the load cells throughout testing.

4.6 Methods

4.6.1 Experimental Procedure

The assembly and setup of the floater-mooring-towers-turbines and all the subsystems were first done as annexed in Appendix A.2, and this ensured the model's readiness for testing and met the specified conditions and configurations (see Figure 4.8). Then, all instruments underwent calibration, as detailed earlier in Section 4.5.4. Afterwards, experiments were conducted utilising the W2Power scale model, whose physical and hydrodynamic parameters are outlined in Table 4.2. The model was consistently aimed at being positioned in the centre at a depth of 2 m for all experiments. The testing scenarios involved subjecting the model to varying degrees and formations of current, wave, and wave-current disturbances generated by the current-drive impellers and surrounding wavemakers.

To streamline the testing procedure, the current direction remains fixed at 0°. However, three distinct wave directions have been defined: 0°, 90°, and 180°. This allows waves to hit the platform from different directions, thus producing cross and opposing scenarios of wave-current conditions. The disturbances induced by waves are generated by specifying the parameters of the wave profiles. For irregular waves, frequency spectra are transformed into a wave height time history, which is then transferred to the wavemakers. This process results in controlled movements to produce the desired waveform during the experiments.

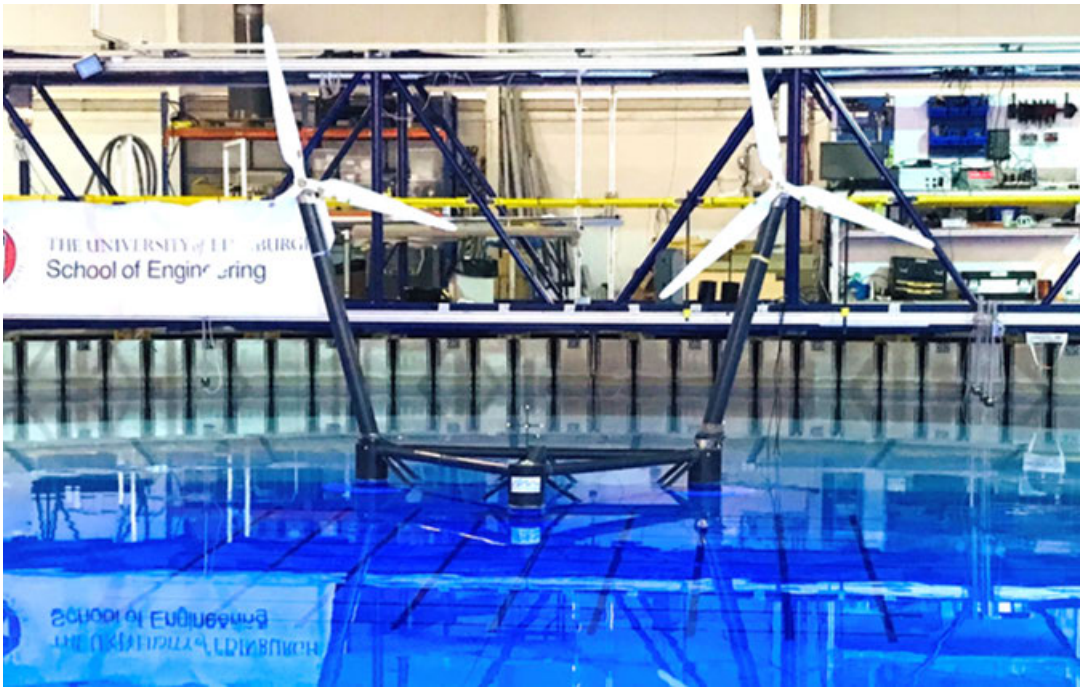

Figure 4.8: Visualisation of the W2Power 1:40 scale model assembled in the centre of FloWave and its readiness for testing. Blue lights indicate the activation of the underwater MoCap Qualisys cameras.

In the simulations, it was assumed that the model remained perfectly stationary, and the oncoming wave was treated as a perfect head sea. However, in the FloWave tank, practical considerations differed. The model was positioned in the centre of the test area, and experiments were conducted consecutively. This sequential testing approach occasionally resulted in offsets of the model from its original position.

These offsets can be attributed to the mooring configuration, specifically the use of lumped chains as anchors, positioned at the edge of the tank, and connected via lightweight Dyneema ropes for safety (see Figure 4.6.b). While the mass of the chains provided sufficient station-keeping, the flexible nature of the Dyneema ropes, coupled with the dynamic forces from consecutive tests, may have allowed slight deviations from the original position. These small offsets reflect the interaction between the floating model and the practical constraints of the mooring system used in the tank environment.

To address these offsets and misalignments observed in some test cases, manual reorientation of the model was carried out using a very long stick. This manual adjustment ensured that the model was relatively aligned and positioned, with the objective of mitigating any potential discrepancies in the motion measurements compared to the original setup during the experiments.

During tests, rigorous monitoring was done to capture crucial parameters. The forces acting on the platform were tracked, as well as the very small motions in all 6 DoFs using the Qualisys MoCap system. Likewise, wave elevations were conscientiously recorded via the WGs and mooring loads at fairleads were documented through the LCs. The capturing time for all measurements was 160 s and 600 s for regular and irregular sea states, respectively.

4.6.2 Metocean Conditions

To answer the research questions in Section 1.7, the proposed mooring system for shallow waters of 80 m is analysed experimentally using the following environmental conditions.

Metocean Conditions

The environmental data considered in these campaigns are for a reference site off Gran Canaria Island named Canary-I, Figure 4.9, whose specifications are provided in Table 4.4. The sites' long-term wind and wave hindcast data of 10 years were obtained from the National and Kapodistrian University of Athens (NKUA) (NKUA-AM&WFG, 2021). The roses for the Canary-I site are displayed in Figure 4.10. It can be seen that big waves predominantly travel towards the North-NorthEast, while currents originate from the South-SouthWest. Notably, currents generally follow or closely align with waves.

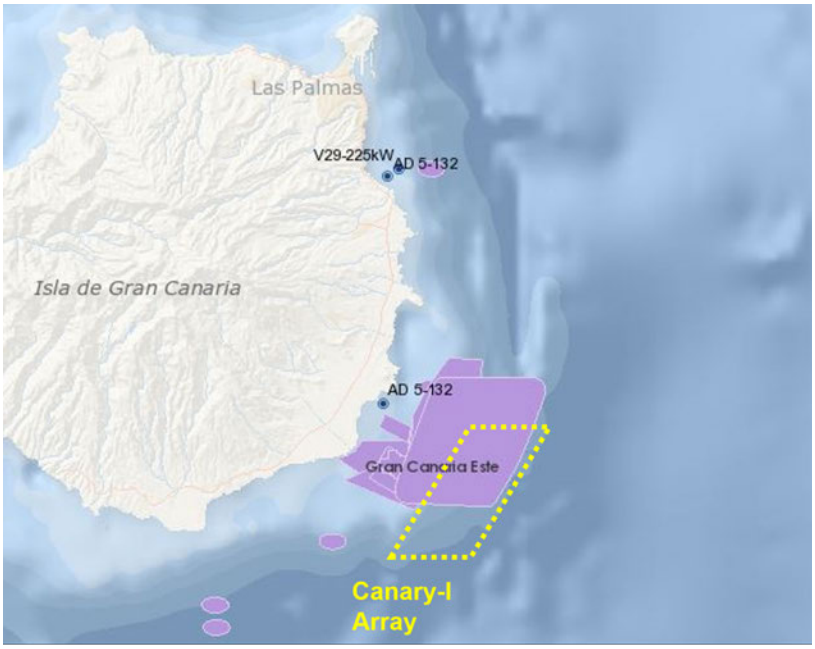

Figure 4.9: Map showing the Canary-I reference site for which the environmental data is considered in test campaigns (Global Wind Atlas, 2021).

Table 4.4: Specifications of the Canary-I reference site (Global Wind Atlas, 2021).

Particular	Unit	Value
Latitude, Longitude	[°]	27.771, -15.373
Water depth	[m]	80
Wind speed at height of 100 m	[m/s]	11.36
Distance to shore (i.e. Arinaga coast)	[km]	10

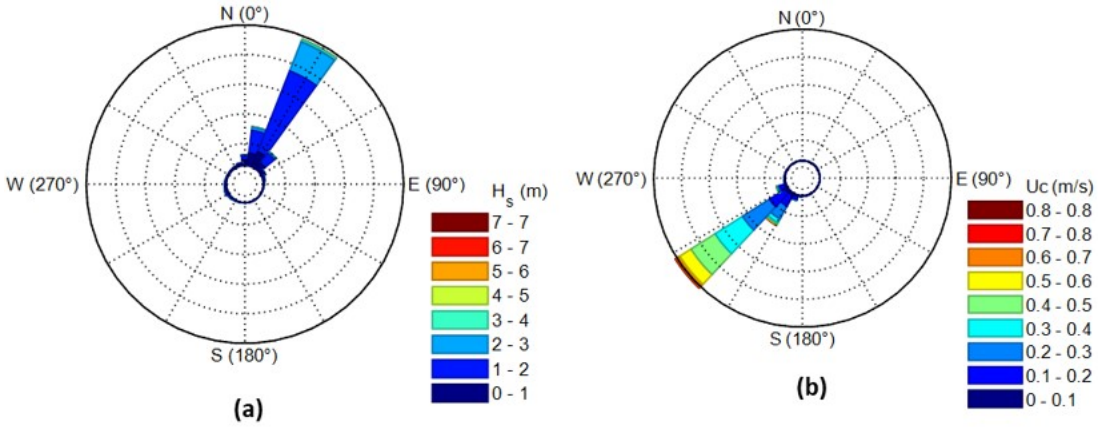

Figure 4.10: Directional distributions for the Canary-I reference site's environmental conditions: (a) significant wave height (H_S) rose and (b) current rose. The roses show big waves travelling towards the North-NorthEast, and currents originate from the South-SouthWest.

Environmental Modelling

In order to assess the survivability and structural reliability of the floating system, environmental contours are established based on joint probabilities of metocean parameters, specifically significant wave height (H_s) and peak wave period (T_p). The process of constructing the contour surfaces involves two consecutive steps:

(i) Estimating the long-term joint distribution of the environment through statistical modelling.

(ii) Constructing a contour based on that joint distribution.

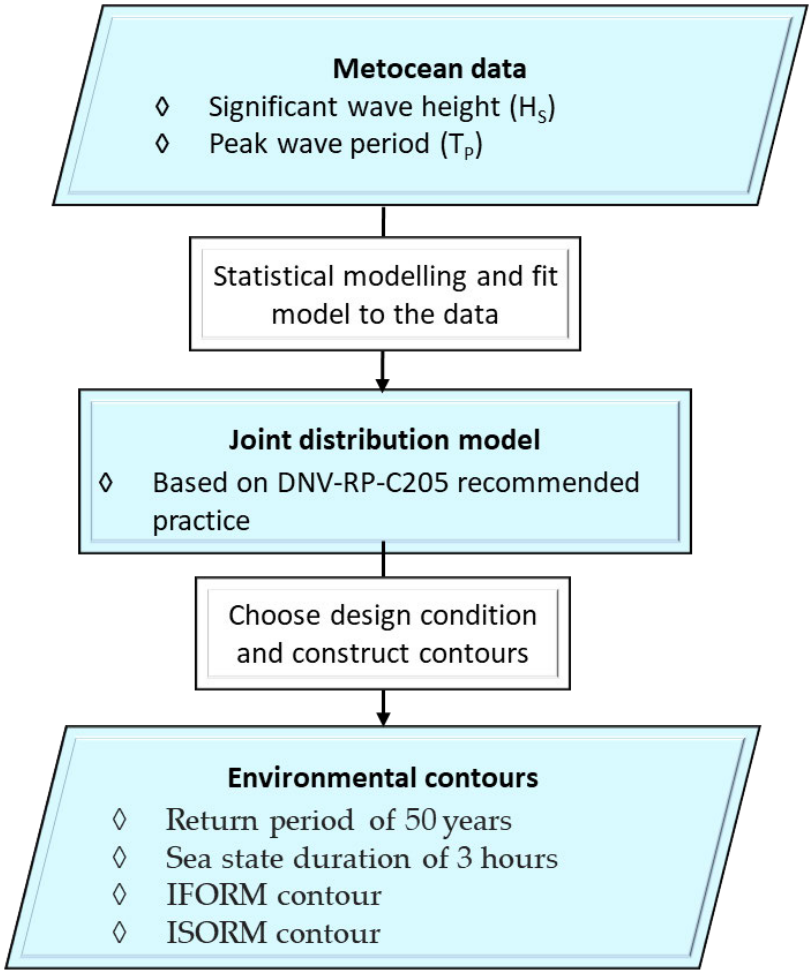

Figure 4.11: Flowchart showcasing the key steps in constructing the environmental contours. Execution and modelling processes were done utilising a Python modelling tool called ViroCon (Haselsteiner et al., 2019).

The procedure, outlined in Figure 4.11, employs the inverse first-order reliability method (IFORM) and inverse second-order reliability method (ISORM) to create contours (Winterstein et al., 1993; Chai & Leira, 2018). These methods estimate the probabilities of exceedance and then seek the corresponding response levels (Haselsteiner et al., 2019). The probability of exceedance (α) is computed using the following formula:

$$\alpha = \frac{T_s}{(365.25 \times 24) \times T_r} \tag{4.6}$$

where T_s is the state duration, and T_r is the return period. As per the recommended practice (DNV-RP-C205, 2017), the values assigned to these parameters are 3 hours for T_s and 50 years for T_r. Accordingly, two environmental contours are established.

As depicted in Figure 4.12, it is evident that ISORM and IFORM contours exhibit similar shapes. However, distinct differences between the IFORM and ISORM contours are observable despite having the same return period. The data perfectly fit within the IFORM contours, underpinned by consistent environmental parameters and appropriate assumptions, implies that the IFORM contour is a conservative candidate for design considerations.

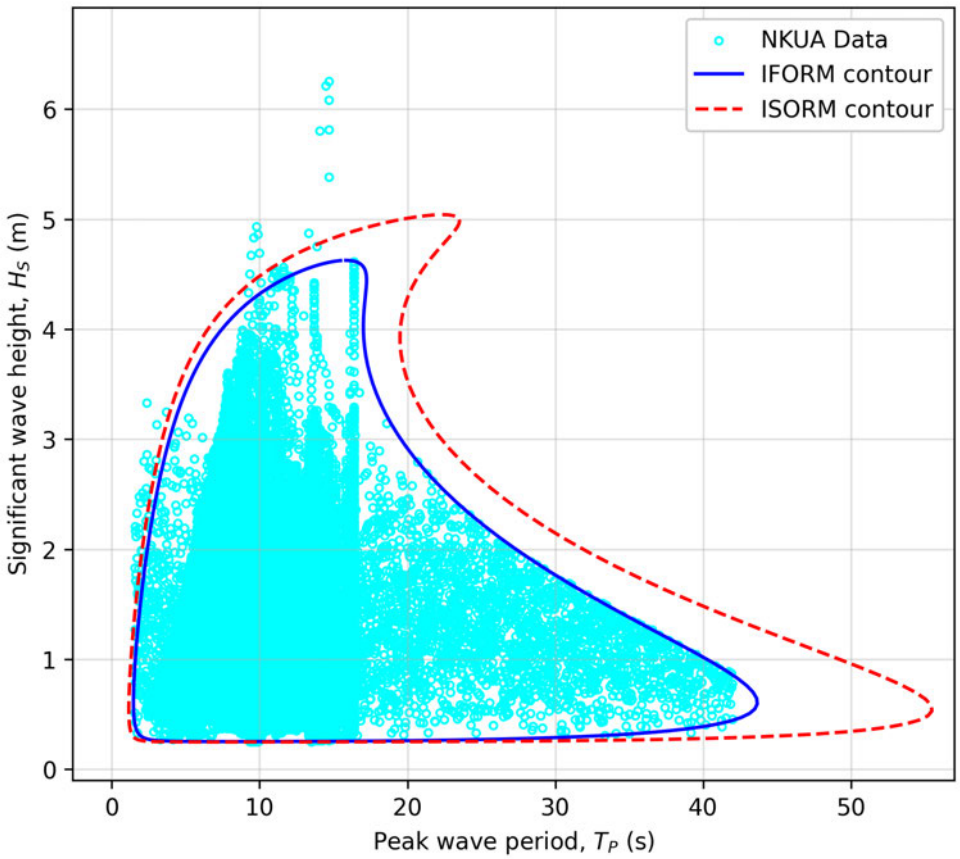

Figure 4.12: Environmental contour lines with a return period of 50 years for (H_S) and (H_S) for wave conditions at the Canary-I site.

4.6.3 Definition of Test Conditions

4.6.3.1 Test Conditions

From the environmental contours constructed in Section 4.6.2, various energetic sea states are defined for both irregular and regular seas. These sea states are specifically selected to reflect the storm "survival" conditions at the Canary-I reference site; during such events, the rotors will be parked. Therefore, this aimed to assess how the W2Power platform and mooring lines behave and weathervanes under such extreme waves and current conditions.

Regular Waves

Extreme environmental conditions are selected from the IFORM contour (Figure 4.12). This involves choosing two different wave amplitudes, each with five different frequencies. Consequently, the selected regular waves are then characterised by the wave height (H) and wave period (T), as outlined in Table 4.5.

Table 4.5: Test parameters used for regular wave observations.

Sea state	Prototype		Scale Model		Direction (°)		
	H (m)	T (s)	H (mm)	T (s)	0	90	180
1	4.63	20	116	3.16	✓	–	✓
2	4.63	16	116	2.53	✓	✓	✓
3	4.63	12	116	1.90	✓	–	✓
4	4.63	8	116	1.26	✓	–	✓
5	4.63	4	116	0.63	✓	✓	✓
6	3.85	20	96	3.16	✓	–	✓
7	3.85	16	96	2.53	✓	✓	✓
8	3.85	12	96	1.90	✓	–	✓
9	3.85	8	96	1.26	✓	–	✓
10	3.85	4	96	0.63	✓	✓	✓

Irregular Waves

Irregular waves are characterised by the significant wave height (H_S) and peak wave period (T_P) and are modelled using the JONSWAP spectrum (Hasselmann et al., 1973). The JONSWAP spectrum, $S(f)$, is a one-dimensional frequency spectrum and is defined as:

$$S(f) = \left(\frac{\alpha g^2}{16\pi^4}\right) f^{-5} \exp\left[-\frac{5}{4}\left(\frac{f}{f_m}\right)^{-4}\right] \gamma^b \tag{4.7}$$

with

$$\alpha = 0.076 \left(\frac{gF}{U_{10}^2} \right)^{-0.22} \tag{4.8}$$

$$b = \exp \left[-\frac{1}{2\sigma^2} \left(\frac{f}{f_m} - 1 \right)^2 \right] \tag{4.9}$$

$$\sigma = \begin{cases} 0.07 & \text{for } f \leq f_m \\ 0.09 & \text{for } f > f_m \end{cases} \tag{4.10}$$

where α denotes the equilibrium range parameter, g is the acceleration due to gravity, f_m is the peak frequency of the spectral peak period ($f_m = 1/Tp$). Besides, γ^b is the so-called peak enhancement factor, F is the fetch of wave growth, U_{10} is the wind speed at a height of 10 m above the sea surface, σ is the peak width parameter.

Subsequently, five energetic sea states, denoted from A to E, are generated using the JONSWAP spectrum with a Gamma (γ) value of 3.3. These load cases are detailed in Table 4.6.

Table 4.6: Test parameters for irregular wave observations generated by the JONSWAP spectrum ($\gamma = 3.3$).

Sea state	Prototype		Scale Model		Direction (°)		
	H_S (m)	T_P (s)	H_S (mm)	T_P (s)	0	90	180
A	4.63	16.40	116	2.59	✓	✓	✓
B	4.42	11.50	111	1.82	✓	–	✓
C	4.21	9.00	105	1.42	✓	–	✓
D	3.85	6.20	96	0.98	✓	✓	✓
E	0.60	43.5	15	6.88	✓	✓	✓

Current Characteristics

The velocity shape of the current profile in the FloWave tank is almost independent of the mean current velocity. It is worth mentioning that when running wave-current conditions, it was found that generating faster currents increased the force on the wavemaker paddles. In order to mitigate this effect, the current velocity is often limited to 0.9 m/s (Noble, 2018). In the present campaigns, the maximum current speed at the Canary-I site is 0.8 m/s, consistently generated at 0° degrees in all trials. Consequently, this ensures there is no potential upsurge in the wavemaker force. The specifications of the current conditions are detailed in Table 4.7.

Table 4.7: Characteristics of current test conditions.

Particular	Unit	Prototype	Scale Model	Direction (°)
Current speed (U_c)	[m/s]	0.8	0.13	0

4.6.3.2 FloWave Coordinates

A top-view sketch of the FloWave facility is presented in Figure 4.13, showcasing the tank's Cartesian coordinate system. Also, Figure 4.13 shows the gantry and crane, which both traverse the tank hall to facilitate the transportation of physical models and the installation of measurement equipment (S. T. Draycott, 2017a).

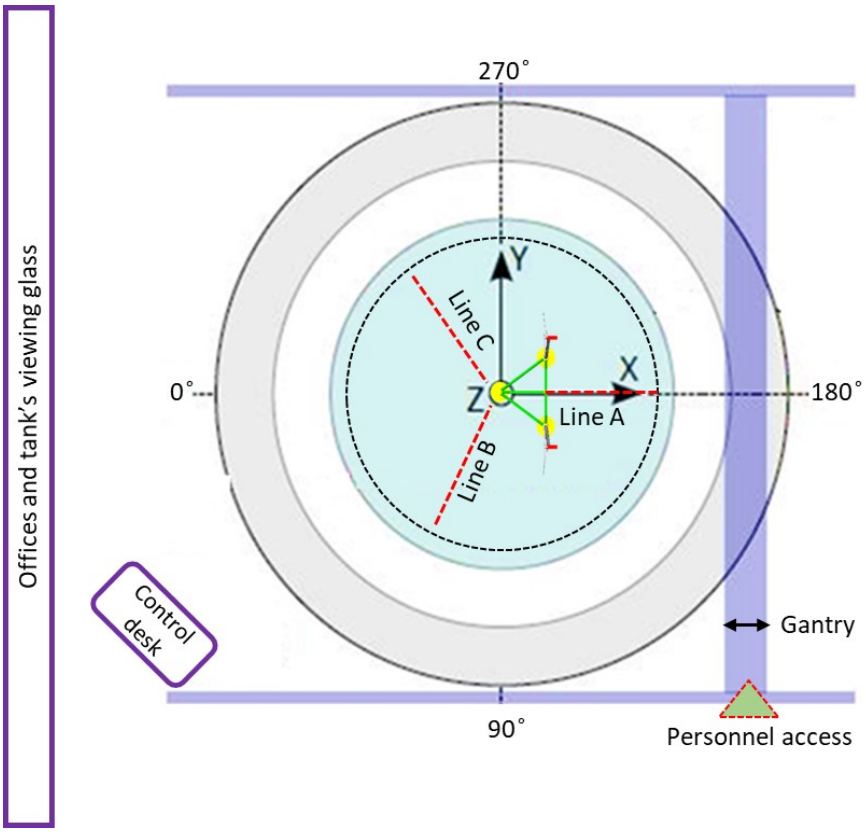

Figure 4.13: Detailed top-view sketch of the FloWave facility, showing the tank's reference coordinates and some components: the control desk, upper viewing glass and offices, and the gantry where wave gauges were installed (S. T. Draycott, 2017a; Noble, 2018).

The tank's origin is located at the centre of the test floor, with the $+X$ axis originating from the tank centre in a direction opposite to that of offices and the control desk towards the rear of the building. Rotations in the system then follow a positive anti-clockwise direction. The $+Z$ axis points upwards; these coordinates can be expressed as (X,Y) or (X,Y,Z) (S. T. Draycott, 2017a; Noble, 2018).

4.6.3.3 Modelling Setting

Motion responses are assessed using a 6-DoF system in reference to the tank coordinate system, as illustrated in Figure 4.14.

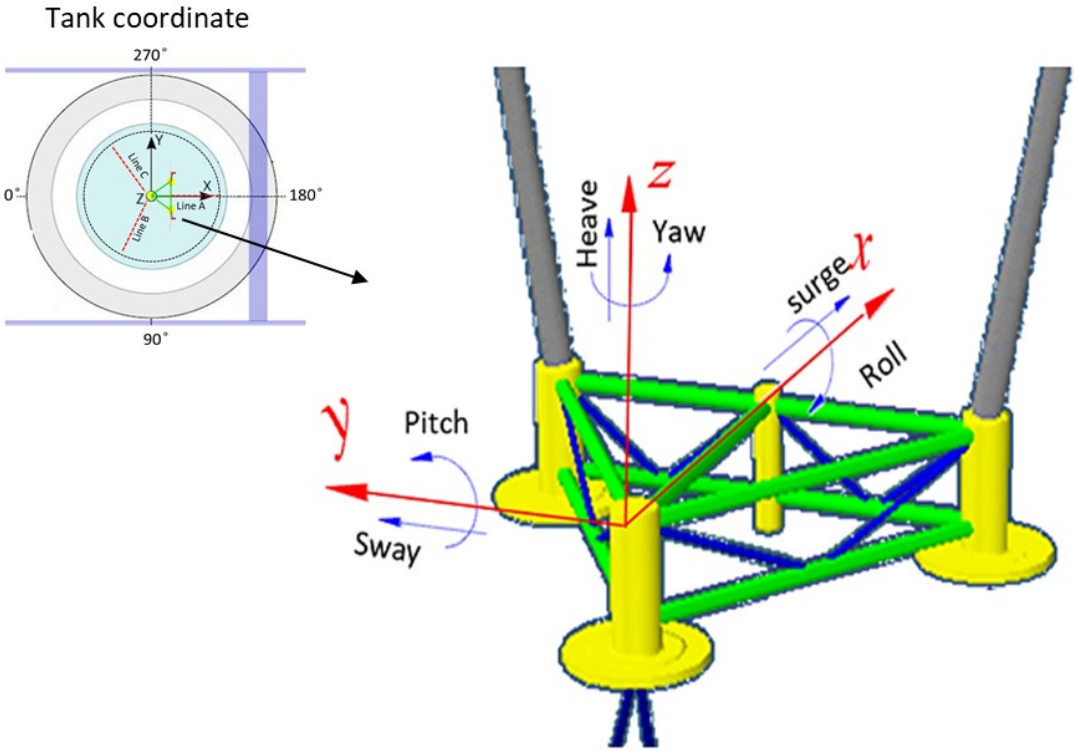

Figure 4.14: Coordinates for the W2Power model positioned at the tank's centre, describing the 6 DoFs of the W2Power platform in relation to the tank's coordinate system.

Subsequently, employing these coordinate definitions shown in Figure 4.14, the test parameters provided in Tables 4.5 to 4.7 are implemented to introduce environmental loads essential for meeting the test objectives. The floating system was subjected to pure current, waves only, and combined waves and currents. Configurations of these loading scenarios are depicted in Figure 4.15.

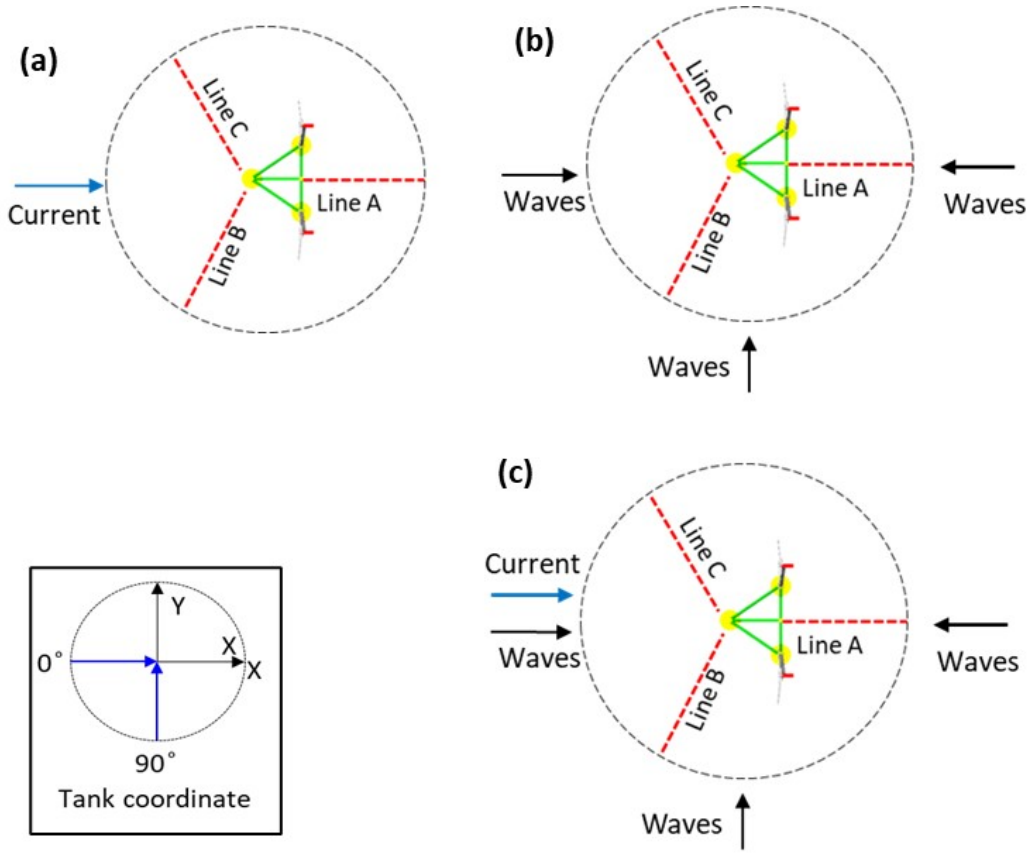

Figure 4.15: Configurations of directional environmental loadings during the test matrices: (a) currents only, (b) waves only, and (c) combined wave-current loads. Also, showing FloWave's coordinate system as the floating model is positioned at the tank's centre.

4.7 Chapter Summary

This chapter detailed comprehensive experimental investigations to explore the dynamic responses of FOWTs under combined wave-current conditions. A theoretical framework was established to guide the experimental procedure.

The test facility used for the experiments was described, including details of different instrumentation and data acquisition systems. This was followed by a description of the physical model employed and its mooring system.

Environmental modelling of metocean conditions and the generation of various load cases for regular and irregular sea states were presented. Then, an in-depth explanation of the experimental procedure was provided. These analyses laid the foundation for the subsequent chapter (Chapter 5), where the results of the experimental modelling are broadly analysed and discussed.

Chapter 5

Experimental Modelling of FOWTs: Results and Discussion

5.1 Introduction

The previous chapter, Chapter 4, established the context and provided detailed analyses necessary for conducting a comprehensive experimental programme to investigate the multi-unit FOWTs and mooring systems under combined wave-current conditions. In order to address the research aims and objectives outlined in Section 1.7, these experiments are designed to observe and quantify the impact of tides and their simultaneous influence with waves on the dynamic responses of mooring systems and MUFOWP motions.

Building on the experimental framework and procedures presented in Chapter 4, this chapter, Chapter 5, delves into the findings regarding the implications of current, wave, and combined wave-current loading on the dynamic responses of mooring tensions and W2Power platform motions. Subsequently, the chapter first reports on the dynamic responses of mooring lines, which utilised a conventional catenary system made of studless chains. Following this, the chapter presents the motion dynamics of the floating system, highlighting how the platform behaves under different environmental loads. The comprehensive data acquired from these tests provides crucial insights into the behaviour and performance of MUFOWPs and mooring systems under realistic ocean conditions.

5.2 Dynamic Responses of Mooring Lines

FOWTs are typically proposed for deep water depths (e.g. $\geq$ 60 m), where the mooring lines play a crucial role in maintaining the overall stability of the floating system and in keeping it at a stationary location. Thus, the loads on these mooring lines are particularly important to quantify. In addition, the comparison of the fairlead forces of the mooring system is of interest.

This section discusses the results of the dynamic responses of the mooring loads at the three fairleads, as measured by the 500 N load cells. Herein, the analysis focuses on exploring the effect of current, waves, and combined wave-current conditions on the three mooring cables.

5.2.1 Effect of Current and Waves

The time histories of fairlead forces for three mooring lines under pure current and regular waves are depicted in Figure 5.1. Notably, the downwind-side line (line A) consistently experiences lower tension compared to the upwind-side mooring lines (lines B and C) across all wave directions, which is attributed to its alignment with the positive x-axis (current direction). Additionally, lines B and C exhibit symmetrical fairlead forces due to the layout of the mooring system.

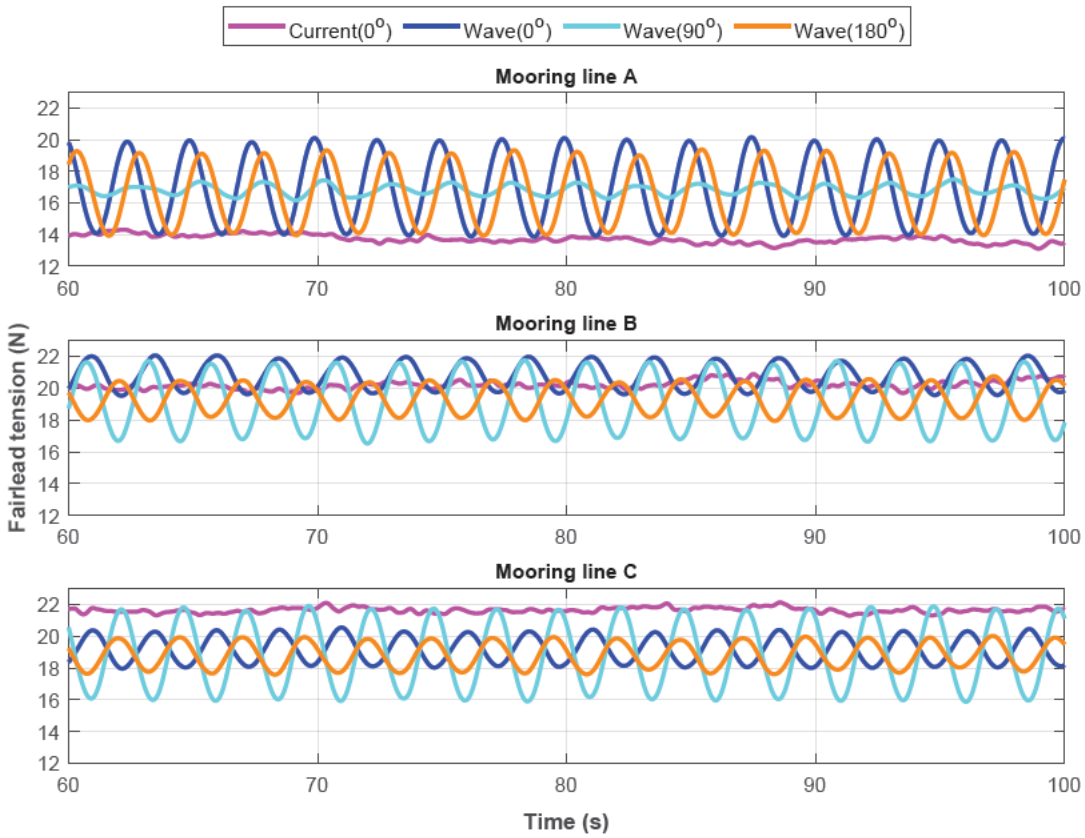

Figure 5.1: Time series of fairlead mooring loads, highlighting the influence of current of a speed of 0.13 m/s and comparing the effects of different wave propagation scenarios for the regular sea state 7 (LC7) of a wave height (H) = 96 mm and wave period (T) = 2.53 s.

It is worth to note that, to note that, as illustrated in Figure 4.4, line A aligns with the positive x-direction and current direction, whereas lines B and C are inclined towards the negative and positive y-direction with an angle, respectively. Under conditions with a current of a speed of 0.13 m/s and a regular wave (LC7) of a height (H) = 96 mm and period (T) = 2.53 s, results reveal that the pure current effect on line A is significantly less than that of pure

waves, regardless of wave direction. Waves propagating from 0° exert the highest impact on line tension, followed by waves from 180°, while crossing waves (from 90°) have the least effect. Conversely, the opposite behaviour has been observed on lines B and C for waves propagating from 0° and 180°.

In addition to the time history analysis, detailed statistical assessments have been carried out for mooring loads at the fairleads of lines A, B, and C under various environmental loading conditions of pure current and waves. Tables 5.1 to 5.3 compare the statistics of the mooring loads for lines A, B, and C, respectively. They summarise the minimum (min), mean, maximum (max), and standard deviation (StDev) of the mooring forces, highlighting distinct load responses influenced by the direction of currents and waves and offering further insights into the load behaviour.

For example, under pure current conditions, mooring line A (i.e. aligns with the current from 0°) consistently experiences the lowest tension, with a maximum of almost 15 N (Table 5.1). In contrast, lines B and C, oriented at angles to the current, exhibit significantly higher loads, with maximum tensions of 20.25 kN and 23.62 kN, respectively (Tables 5.2 and 5.3). This indicates that line A is the least affected by the current alone, while lines B and C are more susceptible due to their orientation relative to the flow.

When following waves (from 0°) hit the platform, all mooring lines show an increase in tension. Line A, which demonstrated lower tensions under pure current, experiences a sharp rise, with maximum tension reaching 20.22 N, demonstrating its sensitivity to waves propagating in the same direction as the current. Lines B and C also experience increased loads, though the rise is less pronounced, indicating the influence of wave-line alignment on their behaviour.

Under crossing waves (from 90°), significant fluctuations in mooring line loads are observed. Line B sees a maximum tension of 21.97 N, while line C experiences the highest load variability, with a standard deviation of 1.98 N, indicating substantial fluctuations in its load response. This highlights the particular sensitivity of these lines (B and C) to waves coming from perpendicular directions, which induces noticeable variations in the forces they experience. Under opposing waves (from 180°), the mean and max loads on line A decrease slightly compared to the following waves. Lines B and C also experience slightly lower maximum tensions under opposing waves compared to crossing waves, though the loads remain significant.

Furthermore, the StDev values highlight how current and wave directions can significantly affect the stability and variability of mooring loads (Table 5.1). Following waves generally induced the highest fluctuations in line A, while crossing waves led to large variability in lines B and C (see Tables 5.2 and 5.3). Such load variabilities are crucial to consider in

the design and optimisation of mooring systems, underscoring the need for bespoke design considerations based on mooring line orientation and environmental conditions. This, in turn, ensures that mooring systems can effectively manage both steady and fluctuating loads, maintaining structural integrity and overall performance.

Table 5.1: Statistical comparison of mooring loads of line A under pure currents of a speed of 0.13 m/s, and regular waves (LC7) with a height of 96 mm and a period of 3.5 s.

Environmental loading	**Fairlead load, (N)**			
(Propagation direction, °)	**Min**	**Mean**	**Max**	**StdDev**
Current (0°)	13.106	13.799	14.910	0.265
Following waves (0°)	13.729	16.952	20.215	2.061
Crossing waves (90°)	15.922	16.781	18.399	0.322
Opposing waves (180°)	13.661	16.602	19.597	1.796

Table 5.2: Statistical comparison of mooring loads of line B under pure currents of a speed of 0.13 m/s, and regular waves (LC7) with a height of 96 mm and a period of 3.5 s.

Environmental loading	**Fairlead load, (N)**			
(Propagation direction, °)	**Min**	**Mean**	**Max**	**StdDev**
Current (0°)	19.617	20.248	20.962	0.250
Following waves (0°)	17.699	20.800	22.172	0.782
Crossing waves (90°)	16.450	19.149	21.965	1.691
Opposing waves (180°)	17.387	19.315	20.753	0.835

Table 5.3: Statistical comparison of mooring loads of line C under pure currents of a speed of 0.13 m/s, and regular waves (LC7) with a height of 96 mm and a period of 3.5 s.

Environmental loading	**Fairlead load, (N)**			
(Propagation direction, °)	**Min**	**Mean**	**Max**	**StdDev**
Current (0°)	20.789	21.581	23.615	0.217
Following waves (0°)	17.369	19.167	20.578	0.787
Crossing waves (90°)	15.772	18.825	22.053	1.981
Opposing waves (180°)	16.673	18.814	20.155	0.754

5.2.2 Impact of Wave Directionality

The influence of wave directionality on mooring line loads is crucial in the design and operation of floating offshore structures. The significance of mooring line model fidelity in simulations of FOWTs has been emphasised, highlighting the need for accurate predictions of mooring dynamic behaviours under various directional loading (Hall et al., 2014).

To elucidate this influence, Figures 5.2 to 5.4 depict fairlead forces for regular waves, while Figures 5.5 to 5.7 showcase the same for irregular waves with varying heights and periods impacting the floating system from different angles. The Violin plots illustrate the load distribution at each fairlead across the three wave directions (0°, 90°, and 180°).

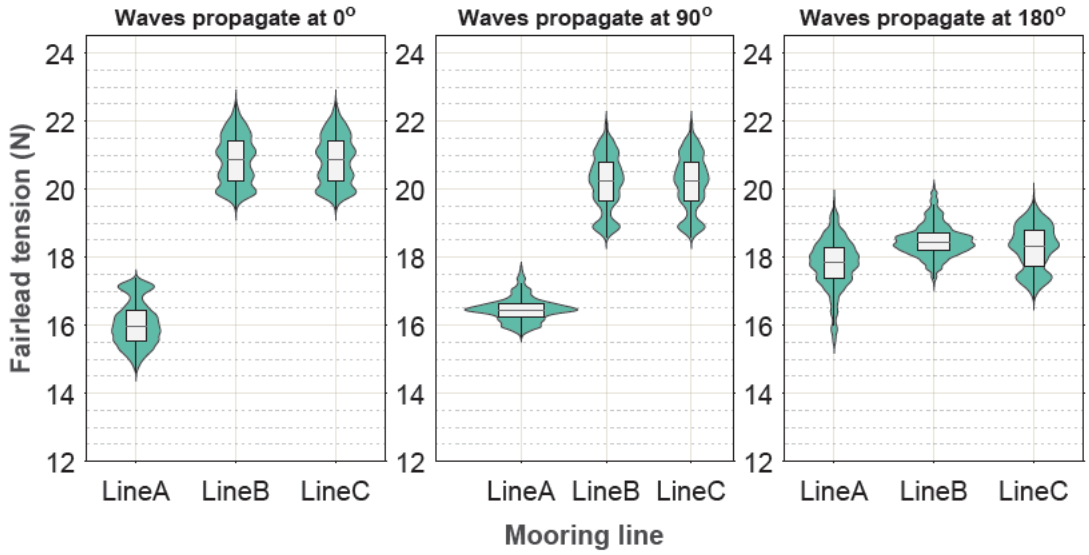

Figure 5.2: Comparison of the impact of wave directionality on fairlead mooring loads for a regular wave load case (LC5); highlighting variations in mooring loads under waves propagating from: 0° (left), 90° (middle), and 180° (right).

Note that the unique shapes of the violin plots are driven by the variability in mooring/motion responses experienced under different conditions. The peaks and widths of the violins indicate the distribution and frequency of the responses experienced. Wider sections indicate a more frequent occurrence of certain response values, while narrower sections signify less common response ranges (Hintze & Nelson, 1998).

The results depicted in Figures 5.2 to 5.7 underscore the influence of wave directionality on mooring line loads, with waves from 0° inducing the lowest tension on Line A across all sea states, followed by waves from 90°, and then 180°. Furthermore, Line A displays a broad range of tension values, indicating varying forces under different wave directions. This line

consistently experienced the lowest tension from wave-induced loading, which is likely due to the platform's orientation and mooring configuration. Interestingly, twin peaks are seen in some violins of mooring loads, which can be attributed to extreme or snap loads on the mooring lines (Davidson & Ringwood, 2017).

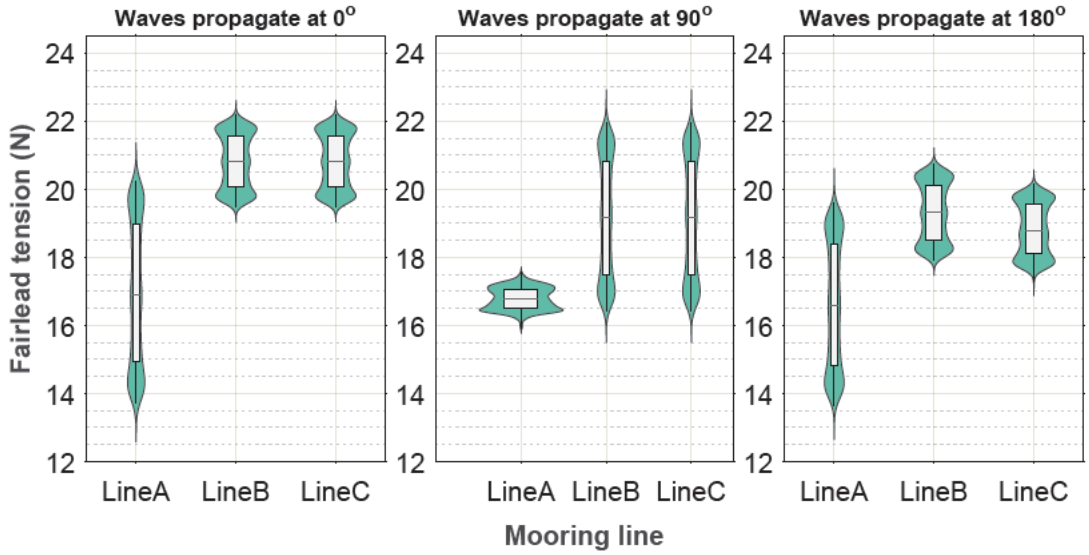

Figure 5.3: Comparison of the impact of wave directionality on fairlead mooring loads for a regular wave load case (LC7); highlighting variations in mooring loads under waves propagating from: 0° (left), 90° (middle), and 180° (right).

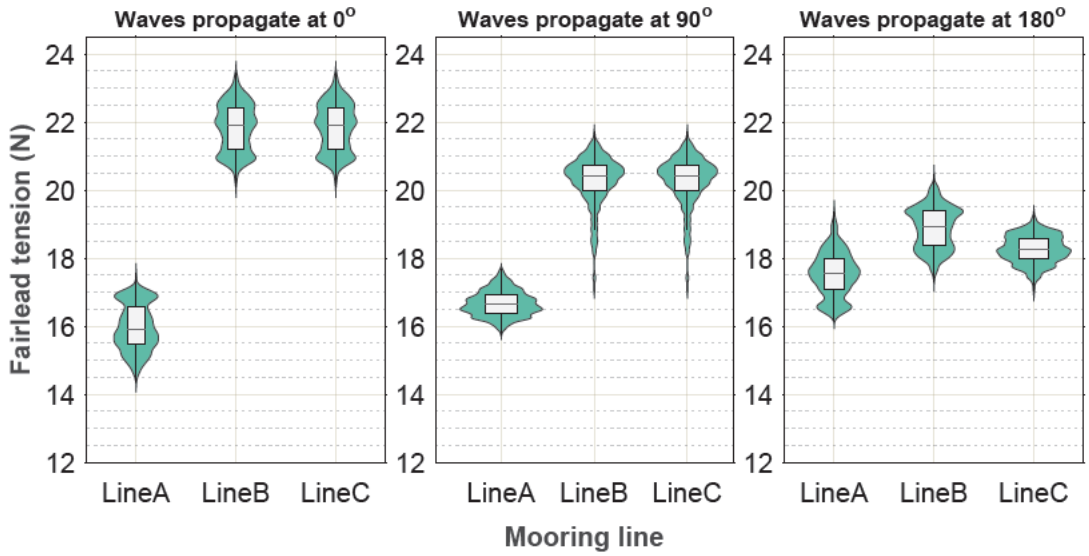

Figure 5.4: Comparison of the impact of wave directionality on fairlead mooring loads for a regular wave load case (LC10); highlighting variations in mooring loads under waves propagating from: 0° (left), 90° (middle), and 180° (right).

For the regular sea states characterised by higher wave steepness, such as states LC5 and LC10 with shorter wave periods (T = 0.63 s), the Violin plots revealed a skewed distribution, notably under 0° and 180° wave directions. These asymmetries in distribution suggest a higher occurrence of lower tension values experienced by the mooring lines under these specific wave directions. This observation is further shown in Figures 5.9 and 5.10, which compare the interaction of following and opposing waves with the current, respectively.

Potential sources of inconsistency in mooring line load measurements stem from experimental setup and environmental conditions. A key discrepancy is the expectation of lower loads under crossing wave conditions, contradicted by higher observed loads in irregular load cases (A, D, and E), as well as lower loads in line A with waves propagating from 180. These inconsistencies and asymmetries are attributed to wave reflections in the tank, influenced by frequency, flow velocity, and angle, causing skewed tension distributions. A detailed explanation is provided in Appendix A.3.

From Figures 5.5 to 5.7, differences have been observed in the mooring loads under irregular waves compared to regular waves with comparable heights (i.e., 3.85 and 4.63 m) and periods (i.e., approximately 6 and 16 s). Irregular sea states resulted in higher mooring loads (Shen et al., 2018), highlighting the dynamic nature of irregular waves and their impact on mooring system nonlinearity and load distributions (Jin et al., 2022).

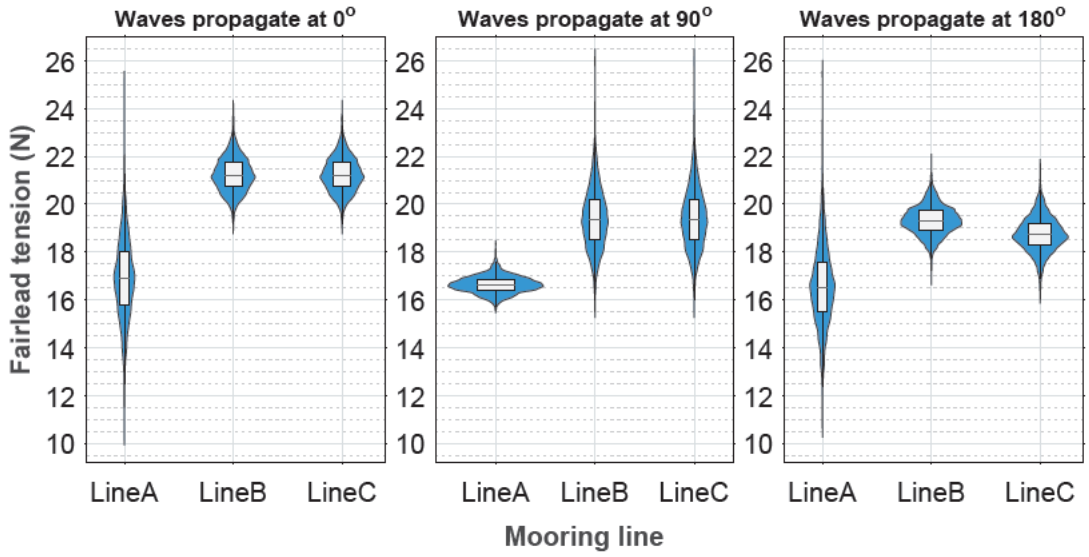

Figure 5.5: Comparison of the impact of wave directionality on fairlead mooring loads for an irregular wave load case (LC: A); highlighting variations in mooring loads under waves propagating from: 0° (left), 90° (middle), and 180° (right).

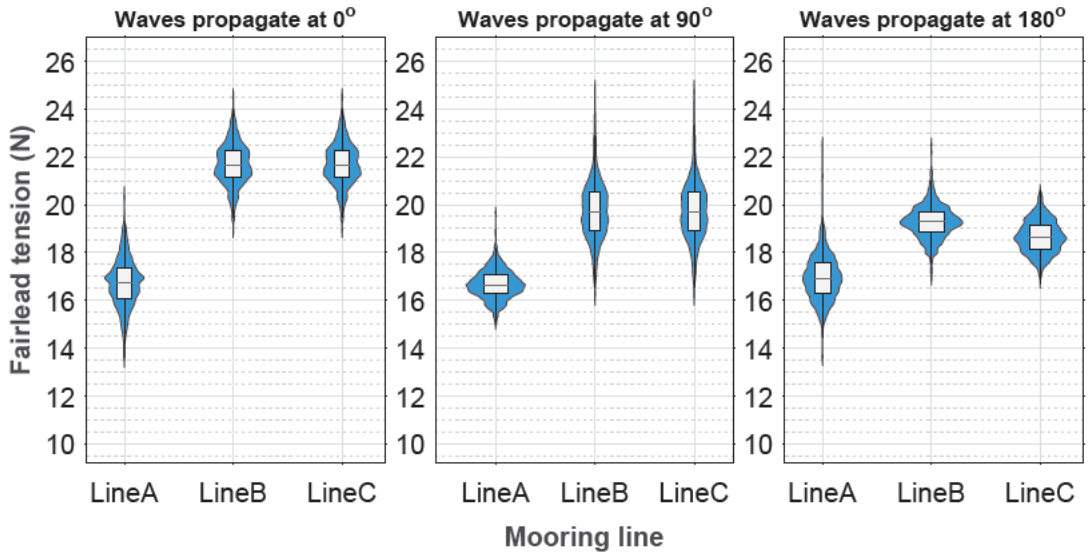

Figure 5.6: Comparison of the impact of wave directionality on fairlead mooring loads for an irregular wave load case (LC: D); highlighting variations in mooring loads under waves propagating from: 0° (left), 90° (middle), and 180° (right).

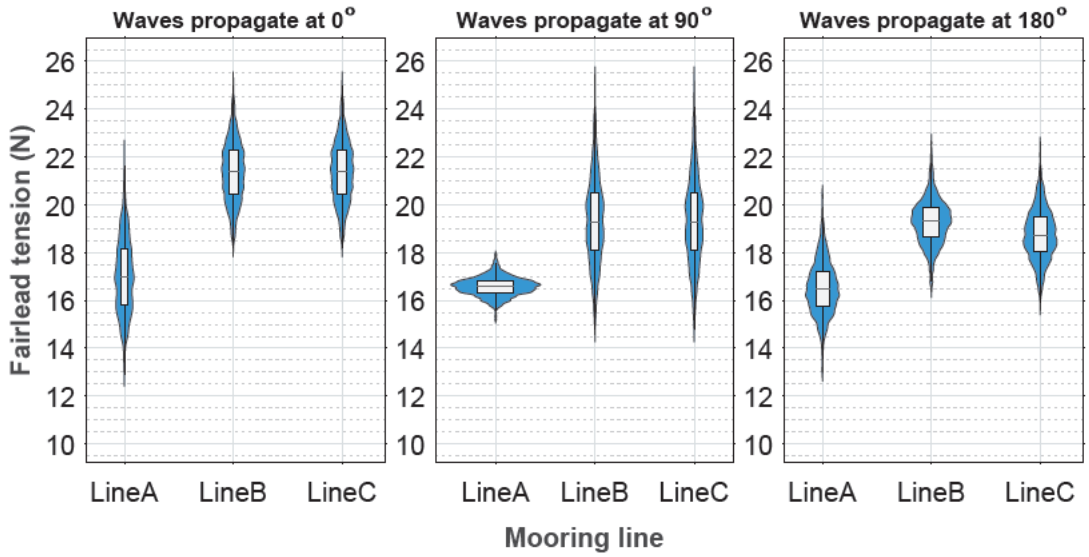

Figure 5.7: Comparison of the impact of wave directionality on fairlead mooring loads for an irregular wave load case (LC: E); highlighting variations in mooring loads under waves propagating from: 0° (left), 90° (middle), and 180° (right).

Pure waves originating from 0° induced the highest peak tension across all lines, followed by waves from 90°, and then waves propagated from 180°, supporting the impact of wave approach direction on mooring line loads. Furthermore, the influence of wave directionality on mooring line loads was evident, consistent with previous research by Z. Liu et al. (2019) and Xiang & Guedes Soares (2020).

Collectively, these observations of higher loads due to irregular sea states indicate the inadequacy of monochromatic waves in capturing the full spectrum of wave-induced loads. Note that maximum wave height (H_{max}) can reach up to twice the significant wave height; therefore, regular wave tests at H_{max} might yield maximum loads similar to those from irregular conditions. This underscores the importance of considering irregular wave conditions in designing and analysing mooring systems for FOWTs, aligning with findings by Kristiansen & Faltinsen (2015) regarding the dominance of mean loads over dynamic loads in combined current and wave conditions.

5.2.3 Impact of Combined Wave-Current

Currents significantly influence platform response, mooring tensions, and the fatigue life of floating structures (T. Ishihara & Liu, 2020; Otter, Flannery, et al., 2022). When currents interact with waves, they can modify wave properties such as height, period, and direction, leading to changes in wave propagation paths and crest shapes (Jonsson et al., 1970; J. Smith, 1997; Moreira & Peregrine, 2010).

The influence of combined wave-current loading on FOWTs' mooring lines is a crucial aspect impacting their overall performance and safety (Otter, Desmond, et al., 2022). However, physical experiments on FOWTs frequently overlook current loading and its combined effect with waves, highlighting the necessity for comprehensive investigations to consider such effects, particularly for designing robust mooring and anchoring systems (A. C. Pillai et al., 2018a; Xu et al., 2022; Pillai et al., 2022, 2022b).

Accordingly, these experiments are specifically designed to explore the implications of this loading on the dynamics of FOWTs. Herein, the impact of combined wave-current loading on mooring lines has been investigated, revealing distinct behaviours in the time history of fairlead forces for mooring lines under pure waves and combined wave-current conditions (see Figure 5.8).

The presence of current interacting with the waves has been shown to alter the dynamic load of mooring lines, with specific impacts varying across different wave-current interaction scenarios (Figure 5.8). The resulting alterations in the mooring loads depend on the orientation of the lines relative to wave and current directions.

For instance, the tension on line A generally decreases with the presence of current, particularly in scenarios that involve combined following waves and currents. This reduction occurs primarily because the current tends to move the model in the direction of Line A, slackening this line. Notably, Line A, aligned with both wave and current directions, experiences reduced load in the presence of current. This is attributed to the reduced wave height caused by the following current, which dissipates wave energy into turbulence and thus reduces the mooring line load.

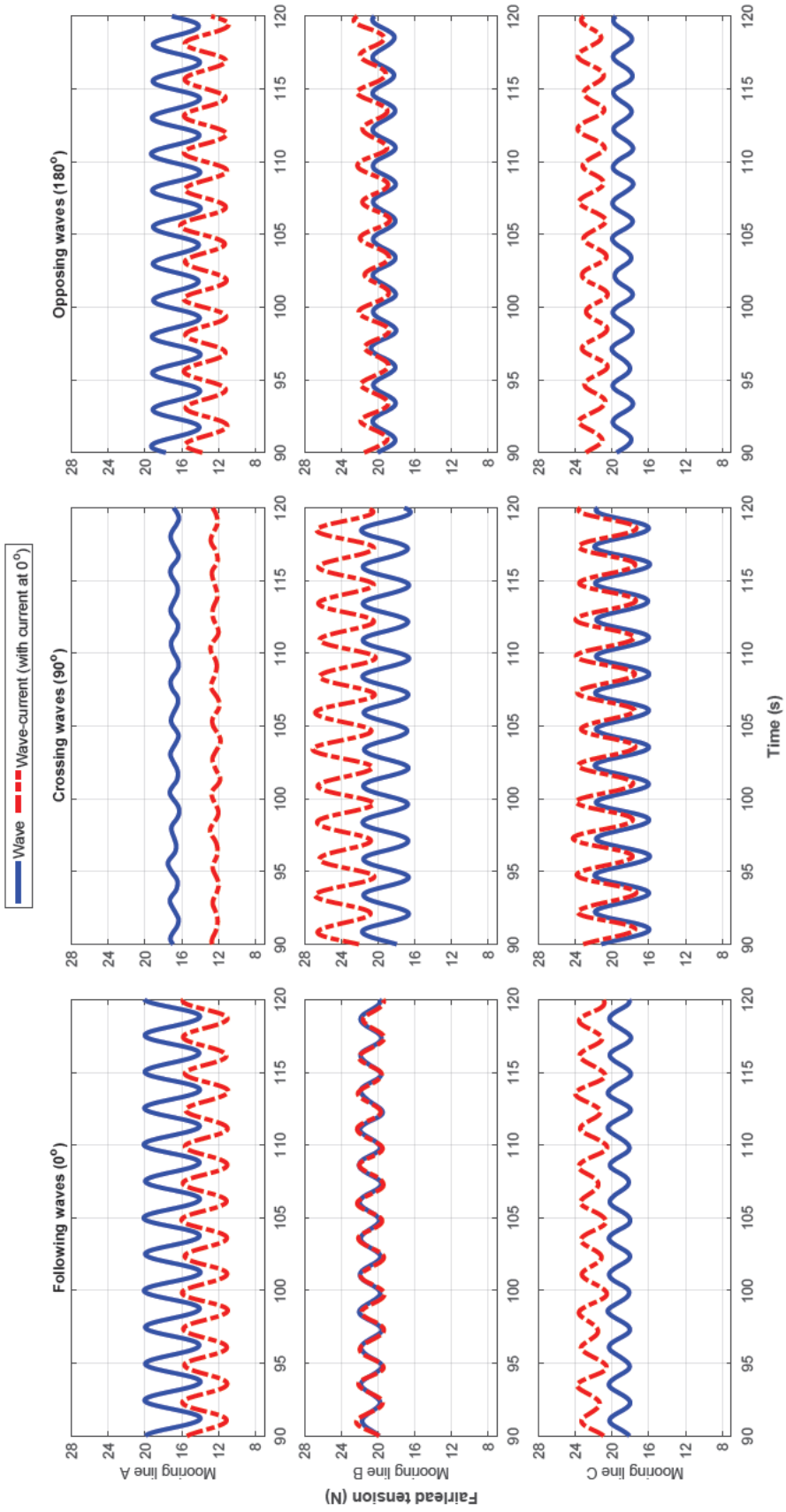

Figure 5.8: Time series of fairlead mooring loads, highlighting the influences of different wave propagation scenarios for a regular wave load case (LC7) of a wave height (H) = 96 mm and wave period (T) = 2.53 s; also showing the impact when these waves interact with a current of a speed of 0.13 m/s, highlighting the combined effects on mooring loads.

On the other hand, lines B and C generally experience increased tension in the presence of current. Remarkably, line B experiences peak load when crossing waves interact with the current, likely due to the wave direction being 30° relative to line B and 150° to line C. Hypothetically, a similar behaviour would be expected for line C under 270° wave conditions.

Overall, tensions in surge directions (positive or negative) are generally larger than those in the sway direction, as shown in Figure 5.8. The reduced impact on the sway direction could be attributed to the interaction between the seabed and the mooring line, resulting in relatively minor transverse motion of the fairleads Touzon et al. (2018); Touzon, Nava, Gao, et al. (2020). Furthermore, similar and comparable tension patterns are observed for crossing waves interacting with the current, showing consistent performance across all lines.

In summary, the findings reveal the intricate interplay between waves, currents, and mooring line tension, fulfilling the project objectives and addressing the research questions defined in (Section 1.7). Specifically, the results demonstrate that wave directionality significantly influences mooring line loads, with line A experiencing the lowest tensions at 0°, thereby refining the MUFOWP design for stability. While wind loads were not considered in these tests, their inclusion could further amplify mooring tensions, particularly when combined with wave and current forces. Hence, future work should integrate wind thrust to provide more comprehensive experimental models for stability and safety considerations.

Furthermore, the outcomes highlight that wave-current interaction causes variations in mooring tension, necessitating accurate modelling for tidal data in the design process to mitigate extreme loads. Furthermore, the findings on wave period and directionality reveal complex dynamics affecting mooring tensions, informing better predictive models and design strategies for safe operation (Faltinsen, 1993).

5.2.4 Impact of Wave Height and Wave Period

Understanding how wave height influences mooring loads is crucial for assessing the behaviour of structures under varying wave and current conditions. Herein, investigations delve into this relationship by analysing the regular waves of different heights and periods, as outlined in Table 4.5, and their interaction with the current, characterised by the parameters specified in Table 4.7. Subsequently, Figures 5.9 and 5.10 illustrate these analyses and provide insights into how different wave conditions influence mooring loads, particularly in the current presence.

When considering waves propagating from 0° (Figure 5.9), it becomes evident that the impact of wave height and period on mooring loads is nuanced. Observations reveal intriguing trends, where the load characteristics in line A exhibit an opposite behaviour compared to Lines B and C. Specifically, for the first set of load cases (LC1-LC5) with a wave height (H) of 116 mm, a reduction in load is observed as the wave period decreases. This reduction in mooring load is further amplified when waves interact with the flowing current. Conversely, similar trends are observed in Lines B and C, albeit with variations.

For instance, considering regular waves with a wave period of 3.16 s and different heights of 116 mm (LC1) and 96 mm (LC6), the impact on mean tensions due to wave height reduction remains relatively constant, with a difference of about 2%, depending on the mooring line's orientation to incident waves. However, the reduction in wave height decreased the maximum tension in line A by up to 10%, while it increased the maximum tension in lines B and C by up to 16.6%.

Furthermore, the interaction between following waves and a following current significantly impacted mooring dynamics, as depicted in Figure 5.9. For example, both the mean and maximum tensions in line A decreased by up to 23.5%, while those in lines B and C increased by 17.5%. This highlights the critical influence of current directionality on load distribution across mooring lines, necessitating meticulous consideration of currents in the design and analysis of mooring systems, particularly when they interact with waves.

Additionally, when comparing the second set (LC6-LC10) with a height of 96 mm with the first set, the effect of wave height on mooring loads becomes more pronounced. Despite both sets having the same wave periods, this disparity is attributed to the varying wave energies associated with different wave heights, where smaller waves exhibit reduced loads due to their lower energy levels (Kristiansen & Faltinsen, 2015).

Distinct behaviours were observed when waves interacted with a following current. Comparing waves approaching from 180° (Figure 5.10) to those from 0° (Figure 5.9) demonstrates the unique nature of wave-structure interactions, particularly concerning wave angles. When waves approach from 180°, hitting the platform from the back side (stern), where there are two columns, as opposed to waves from 0° hitting the front side (bow) of a single column, it introduces notable differences in the distribution of loads on mooring lines.

From a physics-based perspective, waves from either 0° or 180° are not significantly different in terms of the turbulent level of the flow around the platform. This is because waves will eventually propagate over all three columns, with the primary difference being the phase due to the direction of the incident waves (Tao & Thiagarajan, 2003). Due to the absence of wind in the present experiments, the weak sheltering effect is expected to not substantially alter the flow's turbulent characteristics. Thus, these differences are likely attributed to variations in how the wave phase interacts with the platform's geometry, leading to changes in load distribution

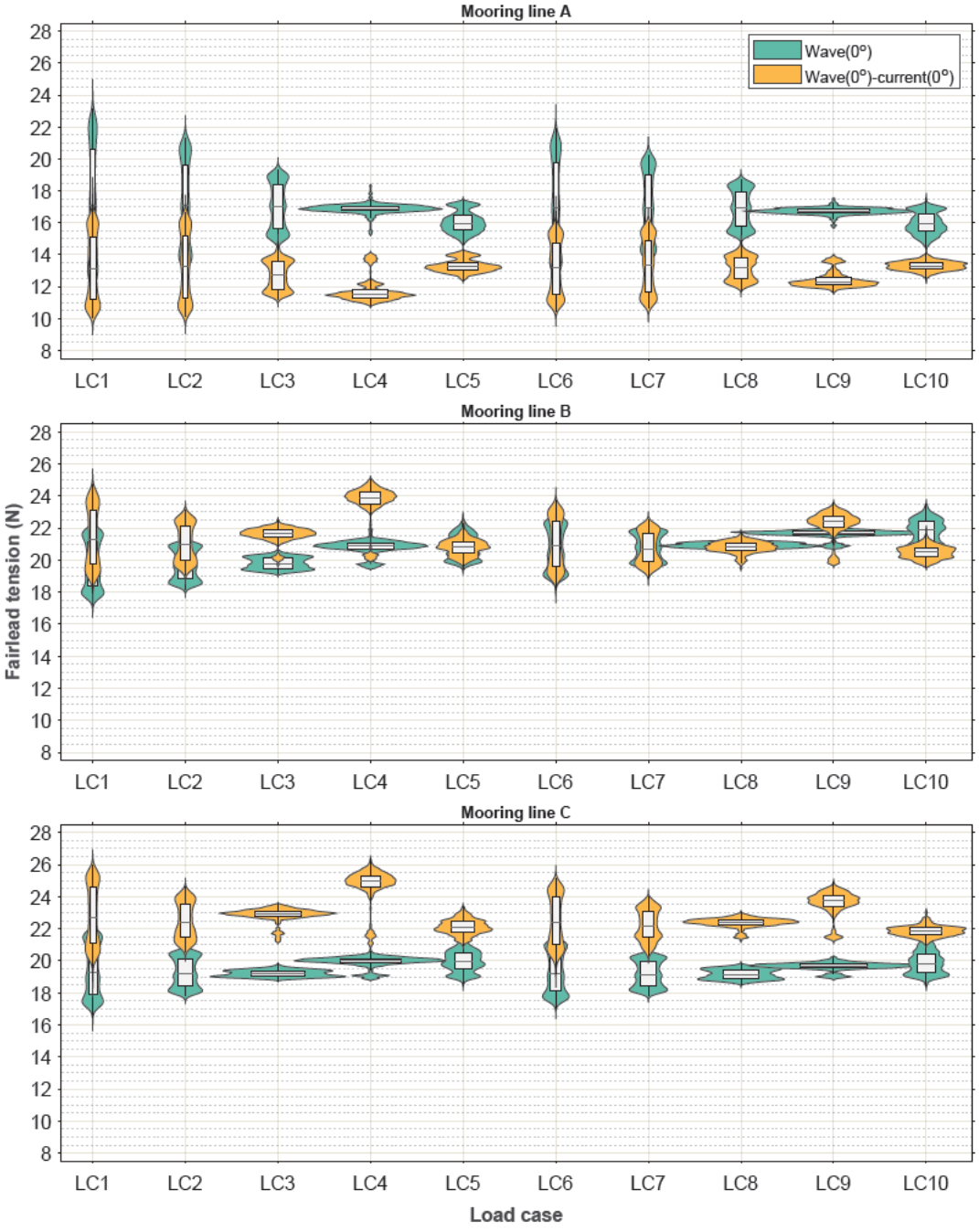

Figure 5.9: Effects of waves and combined wave-current loads on mooring loads. Showing load cases of following regular waves (propagating from 0°) and their interaction with a current from 0°. Panels differentiate tensions at fairleads of mooring lines: (top) line A, (middle) line B, and (bottom) line C.

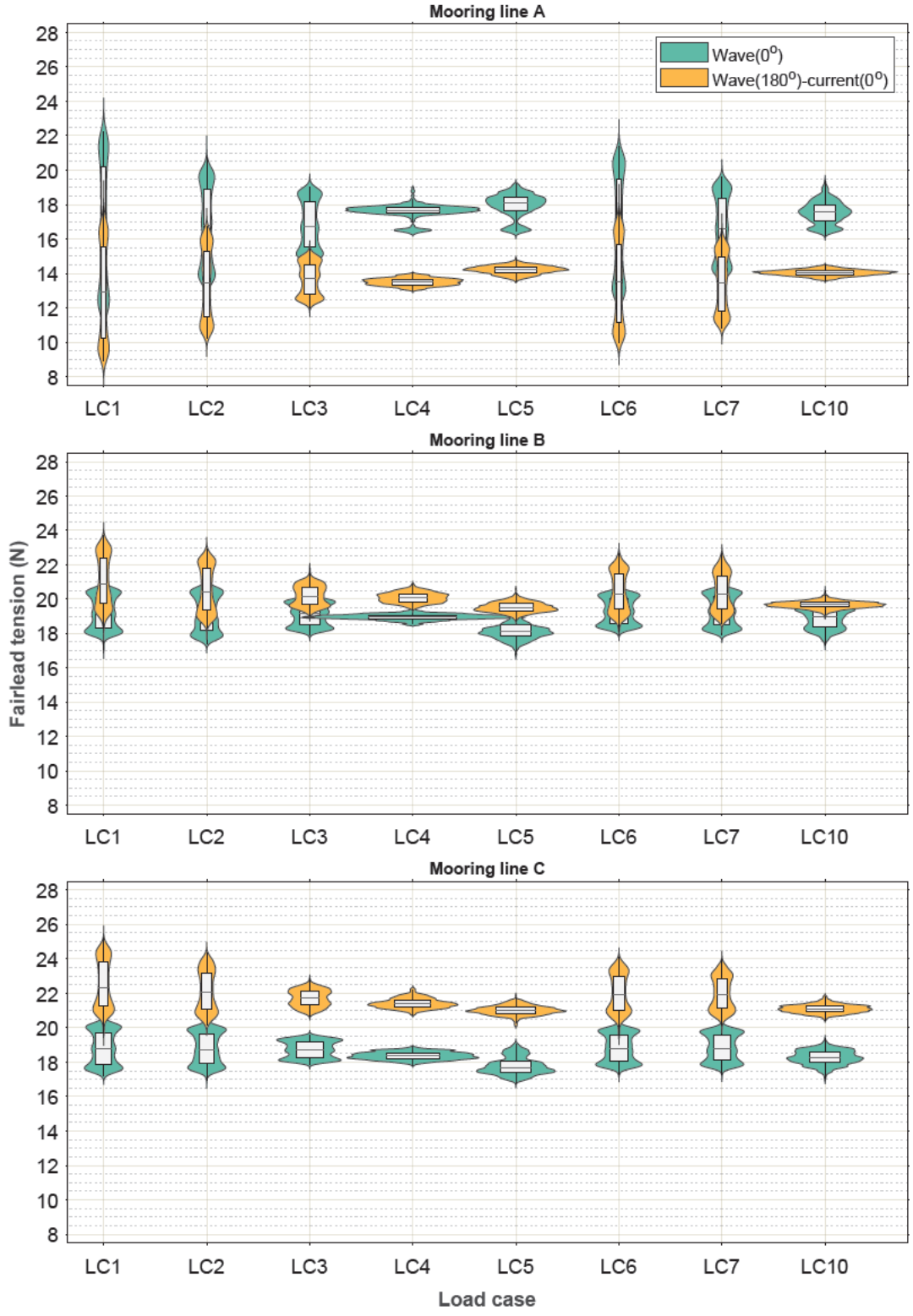

Figure 5.10: Effects of waves and combined wave-current loads on mooring loads. Showing load cases of opposing regular waves (propagating from 180°) and their interaction with a current from 0°. Panels differentiate tensions at fairleads of mooring lines: (top) line A, (middle) line B, and (bottom) line C.

on the mooring lines. While these differences exist, they remain relatively minor compared to the more significant variations introduced by WCI. Instead, the observed variations in mooring line loads are more likely due to changes in flow characteristics resulting from the wave-current interaction (M. Liu et al., 2017).

Furthermore, the VIM effects are unlikely to differ significantly for the two wave directions. This is because VIM is typically dominated by the aspect ratio of the columns and the velocity within the flow field, with platforms possessing extended drafts in high-speed flow fields being more prone to experiencing VIM (Tao & Thiagarajan, 2003). Consequently, the predominant factor contributing to the observed differences in mooring line loads is the interaction between the current and wave direction rather than the turbulence or VIM effects caused by the wave's approach angle.

Wave-current conditions can exacerbate VIM and lead to enhanced VIM with a large angle between the current and waves (X. Li et al., 2023). Besides, when the wave incidence angle is 180°, the upstream vortices keep interacting with the downstream side column (Maximiano et al., 2017). This affects how the vortices shed and the fluid forces acting on the platform columns (Y. Liu et al., 2023; A. Y. Liu et al., 2023). Despite the different wave-structure interactions, the constant current direction from 0° consistently influences the overall load distribution. This highlights the complex interplay between wave direction, platform geometry, and current influence in shaping the induced platform motions and, consequently, mooring loads.

Furthermore, the Violin plots reveal a skewed distribution of load, particularly evident in load cases with shorter wave periods and higher wave steepness ($S \geq 0.021$), which is defined as the ratio of wave height (H) to wavelength (L). Such load cases are LC3-5 and LC8-10 depicted in Figures 5.9 and 5.10. This observation aligns with previous findings highlighting the impact of wave characteristics on load distribution (Tarrant & Meskell, 2016). These findings are instrumental in designing and operating mooring and anchor systems, offering practical guidance for optimising performance and ensuring the integrity of FOWTs in varying waves and current conditions (Hall et al., 2014; Pillai et al., 2022, 2022b).

5.2.5 Frequency Domain Analysis

The power spectral density (PSD) analysis provides valuable insights into the behaviour of mooring lines in the frequency domain, particularly shedding light on the impact of wave-current interaction on load responses across different sea state conditions. Unlike time domain analysis, which focuses on load variations over time, frequency domain analysis allows for the identification of dominant frequencies and energy distribution within the mooring line

loads. PSD analysis helps in determining resonant frequencies, potential fatigue damage, and the FOWT's overall stability under various environmental conditions, offering a deeper understanding of the dynamic responses that are not as easily discernible in the time domain (Youngworth et al., 2005).

Figure 5.11 demonstrates tension PSD of mooring lines under irregular waves of load case D propagate from both 0° and 180° and their interaction with current flows 0°. Waves exhibit dominant responses on mooring lines, with the magnitudes of load responses decreasing notably due to interaction with the current. This is due to the influence of both waves and currents on the tension in the mooring lines, with currents having a more pronounced effect on mooring line tension compared to waves (Matha et al., 2011; H. Yang et al., 2020).

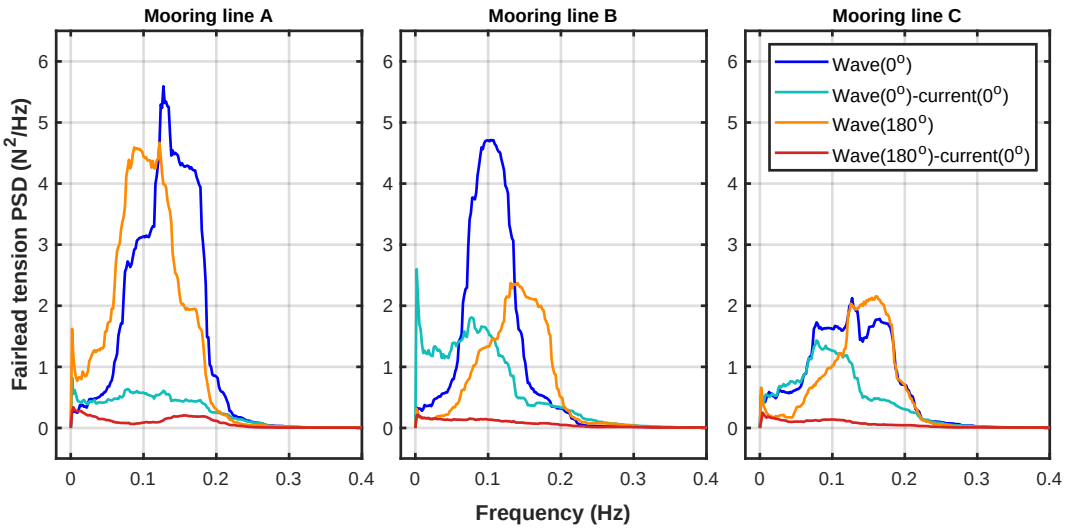

Figure 5.11: Effects of waves and combined wave-current loads on mooring load PSDs. Showing variations in PSDs of tensions at fairleads under irregular waves (LC: D) propagating from 0° and 180°, and their interaction with a current from 0°: (left) line A, (middle) line B, and (right) line C.

As evident in Figure 5.11, the interaction of waves with the current affects the magnitude of load responses because the current can alter the wave characteristics and the relative motion between the waves and the floating structure. Particularly, when the current interacts with waves from 180°, a considerable reduction in peak mooring load magnitudes is observed. These observations align with the behaviours seen in Figure 5.10 for the cases of lines B and C, where opposing waves interact with the current. In turn, this highlights the notable effect that the current can have on wave-induced loads, confirming discoveries by S.-H. Yang et al. (2016).

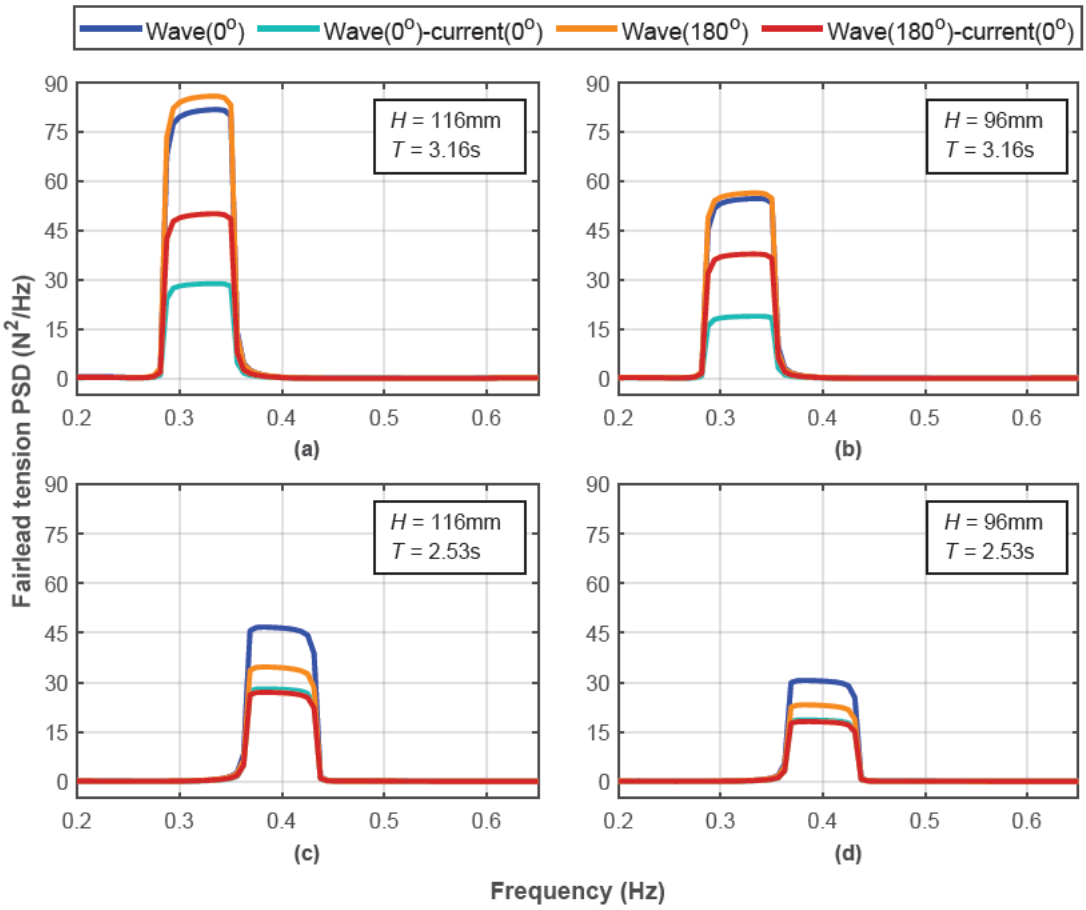

Figure 5.12: Effects of wave height and wave period on the mooring line load. Waves propagating from 0 degrees and 180 degrees, and their interaction with a current from 0. Panels show variations in tension PSDs of mooring line A under different regular load cases (a) LC1, (b) LC6, (c) LC2, and (d) LC7.

Moreover, tension PSDs for line A under regular waves of varying heights and periods are depicted in Figure 5.12 to quantify the influence of wave height and wave period on mooring dynamics[†]. The effect of wave height on the tension PSD was made by comparing Figure 5.12.a and Figure 5.12 .b of different heights and same wave periods of 3.16 s, as well as between Figure 5.12.c and Figure 5.12.d of different heights and a wave period of 2.53 s. From these comparisons, a reduction of 17.24% (from 116 mm to 96 mm) in wave height was found to reduce the magnitude of peak tension by approximately 34% across all loading conditions, including pure following waves, opposing waves, and their interaction with a following current.

[†]. The square shapes of the PSD peaks in Figure 5.12 are due to the smoothing factor or coefficient utilised in the post-processing to denoise the raw measured data.

To further explore the effect of wave period on the tension PSD of line A, comparisons were made between Figure 5.12.a and Figure 5.12.c of the same wave height of 116 mm but different periods, as well as between Figure 5.12.b and Figure 5.12 .d of a wave height of 96 mm and different periods. A 20% decrease in wave period from 3.16 s to 2.53 s led to varying effects under different loading conditions.

For instance, a 60% reduction was observed under opposing waves and a 45% reduction under following waves due to the wave period reduction. Interestingly, when currents interacted with opposing waves, the magnitude of tension PSD decreased by almost 50%. Conversely, the wave period reduction had a negligible effect when the following waves interacted with the current, with only a 2% reduction observed. Thus, indicating the complex effects of wave-current interaction (Shen et al., 2018). These observations align with the findings of Y. Zhao et al. (2019) and Touzon, Nava, de Miguel, & Petuya (2020), who emphasised the differential tension on mooring lines due to varying wave heights and wave periods. Therefore, understanding these dynamics is essential for optimising mooring system designs and ensuring safe installation and operation.

Figure 5.13 compares the PSD of mooring loads under two irregular sea states (A and E), distinguished by wave height and period. Despite the lower wave height in load case E, the order of magnitude of the overall intensity of load responses is quite higher, and this might be attributed to the longer wave period. These notable increases in the PSD peaks of load case E indicate stronger sensitivity to pure waves at these frequencies (X. Zhang, Ni, & Sun, 2022). Additionally, the results showed that current excites the load at low frequencies, particularly in load case A. This led to two relative intensity peaks, with the 0.38 Hz peak becoming dominant, as evident in the left-side subplots of Figure 5.13.

The effect of wave period on mooring loads has been explored through a detailed PSD analysis, as depicted in Figure 5.14. The comparison of mooring loads for regular waves of the same height but different periods revealed a clear trend: the peak load on each line decreases as the wave period decreases. In addition, there are observable shifts in peak frequency, with the peak frequency increasing as the wave period decreases, particularly in scenarios involving wave-current interaction. Likewise, this demonstrates the sensitivity of mooring lines to changes in loading conditions, especially wave period, and its impact on the response characteristics of the mooring system (Slade & Boss, 2015; P. T. Nguyen et al., 2019).

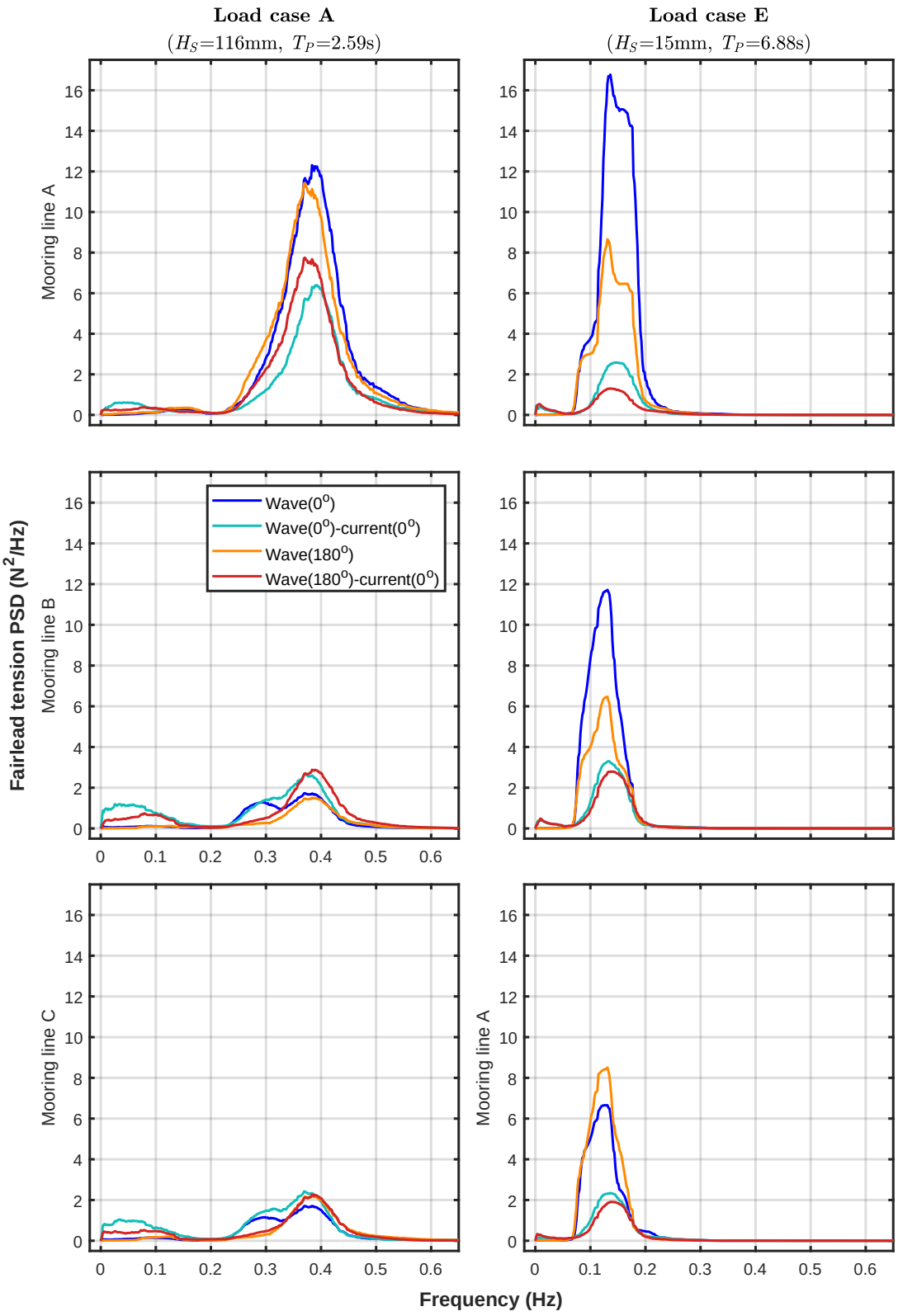

Figure 5.13: Mooring load PSDs under different irregular waves and their interaction with current. Waves propagate from 0° and 180°, interacting with current from 0°. Panels show tension PSDs under irregular load cases A (left-side panels) and E (right-side panels) for the three mooring lines (A, B and C).

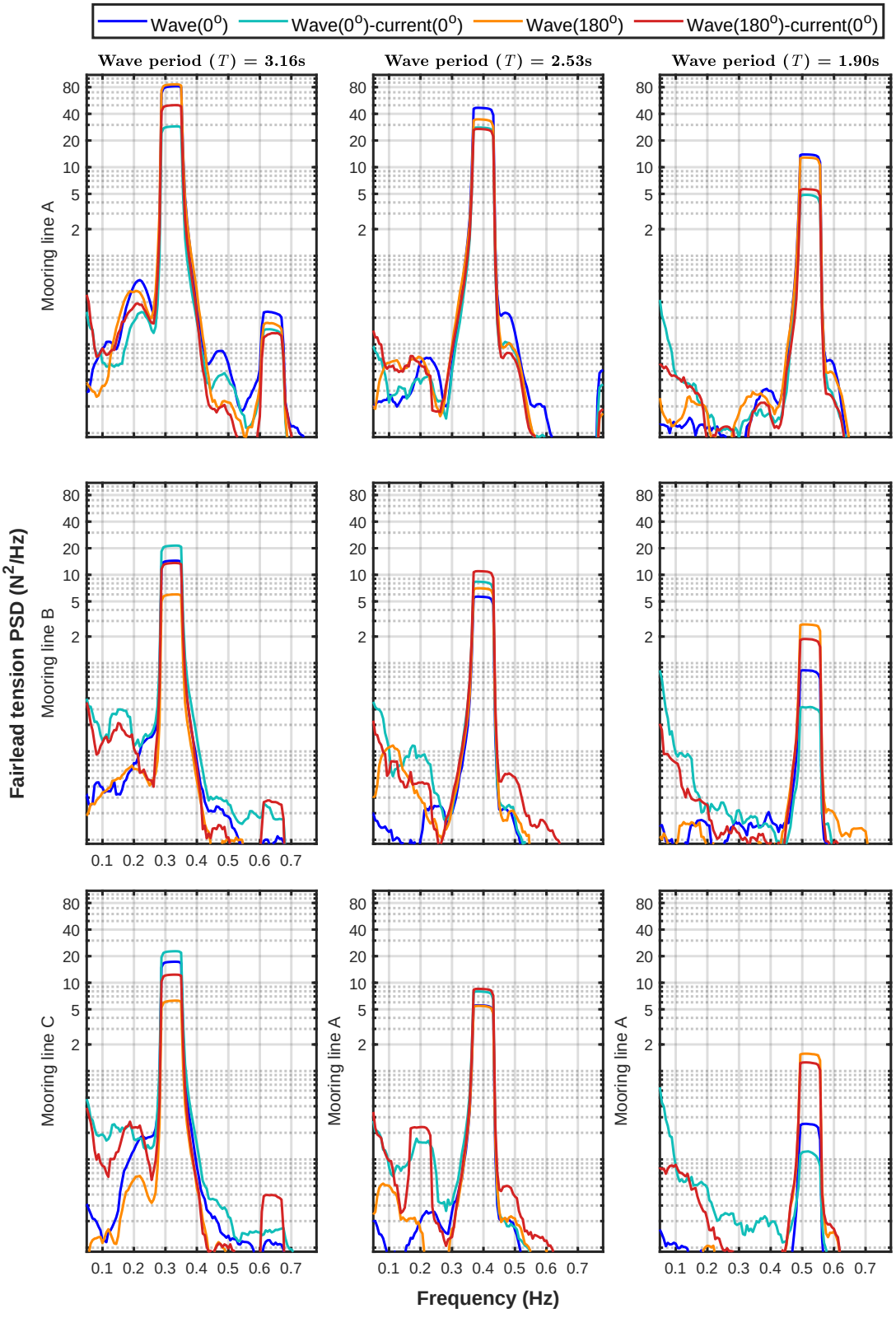

Figure 5.14: Mooring load PSDs under different waves and their interaction with the current. Waves propagate from ° and 180°, interacting with a current from 0°. Panels show tension PSDs of the three mooring lines (A, B and C) under regular wave load cases of a height (H) of 116 mm and different periods: LC1 of T= 3.16 s (left), LC2 of T= 2.53 s (middle), and LC3 of T= 1.90 s (right).

PSD analyses underscore the influence of wave-current interaction on mooring line loads, with varying effects depending on line layout and environmental conditions (Shen et al., 2018). Subsequently, this necessitates bespoke design considerations to mitigate potential load amplifications, particularly at mooring snapping events, which can lead to significant structural failures. Additionally, mooring load PSDs are critical for understanding cyclic loading at the mooring point, where the likely modes of failure may occur at the fairleads or within the mooring system themselves. These, in turn, underline the importance of understanding line-specific sensitivities to wave-current interaction based on PSD analysis to aid in designing mooring systems with appropriate properties and layouts. Such bespoke designs are instrumental in selecting appropriate materials and ensuring structural integrity for robust mooring systems under diverse environmental conditions (Tang et al., 2023).

5.3 Dynamic Motion Responses of the FOWT

5.3.1 Impact of Wave Directionality

After exploring the dynamics of the mooring system, the dynamics of motion responses are essential for comprehending the system's behaviour in diverse environmental conditions (Gueydon et al., 2021). Herein, particular attention is given to the surge, heave, and pitch motions, as these DoFs are deemed most critical for semi-submersible platforms. Analyses encompass load cases given in Tables 4.5 and 4.6 for both regular and irregular waves, respectively, as well as their interaction with the current (Table 4.7), with all data presented based on a scale model.

The time series of displacements of the floating system under waves only are depicted in Figure 5.15, providing insights into the impact of wave direction on surge, heave, and pitch motions. Notably, the surge response magnitude is nearly triple that of the heave, underlining the susceptibility of semi-submersible platforms to surge motion. Specifically, waves propagating from 0° resulted in a slightly larger surge response, while waves from 180° had a more pronounced effect on heave motion. These differences in surge and heave responses of the platform under waves from different directions are likely driven by the orientation of the mooring lines relative to the oncoming waves. Similarly, the pitch response mirrored behaviour consistent with the surge response, indicating a correlation between wave direction and motion responses (Y. Liu et al., 2019).

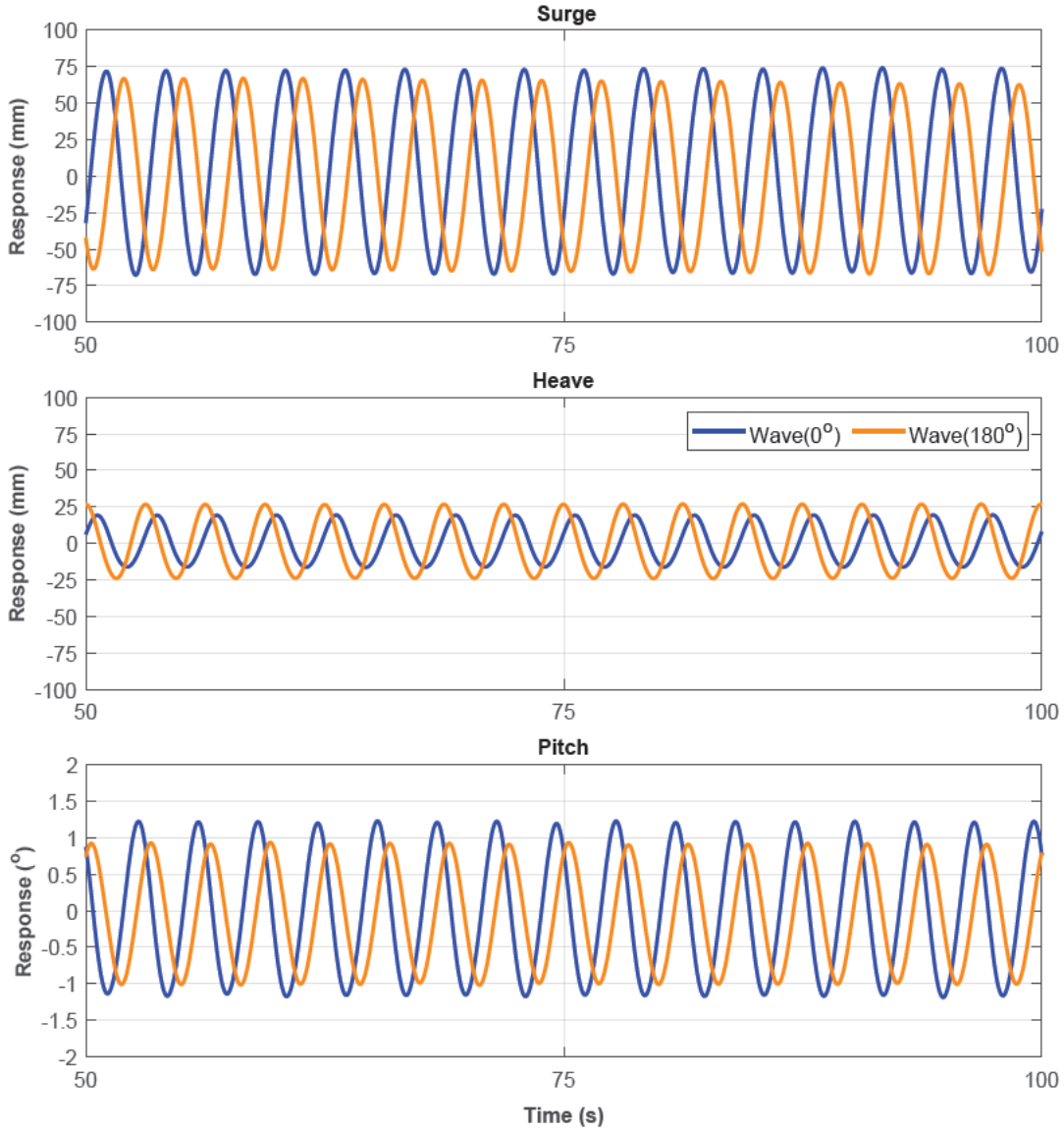

Figure 5.15: Time history of motion responses of surge, heave and pitch DoFs; comparing different propagation scenarios for a regular wave load case (LC7) of a wave height (H)= 96 mm and wave period (T)= 2.53 s.

5.3.2 Impact of Combined Wave-Current

The impact of combined wave-current interactions on the motion responses of the FOWT has been a subject of detailed analysis. To investigate this further, Figure 5.16 compares the effects of different scenarios of wave-current interaction on the platform motion responses in surge, heave and pitch. Specifically, examining the impacts of a current speed of 0.13 m/s from 0° interacting with both following (from 0°) and opposing waves (from 180°) that are characterised by a regular load case (LC3); see Table 4.5.

Under pure wave conditions, behaviours similar to those observed in Figure 5.15 are noted, with following waves resulting in a surge response up to almost 14% higher compared to opposing waves. Conversely, opposing waves lead to smaller heave and pitch responses by up to 9% and 21.5%, respectively, than those induced by following waves.

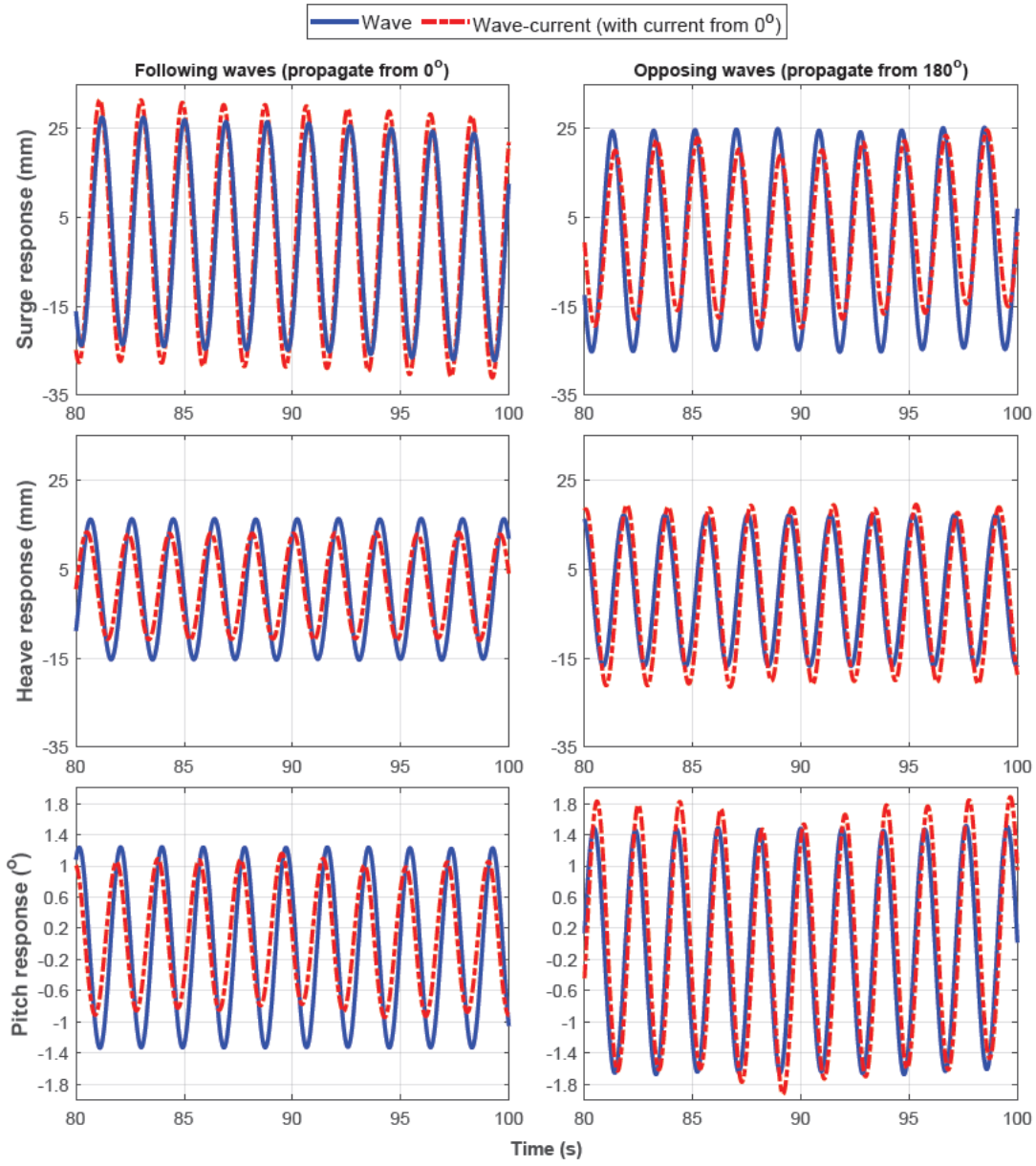

Figure 5.16: Time history of motion responses of surge, heave and pitch DoFs under a regular wave load case (LC3) and combined wave-current. Waves propagate from 0° and 180°; showing the impact on the motion response when these waves interact with a current of a speed of 0.13 m/s.

The results shown in Figure 5.16 further illustrate how the presence of the current influences surge, heave, and pitch, with the current generally altering motion responses in these DoFs. Notably, the interaction of the current with the following waves increases the surge motion and decreases both heave and pitch. Conversely, when the current interacts with opposing waves, it decreases the surge and increases both heave and pitch responses.

Quantitatively, the interaction of the current with the following waves increases surge responses by up to 12% and decreases them by about 16.2% when interacting with opposing waves. On the other hand, heave and pitch responses exhibited opposite trends, with the current interaction with following waves decreasing heave by up to 24.4% and pitch by up to 21%, while its interaction with opposing waves increased heave by about 16.6% and pitch by almost 14.5%.

These findings highlight the nonlinear nature of wave-current interaction and its implications for floating structures (Y. Liu et al., 2019; Karimirad & Collu, 2020; L. Zhang et al., 2020). They align with broader research on FOWTs and semi-submersible platforms, emphasising the impact of static current and wind loads on turbine structures, particularly in surge and heave directions, affecting both motion and mooring responses (L. Chen & Basu, 2019; Murfet & Abdussamie, 2019).

Moreover, the results of Figure 5.16 showed phase lags of motion responses due to the presence of current, which is particularly evident in pitch responses. The interaction of the current with following and opposing waves was found to impact the crests and troughs of motion responses by shifting their peaks. These behaviours are further explained through frequency-based analyses in Figures 5.17 to 5.20 to provide a comprehensive understanding on how wave-current interaction influences motion responses and their periods.

5.3.3 Frequency Domain Analysis

Frequency-domain analysis was performed to further investigate the combined effects of current, wave directionality, and wave height on motion responses. Analyses are carried out for both regular and irregular sea states.

5.3.3.1 Regular Waves

For regular waves, Figures 5.17 to 5.20 compare the impact of current interaction with the following waves (propagating from 0°) and opposing waves (propagating from 180°) for waves of the same periods and different heights: LC2 and LC7 from Table 4.5. The results have shown that current predominantly influences motion responses at low frequencies, particularly below the wave frequency, with varying effects on surge, pitch, heave, and roll motions.

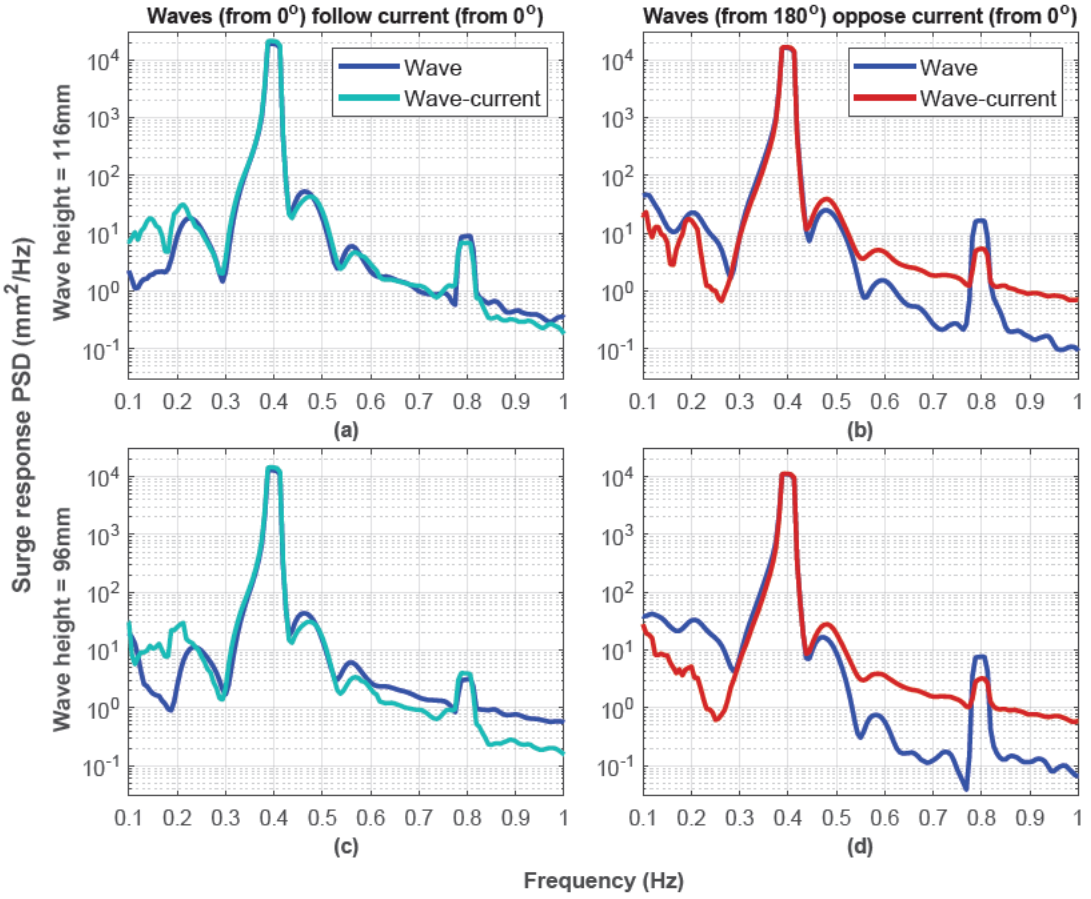

Figure 5.17: PSDs of surge motion response under regular waves and wave-current conditions. Waves propagate from 0° and 180°, interacting with a current from 0°. Subplots show variations in tension PSDs under different load cases of a period of (T) of 2.53 s and different heights: LC2 of H= 116 mm (a-b), LC7 of H= 96 mm (c-d).

Focusing on the frequency shifts observed in the surge responses in Figure 5.17, a consistent frequency peak of around 0.4 Hz is evident across these specific load cases. Frequency shifts at these peaks due to the presence of a current were found to be minor, with differences of no more than ±8%, depending on whether the waves were following or opposing the current. Despite these differences seeming minor for the structure, they could have significant implications for tower stiffness and blade assembly.

However, significant frequency shifts are observed before and after the peaks of the spectra, with variations up to ±70%. Thereby indicating a more pronounced effect of current in these regions. For instance, in these regions, the interaction of the current with following waves tends to decrease their frequency, while interacting with opposing waves leads to an increase in frequency. These current-induced variations in frequency before and after the peak highlight the complex interaction between waves and currents, leading to diverse frequency responses in different regions (Tian et al., 2011; Z. Liu et al., 2016).

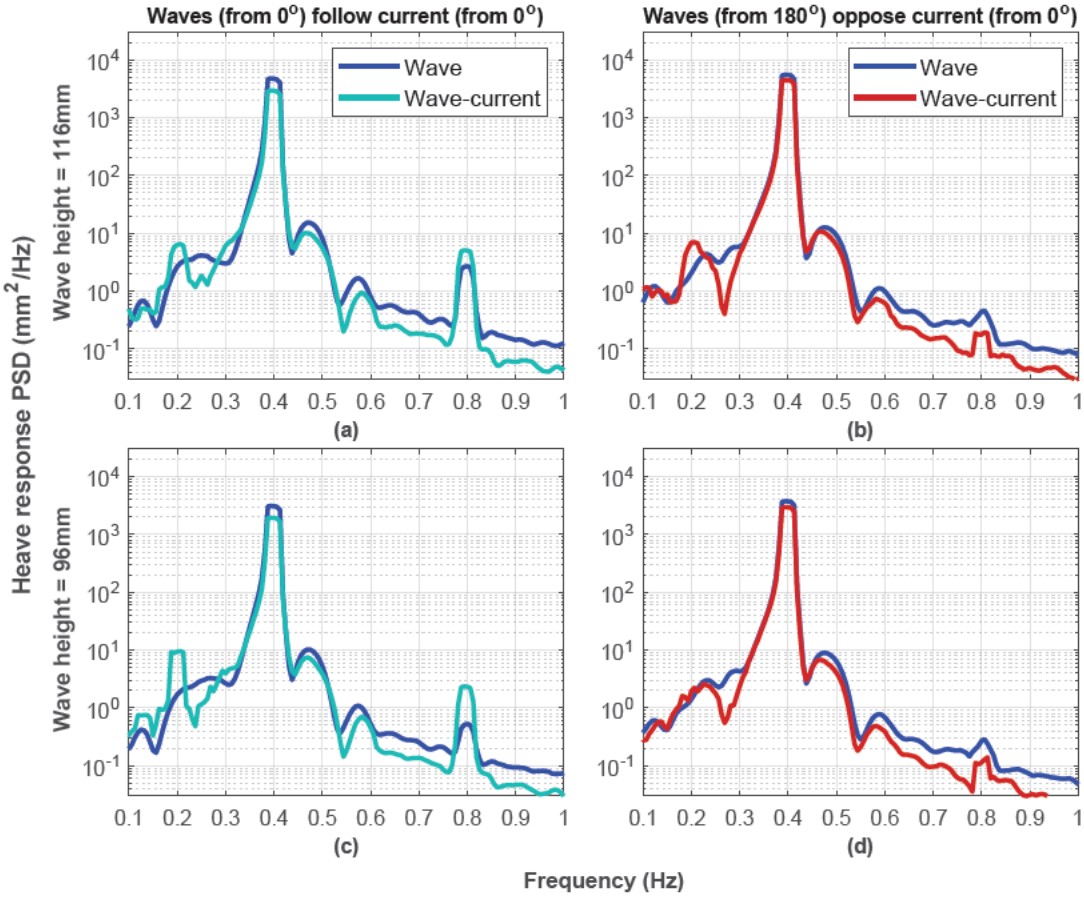

Figure 5.18: PSDs of heave motion response under regular waves and wave-current conditions. Waves propagate from 0° and 180°, interacting with a current from 0°. Subplots show variations in tension PSDs under different load cases of a period of (T) of 2.53 s and different heights: LC2 of H= 116 mm (a-b), LC7 of H= 96 mm (c-d).

Moreover, from Figure 5.17, the presence of the current results in energy dissipation in the higher-frequency regions and energy amplification in the low-frequency regions of the following wave spectra. Such effects on surge response when current interacts with following waves may stem from the additive effect of current and wave forces, enhancing overall motion response. Conversely, when the current interacts with opposing waves, opposite spectral behaviours are observed, with energy dissipation in the low-frequency regions and energy amplification in the higher-frequency regions (Z. Liu et al., 2016).

The dampening effects when current interacts with opposing waves may stem from drifting forces generated by the current, countering the motion induced by the waves. Similarly, the heave response exhibits similar behaviours of the surge at both low and high-frequency regions, as depicted in Figure 5.18. In contrast, pitch and roll responses consistently experienced increasing effects from current at low frequencies, regardless of wave direction (see Figures 5.19 and 5.20).

The overall influence of current on motion responses at frequencies lower than 0.3 Hz in regular waves was observable and found to introduce smaller spectral peaks (Figures 5.17 to 5.20). These peaks coincided with the platform's natural frequencies, suggesting low hydrodynamic damping in these regions. Consequently, these oscillations can be attributed to second-order wave effects, significantly contributing to the dynamics of both motion response and mooring.

The influence of current on motion responses extends beyond low-frequency ranges, as evident in the surge response at higher frequencies (exceeding 0.3 Hz). At these higher frequencies, contrasting behaviours emerge compared to the observed patterns at lower frequencies. Specifically, when current interacts with following waves, it reduces surge response, indicating a dampening effect. Conversely, the interaction of current with opposing waves leads to an increase in surge response, suggesting an amplifying effect. This differential impact of current interaction on surge response across frequency ranges highlights the complex dynamics involved in wave-current interactions and their effects on platform motion.

In the case of heave motion, the behaviour of response under wave-current load varies across different frequency ranges. At low frequencies, heave motion was found to be less affected by current, with slight increases induced by the current. However, at high frequencies, current was seen to dampen the heave response, even when interacting with following or opposing waves, particularly around and beyond the wave frequency. These observations align with studies by L. Chen & Basu (2019), J. Zhang et al. (2021) and H. X. Nguyen (2022).

Moreover, Figures 5.19 and 5.20 illustrate interesting observations regarding pitch and roll motions, respectively. Irrespective of wave direction, current increases the roll and pitch response at low frequencies. However, significant reductions of up to 95% in the amplitudes of the roll response peaks were evident in combined wave-current conditions, especially with opposing waves. This reduction is attributed to the complex interplay with other DoFs and vortex-shedding phenomena (H. Kim, 2018; Iyer et al., 2022).

These findings have significant implications for FOWTs and other offshore structures (Saruwatari et al., 2013). For example, the observed frequency shifts and energy dissipation/amplification in motion responses, as influenced by wave-current interaction, are critical for optimising design, operational strategies, and safety measures. Specifically, the effects of currents on the surge, heave, pitch, and roll motions highlight the need for comprehensive assessments considering wave-current interaction (Z. Liu et al., 2016).

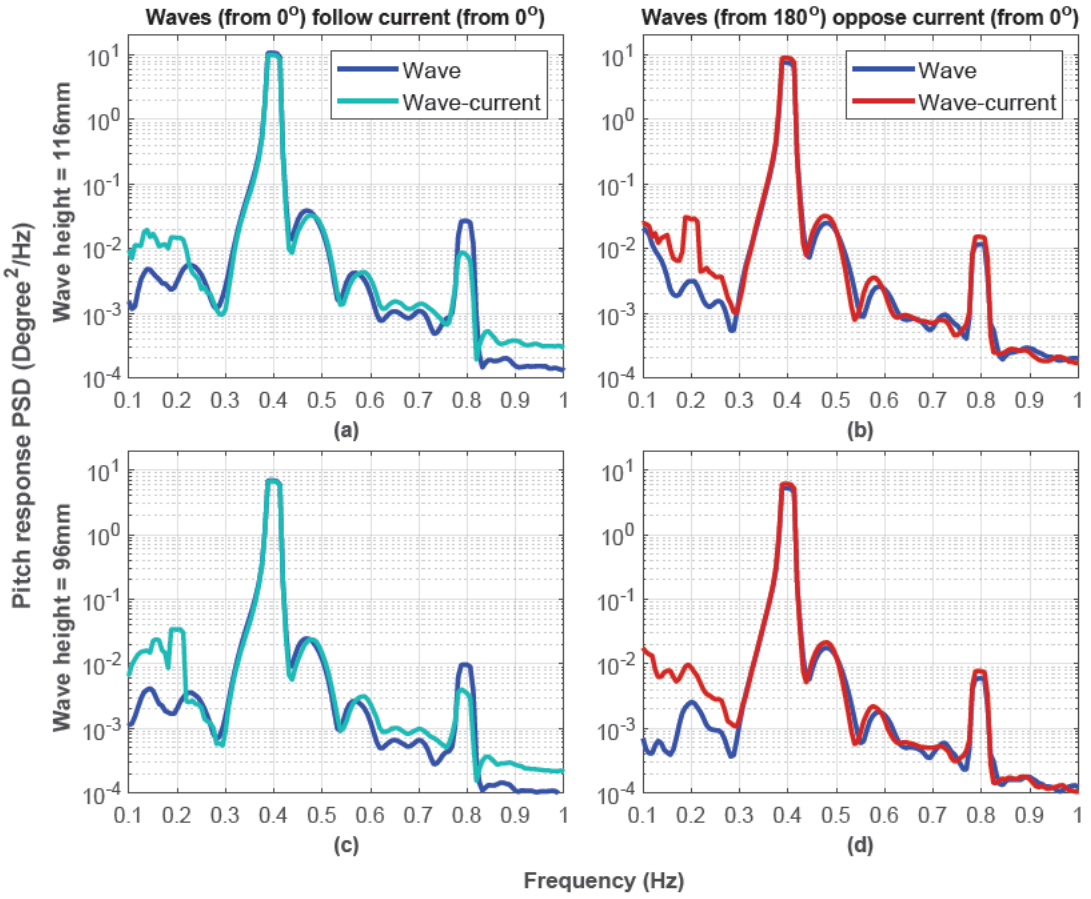

Figure 5.19: PSDs of pitch motion response under regular waves and wave-current conditions. Waves propagate from 0° and 180°, interacting with a current from 0°. Subplots show variations in tension PSDs under different load cases of a period of (T) of 2.53 s and different heights: LC2 of H= 116 mm (a-b), LC7 of H= 96 mm (c-d).

Such an interaction is anticipated to have pronounced impacts on the platform's natural frequencies, necessitating tailored mitigation strategies. Therefore, accurate modelling of this interaction is essential for predicting such dynamic loads and minimising undesirable responses (Sellar et al., 2017; A. C. Pillai et al., 2021). This, in turn, guides design considerations and maintenance schedules, consequently extending the service life of FOWTs and mooring systems.

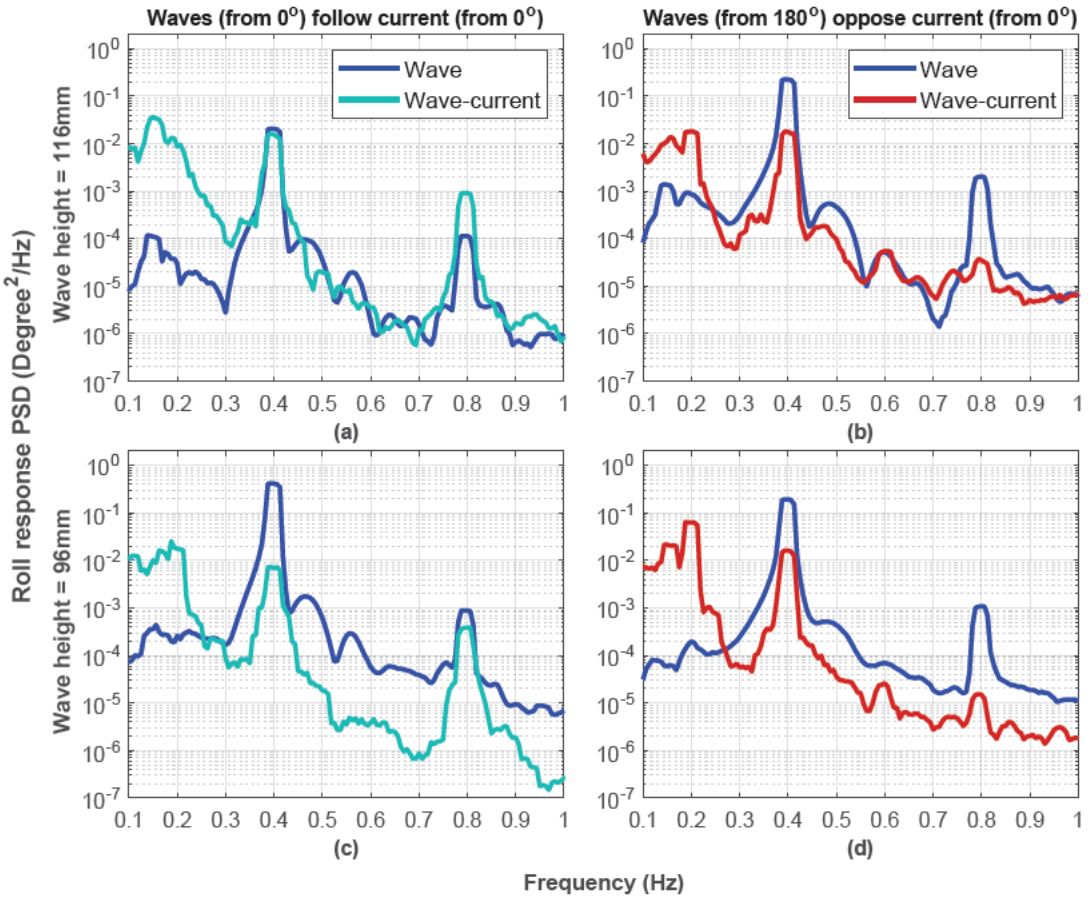

Figure 5.20: PSDs of roll motion response under regular waves and wave-current conditions. Waves propagate from 0° and 180°, interacting with a current from 0°. Subplots show variations in tension PSDs under different load cases of a period of (T) of 2.53 s and different heights: LC2 of H= 116 mm (a-b), LC7 of H= 96 mm (c-d).

5.3.3.2 Irregular Waves

For stochastic seas, the power spectral densities for the surge, heave, and pitch responses corresponding to irregular wave load cases A and B are shown in Figures 5.21 and 5.22. The comparison between waves from 0° and 180° and their interaction with a current from 0° demonstrates distinct effects on motion responses. Opposing waves (from 180°) induce slightly larger intensities in surge and heave responses compared to waves attacking the platform at 0°, while the pitch response exhibits the opposite behaviour.

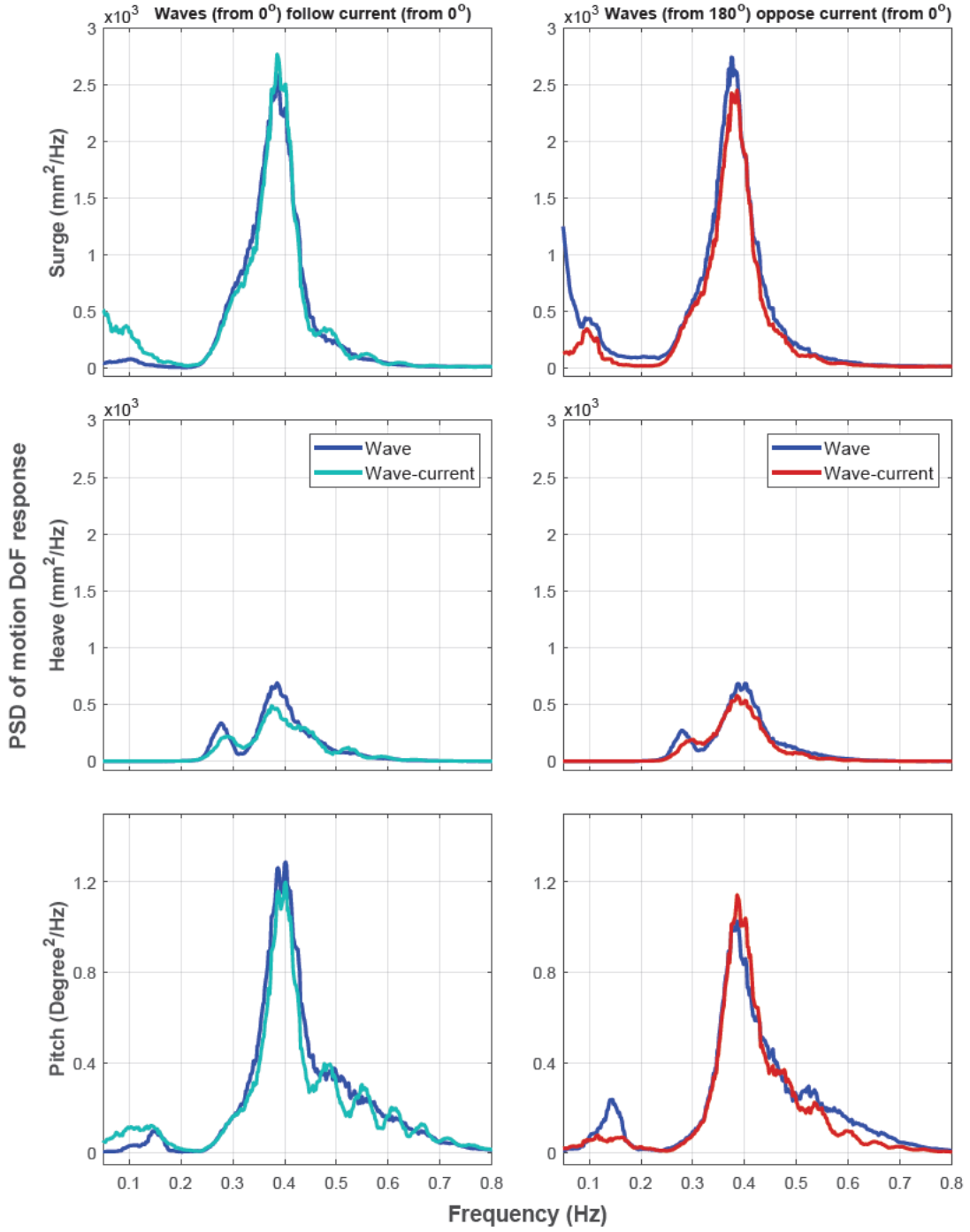

Figure 5.21: PSDs of surge, heave and pitch motion responses under an irregular waves load case (LC: A) and wave-current conditions. Waves propagate from 0° and 180°, interacting with current from 0°. Subplots show PSD variations of surge, heave and pitch responses.

The influence of the current is evident across two distinct frequency zones: low and high regions. This can be attributed to the interaction between the current and waves. In low-frequency zones, the current stimulates responses and results in smaller peaks. At higher frequencies, current influences the pitch motion response differently when interacting with following waves compared to opposing waves, leading to either an increase or reduction in intensity. Additionally, the current induces shifts in the frequencies of peak PSDs.

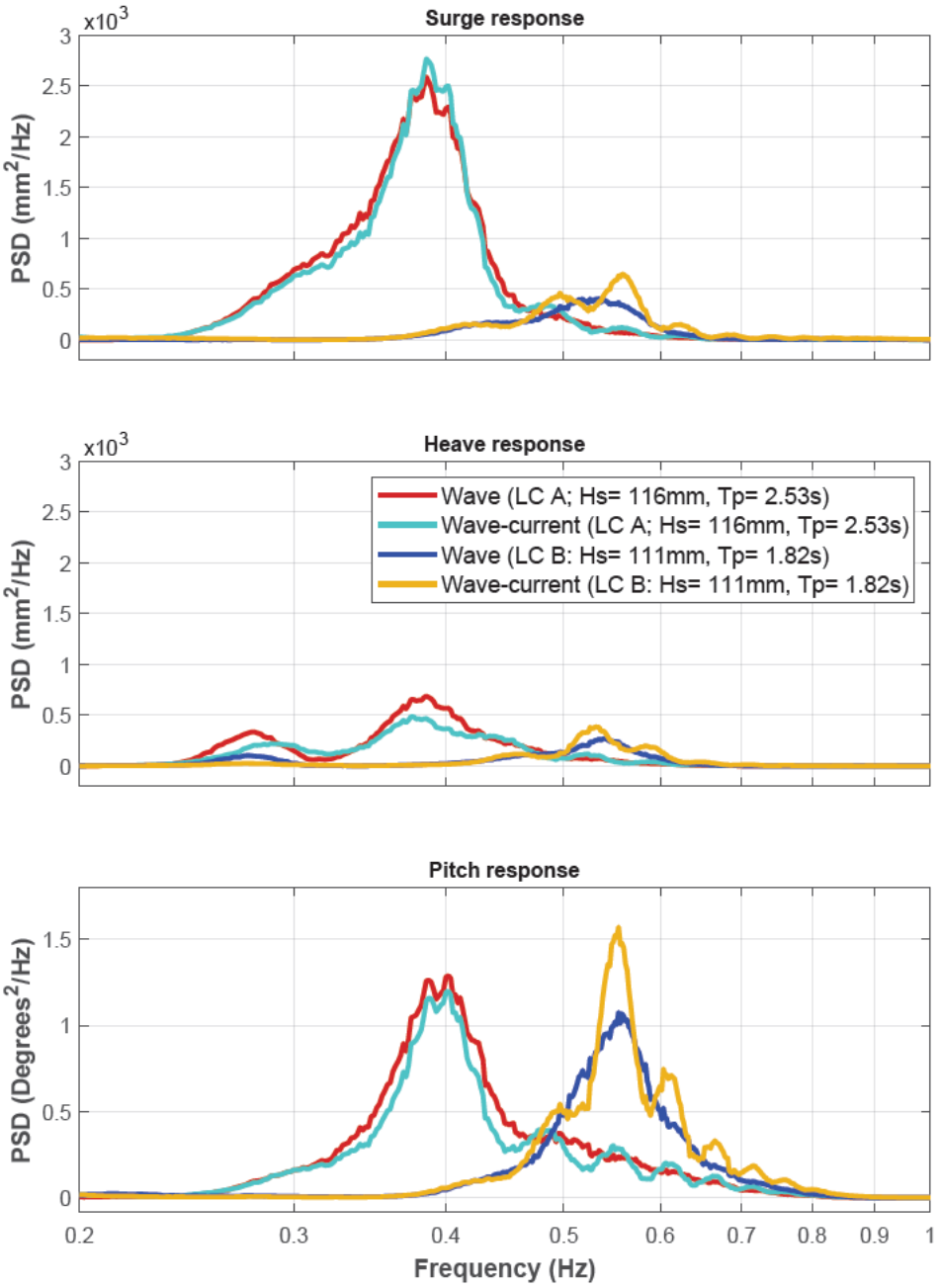

Figure 5.22: PSDs of surge, heave and pitch motion responses under irregular wave load cases (LC: A and B) and wave-current conditions. Waves of different both significant wave heights and peak periods propagate from 0°, interacting with current from 0°. Subplots show variations in response PSD of: surge (top), heave (middle) and pitch (bottom), demonstrating frequency shifts and peak magnitude differences.

Moreover, Figure 5.22 clearly illustrates these frequency shifts, focusing on the current interaction with the following waves. The PSDs for surge, heave, and pitch responses corresponding to irregular waves A and B are compared. Results indicate that PSDs for both load cases A and B peak at their respective wave frequencies, 0.395 Hz and 0.549 Hz, respectively. This is important as it shows the dominant motion frequencies of the FOWT under different wave conditions. Notably, energy densities of motion responses in load case A surpass those in load case B, particularly evident in surge response.

Besides, the results underscore peak-frequency shifts attributed to the presence of the current, particularly evident in the heave response (see mid-subplot in Figure 5.22). Thus, understanding and quantifying how wave-current interaction alters these frequency shifts and energy densities is crucial for optimising floating wind platforms and mooring systems.

Overall, the results highlight the significant influence of wave directionality and the complex interaction between current and waves on the motion responses of FOWTs. The findings demonstrated the dynamic characteristics of motion responses, revealing distinct effects at different frequency ranges depending on the motion DoF and loading conditions (Diep Nguyen et al., 2021). Furthermore, these current-induced alterations in the surge, heave, and pitch motions inherently correlate with corresponding changes in tension loads experienced by the mooring lines.

5.4 Peculiarity of W2Power Floating System

W2Power floating system is distinguished by a range of unique design features; see Appendix A. Among these distinctive features is its unique single-point mooring system that enables the platform to weathervane, thereby responding dynamically to prevailing loading conditions. This capability has been demonstrated in present experiments, showcasing how the platform adjusts to the direction of significant loading.

For example, for the regular load case (LC7), the sway and yaw motions of the platform are influenced by the direction of wave propagation, particularly from 90°. The platform showcases its weathervaning ability by aligning itself with incoming waves, as evidenced by the sway and yaw responses over time, as shown in Figure 5.23.

During experimentation, that model was initially positioned in the centre of the test area with its bow facing 0° and stern facing 180° (close to the gantry), as depicted in Figure 5.24.a. Then, the platform gradually rotates towards the incoming waves (see Figure 5.24.b), showcasing its weathervaning capability.

The platform's dynamic weathervane is further exemplified in combined wave-current loading with current originating from 0°. Despite the crossing influences of waves and currents, the platform responds to the most dominant load condition. This phenomenon is evident in Figure 5.24.c, where the current realigned the model to its initial position in the centre of the tank's test area. This, in turn, resulted in a near-zero yaw response and a more stable sway response (Figure 5.23).

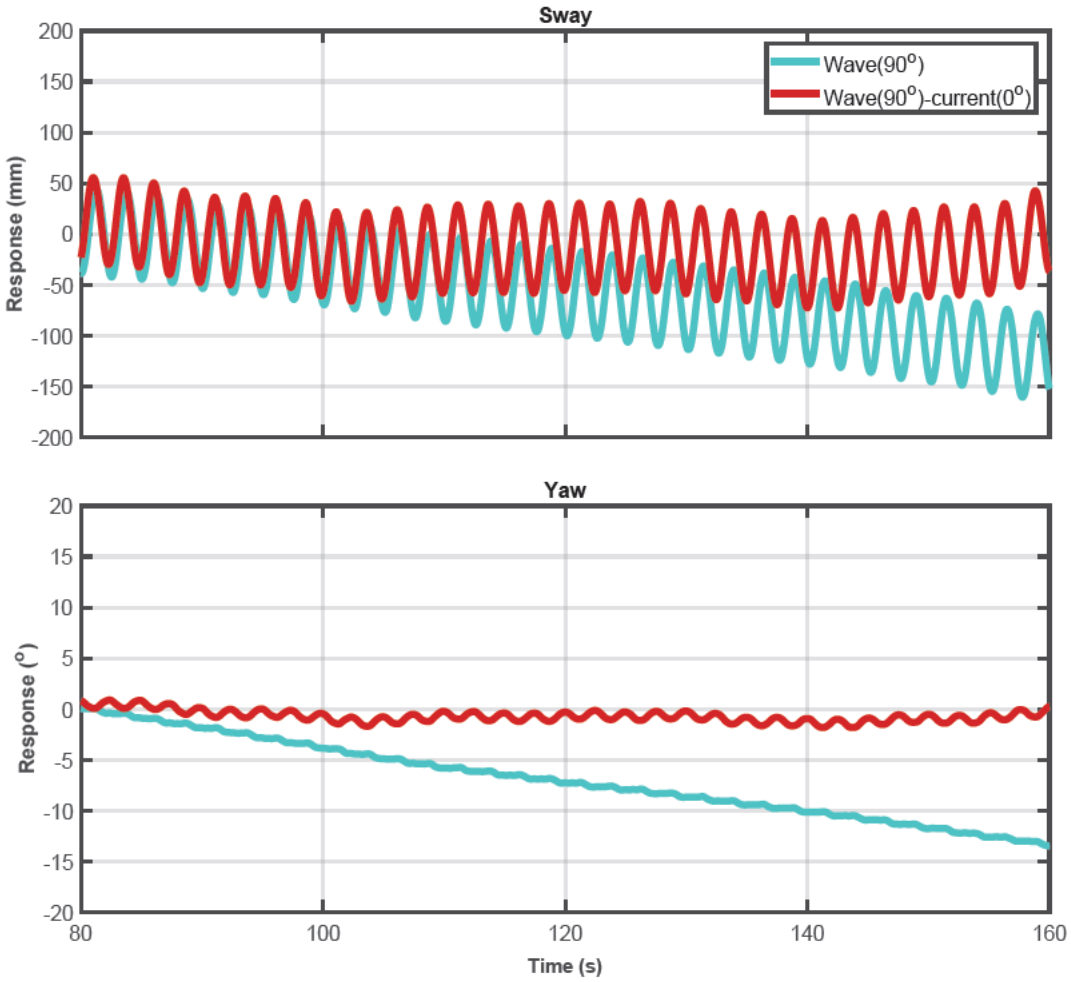

Figure 5.23: Time history of sway and yaw motion responses under a regular wave load case (LC7) and wave-current conditions. Waves propagate from 90°, interacting with current from 0°. Demonstrating the system's weathervaning capabilities and its motion dynamic responses to the dominant loading (combined wave-current).

Moreover, this SPM system allows for a more balanced distribution of loads among mooring lines, thereby reducing fatigue loads on the platform and mooring lines. Such characteristics are particularly evident in the stable sway response observed approaching from 90°, contrary to the significant sway response in single-turbine floating platforms with conventional mooring systems.

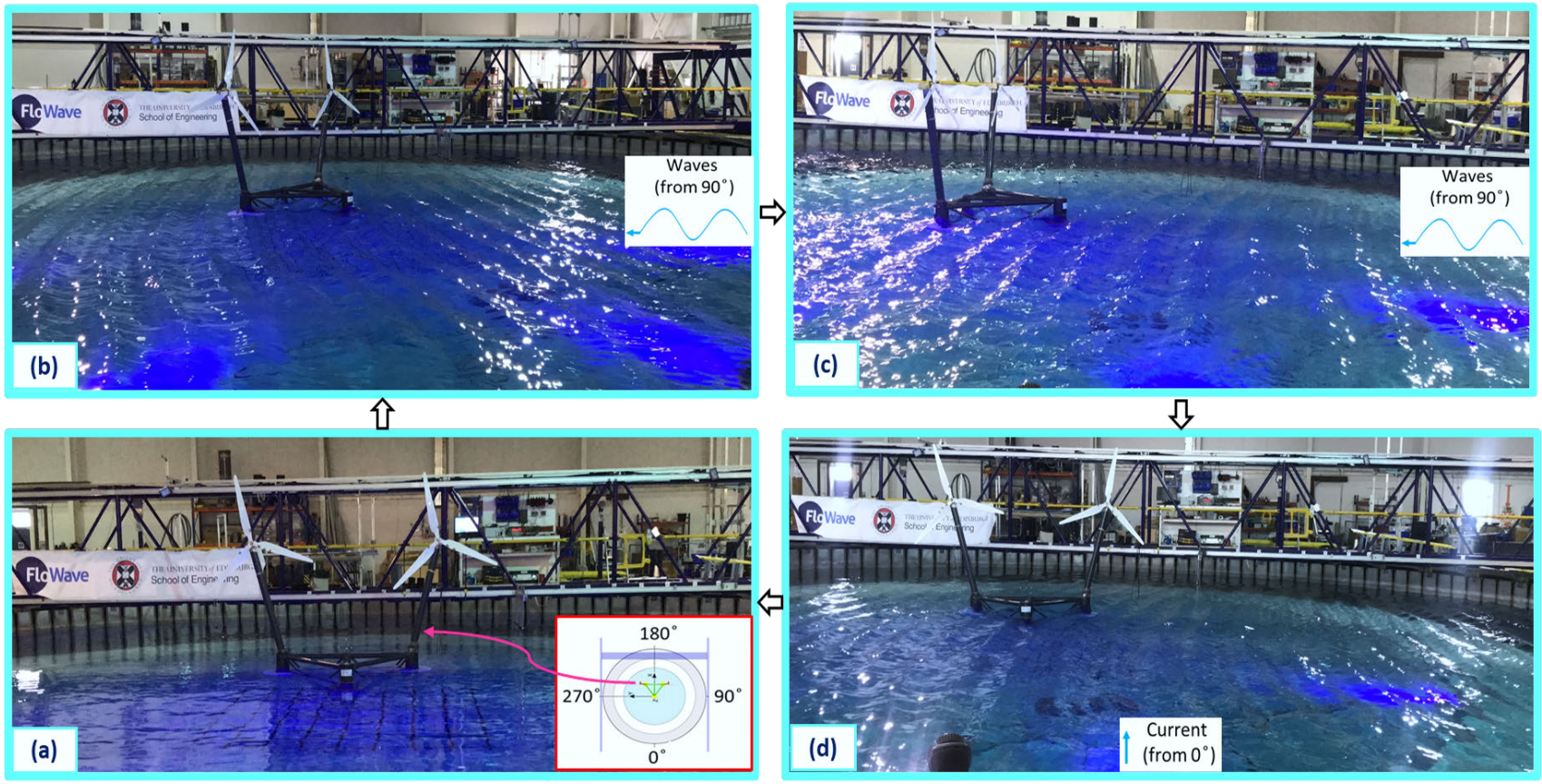

Figure 5.24: Artistic depictions visualising the weathervaning capabilities of the W2Power FOWT model at a scale of 1:40 under waves and wave-current conditions. Proceeding clockwise from the bottom left: (a) the model in still water in the centre of the test area before sea states run and a top view of FloWave coordinates shown in the small picture (bordered in red), (b) waves being run from 90° causing the model to weathervane, with its stern (front column) towards almost 45° (halfway weathervaning of approaching waves), (c) the model fully weathervaned under wave loading, with its stern towards the wave attack angle (90°), and (d) current was generated, forcing the model to weathervane again in the opposite direction, and showing the model returned back to its initial position in the centre of the tank test area.

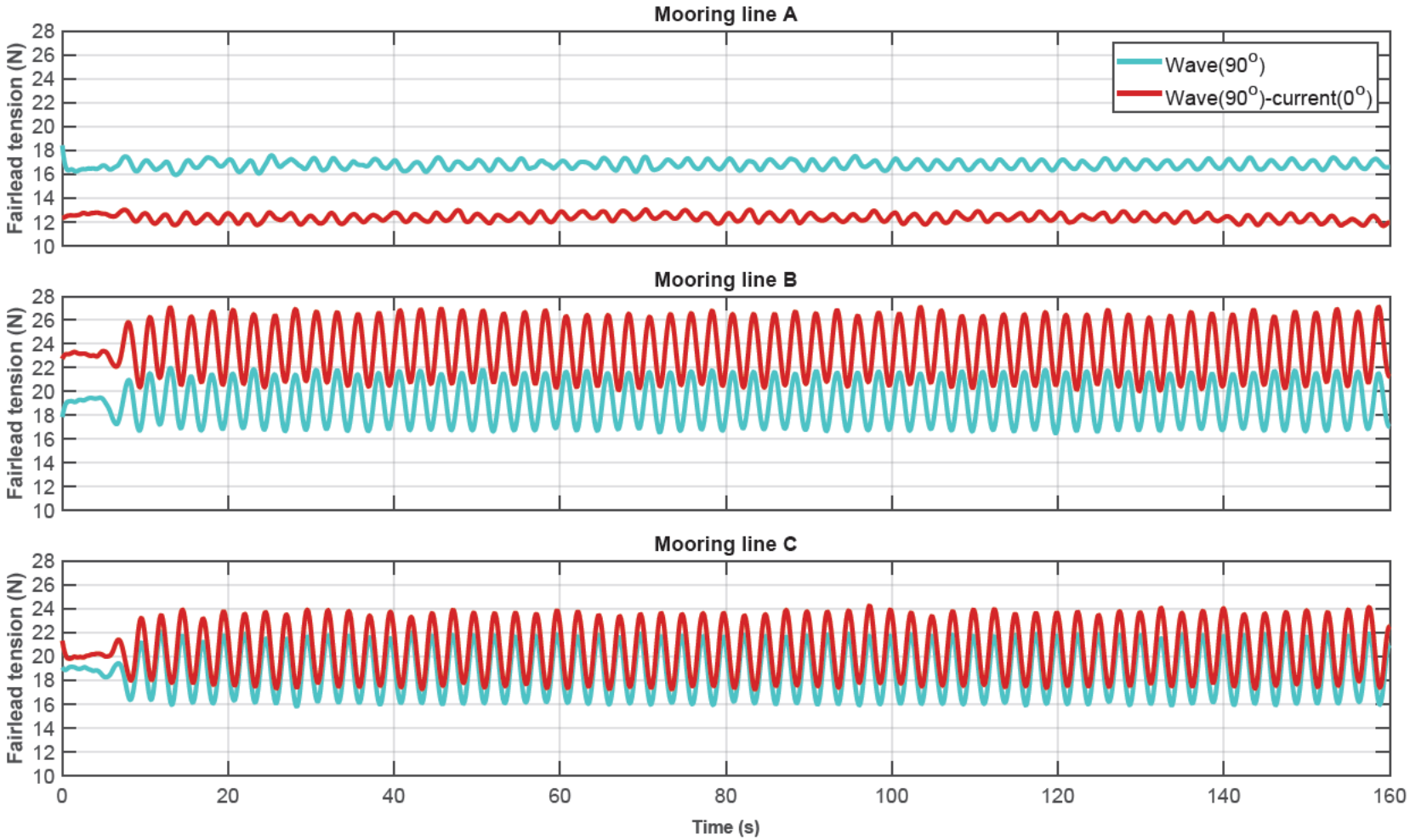

Figure 5.25: Time history of mooring loads under a regular wave load case (LC7) and wave-current conditions. Waves propagate from 90°, interacting with current from 0°. Showing the system's weathervaning capabilities and its mooring dynamic responses to the dominant loading (combined wave-current); evident in balanced load distributions on lines B and C.

The comparison of loads on the mooring lines is present in Figure 5.25, and the balanced load distribution on lines B and C is evident. For instance, under waves, the mean loads are almost equal and about 19 N on both lines and under combined wave-current, the mean loads are 23.6 N on line B and 20.5 N on line C.

These findings underscore the effectiveness of the concept in responding to dominant environmental loads, thereby minimising fatigue loads on the platform and mooring lines. Thus demonstrating the capabilities of W2Power and its potential to optimise performance and enhance structural integrity in the floating wind industry.

5.5 Chapter Summary

This chapter presented and discussed the results obtained from the conducted experimental tests described in the previous chapter (Chapter 4). It encompassed the dynamics of motion responses and the mooring system under various environmental conditions, including wave, current, and combined wave-current scenarios.

Investigations delved into the e ffects of wave directionality under both regular and irregular waves propagating from different directions. Additionally, diverse wave-current interaction scenarios were explored to understand their impact comprehensively. Subsequently, the implications of these loading conditions on mooring loads and platform motion responses were thoroughly analysed and discussed.

Furthermore, frequency-based analysis was conducted for different sea states, providing valuable insights into the system's dynamic characteristics across various frequency ranges. Through experimental measurements, the distinct features of the W2Power floating system were demonstrated, showcasing its weathervaning capabilities under dominant loading conditions, particularly in complex wave-current environments.

Overall, this part (Part II) of the chapters (Chapters 4 and 5) offered a comprehensive examination of the experimental findings, contributing significant insights into the performance and behaviour of the FOWTs in realistic environmental conditions. These findings laid a solid groundwork for further discussions and implications in subsequent chapters.

PART III

Numerical Modelling of MUFOWTs in Combined Wave-Current Environments

Chapter 6

Numerical Modelling of FOWTs: Methodology and Analysis

6.1 Introduction

In order to address the research questions defined in Section 1.7, numerical modelling methods are used. This chapter provides in-depth analytical and numerical investigations into the effects of wave-current interaction on the motion responses of MUFOWPs and the dynamics of their mooring systems. It commences by providing rational and technical background on the dynamic responses of FOWTs when deployed in wave-current environments. Then it presents the development of the W2Power FOWT system (W2Power, 2010), which is equipped with a pair of NREL 5 MW wind turbines and moored to the seabed using a single-point mooring system. Herein, it delves into the development of the W2Power platform model and conducts hydrodynamic analyses. To fix the floating platform to the seabed and ensure it remains in place, the chapter introduces a new mooring system, then details the coupling of the floater-towers-nacelles-rotors model.

Subsequently, it details the development of two analytical models to analyse current interaction with regular and irregular waves. Furthermore, it outlines the environmental conditions and the execution of coupled aero-hydro-servo-elastic analyses in the time domain. The fully coupled analyses considered various loading scenarios to explore to what extent currents and their interaction with waves impact the dynamic responses of platform motions and mooring systems.

6.2 Background and Rational

In realistic ocean environments, waves propagate on a current, and the interaction between currents and waves results in frequency shifts and changes the wave parameters (J. Smith, 1997; Moreira & Peregrine, 2012); as detailed in Section 3.2 and explained in Figure 3.1.

In deep waters, where FOWTs are deployed and WCI coexist, this interaction impacts the dynamic responses of FOWTs during operational and extreme conditions. As a consequence, they might increase the platform's mean surge wave-drift force (R. Zhao et al., 1988) and leads to fatigue in the system's superstructures (e.g. mooring lines and towers) (L. Chen & Basu, 2018; Qu et al., 2020; L. Silva et al., 2021; Sarkar et al., 2020). However, WCI has not been addressed extensively in the coupled analysis of FOWTs, and that is due to two key challenges:

i) the need for a fully nonlinear mooring model capable of incorporating current,
ii) and development and implementation of an appropriate model to account for wave-current interaction.

The recent development of nonlinear mooring models has addressed the first challenge (Palm et al., 2016; Davidson & Ringwood, 2017; A. C. Pillai et al., 2018b). However, the latter has not yet been overcome and is still an ongoing research topic. Moreover, most commercial engineering tools (e.g. FAST, Sima, OrcaFlex) employ the conventional superposition of waves and currents when defining the properties of waves (J. M. Jonkman & Jonkman, 2016; Sima, 2023; OrcaFlex, 2023), such as JONSWAP waves (Hasselmann et al., 1973). What is missing is the Doppler shift modification of the linear dispersion relationship that accounts for the effect of the current (Azcona et al., 2017).

To overcome this limitation, new formulations and derivations for the total fluid particle velocity, the vector sum of the current velocity and wave-induced fluid particle velocity, are needed to incorporate Doppler shift appropriately. Subsequently, custom analytical models must be developed to account for the interaction between currents and waves (both regular and irregular) and then analyse the dynamic behaviours of FOWTs appropriately.

As reviewed earlier in Section 3.7, the well-known models for the interaction of waves (regular and irregular) and currents are based on the Airy wave theory (Thomas, 1981; N. E. Huang et al., 1972; Tung & Huang, 1974). These models have been used in the design and structural response assessment of offshore structures, such as floating bridges and marine platforms (Ismail, 1984; Dai et al., 2022). Furthermore, the utilisation of these WCI models in the dynamic structural responses of bottom-fixed offshore wind turbines is outlined in Section 3.8, and for Spar FOWTs in Section 3.9.

Nevertheless, the effects of WCI on semi-submersible FOWTs that utilise single-point-mooring (SPM) systems have not been investigated. Consequently, this work looks into the effect of wave and current interaction on the mooring loads of an SPM system of a semi-submersible FOWT and explores how this interaction impacts the dynamic behaviour of the entire floating system under realistic environmental conditions.

To achieve this, a nonlinear hydrodynamic model of the mooring system and analytical wave-current models are developed and incorporated into a coupled analysis of the FOWT to account for the interaction. Herein, investigations focus on the mooring system's hydrodynamic loading and nonlinear dynamics and consider the W2Power floating wind system at full scale. Thereby, a coupled model for the W2Power floating wind turbine is developed. Coupled aero-hydro-servo-elastic analyses in the time domain are carried out in the time domain with the incorporation of wave-current interaction.

6.3 Mathematical Models of Wave-Current Interaction

6.3.1 Governing Equations

When wave and current fields coexist, the velocity potential can be divided into a steady current potential and an unsteady wave potential. Then, the water surface elevation surrounding the structure can be calculated by incorporating both the unstable wave potential and the current velocity into the first-order dynamic surface boundary condition (Isaacson & Cheung, 1993). The following coordinate system (x,z), shown in Figure 6.1, is defined to introduce the models for the wave-current flows. The origin, $O_{(0,0)}$, is assumed to be the mean water level (MWL), with the positive x-axis aligned horizontally in the direction of wave propagation, whereas the z-axis points vertically upward.

For a rotational flow of an inviscid and incompressible fluid, the continuity equation and momentum (Euler) equations, introduced in Section 3.3, apply. The Cartesian x-axis is selected to follow the direction of wave propagation (H. Kim et al., 2001). This makes the derivatives of the velocity in the y-axis equal to zero, thereby simplifying Equations (3.1) to (3.4) to the following expressions:

$$\frac{\partial u}{\partial x}+\frac{\partial w}{\partial z}=0 \tag{6.1}$$

$$\frac{\partial u}{\partial t}+u\frac{\partial u}{\partial x}+w\frac{\partial u}{\partial z}=-\frac{1}{\rho}\frac{\partial p}{\partial x} \tag{6.2}$$

$$\frac{\partial w}{\partial t}+u\frac{\partial w}{\partial x}+w\frac{\partial w}{\partial z}=-\frac{1}{\rho}\frac{\partial p}{\partial z}-g \tag{6.3}$$

where, u and w represent the horizontal and vertical components of fluid velocity, p, g, and ρ are the pressure, the gravitational acceleration and water density, respectively.

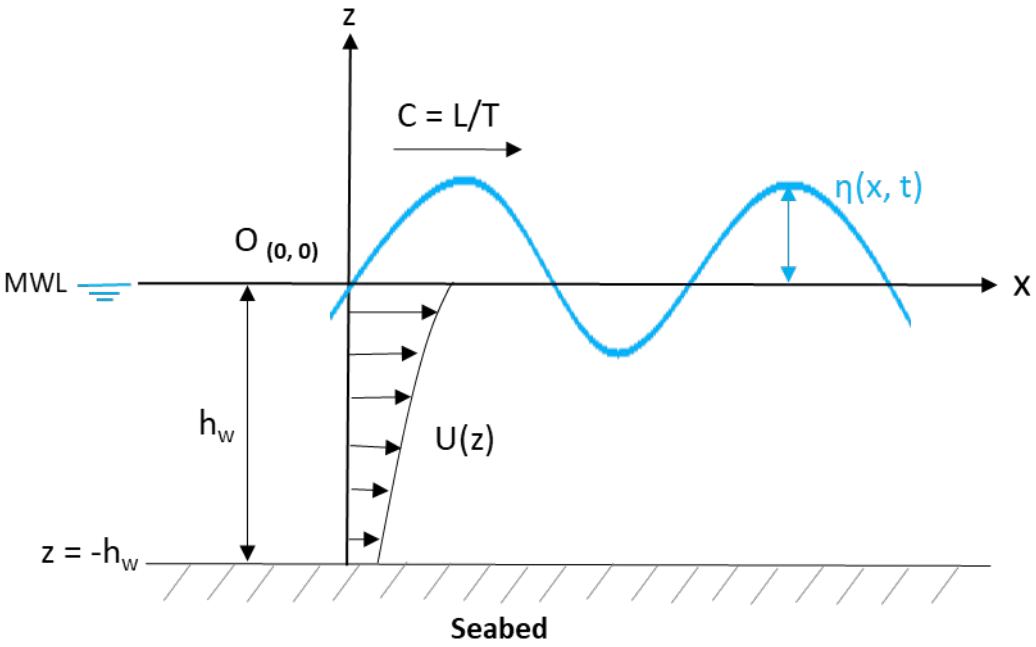

Figure 6.1: Definition of the coordinate system for wave-current interaction of a finite depth.

6.3.2 Regular wave-current mathematical model

For regular wave-current interaction, the model formulations given in Thomas (1981) and M. Silva et al. (2016) are adopted, and the following flow assumptions are made:

- The flow field is irrotational: this implies that the flow lacks vorticity, hence simplifying the mathematical modelling process by eliminating certain complexities associated with rotational flow patterns (Q. Chen et al., 2003).
- Waves are of small amplitudes and propagate on currents: this allows for the linearisation of the wave equations and the use of superposition principles to simplify the interaction between waves and currents (Thomas, 1981).
- No flow fluctuations exist perpendicular to the O_{xz} plane, and the waves undergo no refraction: this simplifies the model by restricting the analysis to a two-dimensional plane, reducing the computational complexity of three-dimensional flow while still capturing WCI effects (Thomas, 1981).
- The time and length scales of the current are relatively larger than the waves' period and wavelength: this allows for the separation of time scales, enabling the decoupling of wave and current effects for a more straightforward analysis (S. Draycott, Steynor, et al., 2018).

These assumptions collectively facilitate the development of a robust and manageable mathematical model for analysing a regular WCI, providing a balance between accuracy and computational feasibility (Q. Chen et al., 2003; Thomas, 1981; S. Draycott, Steynor, et al., 2018).

After applying these assumptions, the resulting fields of the velocities (u_T and w_T) and pressure (p_T) can be represented as the sum of the flow contributions from both currents and waves:

$$u_T(x,z,t) = U(z) + u(z)\cos(\kappa x - \omega t) \tag{6.4}$$

$$w_T(x,z,t) = w(z)\sin(\kappa x - \omega t) \tag{6.5}$$

$$p_T(x,z,t) = -\rho g z + p\cos(\kappa x - \omega t) \tag{6.6}$$

where u, w, and p denote the magnitude of the perturbation caused by the wave, κ denotes the wave number in the direction of wave propagation (i.e. $\kappa = 2\pi/L$; L is the wavelength), and $U(z)$ is the current velocity profile as a function of water depth (h_w) in the absence of waves. ω is the wave's "apparent" angular frequency, and for an observer in a fixed reference system is the sum of the relative or intrinsic frequency in quiescent water (ω_r) and the Doppler frequencies (White, 1999) and can be written as:

$$\omega = \omega_r + \vec{\kappa}\cdot\vec{U} \tag{6.7}$$

in which, $\vec{\kappa}$ and $\vec{U}$ are, respectively, the vectors of the current velocity and wave number.

In the linear Airy wave theory, the water surface elevation $\eta(x,t)$ is sinusoidal and can be expressed as:

$$\eta(x,t) = A\cos(\kappa x - \omega t) \tag{6.8}$$

where A is the current-altered wave amplitude. Substituting the formulae of the resulting fields of velocities and pressure, Equations (6.4) to (6.6), into the continuity, Equation (6.1), and momentum equations, Equations (6.2) and (6.3), give:

$$\frac{\partial w}{\partial z} = \kappa u \tag{6.9}$$

$$p = \frac{\rho}{\kappa^2}\left[\frac{\partial w}{\partial z}(\omega - U(z)\kappa) + w(\kappa\frac{\partial U(z)}{\partial z})\right] \tag{6.10}$$

$$\frac{\partial p}{\partial z} = \rho w(\omega - U(z)\kappa) \tag{6.11}$$

After straightforward elimination of variables and some manipulation, Equations (6.9) to (6.11) yield an alternate equation for vertical velocity, written as:

$$\frac{\partial^2 w}{\partial z^2} - \left[\kappa^2 - \frac{\kappa}{\omega - U(z)\kappa}\frac{\partial^2 U(z)}{\partial z^2}\right] w = 0 \tag{6.12}$$

Equation (6.12) is known as the "inviscid Orr-Sommerfeld" or "Rayleigh" equation of classical hydrodynamic stability theory in the flow domain $-h_w < z < 0$, which must be solved in accordance with the rigid bottom boundary condition:

$$w_T = w(z) = 0 \quad \text{on } z = -h_w \tag{6.13}$$

and the mean free surface linearised boundary conditions:

$$w(z) = A(\omega - \kappa U(z)) \quad \text{on } z = 0 \tag{6.14}$$

$$p = \rho g A \quad \text{on } z = 0 \tag{6.15}$$

Substituting the boundary conditions on $z = 0$, Equations (6.14) and (6.15), into the pressure field equation, Equation (6.10), gives the current-affected dispersion relation.

$$(\omega - \kappa U(z))^2 \frac{\partial w}{\partial z} + \left[\kappa(\omega - \kappa U(z))\frac{\partial U(z)}{\partial z} - g\kappa^2\right] w = 0 \tag{6.16}$$

If the parameters A, ω, and h_w, alongside $U(z)$, can be treated as known values in advance from experimental specifications or measurements, then the system of Equations (6.12) to (6.14) can be solved for the wavenumber κ and the vertical velocity $w(z)$. Accordingly, once these unknowns have been determined, the depth-varying component of the horizontal velocity $u(z)$ can be derived from the continuity equation, Equation (6.1), as:

$$u(z) = \frac{1}{\kappa}\frac{\partial w}{\partial z} \tag{6.17}$$

However, the system is defined by the set of equations, Equations (6.12), (6.13) and (6.16), can not be solved analytically for general wavenumbers and frequencies unless the second derivative of the current velocity profile is equal to zero ($\frac{\partial^2 U(z)}{\partial z^2} = 0$), which corresponds to a depth-independent current or a current that changes linearly with depth. The Rayleigh equation, Equation (6.12), can thus be rewritten as:

$$\frac{\partial^2 w}{\partial z^2} - \kappa^2 w = 0 \tag{6.18}$$

The Rayleigh equation, Equation (6.18), depends on the vertical velocity $w(z)$ and the current velocity profile $U(z)$, and its solution for the wavelike horizontal velocity u(z) can be given by:

$$u(z) = A(\omega - U_0\kappa)\frac{\cosh[\kappa(z+h_w)]}{\sinh(\kappa h_w)}; \tag{6.19}$$

for $w(z)$ by:

$$w(z) = A(\omega - U_0\kappa)\frac{\sinh[\kappa(z+h_w)]}{\sinh(\kappa h_w)}; \tag{6.20}$$

and for $p(z)$ by:

$$p(z) = \rho A(\omega - \kappa U_0)\frac{1}{\kappa\sinh(\kappa h_w)}\left[(\omega - \kappa U(z))\cosh[\kappa(z+h_w)] + \frac{dU(z)}{dz}\sinh[\kappa(z+h_w)]\right] \tag{6.21}$$

Substitution of Equations (6.19) to (6.21) in the resultant velocity and pressure fields, Equations (6.4) to (6.6), yields:

$$u_T(x,z,t) = U(z) + A(\omega - U_0\kappa)\frac{\cosh[\kappa(z+h_w)]}{\sinh(\kappa h_w)}\cos(\kappa x - \omega t) \tag{6.22}$$

$$w_T(x,z,t) = A(\omega - \kappa U_0)\frac{\sinh[\kappa(z+h_w)]}{\sinh(\kappa h_w)}\sin(\kappa x - \omega t) \tag{6.23}$$

$$p_T(x,z,t) = -\rho g z + \frac{\rho A(\omega - \kappa U_0)}{\kappa\sinh(\kappa h_w)}\left([\omega - \kappa U(z)]\cosh(\kappa(z+h_w)) + \frac{\partial U(z)}{\partial z}\sinh(\kappa(z+h_w))\right)\cos(\kappa x - \omega t) \tag{6.24}$$

where U_0 denotes the current velocity at $z = 0$. Substituting Equation (6.20) into Equation (6.16) gives the modified dispersion relation as:

$$(\omega - \kappa U_0)^2 = [g\kappa - (\omega - \kappa U_0)\frac{\partial U(z=0)}{\partial z}]\tanh(\kappa h_w) \tag{6.25}$$

This equation is only valid for both uniform and linear shear current profiles (i.e. when $\frac{\partial^2 U(z)}{\partial z^2} = 0$). For the former, it can thus be simplified to the convenient form of the dispersion relation:

$$(\omega - \kappa U_0)^2 = g\kappa \tanh(\kappa h_w) \tag{6.26}$$

For a current of linear shear profile that can be expressed by:

$$U(z) = U_0 + Bz \tag{6.27}$$

then the modified dispersion relation can be represented as:

$$(\omega - \kappa U_0)^2 = [g\kappa - (\omega - \kappa U_0)B] \tanh(\kappa h_w) \tag{6.28}$$

where B is the current slope, and Equation (6.28) is true for $B = 0$ (i.e. uniform profile), and $B \neq 0$ (i.e. linear shear profile).

Based on the principle of 'wave-action' conservation (Bretherton & Garret, 1970), the modified wave amplitude of Equation (6.8) in the presence of a current, (A), can be rearranged as follows (J. Smith, 1997; S. Draycott, Noble, et al., 2018):

$$A = A_a \left[\frac{C_{g,a}}{C_g} \cdot \frac{1}{1 + \frac{U \cos \alpha}{C_g}} \right]^{\frac{1}{2}}; \tag{6.29}$$

which is similar to Equation (4.3), but with different subscripts. Thus, the subscript 'a' indicates a region with the absence of current, and α is the angle between the propagation directions of the wave and current, and C_g is the velocity of the wave group and is given as:

$$C_g = \frac{1}{2} C \left(1 + \frac{2\kappa h_w}{\sinh(2\kappa h_w)} \right); \tag{6.30}$$

where C is the wave apparent celerity, which is the sum of the wave celerity in the fixed reference frame (C_a) and the current velocity (U), and can be expressed by the wavelength (L) and the corresponding period (T) as:

$$C = C_a + U; \ = \frac{L}{T} \tag{6.31}$$

6.3.3 Stochastic Wave-Current Mathematical Model

Under the wave and current assumptions described in Section 6.3.2, a frequency-domain wave-current model can be established by coupling the spectral representation of irregular waves with the equations of the regular wave-current model (N. E. Huang et al., 1972). Consequently, the spectral density of surface waves in the presence of the current, $S(\omega,U)$, is given by:

$$S(\omega,U)=\frac{4S(\omega)}{\left[1+\frac{4U\omega}{g}\right]^{1/2}\left[1+\left(1+\frac{4U\omega}{g}\right)^{1/2}\right]^{2}} \tag{6.32}$$

in which $S(\omega)$ is the spectral density of waves without the influence of current; U, ω, and g are the current speed, frequency, and gravitational acceleration, respectively. In this thesis, the JONSWAP spectrum was selected to generate the irregular waves (Hasselmann et al., 1973), whose expression is:

$$S(\omega)=\frac{\alpha g^{2}}{\omega^{5}}\exp\left[-\frac{4}{5}\left[\frac{\omega_p}{\omega}\right]^{4}\right]\gamma^{\alpha} \tag{6.33}$$

where ω_p is the peak frequency, γ is the peak enhancement factor, and parameters α and σ are

$$\alpha=\exp\left[\left[-\frac{(\omega-\omega_p)^2}{2\omega_p^2\sigma^2}\right]\right],\quad \sigma=\begin{cases}0.07 & \text{if } \omega<\omega_p\\ 0.09 & \text{if } \omega\geq\omega_p\end{cases}\text{, respectively.}$$

From Equation (6.32), waves tend to shorten and become steeper when they encounter an opposing current (i.e. when the current speed is negative), and vice versa for waves travelling with a following current. Thus, it is worth mentioning that when the current speed is negative, there is a cut-off frequency that can be determined using the following formula:

$$1+\frac{4U\omega}{g}\geq 0 \tag{6.34}$$

Before this critical frequency ($\omega=-\frac{g}{4U}$), surface waves with frequencies close to it become extremely steep, and theoretically, beyond this frequency, no waves can exist. In reality, wave breaking will occur at the current threshold, and since the wave amplitude at this critical speed would be infinite; thus the waves break long before they reach this limit. However, breaking still impacts wave components that propagate onto the current, so there is a limit to how big waves can develop over a certain frequency range (Phillips, 1977). In order to address this issue, T. Hedges (1981) derived the following "equilibrium range limit" for deep water

(T. Hedges, 1981; T. S. Hedges et al., 1985):

$$S_{ER}(\omega,U) = \frac{A^* g^2}{(\omega-\kappa U)^5}\frac{1}{1+\dfrac{2U(\omega-\kappa U)}{g}} \tag{6.35}$$

in which "ER" denotes the equilibrium range, and A^* is a numerical (Phillips-like) constant for the waves generated on currents, its values provided by Phillips in the range $0.008-0.015$ (Phillips, 1977).

Given that the equilibrium range of the spectrum is associated with deep water, the preceding equation, Equation (6.35), can be used to predict spectral densities for the current region whenever $S_{\mathrm{ER}}(\omega,U)$ is smaller than $S(\omega,U)$. Following that, alterations in the spectra corresponding to flow velocity and acceleration driven by the subsurface current can be estimated (T. S. Hedges et al., 1985; Soares & De Pablo, 2006; Peeringa, 2014). By employing these spectral representations, the sinusoidal water surface elevation $\eta(x,t)$ for ith wave components can be written as:

$$\eta(x,t) = \sum_{i=1}^{N} A_i \cos(\kappa_i x - \omega_i t + \phi_i) \tag{6.36}$$

in which ϕ is the random phase angle spread evenly between 0 and 2π, and N refers to the total number of wave components. In this stochastic model, the amplitude of the i^{th} wave component with frequency interval $\Delta\omega$ is given by:

$$A_i = [2S(\omega_i,U)\Delta\omega]^{1/2} \tag{6.37}$$

The corresponding formulae for the resultant horizontal and vertical velocities and pressure fields are:

$$u_T(x,z,t) = U(z) + \sum_{i=1}^{N} A_i(\omega_i-\kappa_i U)\frac{\cosh[\kappa_i(z+h_w)]}{\sinh(\kappa_i h_w)}\cos(\kappa_i x-\omega_i t+\phi_i), \tag{6.38}$$

$$w_T(x,z,t) = \sum_{i=1}^{N} A_i(\omega_i-\kappa_i U)\frac{\sinh[\kappa_i(z+h_w)]}{\sinh(\kappa_i h_w)}\sin(\kappa_i x-\omega_i t+\phi_i), \tag{6.39}$$

$$p_T(x,z,t) = -\rho g z + \sum_{i=1}^{N} \frac{\rho A_i(\omega_i-\kappa_i U)^2\cosh[\kappa_i(z+h_w)]}{\kappa_i\sinh(\kappa_i h_w)}\cos(\kappa_i x-\omega_i t+\phi_i), \tag{6.40}$$

respectively. Differentiating the velocity fields equations, Equations (6.38) and (6.39), with regard to time yields the corresponding resultant accelerations (i.e. the horizontal and vertical) as:

$$\dot{u}_T(x,z,t) = \sum_{i=1}^{N} A_i \omega_i (\omega_i - \kappa_i U) \frac{\cosh[\kappa_i (z+h_w)]}{\sinh(\kappa_i h_w)} \sin(\kappa_i x - \omega_i t + \phi_i), \tag{6.41}$$

$$\dot{w}_T(x,z,t) = \sum_{i=1}^{N} A_i \omega_i (\omega_i - \kappa_i U) \frac{\sinh[\kappa_i (z+h_w)]}{\sinh(\kappa_i h_w)} \cos(\kappa_i x - \omega_i t + \phi_i), \tag{6.42}$$

in which the wavenumber k_i will be obtained from the modified dispersion relation, Equation (6.26), for each wave component. Although this model is stochastic, it cannot capture the full-nonlinear effects of wave and wave-current interaction because it relies on linear wave theory. However, some nonlinear effects (e.g. fluid velocity and acceleration) can be captured by employing kinematic stretching techniques (e.g. vertical, extrapolation, and Wheeler) (Faltinsen, 1993; Nestegård et al., 2019).

In the present simulations, the Wheeler stretching option within OrcaFlex is utilised to account for the amplification of fluid velocity above the mean water level, thereby mitigating the issue of unrealistically large particle velocities associated with linear wave theory (OrcaFlex, 2023). This method operates by linearly stretching or compressing the water column to a height equivalent to the mean water depth (Dresselhaus & Tabor, 1992).

Additionally, the Doppler effect of wave-current interaction is integrated into the model by modifying the wave frequencies and wavelengths based on the relative motion of the current and waves. Such adjustments are crucial for accurately simulating the dynamics of the FOWT under varying environmental conditions. The Doppler shift is taken into account in the aero-hydro-servo-elastic analyses in OrcaFlex models. This is done by changing the wave properties during the simulation runtime to reflect these changes, as explained in Section 6.8.3 and shown in Figure 6.6.

6.4 W2Power floating Offshore Wind Turbine Model

6.4.1 Platform Model Description

In order to investigate the effects of wave-current interaction on the dynamic responses of FOWTs, this work employs an innovative floating wind turbine model called W2Power as a case study EnerOcean S.L. (2007). The present research considers an older version of the platform, and does not represent the current design (Hanssen et al., 2015). W2Power is described earlier in Section 4.5.3, and the main particulars of the platform at full scale are given in Table 4.2.

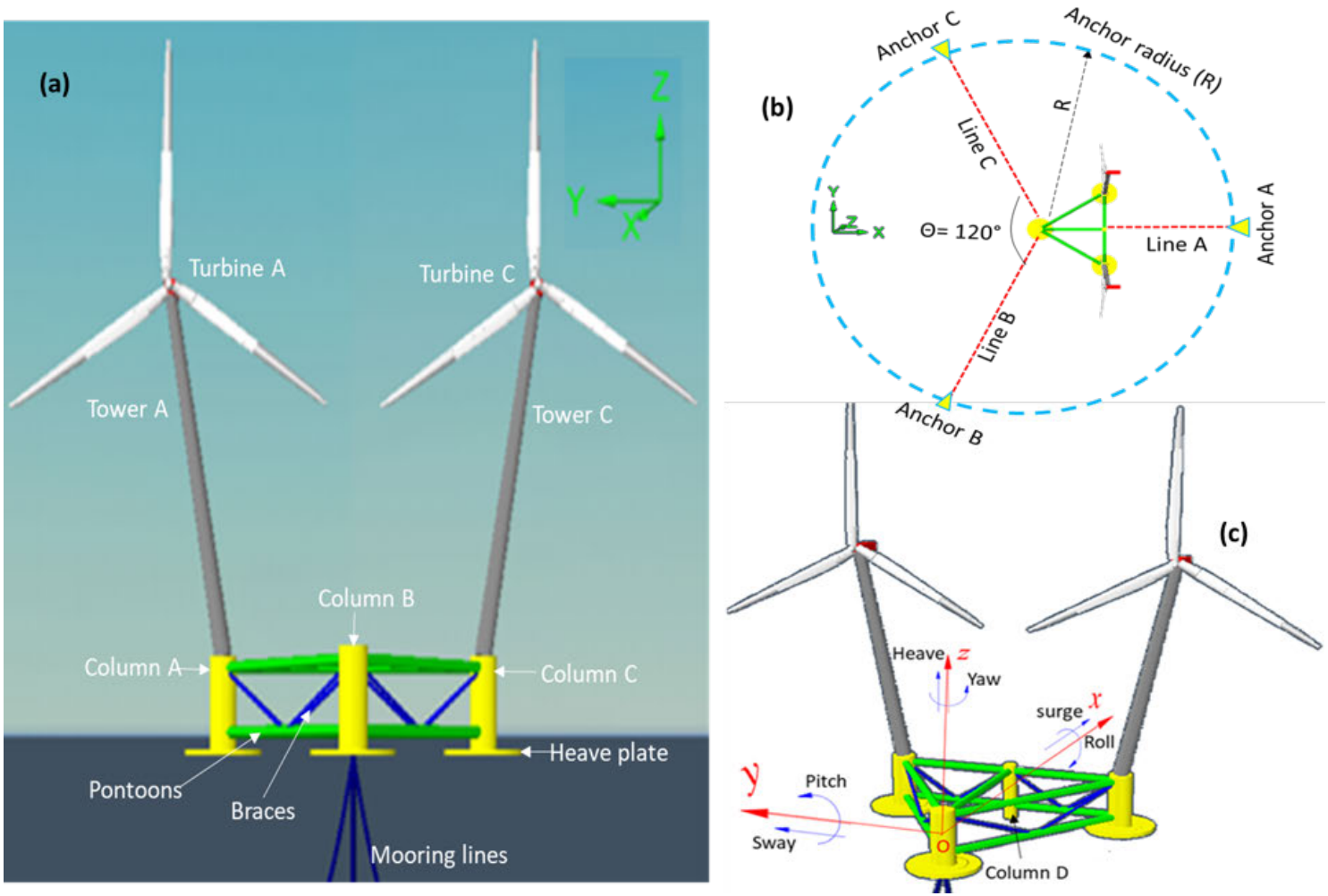

Figure 6.2: Description of the W2Power FOWT: (a) the system's main particulars; (b) the mooring system configuration; (c) the 6 DoFs of the system.

Since this work utilises the W2Power FOWT for numerical modelling in combined wave-current conditions, the coupled model is developed (Figure 6.2). This model integrates hydrodynamic, structural, and environmental aspects to simulate the dynamics of the W2Power system. The following sections (Sections 6.5 to 6.8) detail the key components and methodologies employed in the model development.

6.5 Platform Hydrodynamic Modelling

The hydrodynamic modelling approach includes the development of a panel model to create a mesh file in FEM (finite element method) format, followed by diffraction-radiation to determine hydrodynamic coefficients. Then, a mesh convergence analysis was conducted to optimise the panel model's accuracy and efficiency in predicting platform responses under varying wave conditions.

6.5.1 Panel Model

A panel model was built with GeniE, considering different panel (node) sizes. GeniE, developed by DNV, is an engineering tool for modelling, analysing and code-checking structures such as beams, plates and shells (GeinE, 2020). Using GeniE, a FEM mesh file was generated to carry out hydrodynamic and hydrostatic analyses of the panel model.

6.5.2 Diffraction-Radiation Analysis

Hydrodynamic diffraction-radiation analysis was conducted using OrcaWave, a three-dimensional frequency domain panel code. OrcaWave is based on linear and second-order potential theory and is utilised for diffraction-radiation analysis of floating and submerged bodies in waves (OrcaWave, 2023). The aim of the linear diffraction-radiation analysis is to obtain hydrodynamic coefficients such as added mass, wave radiation damping, wave force, and drift force coefficients for the OrcaFlex model of the W2Power floating wind turbine. The analysis considered 32 wave periods ranging from 3.5 s to 400 s and 9 wave headings between 0° and 180°.

6.5.3 Mesh Convergence Analysis

A sensitivity (convergence) study was conducted to ensure that the mesh provided accurate results without unnecessary density. The full set of periods and headings was included in this study, although a reduced set could be used for efficiency.

Table 6.1: Properties of the panel models.

Panel name	Panel size [m]	Number of panels [-]	Water plane area [m^2]
Mesh1	0.05	1027	206.26
Mesh2	0.025	3647	207.97
Mesh3	0.0125	12639	208.48
Mesh4	0.00625	44342	208.67

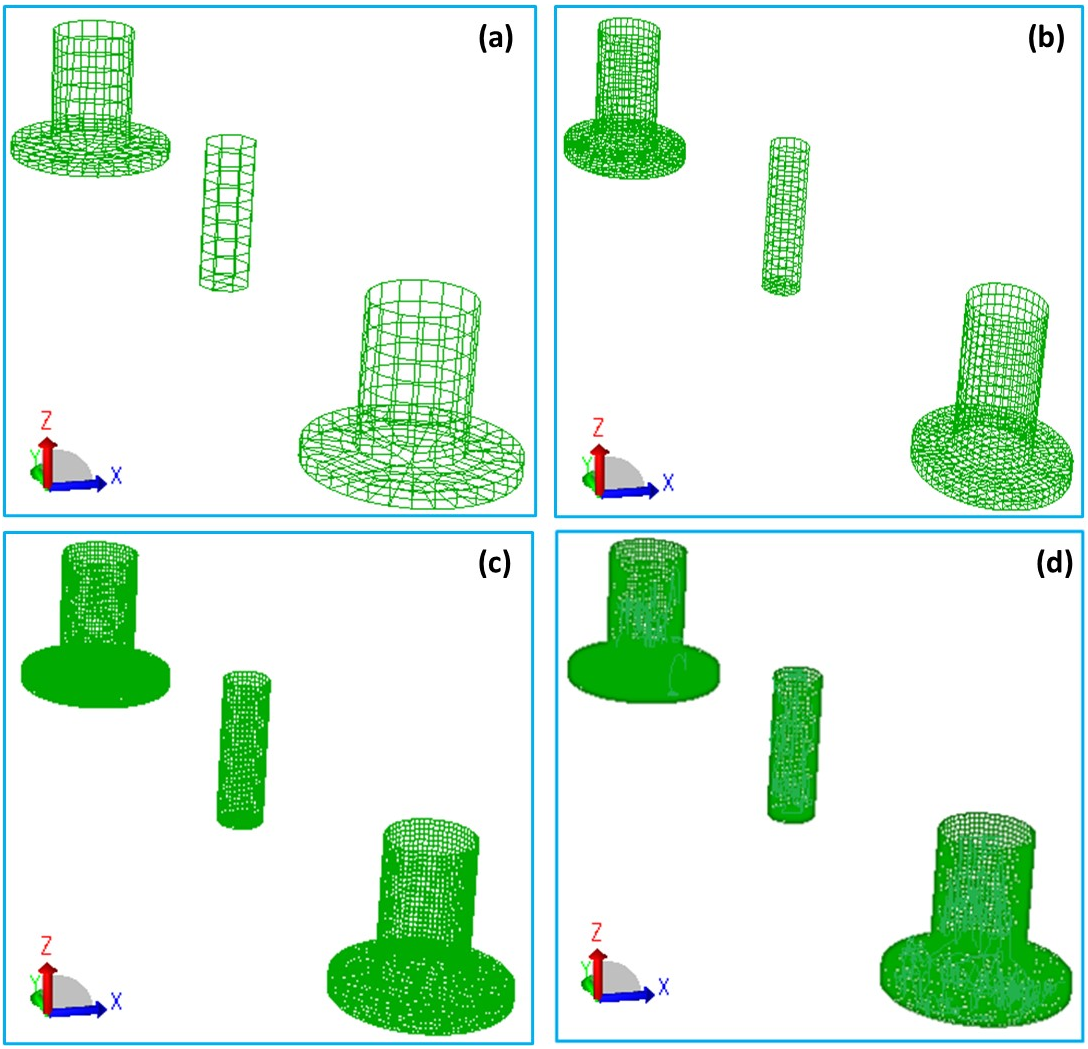

Figure 6.3: Panel models (excluding Column B due to page's space constraints) for mesh sensitivity analysis, employing different characteristic panel sizes (Δx): (a) Mesh1 of $\Delta x = 0.05$ m, (B) Mesh2 of $\Delta x = 0.025$ m, (c) Mesh3 of $\Delta x = 0.0125$ m, and (d) Mesh4 of $\Delta x = 0.00625$ m. Apparent differences in scale/dimensions are due to zoomed screenshots for clarity.

The panel size, denoted by Δ, represents the characteristic length of a panel element, and efforts were made to maintain a uniform mesh size where feasible (see Figure 6.3). Herein, clean-up and manual adjustments were made to some elements of the mesh to address complexities in the platform's geometry, thereby ensuring optimal element distribution and resolution across the model (Moës et al., 2003).

This analysis was performed on four meshes, whose main geometrical properties are summarised in Table 6.1. The element density of the panel models is illustrated in Figure 6.3. Note that increasing the number of elements must be done systematically by reducing each element's characteristic length (Δx) by a factor of 2. This results in the number of panels increasing by a factor of 4 for each refinement.

Wave excitation forces are compared for the surge, heave, and pitch modes obtained with the different panel models. Accordingly, the load RAOs (response amplitude operator) for a wave heading of 45° are presented in Figure 6.4. It is evident from the plots that the results converge as the number of panel elements increases. However, there is a small shift in the peak periods, with relatively steep curves leading to significant differences for a given period, particularly in heave and pitch RAO load. This is likely influenced by the frequency resolution around the natural period, which may not have been sufficient and contributed to these observed shifts.

Subsequently, it was found that Mesh3 ($\Delta x = 0.0125$ m) provided comparable results to the finest mesh, Mesh4 ($\Delta x = 0.00625$ m). Only the coarsest mesh ($\Delta x = 0.05$ m) produced results that are not in complete agreement with the finer-mesh results. Furthermore, Mesh3 and Mesh4 produced very similar results; however, Mesh1 was clearly inadequate. Therefore, Mesh3 was selected as an optimum candidate for this work, hereafter used in all analyses. Detailed analyses encompassed with the results from the convergence study for all DoFs of load RAOs are provided in Appendix B.1.

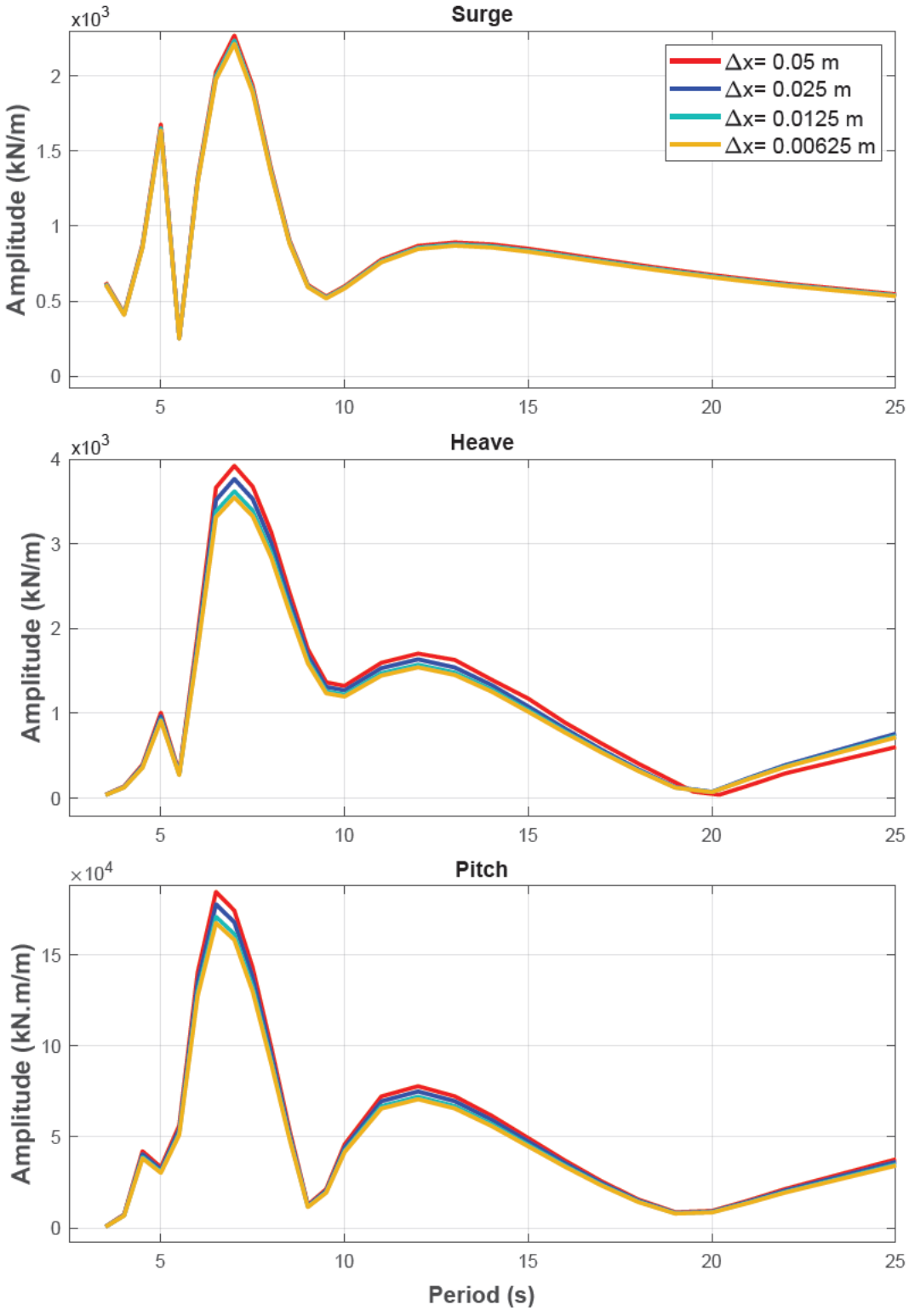

Figure 6.4: Load RAO amplitudes in surge, heave and pitch DoFs for different mesh densities for sensitivity analysis, for a wave heading of 45°.

6.6 Mooring System Modelling

The configuration of the single-point mooring system is a typical catenary that comprises three lines placed symmetrically along the platform's Z-axis and spread by 120°, (see Figure 6.2.b). The individual lines are made of stud-less chains. The W2Power is designed for water depths of 200 m, whilst this study focuses on a potential deployment site of a water depth of 80 m. Thus, a new mooring system is proposed for this water depth.

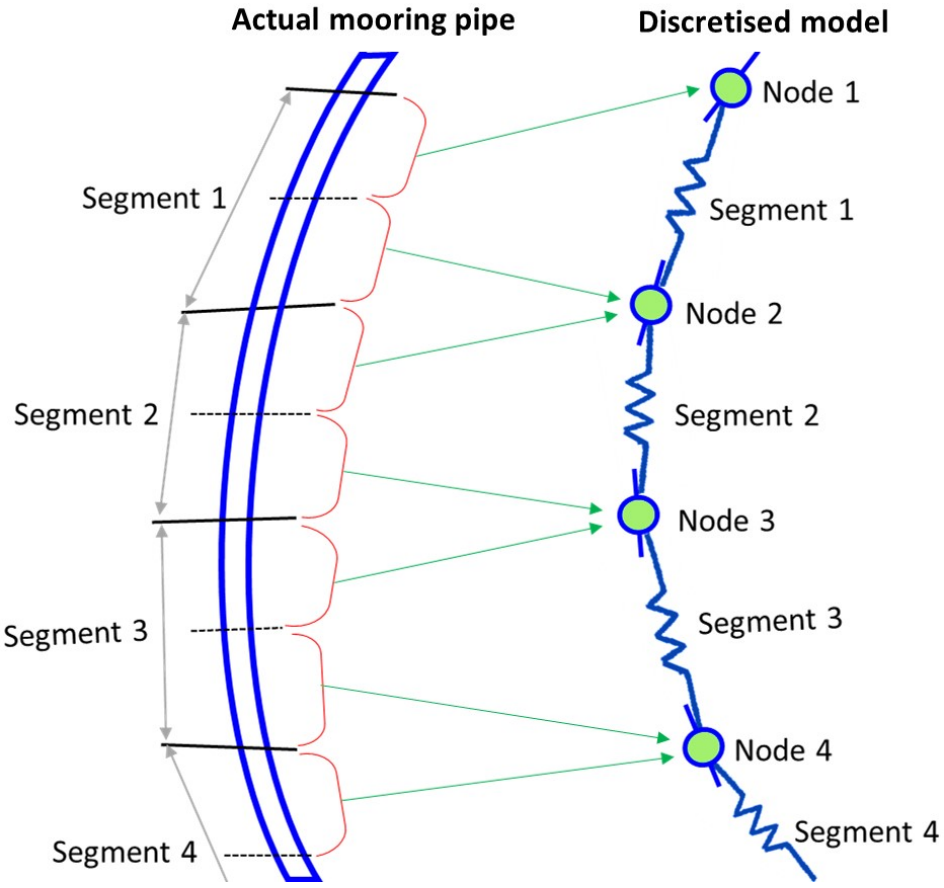

Figure 6.5: Depiction of line model of mooring in OrcaFlex (OrcaFlex, 2023).

The mooring cables were simulated using OrcaFlex's FEM model, as shown in Figure 6.5. Each line was discretised into segments, which were then modelled by straight massless model segments with a node at each end (Van den Boom, 1985). The model segments only capture the line's axial and torsional properties, whereas the other properties, like mass, weight, and buoyancy, were all lumped into the nodes (OrcaFlex, 2023). The seabed was assumed to be horizontal and on a rigid plane.

This FEM model approach was chosen for its accuracy in modelling dynamic interactions and its computational efficiency. Other approaches for modelling mooring lines include lumped-parameter models, which simplify cable dynamics but may not capture detailed interactions, and more complex 3D cable dynamics models, which offer greater accuracy at the cost of higher computational demand (Hall & Goupee, 2015). These alternatives explore various levels of modelling fidelity, with simpler methods like the quasi-static approach and more complex models (Hall et al., 2014).

6.6.1 System Survivability Analysis

To check the system's survivability, contour surfaces for joint wind and wave parameters are first constructed based on long-term joint distributions with the probability of exceeding corresponding to a 50-year return period (see Figure 4.12). Accordingly, different extreme load cases are defined with different wave seeds and summarised in Appendix B.2.

Therefore, as recommended by DNV (DNV-RP-C205, 2017), ultimate limit state (ULS) checks were performed to ensure that individual mooring lines are strong enough to withstand the loads imposed by extreme environmental conditions. According to DNV standards (DNV-OS-E301, 2010), the design equation in the form of a utilisation factor (UF) can be expressed as follows:

$$UF = \frac{T_d}{S_c} < 1 \tag{6.43}$$

$$T_d = (\gamma_{\text{mean}} \cdot T_{\text{mean}}) + (\gamma_{\text{dyn}} \cdot T_{\text{dyn}}) \tag{6.44}$$

where, S_c is the characteristic mooring line strength and was obtained from the minimum breaking strength (S_{MBS}), with $S_c = 0.95 \times S_{MBS}$. Furthermore, T_d is the design tension, γ_{mean} and γ_{dyn} are partial safety factors for the mooring line's mean (T_{mean}) and dynamic (T_{dyn}) tensions, respectively. The values of the partial safety factors for both T_{mean} and T_{dyn} have been determined in accordance with a consequence class 1 (see Table 6.2).

Table 6.2: Partial safety factors for ULS analysis.

Consequence class	Safety factor for mean tension (T_{mean})	Safety factor for dynamic tension (T_{dyn})
1	1.10	1.50
2	1.40	2.10

The current analysis focused solely on the tension relative to the minimum breaking strength of the mooring lines, indicating that the design is primarily based on the strength capacity of the mooring system. By ensuring that the value of the UF remains below 1, the mooring lines are deemed to be within the acceptable limits of the ULS criteria (DNV-OS-E301, 2010; DNV-RP-C205, 2017). Consequently, the designed mooring system is optimised and employed in the current study, and its properties are given in Table 6.3.

Table 6.3: Characteristics of the mooring system.

Parameter	Unit	Value
Water depth	[m]	80
Fairlead depth	[m]	15
Anchor radius (R)	[m]	382.24
Line length	[m]	398.3
Number of lines	[-]	3
Line type (grade)	[-]	Chains (R4–Studless)
Line dry, wet weight	[kN/m]	537, 466.4
Axial stiffness	[kN]	252, 500
Fairlead pretension	[kN]	1153
Nominal chain diameter	[mm]	157
Minimum breaking load (MBL)	[kN]	21, 235

6.7 Coupled Model of Floater-Mooring-Towers-Nacelles-Rotors

The platform is engineered to accommodate two 6 MW WTGs. Due to a lack of data on this WT, it is, therefore, analysed with a pair of the well-documented and publicly accessible NREL-5 MW WTG (J. Jonkman et al., 2009). However, the mass and inertial properties of the NREL baseline models are different from those of the 6 MW turbines, which could lead to variations in the structural requirements and ballasting arrangements of the platform (J. Jonkman et al., 2009; Meng et al., 2018). For safe operation, the ballasts were systematically adjusted until the design operational draft of 15 m was attained. This adjustment ensures that the system maintains its stability and performance despite the change in the turbines' specifications.

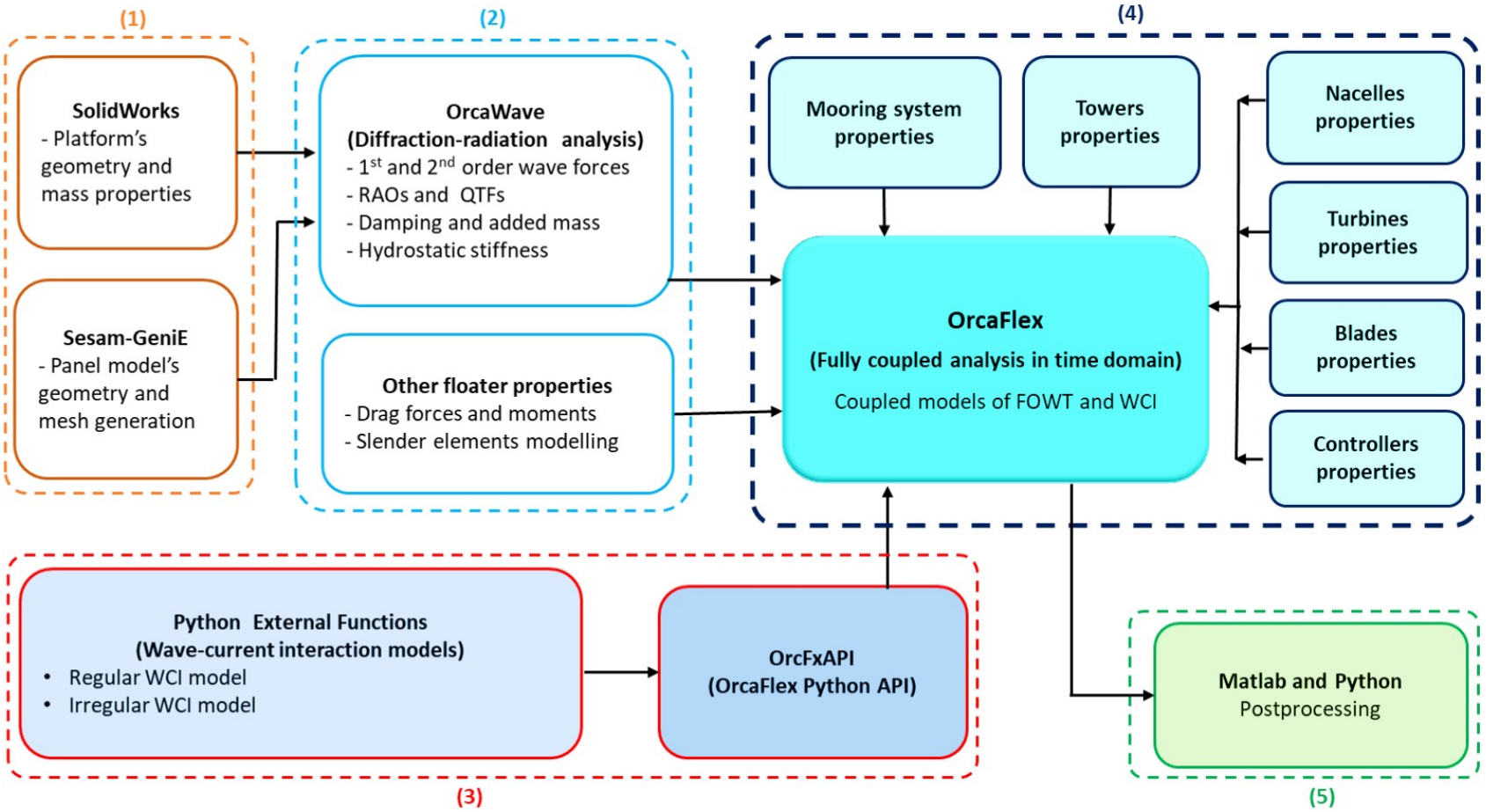

Figure 6.6: Schematic flow chart of the coupled model setup and numerical modelling analysis.

The towers are conical tubular steel structures of a height of 77.6 m and base (at the platform's top) and top diameters of 6.5 m and 3.87 m, respectively. They are cantilevered at an outward 15°atop the floater's stern columns (A and C). Towers' data are adopted from the OC3-Hywind spar FOWT (J. Jonkman, 2010b; Shin, 2011), and provided in Table 6.4. Note that this system (i.e., Hywind FOWT) has experienced significant operational challenges. Due to mooring-related fatigue issues affecting the structure and tower, all five units have been towed back recently to Wergeland Port on the west coast of Norway (Recharge, Jan 12, 2024).

The converging equation is established to calculate the displacement, velocity, and acceleration of the FOWT, as well as the mooring dynamics. It considers the effects of wind, wave, cable forces, and wave-current interaction, and is written to be solved for the 6 DoF motions as follows:

$$(\mathbf{M}+\mathbf{A}_{\infty})\ddot{x}(t)+\int_0^t \mathbf{K}(t-\tau)\dot{x}(\tau)d\tau+\mathbf{B}\dot{x}(t)+\mathbf{C}x(t)=F_m(t)+F_h(t)+F_a(t) \tag{6.45}$$

this equation is known as Cummins equation, in which, $\mathbf{M}$ is the mass matrix of the entire FOWT including ballast, $\mathbf{A}_{\infty}$ is the added mass matrix at infinite frequency, and $\mathbf{K}$(t) is the retardation function matrix (impulse response), which was calculated by the Cummins model (Cummins et al., 1962).

Besides, the convolution integral handles the 'memory' effect of past motions (Rognebakke, 2002), where τ is a 'time' variable ranging from 0 to t. $\mathbf{B}$ is the nonlinear damping matrix, and $\mathbf{C}$ is the stiffness matrix that comprises both the hydrostatic stiffness provided by buoyancy and the mooring stiffness, $\mathbf{C}$ = ($\mathbf{C_h}$ + $\mathbf{C_m}$). The displacement, velocity, and acceleration vectors of the body are, respectively, denoted by x, $\dot{x}$, and $\ddot{x}$. On the right side, F_m is the mooring fairlead tensions, F_h is the hydrodynamic loads (first- and second-order wave forces, and current drag force), and F_a is the aerodynamic loads on the two rotors.

Table 6.4: Specifications of the NREL 5 MW baseline wind turbine.

Parameter	Unit	Value
Rated power	[MW]	5
Number of blades	[-]	3
Rotor configuration	[-]	Upwind
Hub, rotor diameter	[m]	3, 126
Cut-in, rated rotor speed	[RPM]	6.9, 12.1
Drivetrain, control system	[-]	Geared, pitch regulated
Rotor, nacelle, tower mass	[tonne]	110, 240, 249.7
Cut-in, rated, cut-out wind speed	[m/s]	3, 11.4, 25

6.8 Model Setup for the Implications of Wave-Current Interaction

This section establishes the setup of the coupled model to explore the implications of wave-current interaction on the dynamics of the W2Power FOWT. It presents the modelling of the coupled floater-mooring-towers-nacelles-rotors model, detailing the aspect of each subsystem. Additionally, it outlines the integration of wave-current interaction models within the fully coupled framework.

6.8.1 Platform-Mooring Modelling

The numerical modelling tools used are SolidWorks, DNV's Sesam-GeniE, and Orcina Ltd's OrcaWave and OrcaFlex (Solidworks, 2021; GeinE, 2020; OrcaWave, 2023; OrcaFlex, 2023). As detailed in Section 6.5, the floater's geometry was developed using SolidWorks, and its mass and inertia matrices were obtained. The hull's panel model (i.e. heave plates and columns) was meshed using GeniE. OrcaWave was then used to perform the diffraction analysis for the ballasted floater in the absence of the mooring system and superstructures (e.g. turbines, towers, nacelles). This yielded the floater's RAOs and other hydrodynamic parameters such as the hydrostatic stiffness coefficients, the frequency-dependent hydrodynamic added mass and radiation damping, the first- and second-order wave forces, and difference-frequency QTFs.

Then, the OrcaWave-generated model was loaded as a vessel object into OrcaFlex to model the floater as a rigid body, whose motion is defined by three translational displacements (surge, sway, and heave) and three rotational displacements (roll, pitch, and yaw) at the body origin $(0,0,0)$ (see Figure 6.2). Then, the mooring lines of properties listed in Table 6.3 were added between the platform's fairleads and the seafloor.

To account for the contribution of current-induced drag loads on viscous damping and mean platform offsets, the analysis considered drag loads on the submerged structures (mooring lines, heave plates, columns, pontoons, and braces). Thereby, an extended form of Morison's formula was employed to calculate the hydrodynamic loads on the mooring lines and platform (Morison et al., 1950; OrcaFlex, 2023), which can be expressed as follows:

$$f = \overbrace{(C_m\,\Delta\,a_f - C_a\,\Delta\,a_b)}^{\text{Inertia}} + \overbrace{\left(\frac{1}{2}\,\rho\,C_d\,A\,|v_f|v_f\right)}^{\text{Drag}} \tag{6.46}$$

in which, f is the fluid force per unit length exerted on the body. C_m and C_a are, respectively, the inertia and added mass coefficients for the body, and the value of C_m was taken to be $1+C_a$. Δ denotes the mass of the fluid displaced by the body, and a_f and a_b are the fluid and body accelerations relative to the earth, respectively. ρ represents the density of water, C_d is the drag coefficient for the body, A is the drag area, and v_f is the fluid velocity relative to the earth.

6.8.2 Superstructures Modelling

The superstructures (e.g. towers, heavy topsides) are modelled explicitly to include the rotors' rotation and flexing of the towers and blades in the OrcaFlex model. The towers are modelled as profiled cylinders via line objects that utilise homogeneous pipe attributes, which enable the modelling of variable outer and inner diameter profiles and their corresponding physical properties (e.g. mass and inertia). Such modelling allows for accurately capturing the structural behaviour and dynamic responses of the towers under different loading conditions. This, in turn, ensures a realistic simulation of the flexing and rotation of the towers, thereby enhancing the fidelity of the overall structural analysis (OrcaFlex, 2023).

The rotors are then connected to the towers via nacelles that are modelled as lumped 6D buoys with their respective properties, and to increase blade-to-tower clearances, the rotors and nacelles are tilted by 5° (J. Jonkman et al., 2009). Furthermore, blade structural models closely resemble a line model, with segmented blades and nodes at the ends of each segment. The blade discretisation and segment lengths were meticulously adjusted to be consistent with the overall length of the NREL-5MW turbine (J. Jonkman et al., 2009). At each node, the mass and inertia properties are appropriately grouped. BEM theory is utilised to capture aerodynamic loads (Froude, 1920).

6.8.3 Modelling of Wave-Current Interaction

Wave-current interaction is modelled using an external Python function (Van Rossum et al., 1995). This function solves the linear dispersion relation, Equation (6.26), to obtain the current-included wavenumber. It is not possible to solve Equation (6.26) analytically; therefore, it is solved using the physical approximations by Fenton & McKee (1990). The presence of current slightly modifies the solution method; therefore, the well-known Newton-Raphson's method is used to refine the approximation. It is tailored to attain arbitrary customisable accuracy (Ben-Israel, 1966).

Subsequently, these custom analytical models that account for the interaction between currents and waves (regular and irregular) are compiled using the OrcaFlex Python API (OrcFxAPI, 2024). The current-altered wave profiles are then imported into OrcaFlex's environment section, and the simulations are executed accordingly using Python external functions at runtime.

The developed coupled model integrates two key aspects: the influence of current on the mooring lines and the incorporation of WCI in estimating the hydrodynamic loading on the FOWT. The setup of the coupled analysis for the developed model is illustrated in Figure 6.6.

6.9 Models Validation

To ensure the reliability and robustness of the numerical models developed in this chapter, rigorous validations have been undertaken against experiments presented in Chapter 4. This validation involves the utilisation of environmental conditions from the experimental setup to replicate numerical data accurately. The load cases from the experimental campaigns have been simulated using the numerical models developed in this chapter. Specifically, the load cases for regular and irregular waves are detailed in Tables 4.5 and 4.6, respectively, and the characteristics of the current are given in Table 4.7. Subsequently, the outcomes of the model validation are provided in Chapter 7.

Following the validation, further comprehensive numerical investigations have been conducted using the developed models. These investigations encompass different wave-current interaction scenarios distinct from those considered in the validation phase. These scenarios are based on new environmental loads and simulation setups detailed in Section 6.10. The numerical results of these subsequent simulations are presented and discussed in Chapter 8.

6.10 Environmental Loads and Simulation Setup

6.10.1 Environmental Loads

This study investigates the performance of the W2Power floating wind system at a reference site, Canary-I, located off the coast of Gran Canaria in the Atlantic Ocean (Figure 4.9 and Table 4.4). The environmental contours of this site are constructed and presented in Section 4.6.2.

Wind

The rated wind speed (U_w) at the top of the towers is assumed to be 11.4 m/s, corresponding to the mean wind speed at 100 m hub height at the Canary-I site (see Table 4.4). The wind is assumed to be in the same direction as the axes of the rotor and is modelled using the NPD (Norwegian Petroleum Directorate) spectrum (B. Jonkman & Kilcher, 2012).

Waves

Different wave conditions are picked from the contour to represent both "survival" and "operational" loading conditions (refer to Figure 4.12). For the selected sea states, regular wave trains are defined by linear Airy types of height (H) and period (T). While irregular are represented by the JONSWAP spectrum using a peak factor (γ), significant wave heights (H_s), and peak period (T_p).

Current

Current specifications are presented in Table 4.7. As demonstrated in Figure 4.10, the site has maximal and average current speeds (U_c) of 0.8 m/s and 0.3 m/s, respectively, whose profiles are characterised within OrcaFlex environment data. Note that OrcaFlex models currents as applied loads (OrcaFlex, 2023). This approach is a common practice in the field, and it was found to simulate the effects of current with adequate accuracy.

However, it is important to note that this method does not account for the effects of current on the wave profile. Thus, it does not incorporate wave-current interaction, which could introduce additional complexities in real-world scenarios that might implicate the dynamics of the floating system (J. M. Jonkman, 2007). Afterwards, various load cases are defined and tabulated in Table 6.5 along with their identification numbers.

Table 6.5: Load case parameters for coupled-analysis simulations of wave-current interaction.

Load case	**Wave model**	H (H_S) **[m]**	T (T_P) **[s]**	**JONSWAP** γ	U_c **[m/s]**	**Current direction**	U_w **[m/s]**
			Extreme sea states				
LC1	Regular	4.63	16	–	0.8	Following	0
LC2	Regular	4.63	16	–	0.8	Opposing	0
LC3	Regular	3.85	8	–	0.8	Following	0
LC4	Regular	3.85	8	–	0.8	Opposing	0
LC5	Irregular	4.63	16.4	3.3	0.8	Following	0
LC6	Irregular	4.63	16.4	3.3	0.8	Opposing	0
LC7	Irregular	3.85	9	3.3	0.8	Following	0
LC8	Irregular	3.85	9	3.3	0.8	Opposing	0
			Operational sea states				
LC9	Regular	1.4	7.4	–	0.3	Following	11.4
LC10	Regular	1.4	7.4	–	0.3	Opposing	11.4
LC11	Irregular	1.4	7.4	2	0.3	Following	11.4
LC12	Irregular	1.4	7.4	2	0.3	Opposing	11.4

6.10.2 Simulation Setup

During the simulations of extreme sea states, the turbines' rotors are parked. When the rotor is parked, the turbine blades are feathered to minimise the aerodynamic loads. This allows us to focus on the effects of WCI on the dynamic responses of the platform and mooring lines under such loading conditions. Whilst the aerodynamic loads and wind drag forces act on the wind turbine systems are included in the operational conditions.

In all simulated cases, the direction of the waves is fixed at 180°, and the current hits the platform from two directions (i.e. 180° and 0°), hence creating two scenarios when it interacts with waves: following and opposing, respectively. To assess the effect of current and the inclusion of wave-current interaction on the dynamic responses of the FOWT, the simulated scenarios are:

i) waves only,
ii) currents only,
iii) straightforward superposition of wave-current effects without considering any interaction,
iv) and incorporation of the wave-current interaction effects.

Consequently, the load cases defined in Table 6.5 are executed to produce the environmental loadings shown in Figure 6.7.

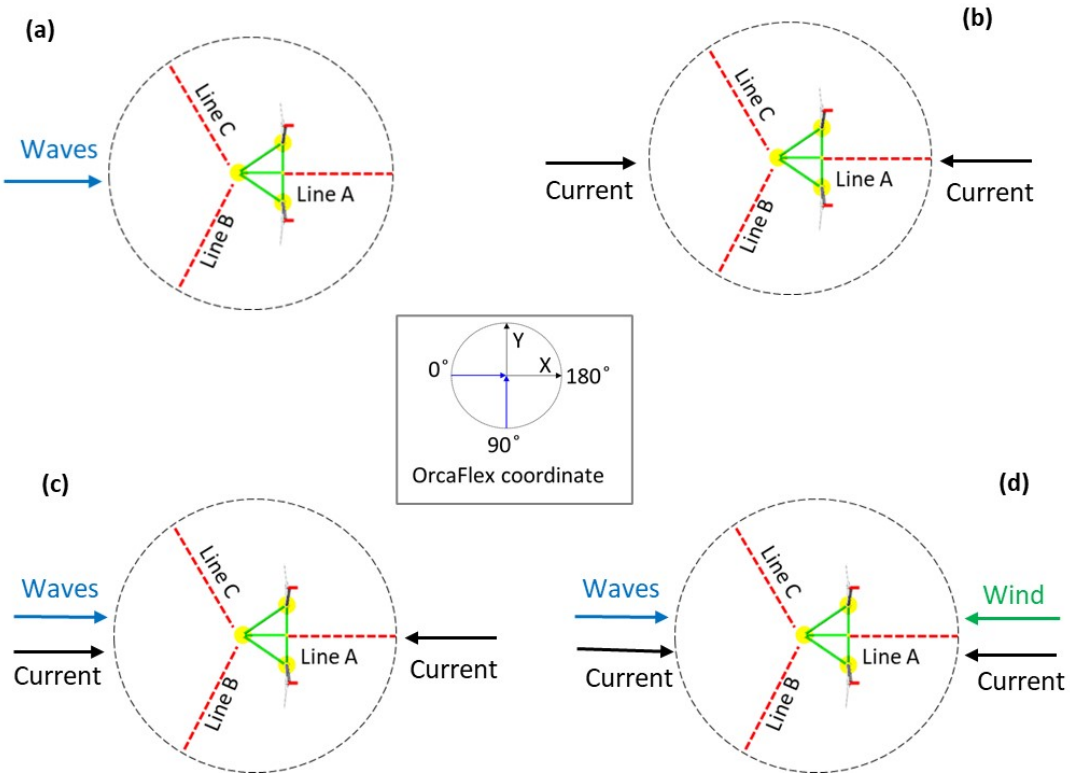

Figure 6.7: Configurations of directional environmental loadings for numerical simulation matrices: (a) waves only, (b) currents only, (c) combined wave-current loads, and (d) combined wind-wave-current loads. Also, showing the coordinate system of OrcaFlex, where W2Power FOWT is positioned at its centre.

6.11 Chapter Summary

This chapter presented the methods used to investigate the dynamic responses of the W2Power FOWT under combined wave-current conditions. The W2Power FOWT model with a pair of NREL 5 MW WTGs was described. Based on the Airy wave theory, two WCI models were developed to account for current interaction with regular and irregular waves.

Furthermore, a comprehensive framework was established to perform aero-hydro-servo-elastic analyses in OrcaFlex, and it incorporates wave-current interaction in coupled analyses. This chapter laid the groundwork for the following two chapters. Chapter 7 will present the results of model validation, and Chapter 8 will provide key findings from additional simulations under different WCI scenarios.

Chapter 7

Numerical Modelling of FOWTs: Models Validation

7.1 Introduction

This chapter presents an extensive validation study comparing the experimental models developed in Part II with the numerical models introduced in Chapter 6. The aim is to evaluate the accuracy and reliability of the coupled model of the W2Power floating wind system, as well as the simulations of the developed wave-current interaction models. Such validation is crucial to ensure that the developed numerical models can reliably predict the dynamic responses of the system under various environmental conditions, thereby fulfilling the thesis's aims and objectives outlined in Section 1.7.

Given that Chapters 4 to 6 aimed to address the research questions by assessing the influence of the MUFOWP concept on structural responses and mooring system dynamics, the impact of tides on the design process, and the effects of wave-current interaction on the dynamic behaviour of the entire floating system, the validation study presented herein is essential. This validation confirms the reliability of the developed numerical models and ensures they can effectively inform the design and optimisation of FOWTs in real-world scenarios.

7.2 Environmental Conditions

For validation purposes, the environmental conditions from the experimental setup are employed to replicate numerical data. Load cases from the experimental campaigns are simulated using the developed numerical models outlined in Chapter 6. The load cases for regular and irregular waves are detailed in Tables 4.5 and 4.6, respectively, and the characteristics of the current are given in Table 4.7.

The tested loading configurations are visually depicted in Figure 4.15. Note that the direction of the current remains constant at 0°, with waves approaching the floating platform from 0° (following the current) and from 180° (opposing the current).

Using the numerical models developed in Chapter 6, comprehensive simulations were performed for two scenarios, with and without wave-current interaction, showcasing the impact of WCI on the system.

The validation process involved upscaling the measured data from the FloWave experiments to the prototype scale using the Froude law (Froude, 1868). This upscaling allowed for a comprehensive evaluation of the experimental data in a manner that aligned with the conditions of the reference site, Canary-I, whose specifications and environmental conditions are provided in Figures 4.9 and 4.10 and Table 4.4. Thus, all experimental data presented here are presented in prototype scale (see Table 4.1). Further detailed information can be found in Section 4.4.

Furthermore, validations of the floating system are categorised into three main parts:

I) assessment of the system responses of the floater-towers-nacelles-turbines model with and without moorings in calm water,

II) assessment of the dynamic responses of the fully-coupled model (floater-mooring-towers-nacelles-turbines) under pure waves and pure current,

III) and assessment of the fully-coupled W2Power model in combined wave-current environments. Additionally, the accuracy of the developed wave-current interaction models will be validated to assess their capability in predicting the dynamic responses of FOWTs.

7.3 Validation in Calm Water

7.3.1 Free-Decay and Static Pull-Out Tests

Prior to conducting tests with wave and current loading, free-decay and static pull-out tests were performed to identify the W2Power system's dynamic characteristics in calm water. Firstly, experimental free-decay tests were carried out for the surge, sway, heave, and pitch DoFs. Herein, the platform was forced to initial offset positions in calm water and then released to oscillate. Subsequently, the displacements of the FOWT during the free-decay tests were recorded by the motion capture system.

It should be noted that considerable efforts have been made to ensure that the examined DoF was excited without cross-excitation for other DoFs. However, free-decay tests for the sway, roll, and yaw DoFs were not conducted due to the difficulty of applying an initial offset in these DoFs without exciting the other degrees of freedom, compounded by the relatively large scale of the physical model (1:40).

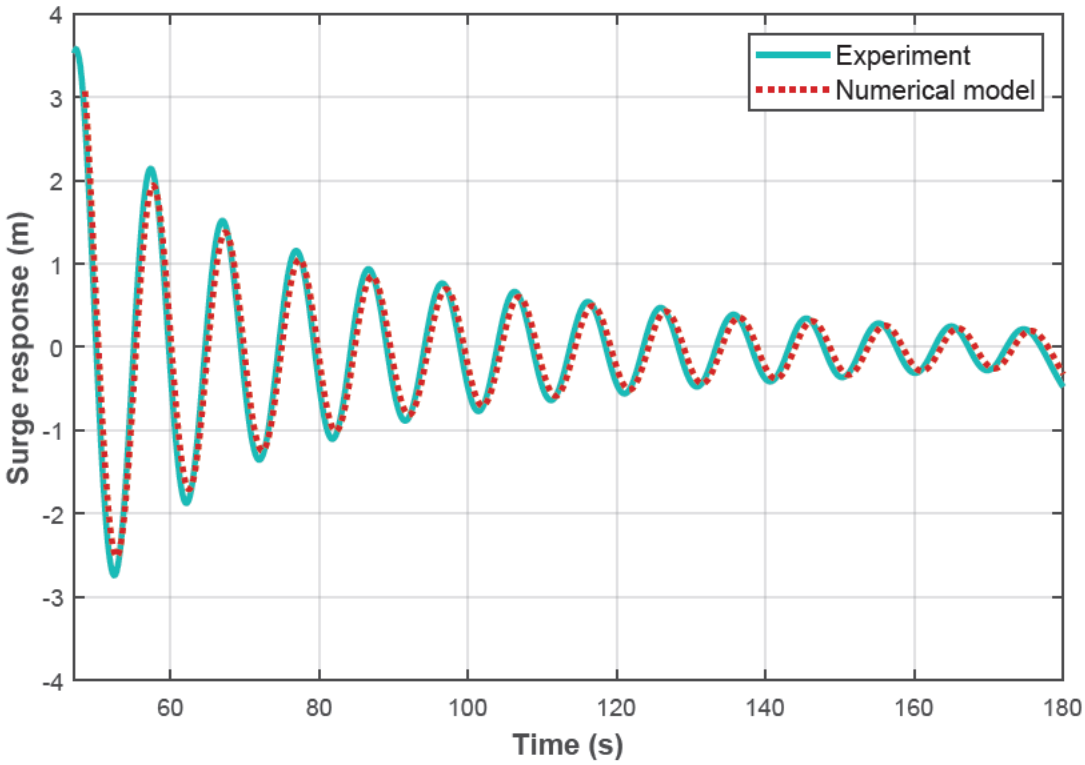

Figure 7.1: Time history of free-decay tests in still water. Validation of measurements against numerical simulations for surge response.

Comparative analysis between the FloWave data and OrcaFlex simulations for the free-decay tests in surge, heave and pitch DoFs are, respectively, presented in Figures 7.1 to 7.3. The results reveal a good agreement in both the amplitude and period of the oscillations between the measured and numerically predicted motion responses.

However, small differences were observed at the beginning of the decay tests, particularly in the heave and pitch DoFs, with the two curves obtaining the same form after the second oscillation of the platform. For instance, the numerical simulations slightly underestimated the surge motion response by about 10% (Figure 7.1). Conversely, overestimations of about 13.5% and 17% were observed for heave and pitch, respectively (Figures 7.2 and 7.3). These overestimations can have implications for the stability of the platform, potentially affecting the dynamics of the entire floating system under similar conditions. Such variations in damping can be attributed to the assumed drag coefficients, necessitating further investigation.

Phase differences are observed between experimental and numerical results at the beginning of the tests and persist throughout the time histories. Specifically, this phase difference is seen in the surge response (Figure 7.1), with numerical simulations lagging, and in the heave response (Figure 7.2), with the experiments lagging.

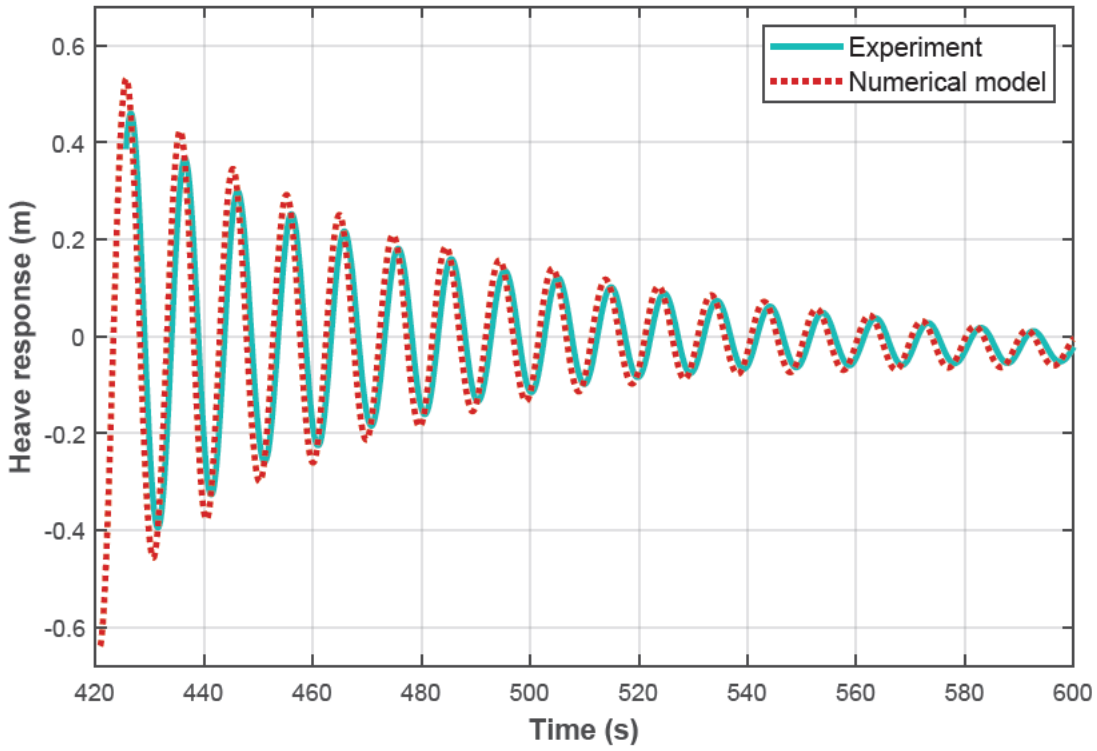

Figure 7.2: Time history of free-decay tests in still water. Validation of measurements against numerical simulations for heave response.

These phase discrepancies can be attributed to various factors, such as initial conditions and setup differences between the experimental and numerical models and uncertainties in experimental data. The measurement accuracy of the Qualisys system is assumed to be ±1% mm, which translates to approximately 0.04 m when upscaled to full scale. Furthermore, the inherent complexities of fluid-structure interactions (Gabl et al., 2019, 2021). Such phase differences might impact the reproducibility of certain load cases. Thus, further efforts are required to minimise these discrepancies and enhance the accuracy of the models.

Despite these initial discrepancies, the oscillations eventually converge, showcasing consistency in the period of the motion responses. To determine whether these differences are phase discrepancies or merely temporal offsets, an alignment of the first peak of the oscillations was attempted. This method allowed for a clearer comparison of the subsequent motion responses. The alignment shown in Figures 7.1 to 7.3 revealed that the overall behaviour of the system, particularly in terms of the oscillation periods, tends to be consistent between the experimental and numerical results as the tests progress. Therefore, the phase differences observed in the surge and heave responses are treated as transient effects that diminish over time as the system reaches a more stable state (Devolder et al., 2018).

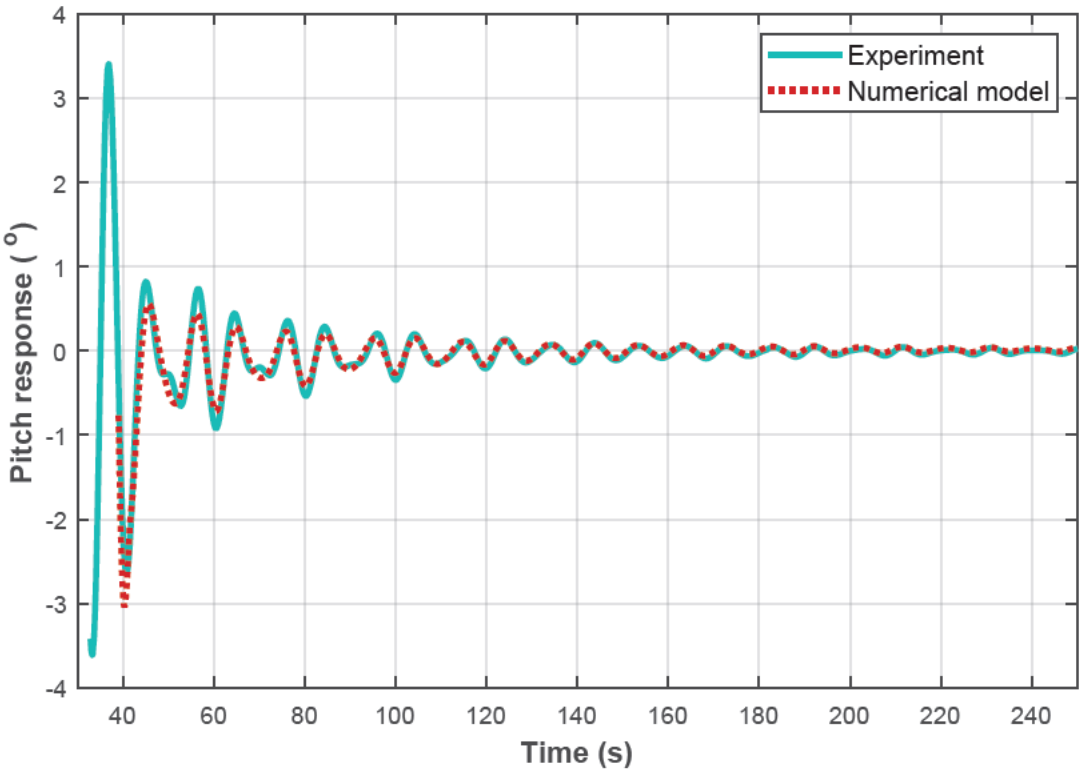

Figure 7.3: Time history of free-decay tests in still water. Validation of measurements against numerical simulations for pitch response.

Furthermore, tests with mooring lines attached were conducted and detailed in Appendix C.1. Similarly, minor disparities between experimental and numerical outcomes were noted (see Figure C.1). Apart from the assumed coefficients, these differences could also stem from technical uncertainties during the tests, such as potential human errors.

7.4 Validation in Current and Wave Environments

To further validate the accuracy of the developed model encompassing the floater-mooring-tower-nacelles-rotors, investigations were conducted under pure current and pure wave conditions. Comparisons between numerical simulations and experiments were made for the same loading conditions.

7.4.1 Dynamic Responses under Current

The system dynamics under current loads are scrutinised, with Figures 7.4 to 7.6 showing the validation results.

7.4.1.1 Mooring Dynamics

Figure 7.4 compares the time histories of mooring loads at the fairleads of the three lines (A, B, and C) between OrcaFlex simulations and FloWave measurements. Note that the current has a speed of 0.8 m/s, hitting the platform from the front side (column B).

Overall, mooring line A experienced lower loads (i.e. 928.5 N) compared to lines B and C (i.e. 1328.5 N), as it is positioned on the downwind side and aligned with the direction of the current stream. The comparison revealed a general agreement between experimental and numerical results, particularly in lines A and B.

However, a discrepancy between the numerical and measured load of mooring line C is noticeable. Herein, the measured load is slightly higher than the simulated one. This variance can be attributed to the excessive pretension on the line (i.e. circled in blue) at the test's onset, as evident from the bottom panel of Figure 7.4. This pretension might be due to the potential misalignment of the model at the predefined position in the centre of the tank test area.

Since the tests were conducted consecutively, this misalignment may have been influenced by carryover (residual) effects from previously run sea states, underscoring the sensitivity of single-point mooring and the dynamic response of the W2Power system. Such observations highlight the need for careful consideration in future experimental setups to enhance model accuracy and reliability.

Moreover, the presence of reflected waves can prolong the settling time of the tank, with multiple reflections potentially occurring across the tank. The circular geometry of the paddles in the tank can lead to curved reflections, and paddle absorption effectiveness decreases for waves below 1 Hz (S. T. Draycott, 2017a). FloWave typically reaches a quiescent state after a period of around one to five minutes, during which reflections decrease sufficiently. However, the presence of a current can significantly alter the time it takes for reflections to dissipate significantly (Noble, 2018).

Consequently, this indicates that the presence of a current in the tank, as observed during experiments, can impact the dissipation of reflections (see Section 7.5). Depending on the direction of the current, it can either prolong or expedite the settling time of the tank. Therefore, ensuring calm water and precise repositioning of the model are necessary steps to overcome potential disturbances caused by reflections and currents during experiments.

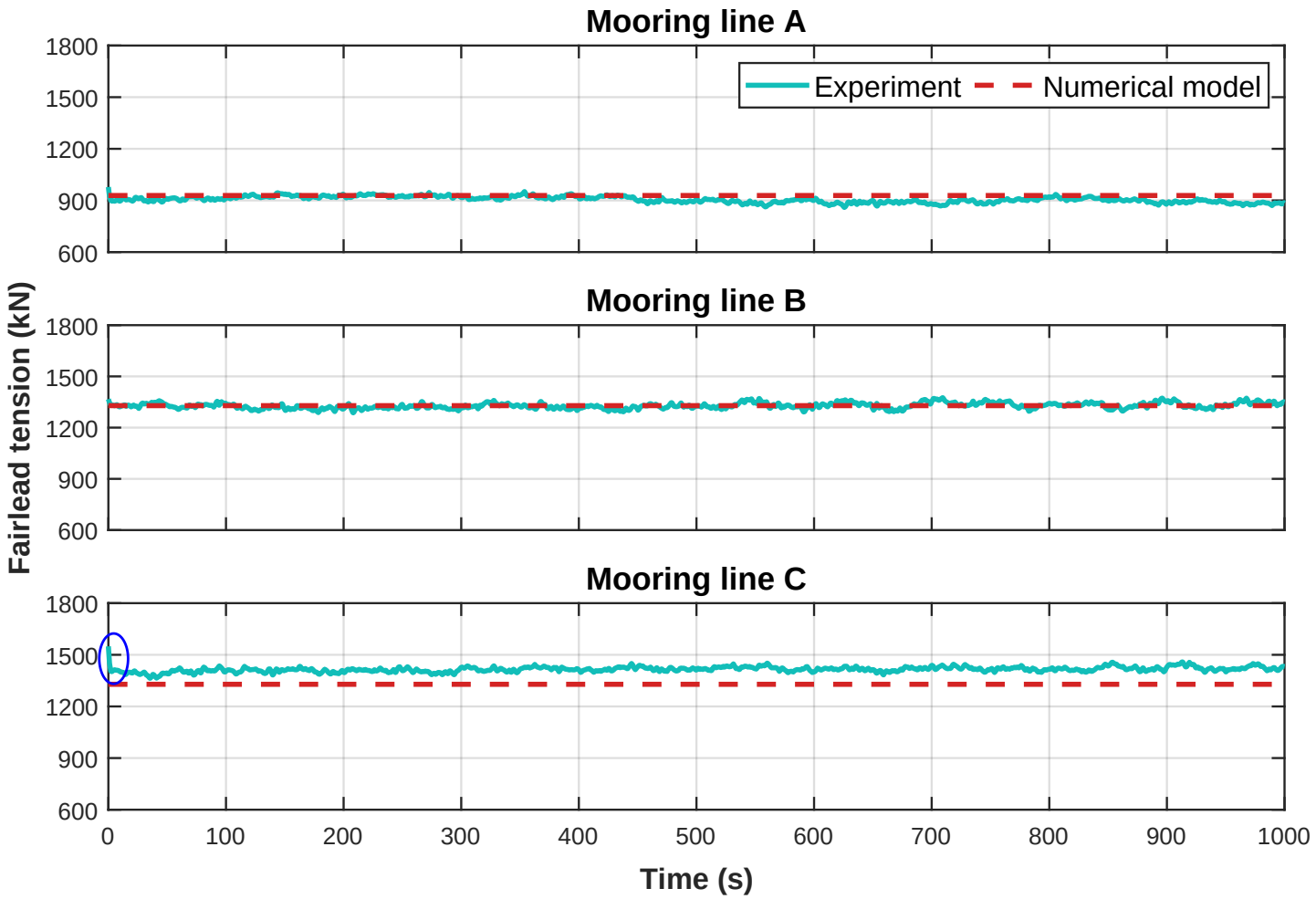

Figure 7.4: Time history of mooring dynamics under current loading at a speed (U_c) of 0.8 m/s. Validation of measurements against numerical simulations for tension at the fairleads of three mooring lines: A, B and C.

Table 7.1: Statistical comparison of mooring loads at fiarleads under currents of a speed of 0.8 m/s propagating from 0°.

Mooring line	Modelling approach	Fairlead load, (kN)			
		Min	Mean	Max	StdDev
Line A	Experiment	859.54	905.19	978.07	17.37
	Numerical	928.59	928.59	928.59	8.03×10^{-5}
Line B	Experiment	1286.64	1328.27	1375.38	16.41
	Numerical	1328.61	1328.61	1328.61	9.14×10^{-5}
Line C	Experiment	1363.60	1415.72	1549.13	14.24
	Numerical	1328.61	1328.61	1328.61	1.41×10^{-4}

In addition to the previous discussion regarding the discrepancy between the numerical and experimental mooring loads, statistical analyses of the mooring loads at the fairleads under different current loading conditions are presented in Table 7.1. This table summarises the minimum, mean, maximum, and standard deviation (StDev) values of the mooring forces for lines A, B, and C under a current speed of 0.8 m/s propagating from 0°.

From Table 7.1, it can be seen that the OrcaFlex results for line A show a constant load of 928.59 kN, while the experimental mean is slightly lower at 905.19 kN, with higher variability in the experiment (i.e. StDev of 17.37 kN). Similarly, for line B, the numerical and experimental mean loads are closely aligned (1328.61 kN vs. 1328.27 kN), though the FloWave data show higher fluctuations (e.g. StDev values ranging from 14.24 to 17.37 kN).

In the case of line C, the discrepancy noted in the discussion of Figure 7.4 is further reflected in Table 7.1. The experimental mean load is 1415.72 kN, while the numerical prediction is lower at 1328.61 kN. This difference can be attributed to excessive pretension and potential tank reflections. The higher experimental maximum and StDev values reinforce the greater variability observed in real-world tests compared to the stable numerical results. These results underscore the importance of addressing potential sources of experimental discrepancy, such as model misalignment and wave reflections, to improve the accuracy and reliability of future tests (Gabl et al., 2021).

7.4.1.2 Motion Dynamics

Motion dynamics of the system under current conditions are examined. Figures 7.5 and 7.6 present the time histories of translational and rotational motion responses, respectively. The numerical predictions closely align with the measured responses, particularly concerning surge and heave motions. This indicates a high level of agreement between the simulated and experimental data, suggesting the numerical model accurately captures the system's dynamic behaviour under current loading.

However, some fluctuations are observed in the sway motion, with the measured response slightly deviating from the numerically predicted. This discrepancy could be attributed to experimental uncertainties or complexities not fully captured by the numerical model.

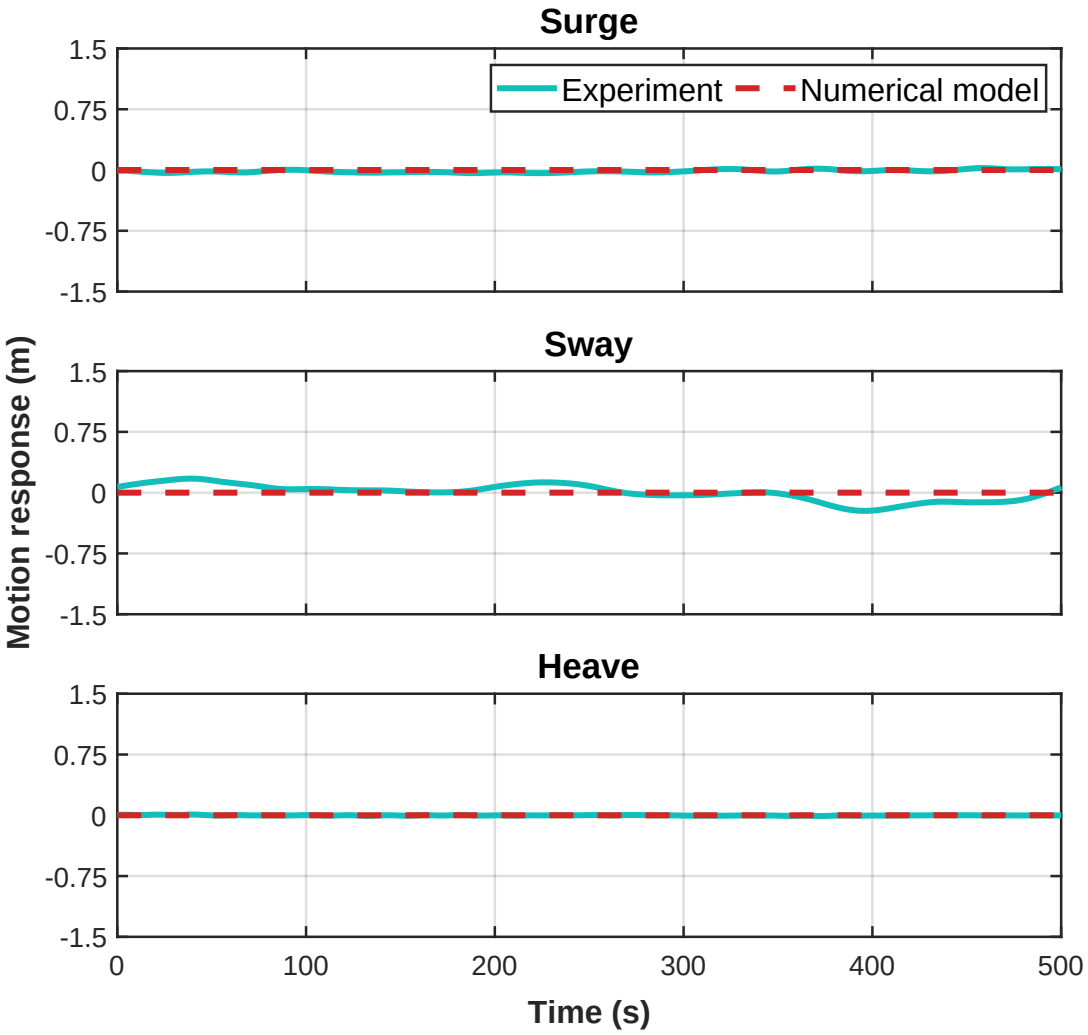

Figure 7.5: Time history of translational motion responses under pure current at a speed (U_c) of 0.8 m/s. Validation of measurements against numerical simulations for motion displacements in the surge, sway, and heave DoFs.

Additionally, the rotational and sway motion responses exhibit relatively low fluctuations, further corroborating the consistency between numerical predictions and experimental observations. This consistency signifies the robustness of the numerical model in simulating the complex interactions between the floating platform, mooring, and environmental loads.

Further to the time history analysis presented in Figures 7.5 and 7.6, statistical comparisons of the platform's motion responses across six DoFs under a pure current of 0.8 m/s are provided in Table 7.2 to shed light on the observed consistencies.

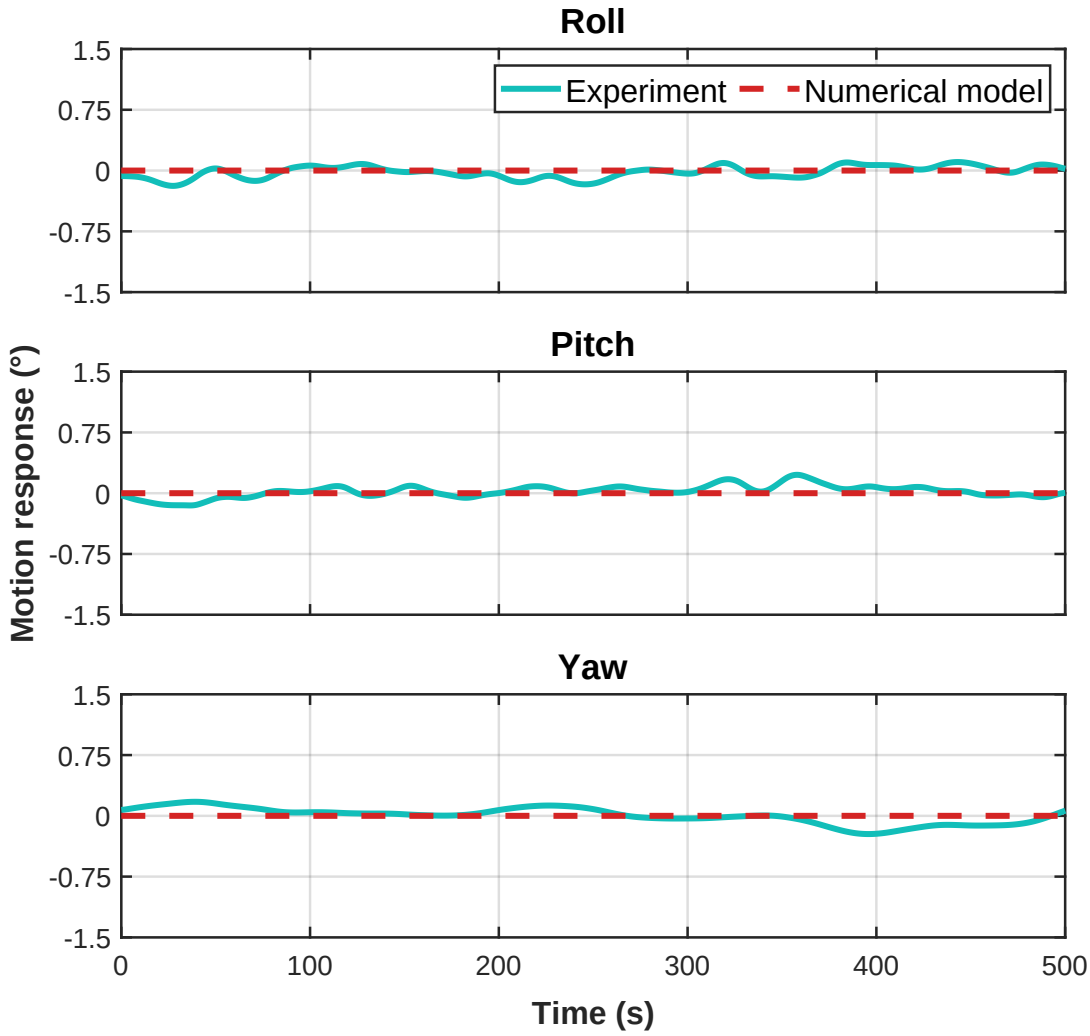

Figure 7.6: Time history of rotational motion responses under pure current of a speed (U_c) of 0.8 m/s. Validation of measurements against numerical simulations for motion displacements in the roll, pitch and yaw DoFs.

For translational motion responses (i.e. surge, sway, and heave), the OrcaFlex predictions closely align with experimental results in terms of mean values, particularly for surge and heave, with minimal discrepancies. However, the sway motion shows notable differences between the experimental and numerical models, with the FloWave data exhibiting higher variability (i.e. StDev of 1.22×10^{-1} m) compared to the numerical results. As further evident in Figure 7.5, such inconsistency indicates that the sway motion is more sensitive to experimental uncertainties or effects not fully captured by the numerical model.

For rotational motion responses (i.e. roll, pitch, and yaw), the numerical model also demonstrates strong agreement with experimental data, particularly the mean values, with minimal fluctuations observed in both roll and pitch. Though yaw shows relatively larger discrepancies in the tank results (StDev of $1.22\times10^{-1}{}^{\circ}$), further emphasising the complexity of rotational

dynamics under current loading. Thus, the statistical data reinforces the accuracy of the numerical model in predicting platform motion, although certain discrepancies, particularly in sway and yaw, highlight areas where experimental uncertainties or model refinements could improve precision.

Table 7.2: Statistical comparison of platform motion responses in six DoFs (translational and rotational) under currents of a speed of 0.8 m/s propagating from 0°.

Motion DoF (response: m, °)	Modelling approach	Platform response		
		Mean	Max	StdDev
Surge (m)	Experiment	2.01×10^{-16}	5.65×10^{-2}	2.48×10^{-2}
	Numerical	1.12×10^{-6}	4.58×10^{-6}	1.48×10^{-6}
Sway (m)	Experiment	-2.40×10^{-2}	1.73×10^{-1}	1.22×10^{-1}
	Numerical	-2.34×10^{-7}	1.76×10^{-7}	2.00×10^{-7}
Heave (m)	Experiment	1.36×10^{-4}	9.67×10^{-3}	2.97×10^{-3}
	Numerical	6.8×10^{-7}	2.78×10^{-6}	8.97×10^{-7}
Roll (°)	Experiment	-9.17×10^{-3}	1.59×10^{-1}	6.70×10^{-2}
	Numerical	9.01×10^{-7}	1.55×10^{-6}	5.25×10^{-7}
Pitch (°)	Experiment	-9.23×10^{-3}	2.27×10^{-1}	8.64×10^{-2}
	Numerical	8.99×10^{-7}	3.66×10^{-6}	1.18×10^{-6}
Yaw (°)	Experiment	-2.40×10^{-2}	1.73×10^{-1}	1.22×10^{-1}
	Numerical	7.90×10^{-7}	5.30×10^{-5}	2.37×10^{-5}

Overall, the close agreements between numerical and experimental results shown in Figures 7.5 and 7.6, and Table 7.2 demonstrate the reliability of the developed model in accurately predicting the motion and mooring dynamics of the W2Power FOWT system under current conditions.

7.4.2 Dynamic Responses under Waves

7.4.2.1 Response Due to Regular Waves

Numerical simulations were performed to examine the system's dynamics under regular wave conditions defined in Table 4.5. These simulations are then compared with tank measurements. Figure 7.7 displays the time histories of mooring loads for load case 1 (LC1), characterised by a wave height of 4.63 m and a period of 20 s. Note that the waves propagate from the direction of the current, resulting in varied responses in mooring loads across the lines.

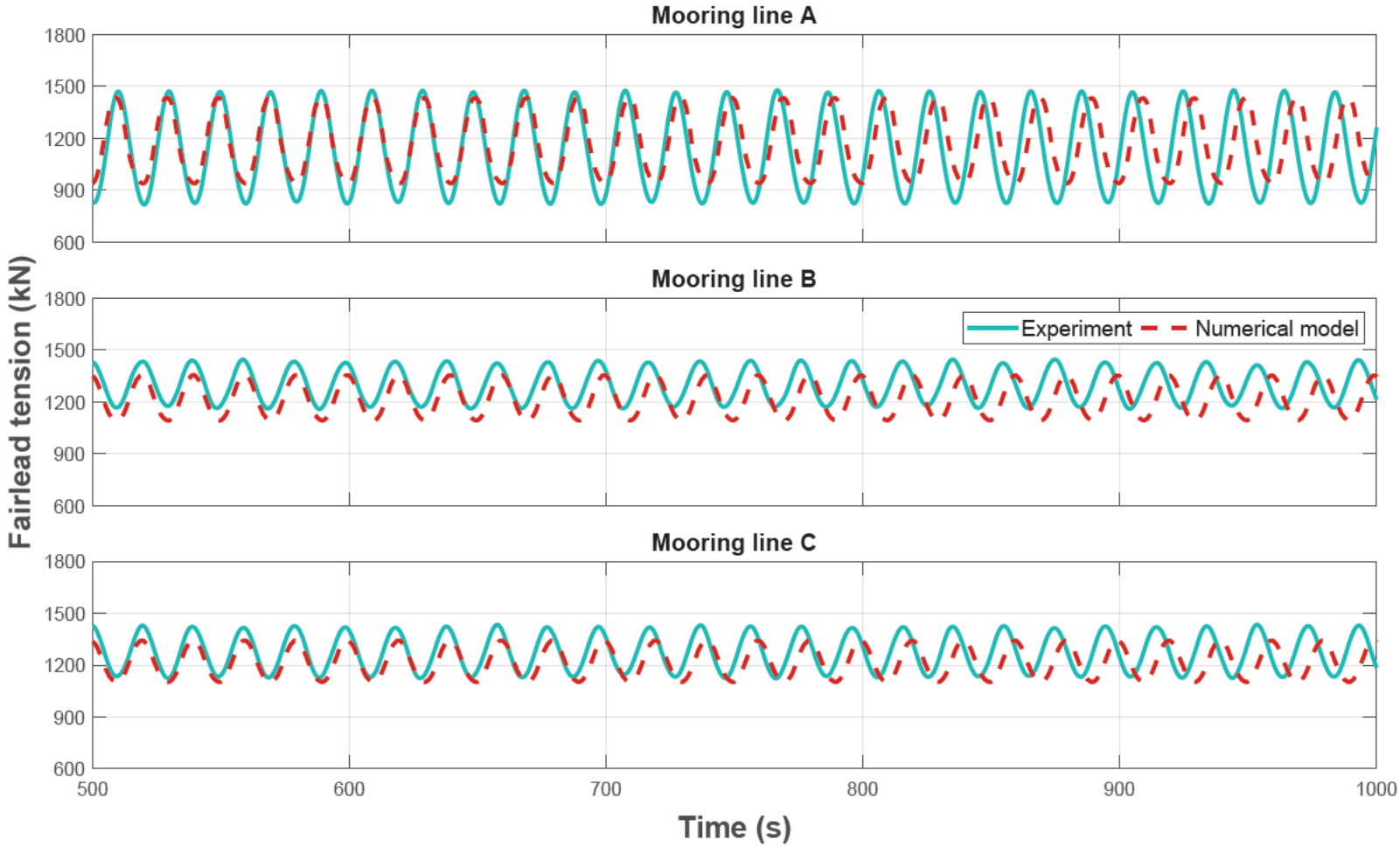

Figure 7.7: Time history of mooring dynamics under a regular wave load case (LC1) of H = 4.63 m and T = 20 s; following waves propagate from 0°. Showing the validation of measurements against numerical simulations for tension at the fairleads of three mooring lines: A, B and C.

Figure 7.7 reveals a distinctive pattern wherein the leeward mooring line (line A) experiences a slightly lower mean load compared to the windward lines (lines B and C) due to the platform's drift that induced by the waves towards the positive surge. This drift effect leads to subtle differences in mooring loads among the lines. The differences in mean loads among mooring lines A, B, and C can be influenced not only by the platform drift induced by waves but also by variations in pretensions resulting from the mooring configuration.

The pretensioning plays a key role in establishing initial tensions in the mooring lines to counteract environmental loads. Mooring lines with higher pretensions are likely to exhibit slightly higher mean loads compared to lines with lower pretensions under similar environmental conditions. Therefore, both the platform drift effect induced by waves and variations in mooring line pretensions due to the configuration contribute to the observed differences in mean loads among lines A, B, and C, depicted in Figure 7.7.

In general, a notable level of agreement is observed between the numerical predictions and experimental findings that are presented in Figure 7.7. However, the measured load slightly exceeds the predicted load, potentially due to the linear wave model utilised in OrcaFlex for generating regular waves. Additionally, there is a consistent period difference, with the numerical predictions showing greater periods than the experimental measurements for all three mooring lines.

These period differences become more pronounced from 700 s onwards in Figure 7.7. This discrepancy in periods is likely attributed to the damping value adopted in the numerical simulation, influencing the dynamic behaviour of the mooring lines. Thereby, adjusting the damping value to better match the experimental conditions can improve the agreement between numerical predictions and experimental findings, particularly in scenarios with noted load prediction discrepancies (Hall et al., 2014).

In addition to the time history analysis shown in Figure 7.7, statistical comparisons of mooring load dynamics under regular waves (LC1) are summarised in Table 7.3. These waves have a height of 4.63 m and a period of 20 s and propagate at 0°. The statistical findings reveal that line A exhibits the largest load variability, with the highest standard deviation of 221.81 kN in the experiment. This is likely due to the platform's drift induced by these following waves and pretension variations in the mooring lines.

Some discrepancies between measured and simulated loads are also seen, especially in line A. Such observations suggest that further improvements for the numerical model are needed, particularly regarding damping values and the linear wave model used. Despite this, the overall trends demonstrate good agreement between OrcaFlex predictions and FloWave experiments. The slightly higher inconsistency in experimental data may stem from the large range of data points captured during testing, reflecting the inherent complexities of structure-wave interaction.

Table 7.3: Statistical comparison of mooring loads at fiarleads under regular waves (LC1) of a high of 4.63 m and a period of 20 s; waves are following and propagating at 0°.

Mooring line	Modelling approach	Fairlead load, (kN)			
		Min	Mean	Max	StdDev
Line A	Experiment	814.47	1132.97	1518.02	221.81
	Numerical	937.01	1168.22	1439.06	181.09
Line B	Experiment	1087.34	1295.72	1476.80	93.79
	Numerical	1129.44	1217.39	1359.38	91.72
Line C	Experiment	1081.92	1273.81	1475.25	102.50
	Numerical	1099.73	1218.08	1344.96	86.43

7.4.2.2 Response Due to Irregular Waves

Comparisons between experimental and numerical results for the load case A of irregular waves, as defined in Table 4.6, are presented in Figures 7.8 and 7.9. Three scenarios of wave propagation are examined: following waves (from 0°), crossing waves (from 90°), and opposing waves (from 180°). Figure 7.8 illustrates the power spectral density of fairlead tension for mooring line A, while Figure 7.9 depicts the similar for lines B and C.

Generally, when waves strike the platform from 0° and 180°, mooring line A experiences higher loads compared to crossing waves. Waves from 0° exhibit slightly higher loads than those from 180°, demonstrating the impact of wave-structure interaction scenarios. This disparity is due to line A being aligned with the wave direction propagating from 0° and 180°, resulting in increased tension. This, in turn, highlights the importance of mooring system configuration in influencing system dynamics (Huo et al., 2023). Conversely, mooring lines B and C exhibit different behaviours, with higher PSDs observed under crossing wave conditions, while following and opposing waves result in slightly lower loads on these lines.

Under crossing waves, lower PSDs are seen in line A (Figure 7.8), while higher PSDs are observed in lines B and C (Figure 7.9). These lower and higher PSDs due to crossing waves are attributed to the oblique impact angle of the crossing waves. When waves hit the platform at an oblique angle, the total wave force on a mooring line is distributed into components based on the angle relative to the primary orientation of that line: a component parallel to the line and a component perpendicular to it. The oblique impact angle leads to a distribution of wave energy across mooring lines. The components of the wave force are spread out, affecting the concentration of energy and thus altering the peak loads and dynamic responses on any single mooring line (Xiao et al., 2014; Z. Liu et al., 2019; S. Draycott et al., 2021).

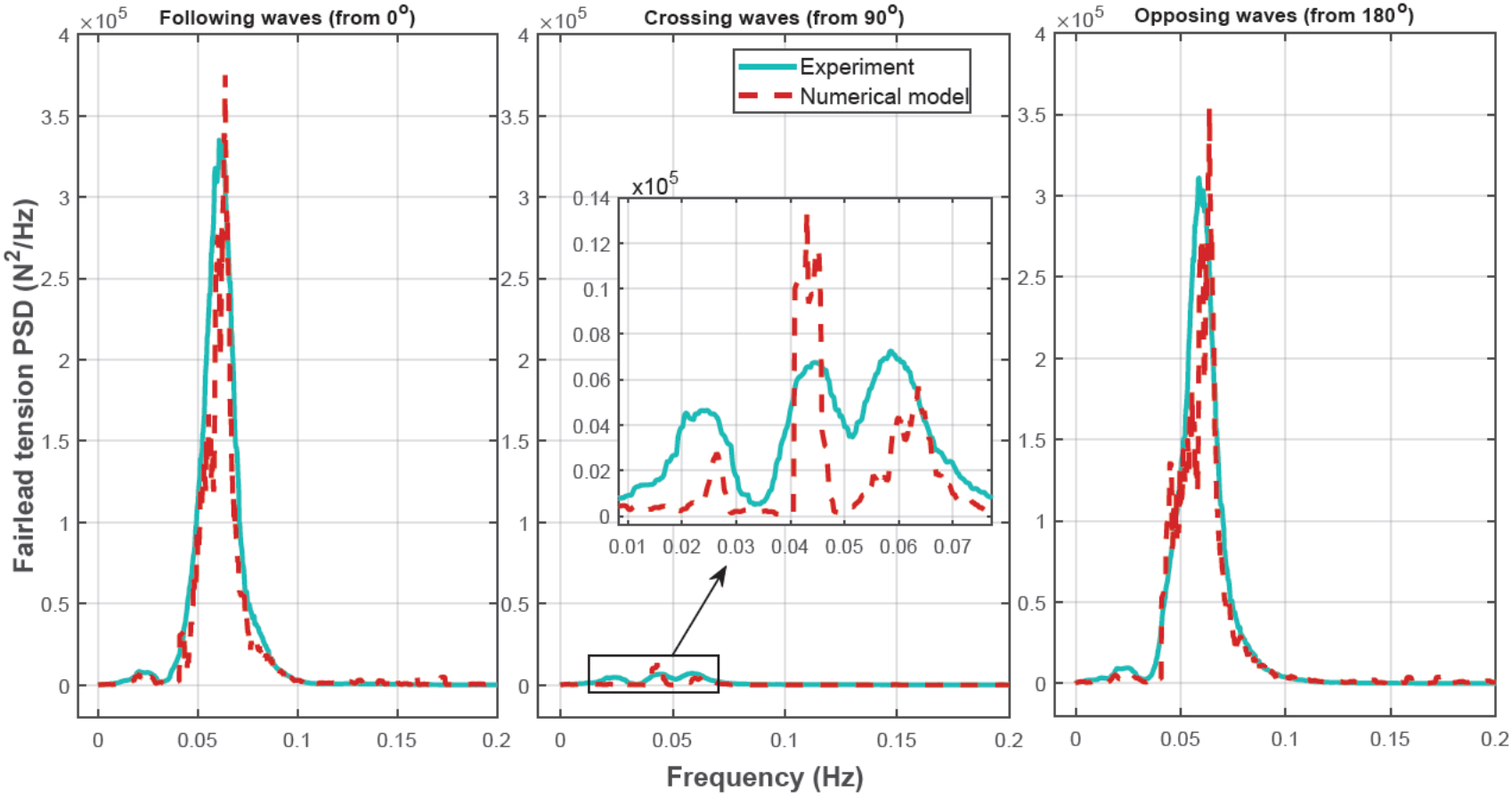

Figure 7.8: Power spectral densities of mooring dynamics under an irregular wave load case A of H_S = 4.63 m and T_P = 16.4 s. Showing the validation of measurements against numerical simulations for tension PSDs at the fairlead of mooring line A considering different propagation scenarios: (left) following waves from 0°, (middle) crossing waves from 90°, and (right) opposing waves from 180°.

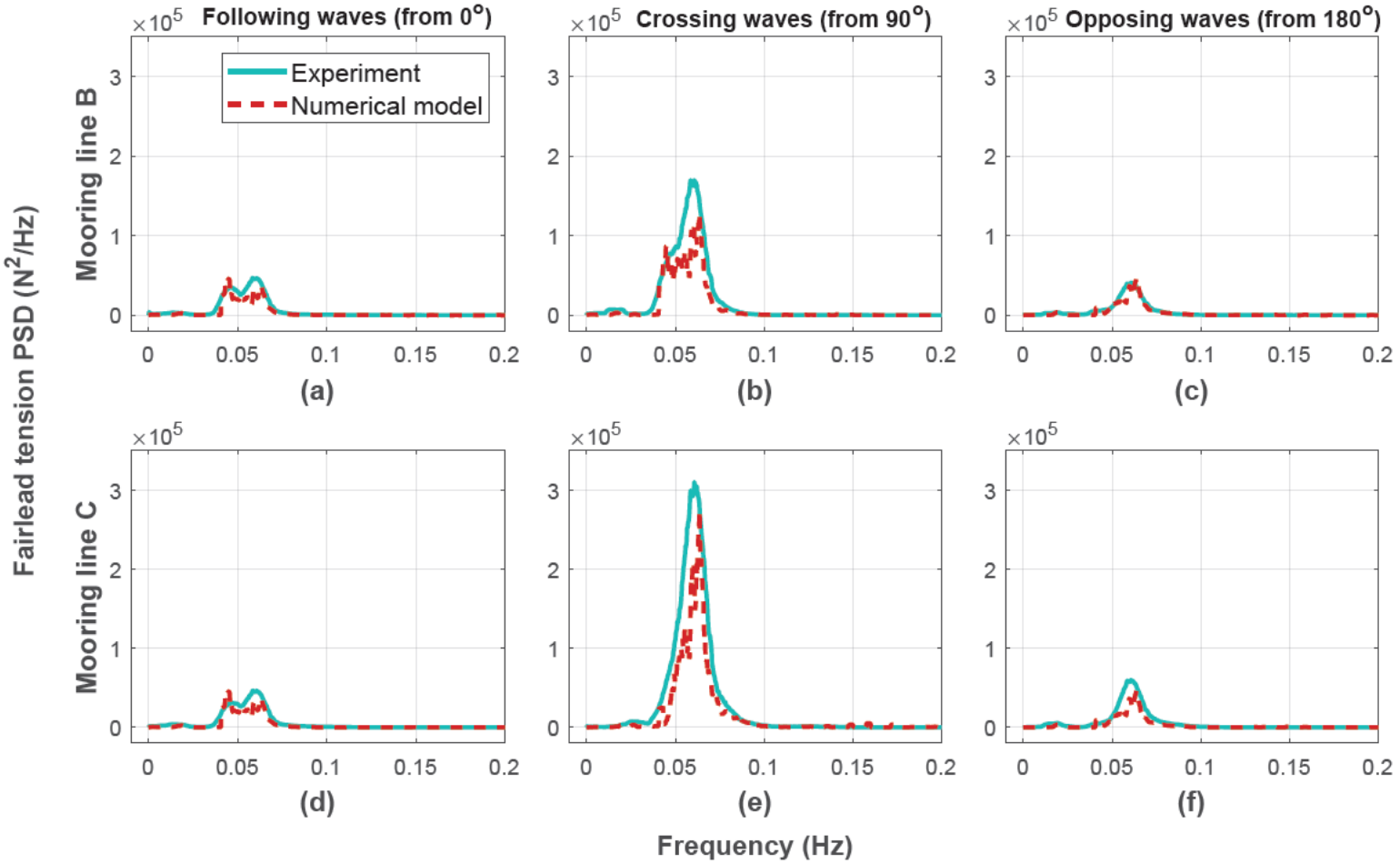

Figure 7.9: Power spectral densities of mooring dynamics under an irregular wave A of H_S = 4.63 m and T_P = 16.4 s. Showing the validation of measurements against numerical simulations for fairlead tension PSDs of (a-c) line A, and (d-f)line B; for different wave propagation: (left) from 0°, (middle) from 90°, and (right) from 180°.

For line A, the oblique impact induced by these crossing waves lowered its peak tension and dynamic response. Meanwhile, the oblique impact causes lines B and C to experience more dynamic interactions and, thus, higher PSDs under crossing wave conditions. In contrast, the aligned waves from 0° and 180° produce more uniform tension distribution across all lines, leading to lower loads on lines B and C. These observations highlight the importance of wave directionality in influencing mooring dynamics and system stability (M. Yang et al., 2012; Y. Zhao et al., 2019) Therefore, understanding how oblique waves affect mooring response is essential for optimising mooring design and ensuring safe operation in varying environmental conditions.

Overall, the comparisons between measured and numerically predicted PSDs generally show agreement, with similarities in the shape of power spectra at peak frequencies. Additionally, shifts in peak frequencies between measured and predicted PSDs highlight the nonlinear stiffness of the mooring system. These differences indicate that the dynamic phenomena influencing catenary chain moorings are captured in the designed mooring model (Hall & Goupee, 2015).

However, discrepancies are noted, with smaller PSDs observed in experiments for mooring line A compared to OrcaFlex predictions, while lines B and C show higher OrcaFlex predictions than tank measurements. These discrepancies are attributed to the nonlinear nature of the mooring system, particularly under stochastic wave conditions (W. Chen et al., 2021). The non-elastic characteristics of the mooring system could also influence such behaviours. Some modern mooring systems do not use traditional steel chains; instead, they employ materials like polyester or nylon, which can exhibit different dynamic responses. In this work, OrcaFlex utilises FEM models to simulate the chain mooring lines (see Section 6.6).

Moreover, scaling effects could play a role in such differences, as the experimental setup involves scaled-down subsystems that may not fully capture the complexities of full-scale dynamics (Froude, 1868; De Graaff & Eaton, 2000). These findings align with the findings of W. Chen et al. (2021), highlighting the effects of mooring line hysteresis on the dynamic response of FOWTs. Thus, further investigations into both nonlinearities and scaling factors are needed to better understand the reasons behind these discrepancies.

Delving deeper into the complete PSD profile and frequency characteristics of the dynamic responses under irregular wave conditions reveals additional insights. The frequency shifts observed in the PSDs, with experimental peak frequencies being slightly lower than those predicted by OrcaFlex, suggest the influence of mooring system hysteresis and other nonlinear dynamic effects (W. Chen et al., 2021). These shifts indicate that while the numerical model captures the primary dynamics, certain aspects, such as damping and energy dissipation, require further refinement. The full PSD analysis, not just the peak amplitudes, is crucial in understanding the overall system behaviour and ensuring accurate predictions under varying wave conditions.

7.5 Validations in Combined Wave-Current Environments

Rigorous validations were undertaken to examine dynamic responses under combined wave-current environments. These involved comparing experimental data with numerical simulations, including considerations for wave-current interaction models developed in Section 6.3. These WCI models and their implementation in the dynamics of FOWTs for the first time are validated against experiments. Figures 7.10 and 7.11 illustrate the validation of these WCI models against FloWave experiments presented in Chapter 4. Subsequently, the implications of wave-current interaction on the structural responses of the W2Power FOWT are validated and shown in Figure 7.12.

7.5.1 Validation of Wave-Current Interaction Models

7.5.1.1 Regular Wave-Current Interaction Model

In assessing the regular wave-current interaction model (Figure 7.10), the time series are compared for measured and predicted free surface wave elevations for a regular wave case (LC1) of a height of 4.63 m and a period of 20 s (see Table 4.5).

Generally, subplots of Figure 7.10 demonstrate how current influences wave profile. Notably, when the current follows the waves, an apparent reduction in wave elevation amplitude is observed, leading to a shallower wave profile (top subplot). Conversely, when the current opposes the waves, it intensifies the energy of the wave profile, which is evident in a steeper wave profile (bottom subplot).

The quality of the generated current in the tank is ensured by precise control of the impellers and turning vanes, as demonstrated by the FloWave basin's design (Robinson et al., 2015a), which ensures a developed flow profile with low turbulence, as validated in Section 7.4.1. Moreover, the measured wave profile closely aligns with the predictions of the regular WCI model. Particularly, when a following current interacts with waves, the results exhibit near identicality.

However, in cases where waves oppose the current, the WCI model slightly underpredicts the wave elevation, as shown by the measured elevation being slightly higher than the predicted one. Potential sources of error in wave probe measurements, such as gauge bending or run-up due to current, could slightly affect accuracy. However, the small deflection angle makes these effects minimal (S. T. Draycott, 2017b; Noble, 2018). These discrepancies are likely attributed to the capabilities of the current WCI models in capturing full nonlinear effects, as they are based on the Airy wave theory (Thomas, 1981; Z. Liu et al., 2016). Additionally, the presence of current induces frequency shifts due to the modified wave number.

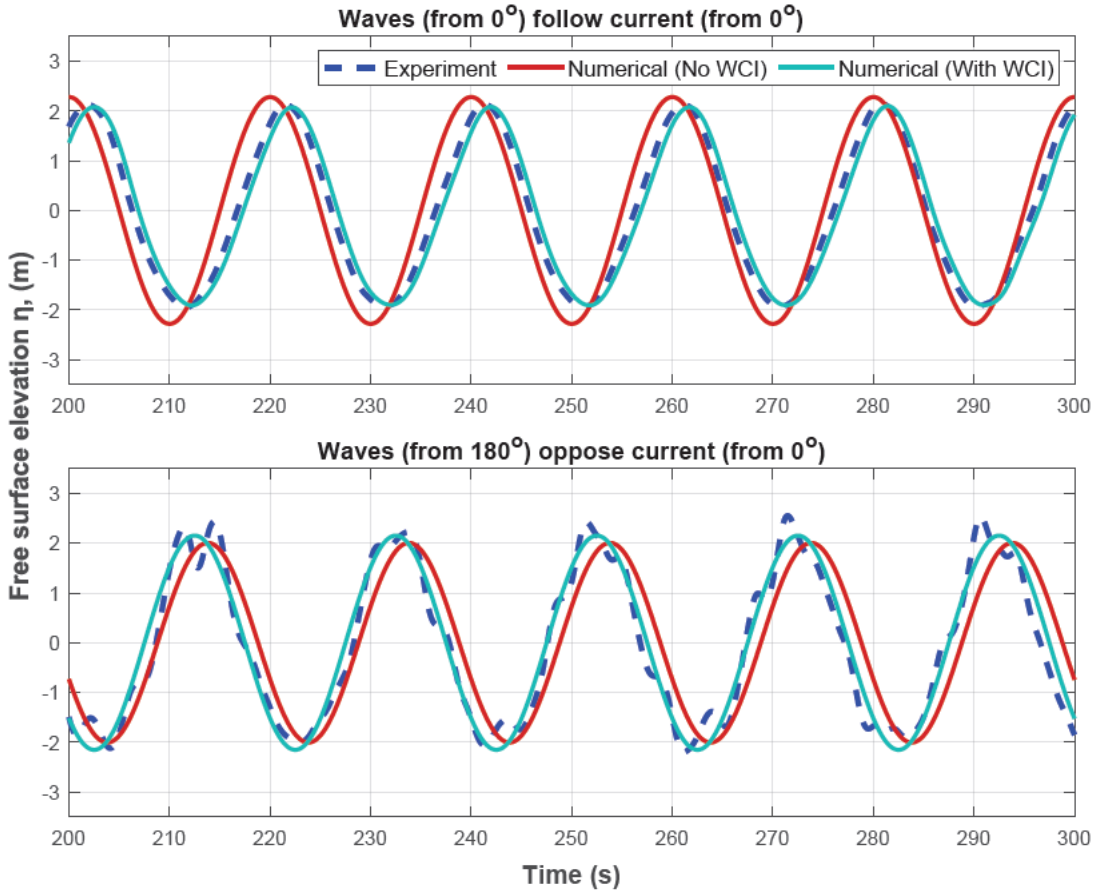

Figure 7.10: Effects of current of U_c = 0.8 m/s on free surface elevations (η) of regular waves with H = 4.63 m and T = 20 s. Showing the validation of measured wave profiles against numerically simulated profiles with and without considering wave-current interaction. Two WCI scenarios: (top) waves follow the current, and (bottom) waves oppose the current.

7.5.1.2 Stochastic Wave-Current Interaction Model

For the validation of the stochastic WCI model, Figure 7.11 presents a comparison between measured and numerically predicted wave spectra of irregular wave case A of H_S of 4.63 m and T_P of 16.4 s (see Table 4.6).

The influence of current on wave profiles is evident, with the following waves (from 0°) interacting with the current (from 0°), resulting in a reduced and less steep spectrum. Conversely, opposing waves (from 180°) interacting with the current lead to an increased and steeper spectrum.

Overall, there is good agreement between the measured and predicted spectra, particularly when the current follows the waves. However, discrepancies are observed when waves oppose the current. This is attributed to the nonlinear effects at the free surface that the current model can not fully capture. Moreover, frequency shifts occur due to the current-altered wave number.

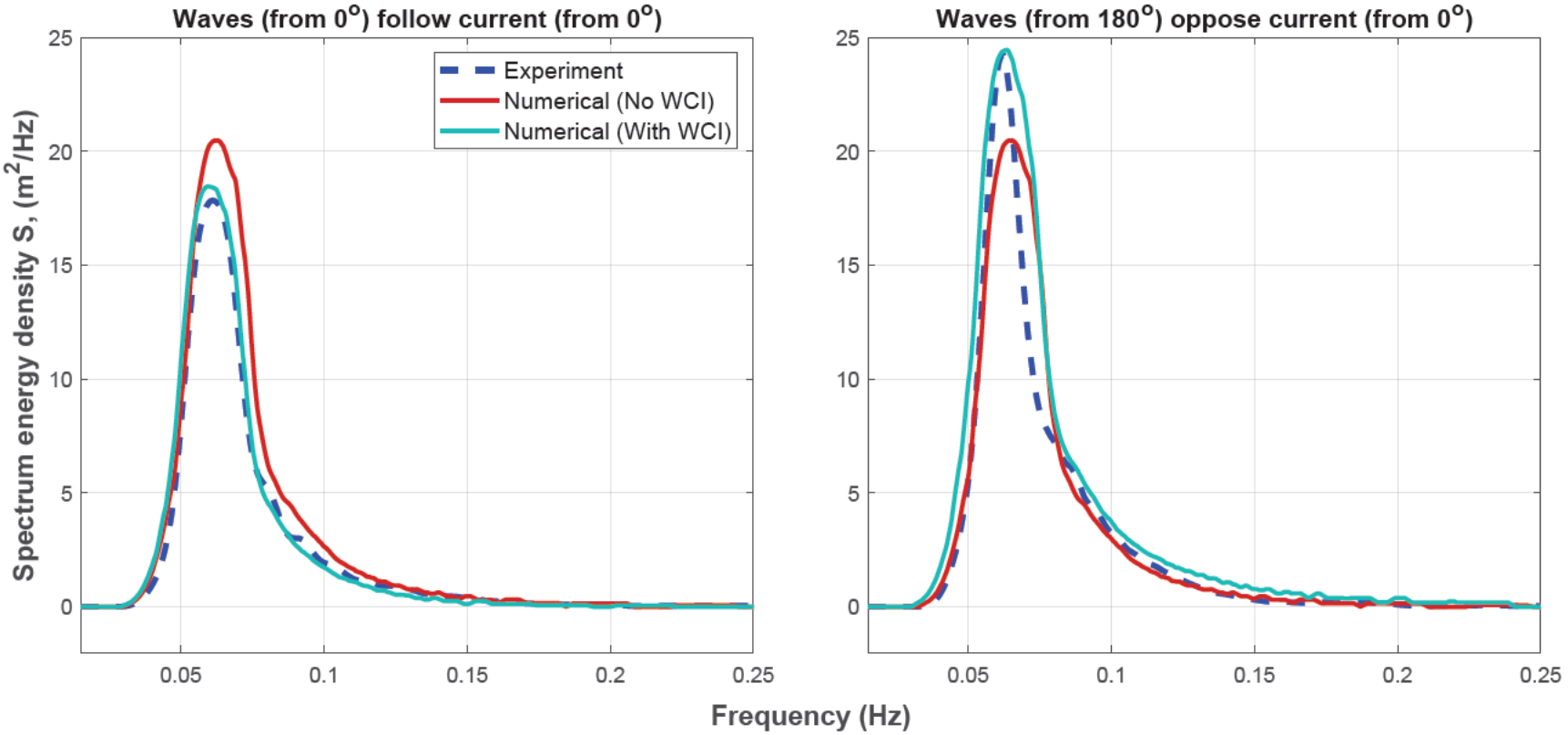

Figure 7.11: Effects of current of U_c = 0.8 m/s on spectra (S) of irregular waves with H_S = 4.63 m and T_P = 20 s. Showing the validation of measured wave spectrum against numerically simulated spectra with and without considering wave-current interaction. Two WCI scenarios: (left) waves follow the current, and (right) waves oppose the current.

7.5.2 Validation of WCI Implications for Dynamic Responses

To validate the impact of wave-current interaction on the dynamic responses of FOWTs, response amplitude operators (RAOs) were analysed. Although the time-series motions for all the tested and simulated load cases are not included here to avoid the repetition of figures, RAOs offer a comprehensive representation of the hydrodynamic characteristics of the W2Power FOWT.

Consequently, RAOs were derived from both experimental and simulation data, capturing platform motion across different DoFs. The RAOs are calculated using the following equation:

$$RAO(f) = \frac{A(f)}{A_{\text{wave}}(f)} \tag{7.1}$$

where A denotes the amplitude of the motion excited by a wave of amplitude A_{wave} and frequency f.

7.5.2.1 Implications Due to Regular WCI

For the regular wave-current model, the RAOs of FloWave measurements and numerical simulations, both with and without considering WCI, correspond to different wave periods for a wave height of 3.85 m, which are derived by the above equation, Equation (7.1), presented in Figure 7.12. Specifically, these correspond to load cases LC6-LC10, as listed in Table 4.5. Figure 7.12 compares the RAOs for surge, heave, and pitch DoFs under current interaction with following and opposing waves.

Generally, the RAO magnitudes across the surge, heave, and pitch DoFs were comparatively lower when the current interacted with following waves than when it interacted with opposing waves. These results align with the patterns found in the current-modified elevation of the free surface wave (Jonsson, 1990; J. Smith, 1997) (see Figure 7.10).

Surge RAOs exhibit a clear decrease with increasing frequency, with the highest values observed at the lowest frequency of 0.05 Hz and the lowest at the highest frequency of 0.25 Hz. Similarly, this trend is observed in pitch responses, with maximum values occurring at a frequency of 0.083 Hz (T = 12 s). However, the maximum value for heave response was observed at a frequency of 0.083 Hz when waves follow the current and at 0.05 Hz when waves oppose the current.

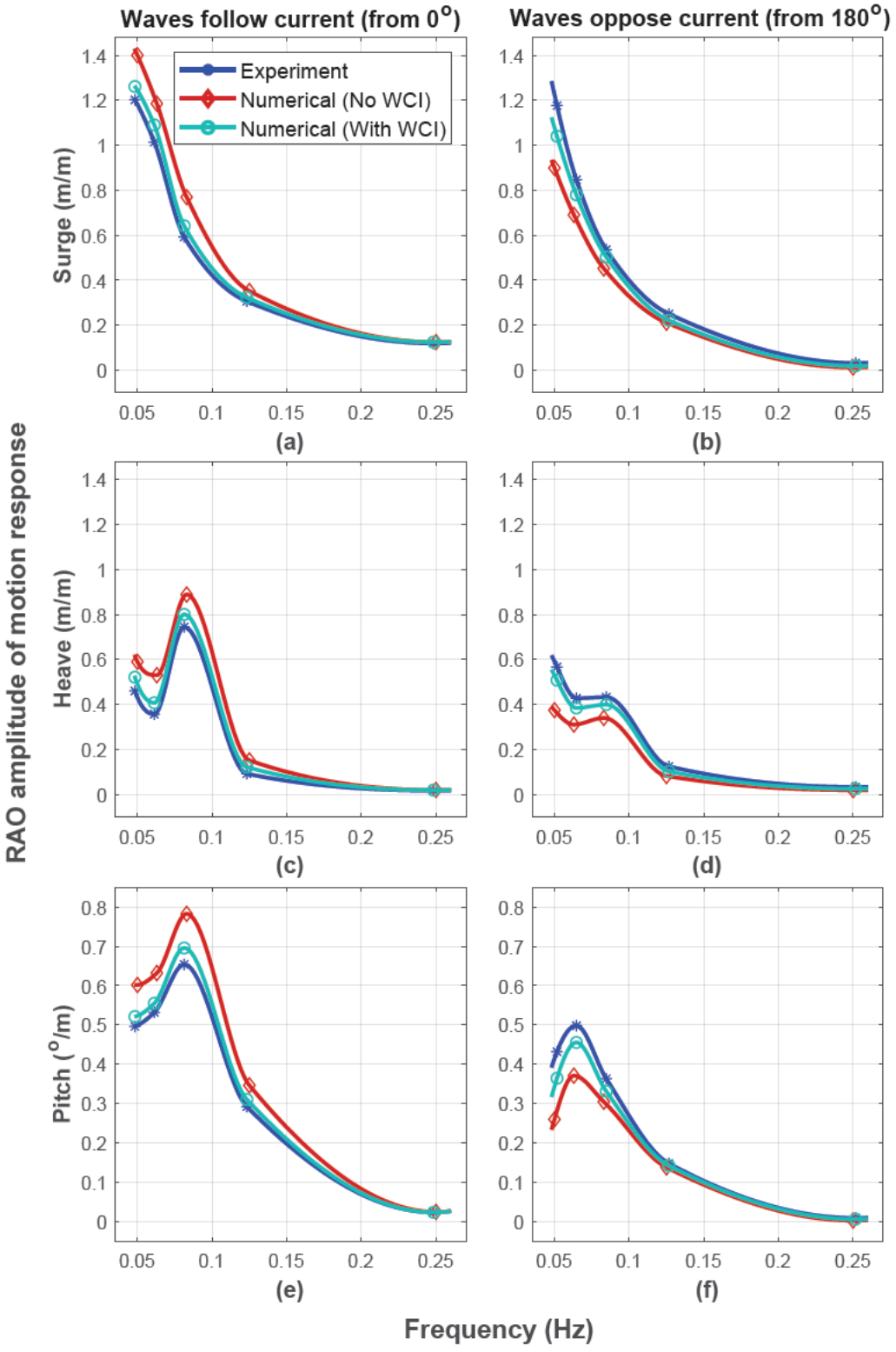

Figure 7.12: Motion RAOs under a current of U_c = 0.8 m/s of and regular waves of H = 3.85 m and different periods. Showing the validation of measured RAOs against numerically simulated ones (with and without WCI) in different DoFs: (a-b) surge, (c-d) heave, and (e-f) pitch. Waves follow (left panels) and oppose the current (right panels).

From Figure 7.12, comparisons of RAOs revealed that when waves follow (hit the platform's bow) the current, they lead to higher normalised response amplitude in surge, heave, and pitch than when waves oppose the current. This behaviour was attributed to the different wave-structure and wave-current interactions. Note that the direction of the current is constant, and it is hitting the platform from the bow side (column B); refer to Figures 4.3 and 6.2. These combined interaction effects potentially resulted in these discrepancies and thus demonstrated that it is crucial to consider WCI in the numerical simulations of FOWTs to accurately assess their dynamic performance (H. Zhang et al., 2022).

Furthermore, the comparison of numerically predicted RAOs with and without WCI against the measured ones indicated that the numerical simulations with the incorporation of WCI agreed relatively well with experimental RAOs, while those without the inclusion of WCI did not. As can be seen from Figure 7.12, the absence of WCI in numerical modelling led to overestimating motion responses when waves followed the current (left subplots: a, c and e). Conversely, despite variations in wave-structure interactions, underpredictions were observed when waves opposed the current (right subplots: b, d and f).

In order to assess the accuracy of the developed models, relative errors are further investigated to provide confidence in the numerical predictions. The percentage of the relative error is calculated as:

$$\text{Relative error (\%)} = \left(\frac{X_{\text{Exp}} - X_{\text{Num}}}{X_{\text{Num}}} \right) \times 100 \tag{7.2}$$

where X_{Exp} represents the experimental (measured) value, and X_{Num} is the numerically predicted value, which is predicted with and without considering the WCI. Subsequently, for the surge, heave, and pitch motion responses shown in Figure 7.12, the relative errors are calculated and provided in Tables 7.4 to 7.6.

The analysis revealed that the relative errors of the numerical predicted motion response with consideration of WCI were lower than those when WCI was not incorporated in the simulations. Thus, this indicates the capability of WCI models to predict accurate responses that closely align with the measured ones. Notably, small relative errors were observed at low frequencies, which are attributed to the low energy in the wave at the specified periods.

Consequently, the inclusion of WCI did not significantly impact the relative errors at low frequencies, demonstrating good agreement between the WCI models and the tank measurements compared to the predictions when WCI was not included. At low frequencies, the wave energy is insufficient to induce significant interaction effects, leading to minimal discrepancies between the two models.

Table 7.4: Relative error percentages of numerically predicted surge motion RAOs with and without consideration of wave-current interaction in regular seas.

Frequency [Hz] (Period [s])	Relative error [%] (Waves follow current)		Relative error [%] (Waves oppose current)	
	Numerical (No WCI)	Numerical (With WCI)	Numerical (No WCI)	Numerical (With WCI)
0.25 (4)	4.65	4.02	-75.58	-38.25
0.13 (8)	12.99	5.33	-18.33	-12.76
0.08 (12)	23.01	7.72	-18.46	-6.60
0.06 (16)	14.44	6.97	-22.61	-8.65
0.05 (20)	14.17	4.72	-30.84	-13.09

Table 7.5: Relative error percentages of numerically predicted heave motion RAOs with and without consideration of wave-current interaction in regular seas.

Frequency [Hz] (Period [s])	Relative error [%] (Waves follow current)		Relative error [%] (Waves oppose current)	
	Numerical (No WCI)	Numerical (With WCI)	Numerical (No WCI)	Numerical (With WCI)
0.25 (4)	13.45	4.22	-75.65	-31.94
0.13 (8)	39.54	24.62	-51.87	-21.73
0.08 (12)	16.27	7.00	-27.23	-8.29
0.06 (16)	32.75	12.45	-37.72	-11.26
0.05 (20)	22.05	11.76	-51.45	-11.63

Table 7.6: Relative error percentages of numerically predicted pitch motion RAOs with and without consideration of wave-current interaction in regular seas.

Frequency [Hz] (Period [s])	Relative error [%] (Waves follow current)		Relative error [%] (Waves oppose current)	
	Numerical (No WCI)	Numerical (With WCI)	Numerical (No WCI)	Numerical (With WCI)
0.25 (4)	8.16	4.26	-67.48	-30.90
0.13 (8)	15.67	5.90	-7.12	-3.84
0.08 (12)	16.45	6.00	-19.25	-9.70
0.06 (16)	15.83	4.16	-34.30	-9.39
0.05 (20)	17.55	4.80	-66.18	-18.50

The low energy at these frequencies suggests reduced cyclic loading on the mooring lines and tower, potentially lowering fatigue loads and extending the components' fatigue life under these conditions. Note that the frequencies provided in Tables 7.4 to 7.6 refer to the wave periods of corresponding load cases in regular seas, specifically LC6-LC10 from Table 4.5.

For instance, when waves follow the current, the relative error at a frequency of 0.083 Hz for the surge motion was found to be 7.72% when WCI was included, whereas it was 23.015% (maximum) when WCI was not considered. On the contrary, when waves oppose the current, the inclusion of WCI led to a relative error of -6.595% with respect to the FloWave experiments, while the non-inclusion of WCI resulted in a relative error of -18.45%.

The increase in relative errors observed around a period of 12 s can be attributed to higher wave energy, which enhances the effects of wave-current interaction, leading to greater discrepancies. As the frequency decreases further, the impact of WCI diminishes again, resulting in smaller differences. The negative sign denotes the underprediction of the numerical models compared to the measured values.

7.5.2.2 Implications Due to Irregular WCI

In the context of the irregular wave-current model, the RAOs obtained from the tank measurements and numerical simulations, both with and without consideration of WCI, are examined for an irregular load case (A) characterised by a significant wave height of 4.63 m and a peak wave period of 16.4 s (see Table 4.6). Likewise, employing Equation (7.1), the RAOs are derived for surge, heave, and pitch DoFs. Subsequently, the results are presented in Figure 7.13 for the three motion RAOs under current interaction with the following (left-side subplots) and opposing waves (right-side subplots).

From Figure 7.13, it can be observed that when the current interacted with the following waves, lower RAO responses are evident across the surge, heave, and pitch DoFs compared to those when the current interacted with the opposing ones. These observations are consistent with the trends observed in Figure 7.11 for the current-altered wave spectra (Jonsson, 1990; J. Smith, 1997).

Furthermore, comparisons between experimental data and numerical simulations reveal that the RAOs predicted with consideration of WCI align well with tank measurements, while relative agreements are observed when WCI is not incorporated. Notably, the inclusion of WCI in the numerical simulations accurately predicts the system dynamics at low and peak frequencies, as demonstrated by the agreement of these predictions with measured RAOs. While these findings are specific to load cases LC6-LC10 (Table 4.5), they suggest potential generalisability to similar load cases due to the consistent alignment of predictions with experimental data. However, further validation across a broader range of conditions is needed to confirm the generalisability and applicability of the findings beyond the specific load cases investigated.

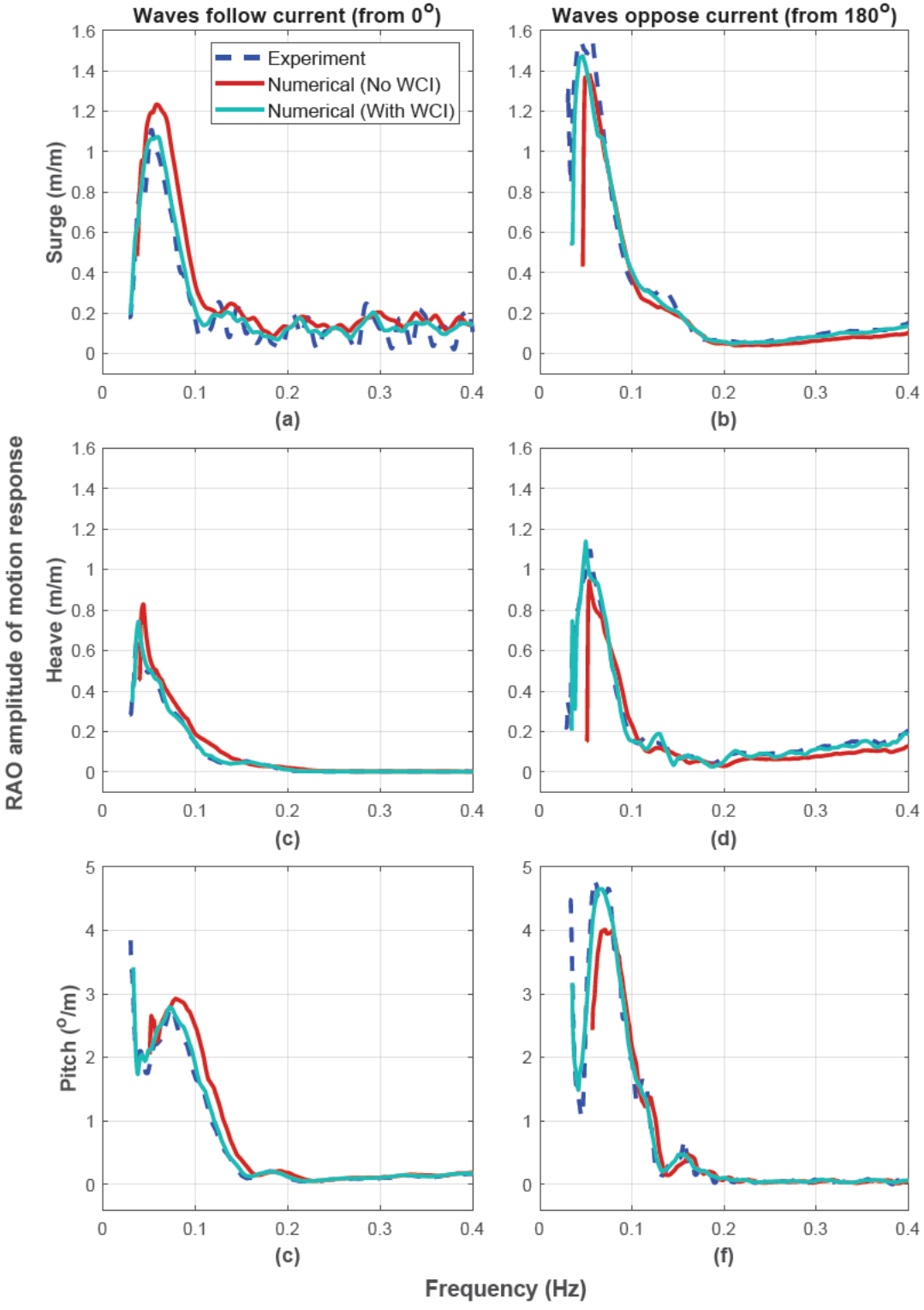

Figure 7.13: Motion RAOs under a current of U_c = 0.8 m/s of and irregular waves of H_S = 4.63 m and T_P = 16.4 s. Showing the validation of measured RAOs against numerically simulated ones (with and without WCI) in different DoFs: (a-b) surge, (c-d) heave, and (e-f) pitch. Waves follow (left panels) and oppose the current (right panels).

Conversely, the absence of WCI in the numerical simulation led to an overestimation of RAOs when waves follow the current, and underpredictions are observed when waves oppose the current. These observations align with expectations and the results shown in Figure 7.11, as the changes in wave height and wavelength induced by the current affect the hydrodynamic loading on the structure. Quantitatively, the inclusion of WCI was found to decrease the peak RAOs of surge by up to 15%, heave by up to 11.5%, and pitch by up to 5% when waves follow the current. On the other hand, when waves counter the current, the incorporation of WCI increased the RAOs of surge by up to 6.4%, heave by up to 17.2%, and pitch by up to 13.5%.

However, inconsistencies in the increase and decrease percentages of the same motion DoF are detected. These inconsistencies are primarily attributed to the nonlinearities of the wave-current interaction and are further compounded by the effects of different wave-structure interactions (Z. Liu et al., 2016). Meanwhile, for the same wave-structure interaction, consistencies between the increment and decrement percentages are observed and discussed earlier in Chapter 8 (i.e. refer to Sections 8.3 and 8.4). This discovery, in turn, emphasises the significant impact of wave-structure interactions on the dynamic response of FOWTs in the presence of current, hence highlighting the need for further investigation (R. Zhao & Faltinsen, 1989).

Moreover, frequency shifts are observed at peaks, as depicted in Figure 7.13. Despite the different structure-wave-current interactions, the current was seen to decrease the frequency when it interacted with following waves, and it increased the frequency when waves opposed its direction (Peregrine, 1976).

These frequency alterations are evident at the peaks of the spectra and are attributed to the modified wave number in the presence of current. For instance, for heave responses, when the current interacts with following waves, it decreases the peak frequency by up to 14.3%, whereas when the current interacts with opposing waves, it increases the peak frequency by up to 8%.

Overall, these findings underscore the implications of wave-current interaction on the dynamic responses of FOWTs, emphasising the need for comprehensive understanding and consideration of these interactions in numerical simulations and experimental studies (L. Chen & Basu, 2019). This highlights the importance of incorporating wave-current interaction in numerical simulations, as it influences the accuracy of predicted responses for FOWTs. Moreover, the results underline the effectiveness of WCI models in capturing the dynamic behaviour of FOWTs, particularly in scenarios where waves follow or oppose the current.

7.6 Chapter Summary

This chapter presented a comprehensive validation of the numerical models developed in Chapter 6 through comparisons with the measurements established in Part II. Across various metrics, the numerical simulations largely achieved validation against experimental data, demonstrating the robustness of the developed models.

Section 7.3 focused on evaluating the system responses of the W2Power FOWT in calm water. Validations were conducted for free-decay tests without mooring lines and pull-out tests with mooring lines attached, showing consistent agreement between measured and numerically predicted responses.

In Section 7.4, dynamic responses of the fully-coupled model of floater-mooring-towers-nacelles-turbines were assessed in pure current and pure wave environments. Section 7.5 extended this evaluation to combined wave-current environments, emphasising the importance of including wave-current interaction in FOWT simulations. Furthermore, the inclusion of wave-current interaction was found to influence the dynamic responses of the FOWT. For example, reductions in the motion RAOs were observed when waves followed the current and increased when waves counteracted the current.

The results demonstrated a high level of consistency between numerical simulations and FloWave data, indicating that the hydrodynamic characteristics were accurately reproduced by the experimental model. Moreover, the reliability of the WCI models in predicting system responses under both regular and random waves was affirmed.

On the other hand, some discrepancies between the numerical predictions and measurements were observed. Consequently, potential attributes for these disparities, such as excessive pretension on mooring lines and assumed drag coefficients, as well as technical uncertainties during testing (e.g. human errors), were explored to provide insights for future research.

After rigorously validating the developed models, the next chapter, Chapter 8, delves into further numerical investigations that consider different scenarios of structure-wave-current interaction.

Chapter 8

Numerical Modelling of FOWTs: Further Results and Discussion

8.1 Introduction

Chapter 6 provided the methodological and conceptual analyses required for comprehensive numerical modelling to investigate the implications of wave-current interaction on the structural responses of FOWTs. The preceding chapter, Chapter 7, detailed the validation of both experimental and numerical models, establishing the reliability and accuracy of the developed numerical models. Building upon these foundations, this chapter (Chapter 8) presents the findings regarding the implications of wave-current interaction on the mooring and platform motion responses of MUFOWTs and their mooring systems.

It presents and discusses the results from Chapter 6 to shed light on the effects of wave-current interaction on the dynamic responses of the W2Power platform motions and SPM system, quantitatively assessing such implications to accomplish the main aims and objectives of this work defined in Section 1.7. The chapter further analyses the presence of current and its interaction with waves on the dynamic response of nacelles.

8.2 Current Effects on Wave Fields

Wave-current interaction models established in Section 6.3 are employed to investigate the influence of current on regular and irregular waves. Two current velocities are considered: 0.3 and 0.8 m/s, and these, respectively, reflect the average and maximum current speeds at the Canary-I reference site (see Figure 4.9 and Table 4.7).

For regular waves and utilising Equations (6.8) and (6.29), current alters both the mean value and the amplitude of the wave free-surface elevation (η), whether the current is following or opposing, as shown in Figure 8.1.

For clarity, the following current refers to a flow with a velocity in the same direction as wave propagation. In contrast, an opposing current propagates in the opposite direction as the waves, resulting in a negative velocity. Furthermore, frequency shifts were observed, as evident at the peaks of both the crests and troughs of the wave.

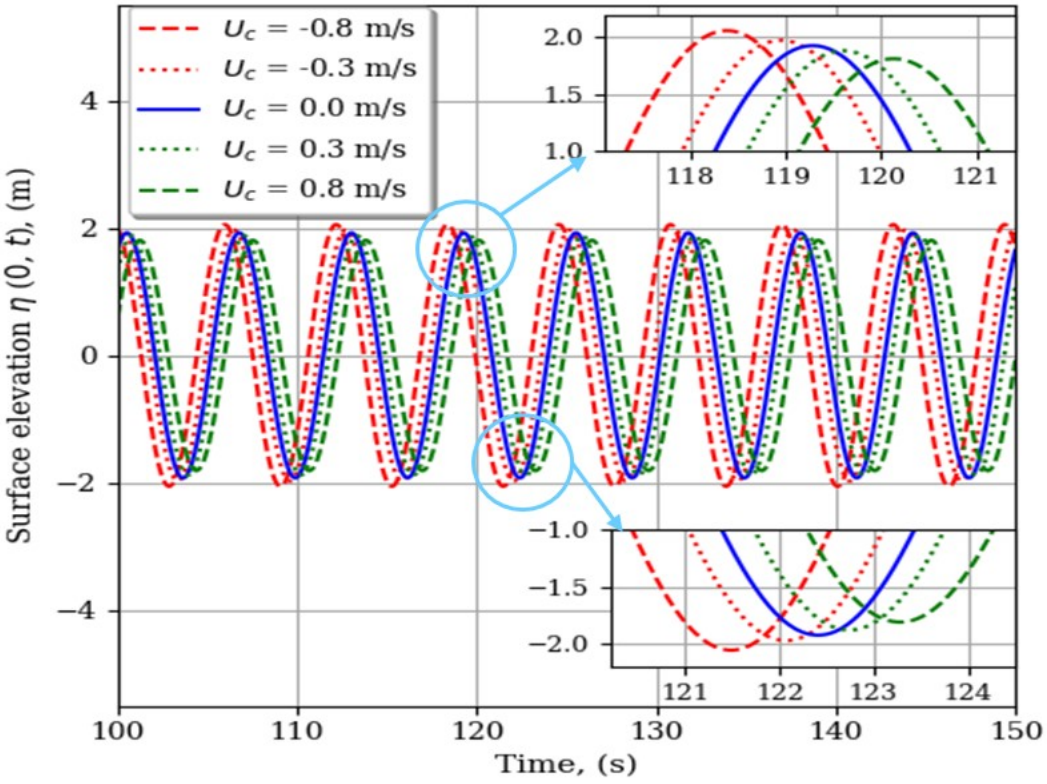

Figure 8.1: Current effect on the free surface elevation, $\eta(0,t)$, for a regular wave of $H = 3.85$ m and $T = 6.2$ s

Equations (6.32) and (6.35) are executed to generate the energy spectrum for stochastic waves with a JONSWAP spectrum of γ =1, which reduces to the Pierson-Moskowitz (PM) spectrum (Pierson Jr & Moskowitz, 1964). In turn, the spectra are obtained for four different current velocities and shown in Figure 8.2.

From Figure 8.2, it can be seen that the presence of current significantly modifies the peak value of the wave spectra. For opposing currents of speeds of -0.3 and -0.8 m/s, the peak spectrum increases by 5 and 14.2 percentage points, respectively, while it decreases by 5 and 11.2 percentage points when the currents are following. The peak frequency is also shifted, as observed in the inset plots. Increasing the absolute value of the current speed results in a more significant alteration of the peak value and changes the shape of the wave spectrum.

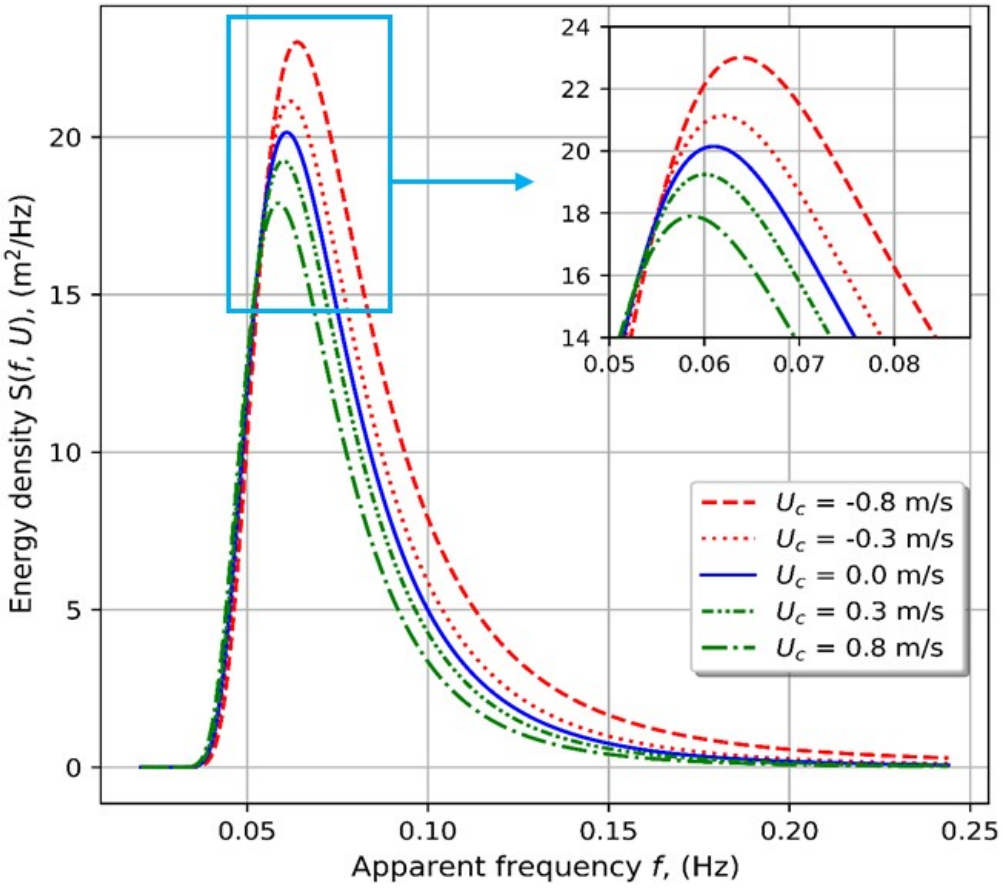

Figure 8.2: Current effect on an irregular wave profile represented by a reduced JONSWAP (PM) spectrum of H_s = 4.63 m and T_p = 16.4 s.

Furthermore, for opposite currents, the high-frequency tails of the spectra are adjusted using Equation (6.35) with a Phillip's constant, A^*, of 0.015 (Phillips, 1977). This adjustment ensures that the wave spectra are truncated beyond a specified cutoff frequency. Accordingly, the current-altered wave spectra are truncated beyond the cutoff frequency, and the cutoff frequency (i.e. $\text{cutoff} = 0.244$ Hz, 1.532 rad/s) is chosen to be four times the peak spectral frequency (i.e. $\text{peak} = 0.061$ Hz, 0.383 rad/s) (J. M. Jonkman, 2007). This approach optimises computational efficiency by focusing simulations on frequencies most relevant to wave dynamics while maintaining accuracy in representing wave energy dissipation.

Moreover, the increase in energy observed for opposing currents or the reduction for following currents is due to the redistribution of wave energy across different frequency bands. In opposing currents, energy is shifted toward lower frequencies, increasing the peak energy, while high-frequency components are reduced (see Figure 8.2). Conversely, in following currents, energy shifts toward the high-frequency range, leading to a decrease in peak energy, consistent with the overall energy conservation principle (J. Smith, 1997).

The findings depicted in Figures 8.1 and 8.2 shed light on the fundamental physics of wave-current interaction in extreme and operational conditions at the reference site, Canary-I of Gran Canaria. These results serve as a foundation for understanding the dynamic responses of the W2Power FOWT. Therefore, the following sections demonstrate the implications of these findings on the dynamic responses of the W2Power FOWT.

8.3 WCI Implications for Motion Dynamic Responses

The motion responses of the W2Power FOWT under the influence of wave-current interaction have been investigated. The simulation results for the floating system's motion responses under extreme and operational conditions of regular and irregular waves interacting with a uniform current are analysed. The presence of the current induces offsets in the FOWT's structural responses and alters the system's equilibrium position; thereby, the current influences both the static and dynamic responses (L. Chen & Basu, 2018).

In order to account for the current effect when simulating WCI load cases in OrcaFlex, the platform was first subjected to a pure current until it reached its static position. Subsequently, this new current-induced static position was then implemented into OrcaFlex simulations that include WCI. During these simulations, the floater object's DoFs were deliberately deselected. This procedure ensured that the current-modified wave profile, modelled using the Python external function in Section 6.8.3, was appropriately imported into OrcaFlex, and the current effect on the platform's static analysis was accurately incorporated.

The simulations in this study were run for 3800 s, with 200 s allocated for wave build-up and transient effect elimination. This is done to allow for a comprehensive analysis of each load case over a one-hour (3600 seconds) simulation period, which is deemed adequate for identifying characteristics of the system dynamics (A. C. Pillai et al., 2019; Shittu et al., 2020).

Figures 8.3 and 8.4 illustrate the effect of wave-current interaction on the translational and rotational motion responses of the platform, respectively. Focusing on the dynamic behaviour of the motion responses, surge and heave DoFs being the most affected, while the pitch was moderately impacted, and the rest were less influenced.

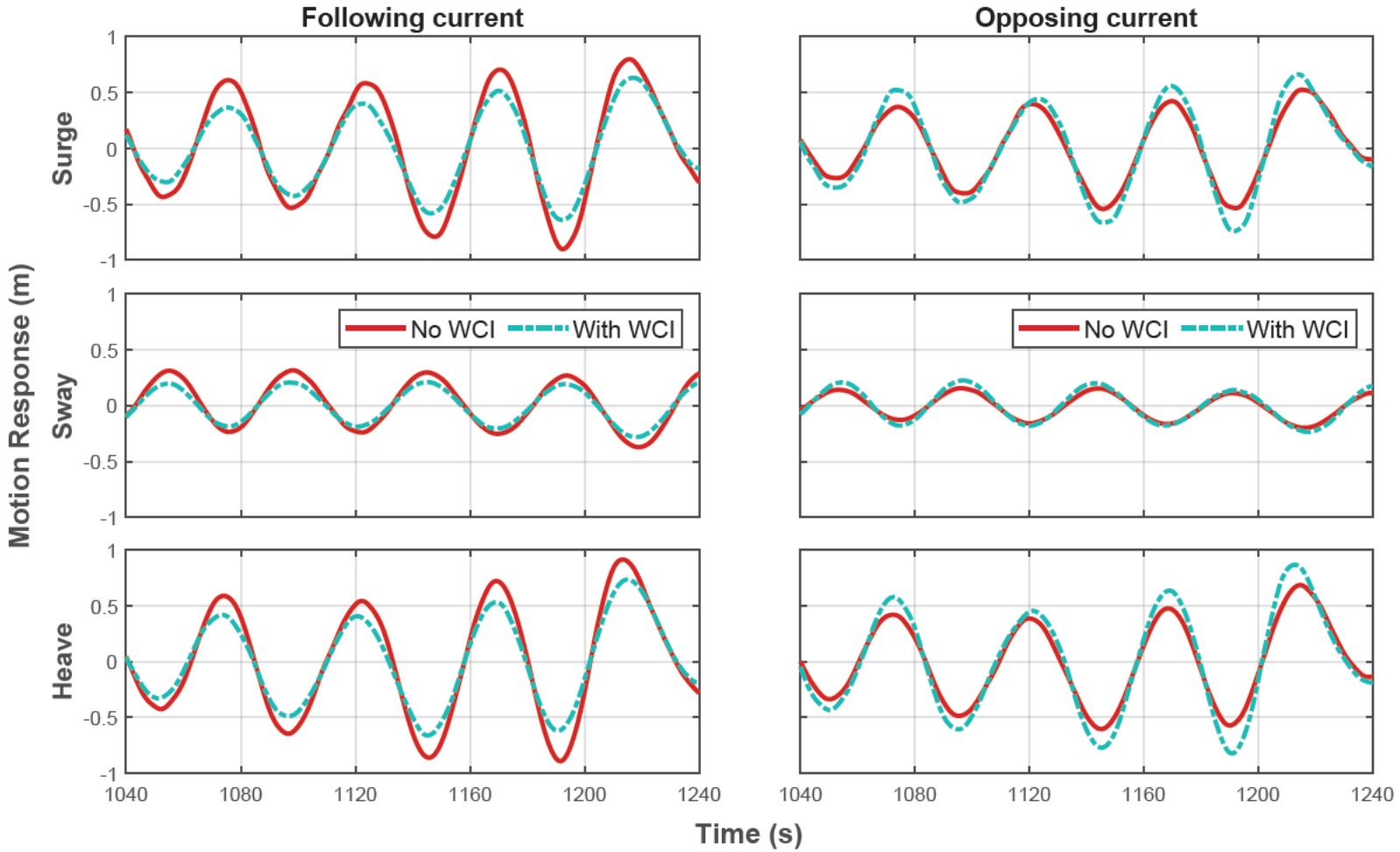

Figure 8.3: Time history of surge, heave and pitch motion responses considering wave-current interaction under operational conditions: (left) load case, LC11, of a following current, and (right) load case, LC12, of an opposing current.

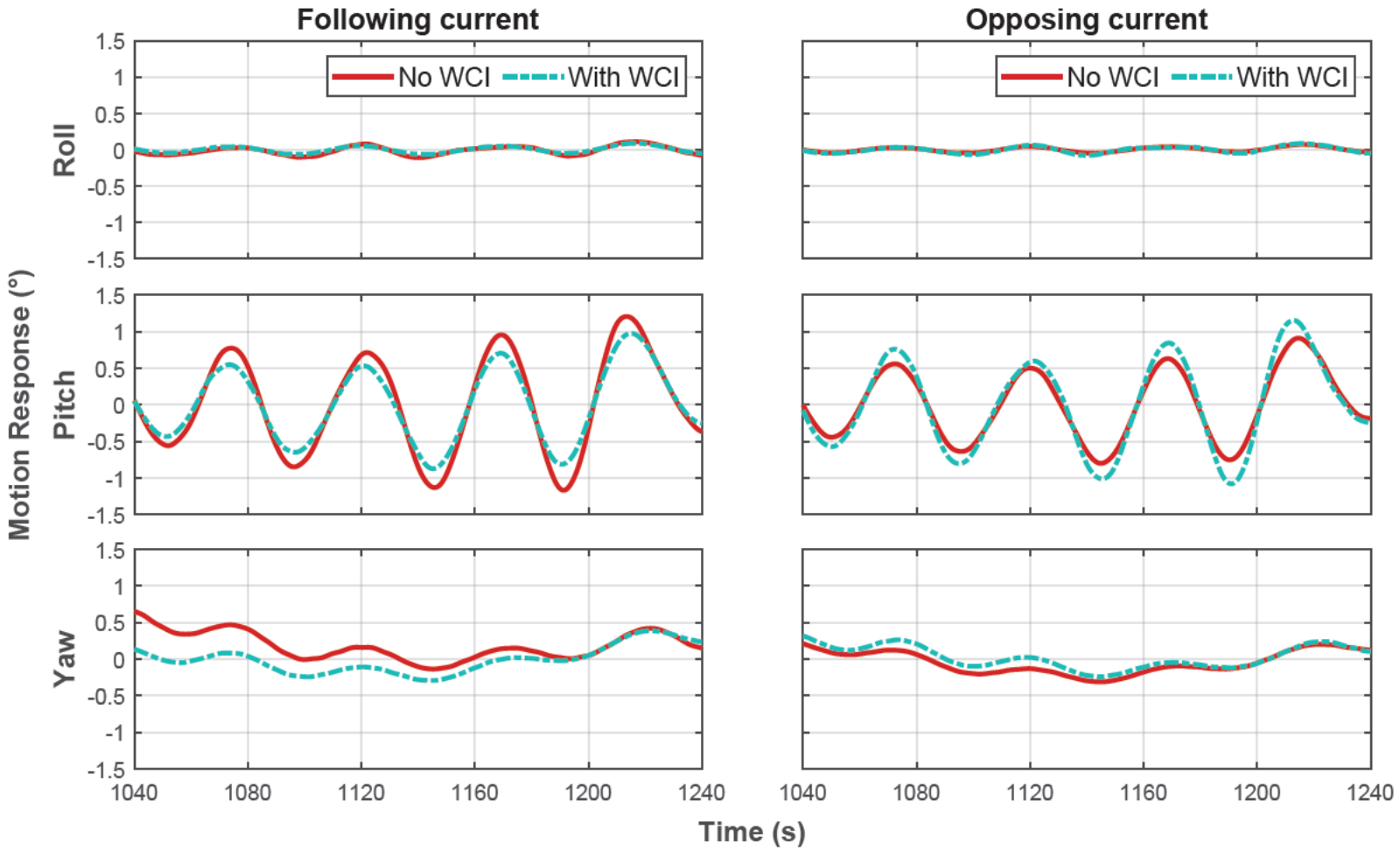

Figure 8.4: Time history of roll, pitch and yaw motion responses considering wave-current interaction under operational conditions: (left) load case, LC11, of a following current, and (right) load case, LC12, of an opposing current.

Notably, a following current reduces the motion response, whereas an opposing current enhances it. Slight frequency shifts are also observed as a result of the current-altered wave spectrum (Janssen, 1989; J. Smith, 1997).

Despite the considered wind conditions depicted in Figure 6.7.d, there were slight changes in the mean values of surge, heave and pitch due to this interaction with a current speed of 0.3 m/s. Hypothetically, the interaction's effect should be more pronounced in the absence of wind, which is demonstrated in Figure 8.5 for an extreme case of a current speed of 0.8 m/s. As can be seen, the mean values of the surge and heave decrease in the presence of the following current and increase with the opposing current due to the current drag force. Moreover, the relative maximum and minimum values are amplified by the opposing current, whereas the following current attenuates them.

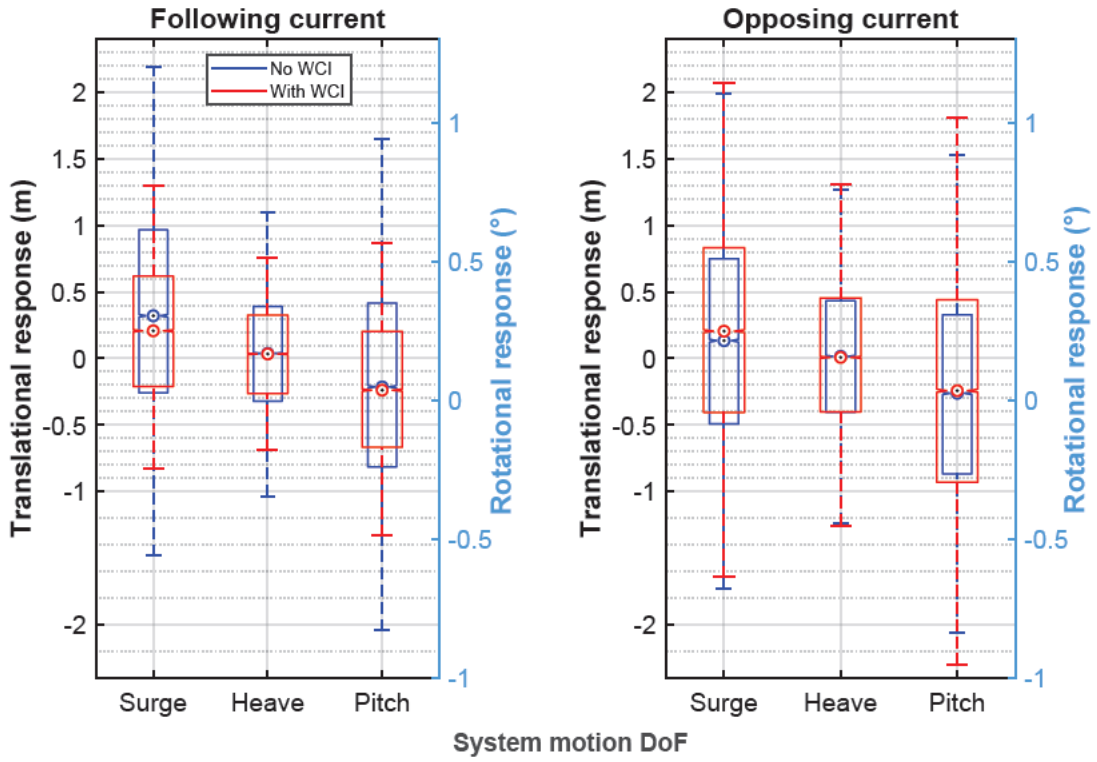

Figure 8.5: Statistical distributions of surge, heave and pitch motion responses for irregular waves considering wave-current interaction: (left) load case, LC5, with a following current; (right) load case, LC6, with an opposing current.

For statistical analyses, the mean, maximum, and standard deviation of the surge, heave, and pitch motion responses are provided in Table 8.1. It can be seen that an opposing current increases the mean values of the three motion responses while a following current decreases them. In the absence of wind, the opposing current can increase the maximum surge and heave responses by up to 40% when interacting with regular waves (i.e. LC2 and LC4).

Table 8.1: Statistical comparison of FOWT motion responses considering wave-current interaction.

Load case	Coupled model	Surge (m)			Heave (m)			Pitch (°)		
No.	**No (With) WCI**	**Mean**	**Max**	**StdDev**	**Mean**	**Max**	**StdDev**	**Mean**	**Max**	**StdDev**
LC1	No WCI	0.404	2.139	1.231	0.065	1.068	0.910	0.084	0.910	0.583
	With WCI	0.229	3.612	2.347	0.037	3.725	2.520	0.036	0.885	0.591
LC2	No WCI	0.043	2.978	1.289	0.097	1.312	0.741	0.008	0.963	0.435
	With WCI	0.072	3.606	2.544	0.050	4.792	3.371	0.031	0.512	0.333
LC3	No WCI	1.529	2.076	0.381	0.069	0.320	0.172	0.096	0.526	0.298
	With WCI	0.155	2.952	1.953	0.024	3.200	2.126	0.023	0.709	0.472
LC4	No WCI	0.720	1.093	0.435	0.123	0.688	0.240	0.031	0.799	0.180
	With WCI	0.129	5.070	2.174	0.097	4.406	2.815	0.006	0.956	0.400
LC5	No WCI	0.385	3.481	0.873	0.045	1.743	0.519	0.057	1.540	0.436
	With WCI	0.282	3.937	0.843	0.033	1.811	0.514	0.043	1.589	0.394
LC6	No WCI	0.136	2.944	0.872	0.017	1.821	0.603	0.025	1.447	0.423
	With WCI	0.212	2.964	0.912	0.025	1.952	0.622	0.037	1.739	0.483
LC7	No WCI	0.781	3.225	0.600	0.045	0.836	0.196	0.062	1.260	0.306
	With WCI	0.512	2.527	0.493	0.035	0.712	0.186	0.047	1.098	0.293
LC8	No WCI	0.327	1.146	0.403	0.138	0.985	0.235	0.012	0.825	0.169
	With WCI	0.692	2.225	0.400	0.050	1.128	0.217	0.069	1.291	0.307
LC9	No WCI	2.587	4.113	0.466	2.488	4.182	0.483	3.223	5.435	0.635
	With WCI	2.581	4.952	1.099	2.496	5.398	1.091	3.240	5.529	0.636
LC10	No WCI	2.652	4.155	0.417	2.490	4.257	0.473	3.229	5.552	0.622
	With WCI	2.527	5.090	1.087	2.481	5.481	1.257	3.222	5.265	0.635
LC11	No WCI	2.626	4.168	0.485	2.494	4.219	0.517	3.230	5.528	0.682
	With WCI	2.638	4.192	0.485	2.496	4.253	0.521	3.232	5.512	0.687
LC12	No WCI	2.627	4.056	0.435	2.491	4.287	0.505	3.230	5.621	0.667
	With WCI	2.628	4.060	0.431	2.491	4.277	0.500	3.231	5.639	0.661

On the other hand, when interacting with irregular waves (i.e. LC6 and LC8), the opposing current can increase surge motion by up to 26% and heave motion by up to 30%, while the following current decreases both surge and heave motions (i.e. LC1, LC3, LC5 and LC7). The interaction has minimally affected the pitch motion, even though this can induce an extra restoring force in the negative heave direction. Accordingly, the heave response has experienced alterations when considering the nonlinear coupling effect of heave and pitch responses, particularly for a single-point mooring system (Y. Li et al., 2018; Qu et al., 2020).

The inclusion of wind speed in operational load cases induced stronger responses of surge, heave, and pitch in operational sea states compared to extreme sea states, as highlighted in Table 8.1. This observation is attributed to the significant impact of wind on FOWTs. The aerodynamics of wind are expected to be the dominant loading in extreme wind events, potentially diminishing the comparative impact of WCI on the floating system. The deliberate exclusion of wind in extreme sea states aligns with the rationale of highlighting the impact of WCI during conditions where it might be more pronounced.

Nevertheless, it is imperative to acknowledge the significant impact of wind on the twin-turbine system and the importance of including it in the operational conditions. Thus, these load cases (LC9-LC12) were selected to mirror the environmental conditions of the reference site, providing additional insights into the system's behaviour under realistic scenarios (L. Chen & Basu, 2018). These findings underline the significance of simulating holistic environmental conditions, encompassing both wind and WCI dynamics, to comprehensively estimate the dynamics of FOWTs. Hence, it is crucial to understand the intricate interaction between wind and wave-current dynamics and their combined implications.

8.4 WCI Implications for Mooring Dynamic Responses

Mooring lines play a crucial role in maintaining the overall stability of the FOWT and ensuring its stationary positioning. Furthermore, fairlead tensions in mooring lines are directly influenced by the motion of the platform. Alterations of wave profiles due to current presence, Figures 8.1 and 8.2, were found to affect platform motion responses (see Section 8.3). Thus, it is of interest to investigate different current scenarios with structure-wave interaction to understand their impact on mooring dynamics.

Among the three mooring cables, lines A and B are chosen to investigate the impact of wave-current interaction. Mooring line A aligns with the incoming waves, while lines B and C are inclined towards the negative and positive y-direction, respectively, as shown in Figure 6.2.(b). Since the mooring system layout is symmetrical, the fairlead forces of cable C are identical to those of cable B and, thus, are not presented.

Figures 8.6 and 8.7 display the time histories of fairlead forces for lines A and B, respectively, under different WCI scenarios during operational conditions (LC11 and LC12). In general, the fairlead force in line A consistently surpasses that in line B, irrespective of the wave-current interaction scenario being following or opposing.

Wave-current interaction notably impacts the dynamic response of mooring lines. For line A, the following current interacting with waves results in decreased fairlead load, while the opposing current increases tension force, as illustrated in Figure 8.6. Conversely, contrasting behaviour is observed in mooring line B (see Figure 8.7).

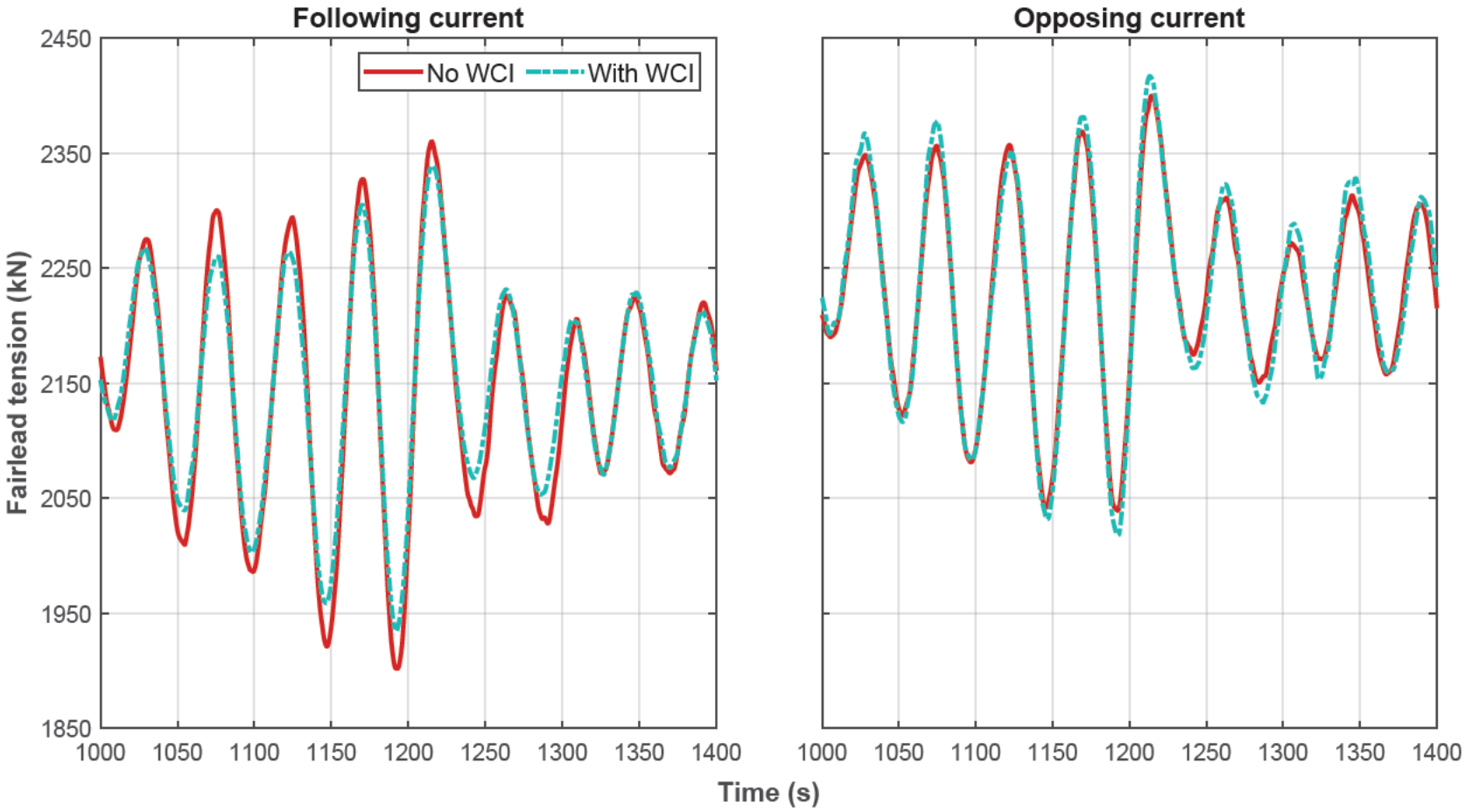

Figure 8.6: Time history of the mooring load at the fairlead of line A considering wave-current interaction under operational conditions: (left) load case, LC11, of a following current, and (right) load case, LC12, of an opposing current.

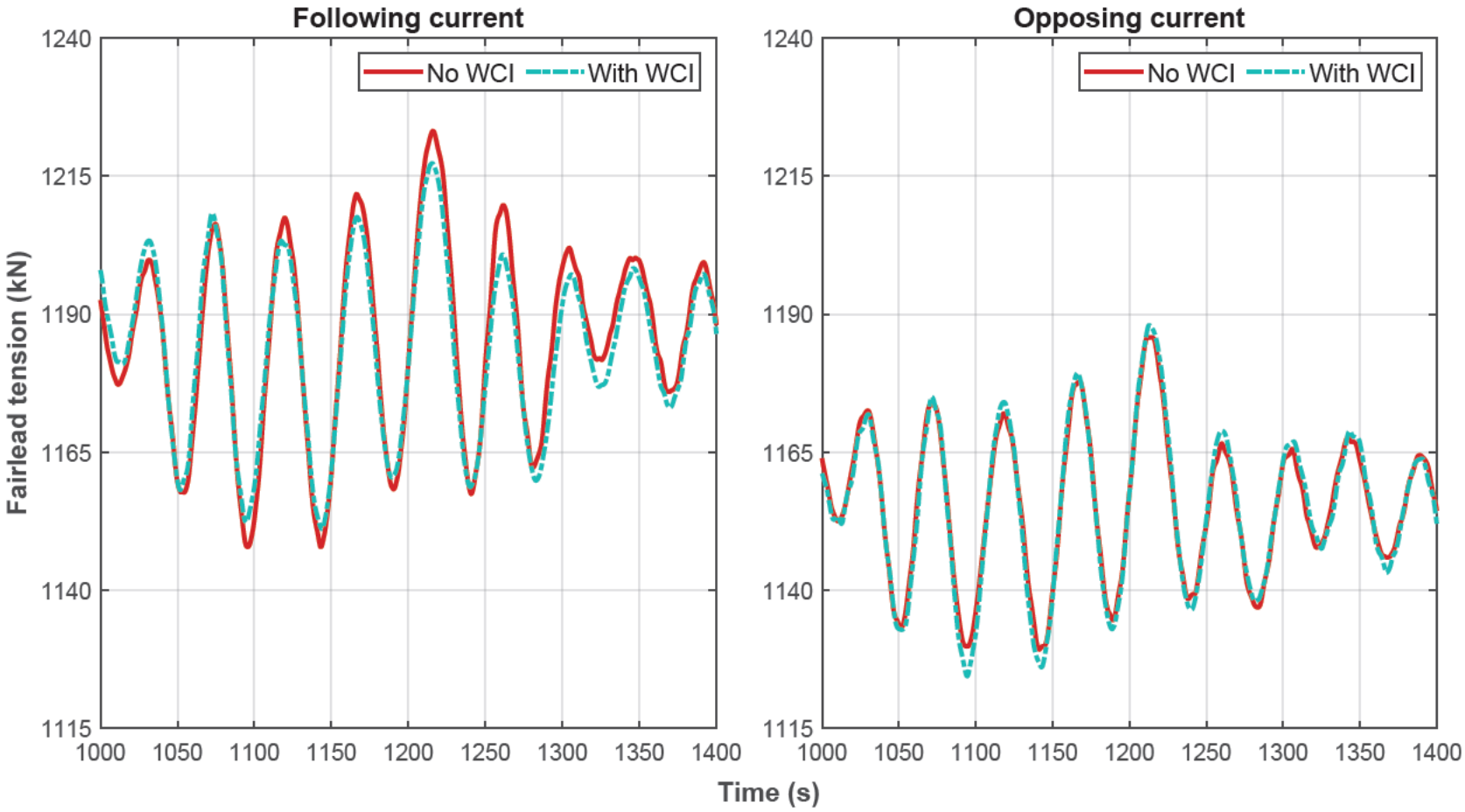

Figure 8.7: Time history of the mooring load at the fairlead of line B considering wave-current interaction under operational conditions: (left) load case, LC11, of a following current, and (right) load case, LC12, of an opposing current.

Moreover, slight frequency shifts in fairlead forces can be observed in the time histories, attributed to the modified wave spectrum caused by the current. By scrutinising these frequency shifts, valuable insights can be obtained regarding how current-altered wave properties impact the overall motion and stability of FOWTs.

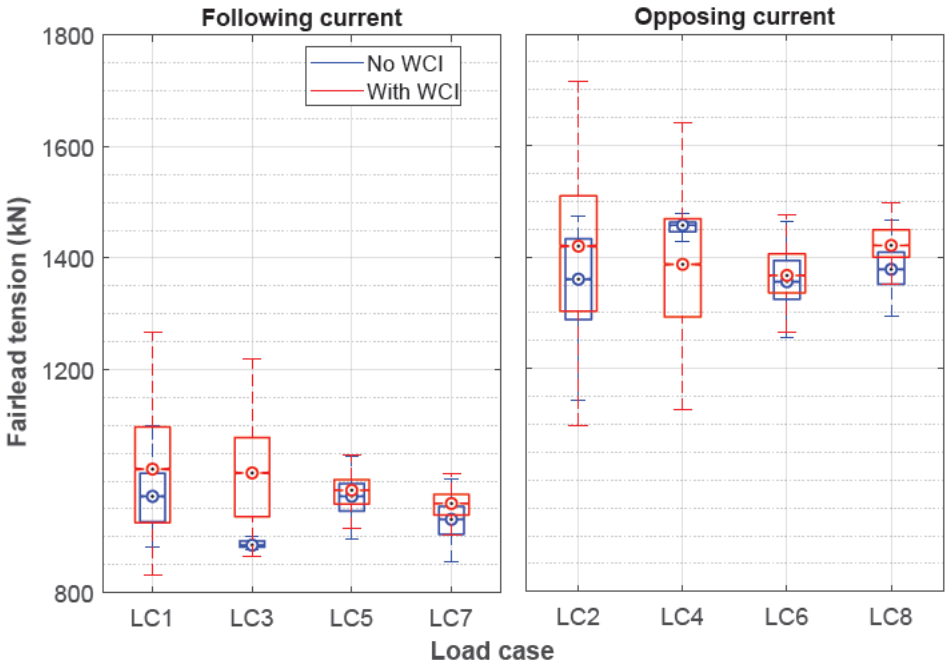

Figure 8.8: Statistical distributions of the mooring load at the fairlead of line A considering wave-current interaction under extreme conditions: (left) load cases with following currents, and (right) load cases opposing currents.

The implications of WCI on mooring dynamics are further analysed. Herein, the statistical results of the effective tension at the lines' fairleads are depicted in Figures 8.8 and 8.9 for line A, and in Figures 8.10 and 8.11 for line B. In order to provide a clearer illustration of the effect of WCI, the results are presented separately for extreme load cases (LC1-LC8) and operational load cases (LC9-LC12) under following and adverse current scenarios.

Overall, WCI was found to impact the mooring lines' mean and maximum fairlead tension; in particular, the interaction significantly impacts the maximum tension, while their effect on the mean tension is insignificant. For mooring line A, as depicted in Figure 8.8, when regular waves (extreme cases: LC1-LC4) interact with a following current, the maximum tension increases, whereas the opposite effect is observed for an opposing current, with a difference of up to 22%.

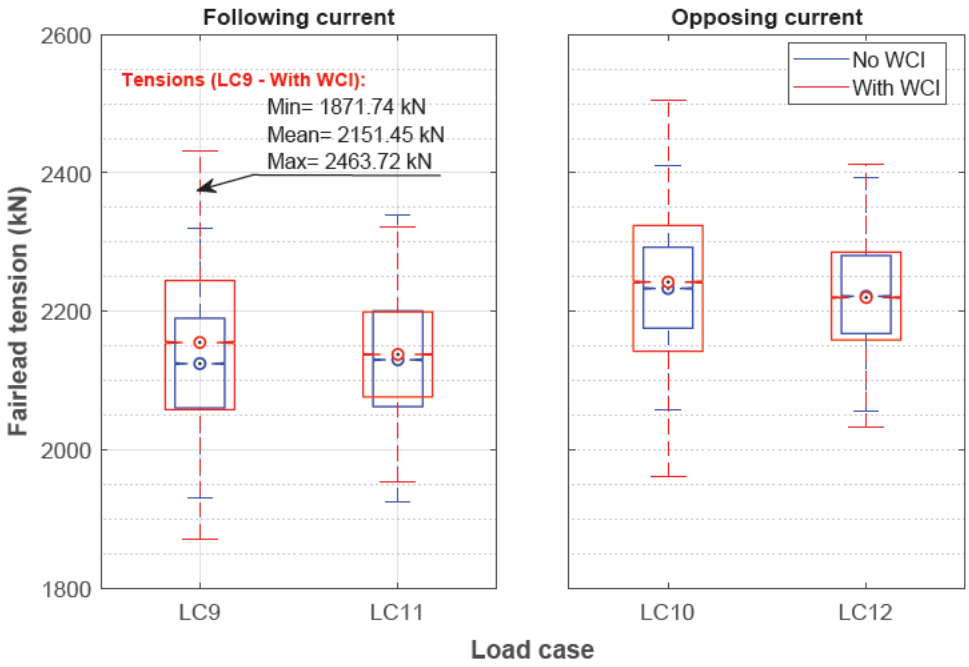

Figure 8.9: Statistical distributions of the mooring load at the fairlead of line A considering wave-current interaction under operational conditions: (left) load cases with following currents, and (right) load cases opposing currents.

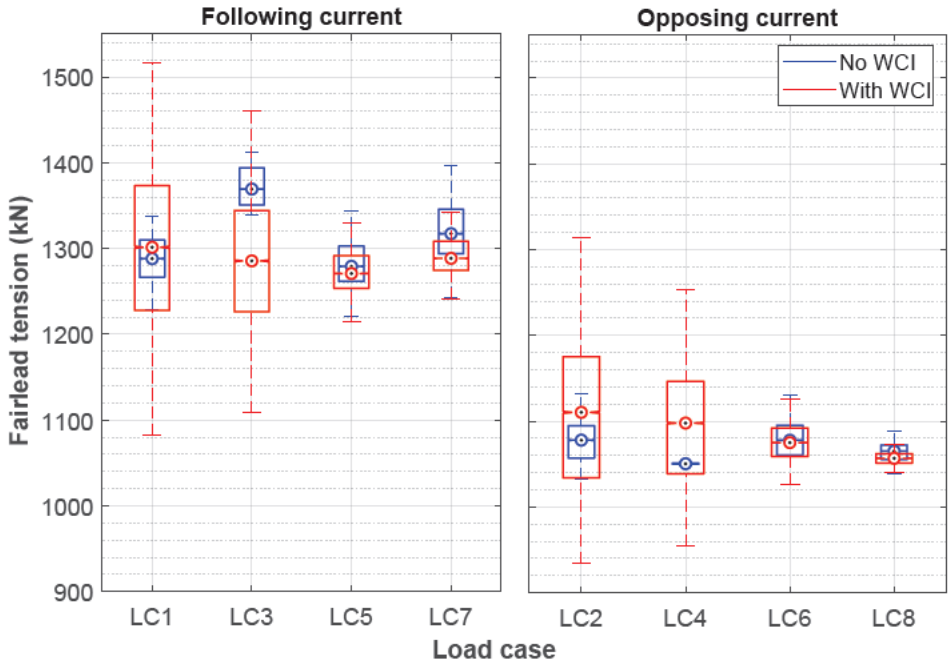

Figure 8.10: Statistical distributions of the mooring load at the fairlead of line B considering wave-current interaction under extreme conditions: (left) load cases with following currents, and (right) load cases opposing currents.

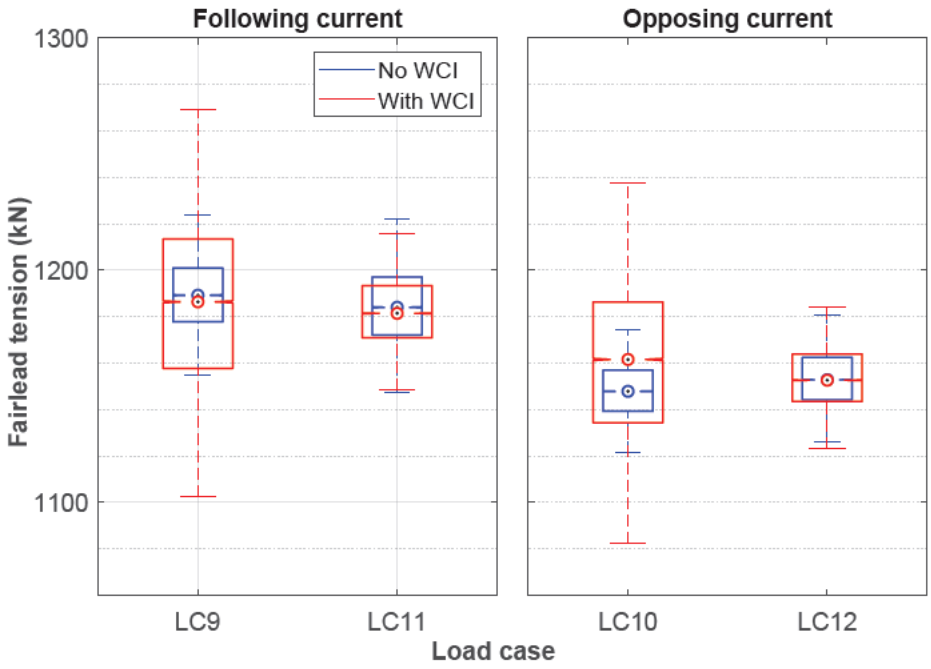

Figure 8.11: Statistical distributions of the mooring load at the fairlead of line B considering wave-current interaction under operational conditions: (left) load cases with following currents, and (right) load cases opposing currents.

For example, for line A and under extreme conditions with an opposing current (LC2), incorporating WCI resulted in a maximum fairlead tension increase of up to 1723 kN, compared to approximately 1440 kN without interaction, indicating a significant increase of almost 20%. The changed surge brought on by WCI may account for these tension load differences. Hence, this highlights the importance of properly handling the increased fairlead tension in mooring design.

Since WCI alters the hydrodynamic loading on the platform and moorings, thus it potentially impacts the responses of superstructures like towers and nacelles. Even though the hydrodynamic loading on moorings may be relatively small compared to the platform, WCI contribution remains significant. Thus, during real-time simulations, it should be added to the hydrodynamic loading on the coupled floating system utilising Morison and motion equations, Equations (6.45) and (6.46), respectively. Consequently, considering WCI in mooring standards can help minimise uncertainties in estimated loads. This, in turn, reduces the substantial safety factors that the mooring systems are conventionally designed with.

8.5 WCI Implications for Nacelles Dynamic Responses

Given that FOWTs are complex coupled systems where the dynamic responses of the platform, mooring, and wind turbines are interlinked, it is imperative to consider the impact of wave-current interaction on the dynamics of the turbines. As previously demonstrated in Sections 8.3 and 8.4, WCI influences both the platform's motion responses and mooring behaviour. These WCI-induced alternations in motion and mooring dynamics are expected to propagate to other components of wind turbines, such as nacelles and towers.

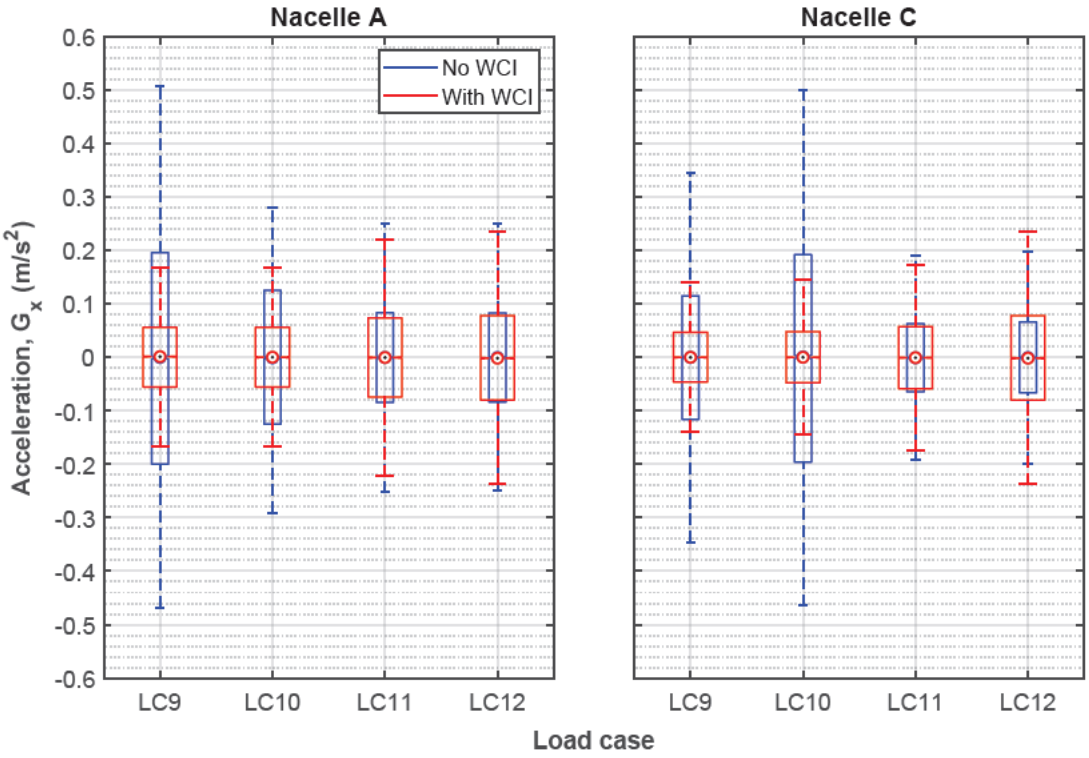

Figure 8.12: Effect of wave-current interaction on the longitudinal component (G_x) of nacelles' accelerations under operational conditions: (left) nacelle A (starboard nacelle), and (right) nacelle C (port nacelle).

Therefore, exploring the potential effects of WCI on the dynamics of other turbines' elements is vital for assessing the dynamics of the entire floating system (B. Liu & Yu, 2022). Thereby ensuring the nacelle accelerations of a FOWT system remain within acceptable limits for its safe operation in a specific location. Thus, the impact of wave-current interaction on the magnitudes of nacelle accelerations (G) and their longitudinal (surge), transverse (sway), and vertical (heave) components, denoted as G_x, G_y, and G_z, respectively, are analysed for four operational load cases (LC9-LC12). The findings are presented in Figures 8.12 to 8.14 and Table 8.2.

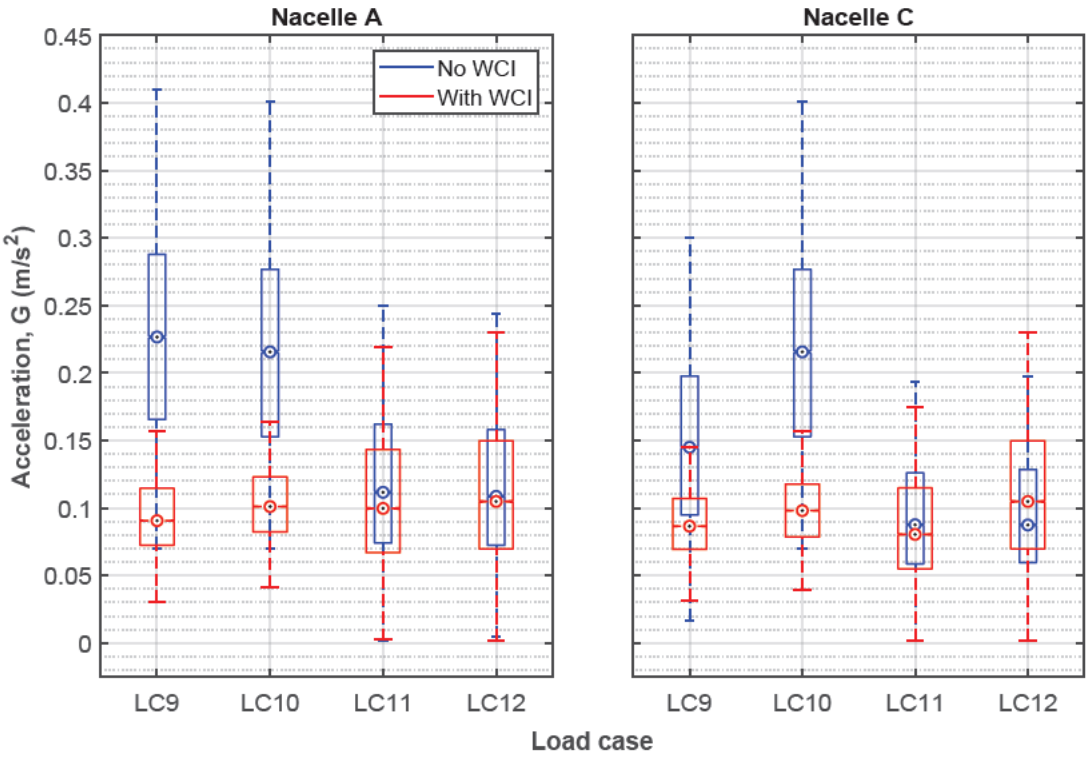

Figure 8.13: Effect of wave-current interaction on nacelles' accelerations (G) under operational conditions: (left) nacelle A (starboard nacelle), and (right) nacelle C (port nacelle).

Furthermore, it is important to note that with two turbines acting as separate mass points, their potential for moving out of phase could result in varying periods of motion, which may extend the fatigue load into their respective transition points and towers. This could lead to either a dampening or enhancement of motion, depending on the interaction between the two turbines.

Figure 8.12 demonstrates that incorporating WCI reduces the maximal longitudinal acceleration, G_x. This reduction is particularly pronounced for regular waves (i.e. LC9 and LC10), herein a decrease of up to 48% is observed, whereas irregular waves (i.e. LC11 and LC12) experienced a drop of up to 22%. Consequently, these reductions notably influence the mean values of acceleration magnitudes, which decrease by approximately 50% and 10% when considering the current interaction with regular and irregular waves, respectively (see Figure 8.13).

Table 8.2: Statistical comparison of nacelles' accelerations (G) under operational conditions considering wave-current interaction.

Load case	Coupled model	Nacelle A acceleration, G (m^2/s)				Nacelle C acceleration, G (m^2/s)			
No.	**No (With) WCI**	**Min**	**Max**	**Mean**	**StdDev**	**Min**	**Max**	**Mean**	**StdDev**
LC9	No WCI	0.070	0.519	0.230	0.079	0.171	0.397	0.150	0.066
	With WCI	0.004	0.283	0.096	0.035	0.002	0.026	0.090	0.031
LC10	No WCI	0.070	0.509	0.219	0.078	0.020	0.418	0.162	0.068
	With WCI	0.004	0.264	0.104	0.035	0.006	0.253	0.099	0.032
LC11	No WCI	0.002	0.514	0.125	0.067	0.001	0.401	0.097	0.052
	With WCI	0.023	0.392	0.111	0.059	0.002	0.033	0.089	0.047
LC12	No WCI	0.005	0.494	0.121	0.066	0.001	0.397	0.099	0.054
	With WCI	0.002	0.483	0.117	0.063	0.002	0.401	0.096	0.052

Moreover, the observed differences in the accelerations between nacelle A (i.e. starboard turbine) and nacelle C (i.e. port turbine) can be attributed to the wake effects in this twin wind turbine system. Since the rotors are in close proximity, aerodynamic interaction between their wakes causes non-uniform load distribution across the two turbines (Udoh & Zou, 2020), even in the absence of WCI. This aerodynamic wake interaction can result in asymmetric responses in the numerical simulations, leading to slight differences in the accelerations of the two nacelles (Y. Bae & Kim, 2014; H. Kim, 2018).

Since the pitch response was found to be less impacted by WCI, the significant changes observed in the G_x could be attributed to the WCI-altered surge. Furthermore, Table 8.2 summarises the statistics for nacelles accelerations. Notably, incorporating wave-current interaction reduces the minimum, mean, maximum, and standard deviation values, further emphasising the impact of WCI on the nacelle dynamics.

On the contrary, the statistical distribution presented in Figure 8.14 reveals minor differences in the transverse (G_y) and vertical (G_z) accelerations when considering the interaction effect. These subtle variations can be attributed to the collinearity of the environmental conditions. It is worth noting that the wind, with a speed of 11.4 m/s, opposes the direction of the waves. Given the dominance of these loads (wind and wave), distinguishing the specific influence of the current, with a speed of 0.3 m/s, becomes challenging when it is either following or opposing. Such an observation is primarily due to the wind and wave loads being significantly larger in magnitude compared to the current. The collinearity of the environmental conditions (i.e. wind and waves) further reduces the impact of the current.

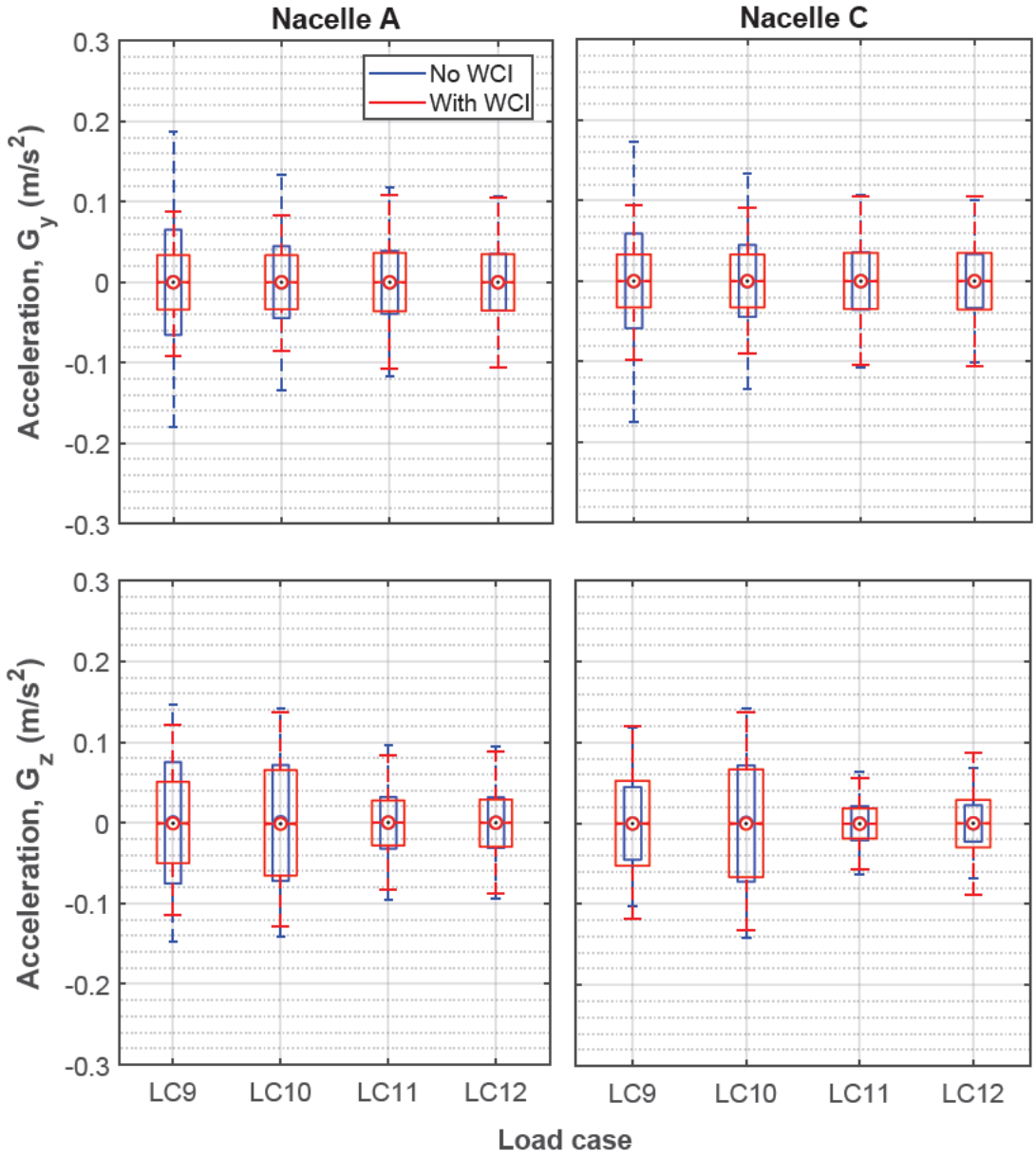

Figure 8.14: Effect of wave-current interaction on translational accelerations of the nacelles under operational conditions: (top panels) transverse, sway, component (G_y), and (bottom panels) vertical, heave, component (G_z). The left panels display the results for nacelle A (starboard nacelle), and the right panels show the results for nacelle C (port nacelle).

To delve further into the impact of WCI on nacelle structural responses, time series for regular waves and power spectral densities for irregular waves are depicted in Figures 8.15 and 8.16, respectively. Subsequently, the consideration of WCI effectively was found to reduce nacelle accelerations, as shown in Figures 8.15 and 8.16. For instance, Figure 8.16 illustrates the impact on irregular waves, indicating an apparent reduction in acceleration PSDs under the influence of WCI, particularly within the frequency range of 0 to 0.25 Hz, irrespective of

the current direction. Interestingly, nacelle A exhibited higher acceleration than nacelle C at very low frequencies. Such behaviours can be attributed to the differing hydrodynamic and aerodynamic conditions acting on the twin nacelles due to their relative positions in the system.

From Figure 8.16, the observed reduction in the PSD under opposing current (LC12), specifically for Nacelle C, can be more attributed to the changes in wave dynamics and energy distribution induced by the interaction between the wave and the opposing current. Opposing currents tend to shorten wave periods and increase wave heights, leading to alterations in the energy distribution across the spectrum (Gabl et al., 2018; S. Draycott et al., 2021). This results in a shift and reduction of energy at certain frequencies, directly impacting the nacelle's dynamic response. The complex interaction between these modified wave characteristics and the structural responses of the FOWT system results in decreased PSD responses (Z. Liu et al., 2016). Additionally, the more pronounced acceleration reduction for Nacelle C might be a consequence of the aerodynamic interaction as a result of the positioning of the two rotors.

Moreover, the increased hydrodynamic damping effect under opposing currents enhances energy dissipation mechanisms, further reducing the structural responses of the FOWT's subsystems (Z. Liu et al., 2016; T. Ishihara & Liu, 2020). For instance, opposing currents increase the drag force acting on the nacelle, which diminishes its relative motion with the surrounding water and consequently lowers accelerations.

The observed reductions in nacelles' accelerations when incorporating WCI can be attributed to the complex hydrodynamic interaction caused by the coupling of waves and currents. The intricate WCI introduces additional forces and moments, thereby modifying the flow conditions around the entire floating system. These altered flow fields influence the inertia of the system, which, in turn, contributes to the system's dampening response (Goupee et al., 2014). Furthermore, twin-turbine FOWTs add another level of complexity due to the wake interaction between the rotors, which is not considered in this study. Therefore, the assessment of their aerodynamics is a topic of ongoing research (Martín San Román, 2022).

Commonly, the interaction of the current with the incoming waves results in a larger excitation force in surge and excitation moment in pitch. The surge drift force also changes with the current-altered wave height (S. K. Chakrabarti, 1984). Unlike conventional offshore structures, FOWTs are distinguished by their towering superstructures. These towers lead to a significant rotor displacement from even a minor pitch motion of the floating platform.

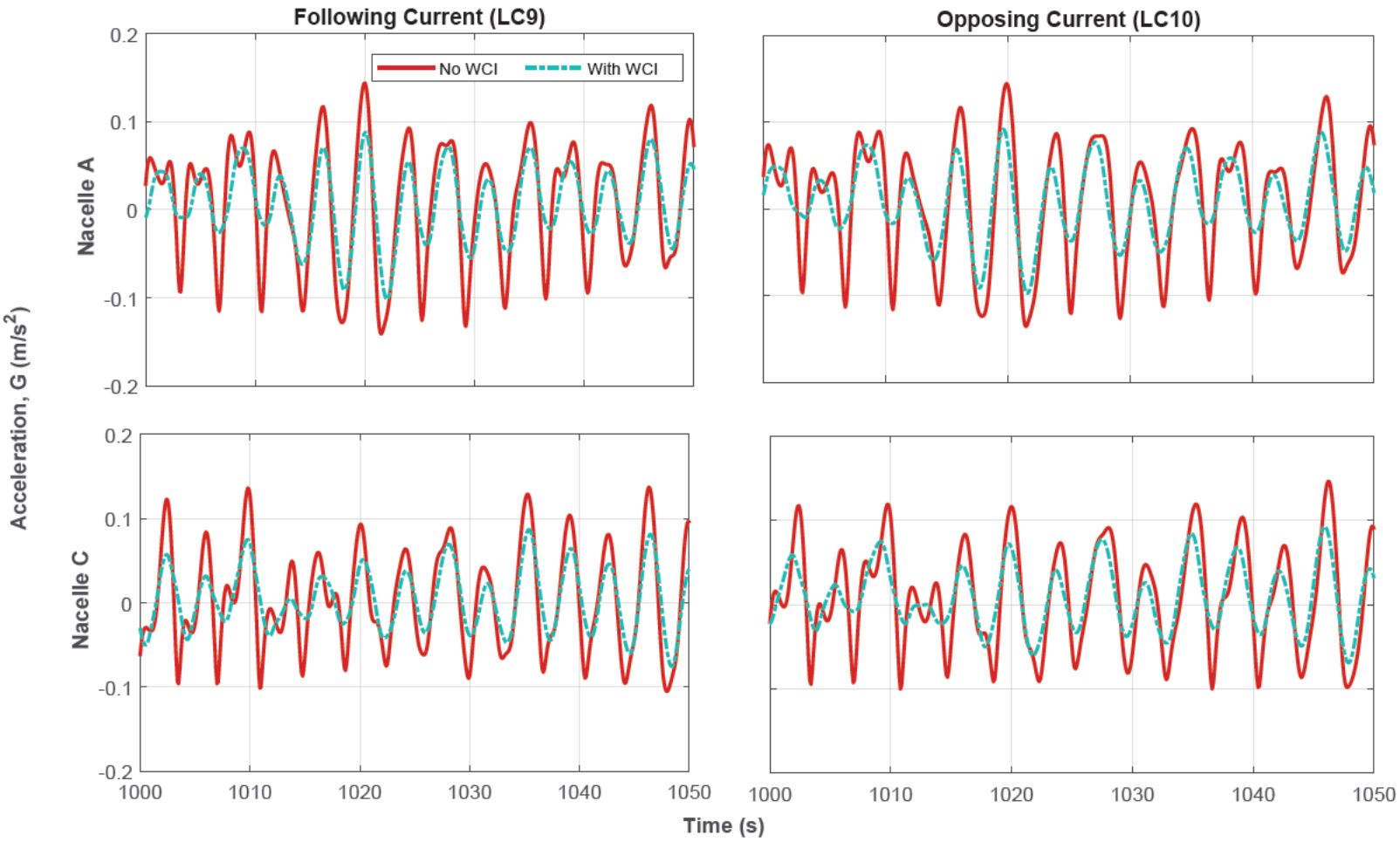

Figure 8.15: Time histories of nacelles' accelerations (G) considering wave-current interaction under operational conditions for regular waves: (left) load cases, LC9, with following currents, and (right) load cases, LC10, with opposing currents. The top panels display the results for nacelle A (starboard nacelle), and the bottom panels show the results for nacelle C (port nacelle).

Moreover, in this peculiar FOWT design with a single-point mooring system, the presence of wind could potentially tilt the platform, inducing pitch motion and vibrations in the tower fore-aft that could affect nacelle acceleration (Antonutti et al., 2016). Consequently, it impacts the generated power efficiency and contributes to the accumulation of fatigue loads. Therefore, the inclusion of WCI is considerably effective for capturing more accurate wind-wave effects. Then, a trade-off between vibration reduction and rotor speed enhancement could be advantageous for extending the operational life of wind turbine components.

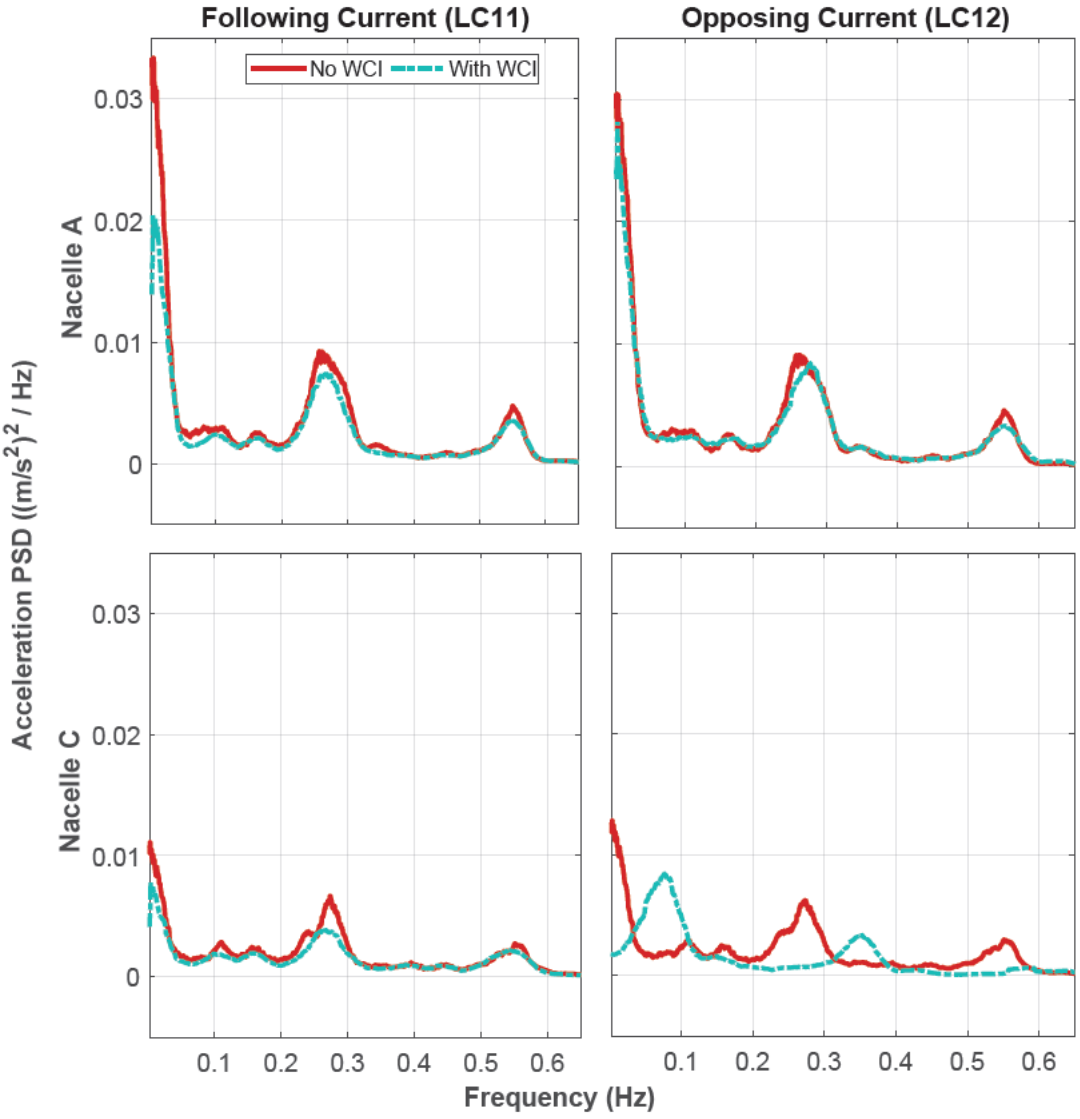

Figure 8.16: Power spectral densities of nacelles' accelerations (G) considering wave-current interaction under operational conditions for irregular waves: (left) load cases, LC11, with following currents, and (right) load cases, LC12, with opposing currents. The top panels display the results for nacelle A (starboard nacelle), and the bottom panels show the results for nacelle C (port nacelle).

8.6 Chapter Summary

This chapter delved into the findings of the developed models of the W2Power FOWT and WCI introduced in the preceding chapter (Chapter 6). Firstly, the effects of following and opposing currents on wave characteristics were investigated, revealing alterations in the regular and stochastic wave fields.

Then, the implications of wave-current interaction on the W2Power FOWT were comprehensively investigated. These encompassed the dynamic responses of platform motion, mooring system, and nacelles. Key findings are summarised:

- The presence of current significantly impacted the FOWT's static equilibrium and, consequently, its mooring and motion dynamics. This highlights the necessity for accurately accounting for currents in the design and operational planning of FOWTs to ensure stability and safety.
- WCI affected the translational motion responses of the FOWT system, while rotational motions were relatively unaffected. These differential impacts suggest that translational movements are more sensitive to environmental conditions, which can influence the overall stability and operational efficiency of the system.
- WCI impacted the mooring system's dynamics, with notable effects observed on the maximum tension at the fairlead, while the mean tension was insignificantly affected. The increased maximum tension due to WCI could lead to higher fatigue loads on the mooring lines, potentially reducing their lifespan and increasing maintenance requirements.
- Under operational conditions with the inclusion of wind loads, the impact introduced by WCI becomes relatively negligible compared to the dominant aerodynamic forces. This negligible effect was more pronounced in the mooring loads and heave responses, where the presence of wind significantly overshadowed the influence of WCI. Therefore, WCI can be ignored when wind load is considered in mooring systems design. However, the significance of WCI depends on the current strength and its direction, as well as the wind conditions (e.g. speed and direction). In cases where the current is stronger or aligns unfavourably with the wind, WCI might have a more pronounced effect.
- Despite the relatively minor impact of WCI under wind-dominated conditions, WCI was found to substantially minimise maximum longitudinal accelerations of the nacelles (G_x) in this specific twin-turbine system. Meanwhile, the transverse and vertical accelerations showed slight variations due to the collinearity of environmental conditions along the x-axis. This reduction in longitudinal acceleration could enhance the structural integrity of the platform and reduce the fatigue loads on the nacelles and tower.

Overall, the outcomes of this part (Part III) highlight the significance of incorporating WCI to accurately simulate the dynamic responses of FOWTs and ensure operational safety. The consideration of WCI makes these twin-turbine systems more viable by providing a more realistic assessment of their performance under varying environmental conditions, thereby enhancing design reliability and operational planning. However, the increased maximum tension and potential fatigue impacts necessitate careful consideration in the design and maintenance planning to mitigate long-term operational risks.

Moreover, the current framework and results of the parametric studies presented in this chapter can form the basis for the application of advanced wave-current interaction models in future studies. For instance, nonlinear WCI models, such as those developed by Moreira & Peregrine (2012), can be established to account for more nonlinear effects of such interaction and their implications on the structural responses of FOWTs. This can further refine the understanding of FOWT dynamics and improve the accuracy of simulations, ultimately contributing to more robust and efficient offshore wind energy systems.

Chapter 9

Conclusions and Future Work

This chapter draws conclusions from the thesis and considers opportunities for further work in relation to the dynamic assessment and development of floating offshore wind turbines.

9.1 Overall Thesis Conclusions

This research was undertaken in partnership with EnerOcean S.L. to present an innovative concept and provide a better understanding of the coupled dynamic behaviours of FOWTs in wave-current environments (EnerOcean S.L., 2007). The major contributions centre around developing the W2Power FOWT model. Furthermore, it established WCI models and explored their implications on the dynamic responses of FOWTs. Due to the coverage of cross-disciplinary research areas, the more detailed conclusions are split into the following sections:

9.1.1 Original Research Contributions

In order to develop numerical and experimental data models, the following contributions were made at both prototype and 1:40 model scales (Chapters 4 and 6):

- Developed W2Power floater numerical models and assessed their hydrodynamic performance.
- Designed new single-point mooring systems of three catenary lines made of chains.
- Development of the floater-mooring-towers-nacelles-turbines models: The prototype model was equipped with a pair of NREL 5 MW wind turbines.
- Developed two numerical models to investigate WCI: (i) regular WCI model, and (ii) irregular WCI model.
- For the first time, a novel framework was introduced by integrating the WCI models with the OrcaFlex programme.
- Quantitatively benchmarked the impacts of WCI on the dynamics of FOWTs by conducting fully coupled analyses in the time domain
- Assembled and tested a 1/40th-scale physical model of FOWTs in combined wave-current conditions at FloWave Ocean Energy Research Facility (FloWave, 2014).

- Provided validation assessments on the implications of WCI for structural responses of FOWTs.

9.1.2 Main Research Findings

Realistic environmental conditions for a reference site were considered (NKUA-AM&WFG, 2021), and the main conclusions are:

◊ **Waves Effects:** Wave directionality significantly influenced mooring and motion dynamics. Following waves induced the highest peak tension across all lines, followed by opposing waves, with crossing waves having the least effect. Collinear waves induced larger platform motions than crossing ones. Specifically, following waves resulted in slightly larger surge and pitch responses, while heave motions were more influenced by opposing waves. Irregular waves yielded larger responses than regular ones with the same wave parameters, demonstrating that monochromatic waves were inadequate to capture the full spectrum of wave-induced loads.

◊ **Combined Wave-Current Effects:** Firstly, different wave-structure scenarios interacting with current were tested, maintaining the current's direction while waves followed, crossed, and opposed the current (Chapter 5). WCI resulted in larger mooring tensions in the surge direction than in the sway direction, indicating differential responses to wave and current loading. This highlights the need for reinforced mooring systems to ensure structural integrity and operational safety. Consistent tension patterns were also observed across all mooring lines when waves crossed the current, with mean mooring loads dominating over dynamic ones.

Mooring PSDs showed that steeper waves led to higher load responses, emphasising the need for bespoke design considerations for line-specific sensitivities to WCI (Tang et al., 2023). At the upper end of the wave spectrum, breaking waves may occur, introducing additional forcing factors on the structure that could significantly amplify mooring loads and dynamic responses. Such effects require careful consideration when designing for extreme conditions (Chawla & Kirby, 1998). The presence of current significantly reduced peak wave-induced mooring loads, especially with following waves, and caused frequency shifts, exciting mooring responses at low frequencies (S.-H. Yang et al., 2016).

Platform motion PSDs revealed current influence at low and high frequencies. Following waves increased surge and heave responses at low frequencies but decreased them at high frequencies while opposing waves had the opposite effect. Current interaction consistently reduced pitch and roll responses at low frequencies and increased them at high frequencies, regardless of wave direction (Y. Liu et al., 2019). The peculiar W2Power FOWT demonstrated effective weathervaning and dynamic response to environmental loads, with sway and yaw motion responses and mooring loads validating its performance in wave-current conditions.

Secondly, comprehensive validations were conducted between FloWave data and OrcaFlex simulations across various environments: calm water, current, waves, and combined wave-current scenarios (Chapter 7). In calm water, free-decay tests without mooring lines showed very good agreement in amplitude and period of oscillations between measured and predicted motions in surge, heave, and pitch DoFs. Static pull-out tests with mooring lines further demonstrated the decay behaviour of the coupled floating system. Under current-only and pure waves, high agreement was observed between measured and simulated mooring tensions and motion responses, validating the numerical model's accuracy under current loading. Notable mooring load discrepancies, which attributed to excessive pretension at the test's onset.

For the first time, the effects of WCI on FOWT structural responses were validated against experiments. Good agreements were found between measured and predicted free surface elevations of regular waves and spectra of irregular waves with WCI. Without WCI, simulations overestimated wave profiles with following waves and underestimated them with opposing waves. These discrepancies lead to inaccurate predictions for the mooring loads and motion responses of the FOWT, potentially compromising the design and safety of these floating systems. Furthermore, comparisons of RAOs indicated better alignment of simulations with WCI to experimental results. The absence of WCI in simulations led to an overestimation of RAOs with following waves and an underestimation with opposing waves. Inclusion of WCI decreased peak RAOs of surge by up to 15%, heave by up to 11.5%, and pitch by up to 5% with following waves while increasing surge by up to 6.4%, heave by up to 17.2%, and pitch by up to 13.5% with opposing waves. Relative errors between measured and predicted RAOs were lower with WCI, demonstrating the developed WCI models' accuracy in capturing FOWT dynamics.

Thirdly, after validating the numerical models developed, various current-structure scenarios were simulated with waves maintaining their direction while the current followed and opposed the waves (Chapter 8). The inclusion of WCI significantly altered the translational motion responses of the FOWT system. Specifically, the mean values of surge and heave decreased with a following current and increased with an opposing current, resulting in differences of up to $\pm 26\%$ and $\pm 30\%$, respectively. In contrast, the rotational motions were relatively unaffected.

The dynamics of the mooring system were notably impacted, with maximum tensions at the fairlead varying by up to $\pm 22.5\%$, depending on the current direction and mooring layout, while mean tensions remained largely unchanged. The fairlead experiences significant impact, but over the long term, the mooring lines are more likely to take on the cumulative fatigue load,

making them the potential weak link in terms of fatigue failure. Under operational conditions, WCI reduced maximum longitudinal accelerations of nacelles (G_x) by up to 48% and 22% in irregular waves. Slight variations in transverse and vertical accelerations were observed due to the collinearity of environmental loads along the surge direction.

Under wind-dominated operational conditions, the impact of WCI is generally negligible, particularly affecting mooring loads and heave responses. However, WCI can still significantly influence nacelles accelerations in this specific twin-turbine system, enhancing structural integrity and reducing fatigue loads.

Overall, these findings collectively underscore the significant impact of WCI on FOWT dynamics, particularly in platform motions, mooring loads, and nacelle accelerations. Thus highlighting the need for accurate WCI modelling to enhance design optimisation and ensure safe and reliable operation of FOWT systems.

9.2 Recommendations for Future Work

The findings provided in this thesis have yielded valuable insights into the dynamic responses of FOWTs in combined wave-current environments. However, further research into specific aspects is needed to propel the advancement of FOWT technologies. Consequently, building on this research, these aspects are categorised and identified as follows:

Experimental Modelling Aspects

- Conduction of open-tank experiments to assess disturbances introduced by the model to the WG measurements.
- Performing free-decay tests for motion responses in sway, roll, and yaw DoFs. Moreover, investigating observed discrepancies for the performed decay tests (i.e. Section 7.3) and exploring potential reasons behind them.
- Completion of pull-out tests, appended in Appendix C.1, to further optimise characteristics of the designed mooring system.
- Extending the test programme to cover oblique waves (both regular and irregular) over a wider range of angles (e.g., including angles such as 30°, 60°, 120°, and 150°) and their interaction with currents of different profiles.
- Testing operational conditions with the inclusion of effects of wind forces on two rotors and validating the simulated WCI implications on the nacelles presented in Section 8.5.
- Carrying out comprehensive uncertainty analyses, accounting for both systematic and random uncertainties, particularly focusing on single-point mooring systems, where the ability of the model to return to its initial position after displacement presents distinct challenges.

Numerical Modelling Aspects

- Incorporating floater flexibility into real-time numerical simulations, as it was modelled as a rigid body.
- Investigating the remaining DNV or IEC design load cases (IEC-61400-3, 2009; DNV-OS-E301, 2010; DNV-RP-C205, 2019), considering ultimate, accidental, and fatigue limit states with different wind, wave, and current parameters, as the evaluation of the W2Power FOWT adopted extreme environmental conditions for a reference site.
- Expansion of the developed WCI models so that fully nonlinear models, such as those developed by Moreira & Peregrine (2012), can be established to account for more nonlinear effects.
- This study assumed that wave fields are 2-D, long-crested, and uni-directional and that random waves are linear and single-peaked. However, real ocean environments can be more sophisticated (Section 6.3). Therefore, further research should include an accurate depiction of the sea state, such as short-crested waves, freak waves, focused waves, bichromatic waves, greater extreme waves, and multi-directional waves. This, in turn, will allow for comprehensive assessments for designing optimisation and risk assessment strategies for FOWTs under various and real ocean environments.
- Since tidal variances between neap and spring tides could affect these results (i.e. especially in the presence of varying current velocities), it would be beneficial to map out these effects to capture the full range of potential WCI implications.
- Inclusion of the aerodynamic wake interactions between the turbines' rotors via the development of a third-party CFD model. Then, investigate their consequences on the dynamic responses of the floating system and power production.
- Exploring scenarios involving the failure of a single turbine under various conditions (i.e. with and without WCI). Such scenarios could provide valuable insights into system resilience and performance, as well as lessons to be learnt in the event of emergency shutdowns.

Bibliography

Aanesland, V., Faltmsen, O., & Zhao, R. (1990). Wave-drift damping of a tlp. In *Sut environmental forces on offshore structures and their predictions: Proceedings of an international conference* (pp. SUT–AUTOE).

Aerodyn. (2023). *aerodyn engineering gmbh.* Büdelsdorf, Germany. Retrieved from https://www.aerodyn-engineering.com/scd-technology/patents/?L=570

Ahmed, M., Nizamani, Z., Nakayama, A., & Osman, M. (2020). Some recent fluid-structure interaction approaches for the wave current behaviour with offshore structures. *CFD Letters*, *12*(9), 15–26.

Amaechi, C. V., Wang, F., & Ye, J. (2022a). Experimental study on motion characterisation of calm buoy hose system under water waves. *Journal of Marine Science and Engineering*, *10*(2), 204.

Amaechi, C. V., Wang, F., & Ye, J. (2022b). Investigation on hydrodynamic characteristics, wave-current interaction and sensitivity analysis of submarine hoses attached to a calm buoy. *Journal of Marine Science and Engineering*, *10*(1), 120.

Amaechi, C. V., Wang, F., & Ye, J. (2022c). Numerical studies on calm buoy motion responses and the effect of buoy geometry cum skirt dimensions with its hydrodynamic waves-current interactions. *Ocean Engineering*, *244*, 110378.

Aminoroayaie Yamini, O., Mousavi, S. H., Kavianpour, M. R., & Movahedi, A. (2018). Numerical modeling of sediment scouring phenomenon around the offshore wind turbine pile in marine environment. *Environmental earth sciences*, *77*, 1–15.

ANSYS. (2016). Ansys fluent - cfd software. *Ansys, Inc., Pennsylvania, USA*, *18*. Retrieved from http://www.ansys.com/products/fluids/ansys-fluent

Antonutti, R., Peyrard, C., Johanning, L., Incecik, A., & Ingram, D. (2016). The effects of wind-induced inclination on the dynamics of semi-submersible floating wind turbines in the time domain. *Renewable Energy*, *88*, 83–94.

Applied Measurements Ltd. (2020). *Submersible load cell - dden.* Reading, UK. Retrieved from https://appmeas.co.uk/products/load-cells-force-sensors/in-line-submersible-load-cell-dden/

AquaWind. (2022). *Aquawind: a european project to merge wind energy and aquaculture.* Europe. Retrieved from https://aquawind.eu/ (2021-2030)

Arapogianni, A., Genachte, A. B., Ochagavia, R. M., Vergara, J. P., Castell, D., Tsourouk-dissian, A. R., ... others (2013). Deep water—the next step for offshore wind energy. *European Wind Energy Association (EWEA)*, 978–972.

Atcheson, M., Garrad, A., Cradden, L., Henderson, A., Matha, D., Nichols, J., ... Sandberg, J. (2016). Floating offshore wind energy. *by Joao Cruz and Mairead Atcheson. Springer International Publishing. Chap. Looking back. doi*, *10*(1007), 978–3.

Azcona, J., Palacio, D., Munduate, X., Gonzalez, L., & Nygaard, T. A. (2017). Impact of mooring lines dynamics on the fatigue and ultimate loads of three offshore floating wind turbines computed with iec 61400-3 guideline. *Wind Energy*, *20*(5), 797–813.

Bae, Y., & Kim, M. (2014). Coupled dynamic analysis of multiple wind turbines on a large single floater. *Ocean Engineering*, *92*, 175–187.

Bae, Y. H. (2013). *Coupled dynamic analysis of multiple unit floating offshore wind turbine* (Unpublished doctoral dissertation). Department of Civil Engineering.

Bae, Y. H., & Kim, M.-H. (2015). Influence of asymmetric aerodynamic loading on multiple unit floating offshore wind turbine. *Journal of Ocean Engineering and Technology*, *29*(3), 255–262.

Bakker. (1974). Sand concentration in an oscillatory flow. In *Coastal engineering 1974* (pp. 1129–1148).

Bakker, & Van Doorn, T. (1978). Near-bottom velocities in waves with a current. In *Coastal engineering 1978* (pp. 1394–1413).

Barber, N. F. (1949). The behaviour of waves on tidal streams. *Proceedings of the Royal Society of London. Series A. Mathematical and Physical Sciences*, *198*(1052), 81–93.

Barltrop, N. (1993). Multiple unit floating offshore wind farm (mufow). *Wind Engineering*, 183–188.

Barnes, T., Brocchini, M., Peregrine, D., & Stansby, P. (1996). Modelling post-wave breaking turbulence and vorticity. In *Coastal engineering 1996* (pp. 186–199).

Bashetty, S., & Ozcelik, S. (2020). Design and stability analysis of an offshore floating multi-turbine platform. In *2020 ieee green technologies conference (greentech)* (pp. 184–189).

Bauer, J. (2020, April). Offshore wind turbines on the rise. *NREL Webinar: Overview of Floating Offshore Wind*. Retrieved from https://www.nrel.gov/wind/newsletter-202004.html

Ben-Israel, A. (1966). A newton-raphson method for the solution of systems of equations. *Journal of Mathematical analysis and applications*, *15*(2), 243–252.

Beveridge, M. C. (2008). *Cage aquaculture*. John Wiley & Sons.

Bloom, G. S., & Golomb, S. W. (1977). Applications of numbered undirected graphs. *Proceedings of the IEEE*, *65*(4), 562–570.

Bogdanov, D., Gulagi, A., Fasihi, M., & Breyer, C. (2021). Full energy sector transition towards 100% renewable energy supply: Integrating power, heat, transport and industry sectors including desalination. *Applied Energy*, *283*, 116273.

Bretherton, F. P., & Garret, C. (1970). Wavetrains in inhomogeneous moving media. In *Hyperbolic equations and waves* (pp. 211–236). Springer.

Breton, S.-P., & Moe, G. (2009). Status, plans and technologies for offshore wind turbines in europe and north america. *Renewable energy*, *34*(3), 646–654.

Brevik, I. (1980). Flume experiment on waves and currents ii. smooth bed. *Coastal Engineering*, *4*, 89–110.

Brevik, I., & Bjørn, A. (1979). Flume experiment on waves and currents. i. rippled bed. *Coastal engineering*, *3*, 149–177.

Brunel. (2023). *Brunel - floating wind turbine.* Oslo, Norway. Retrieved from https://www.fredolsen1848.com/technologies/brunel/

Burrows, R., & Hedges, T. (1985). The influence of currents on ocean wave climates. *Coastal Engineering*, *9*(3), 247–260.

Butterfield, S., Musial, W., Jonkman, J., & Sclavounos, P. (2007). *Engineering challenges for floating offshore wind turbines* (Tech. Rep.). Golden, Colorado, USA: National Renewable Energy Lab. (NREL).

Byrne, B., & Houlsby, G. (2003). Foundations for offshore wind turbines. *Philosophical Transactions of the Royal Society of London. Series A: Mathematical, Physical and Engineering Sciences*, *361*(1813), 2909–2930.

Cahay, M., & Milde, L. (2023). Nextfloat: structural benefit of innovative downwind floating wind concept. *7th Offshore Energy & Storage Symposium (OSES-2023)*.

Campagnolo, F., Petrovic, V., Nanos, E. M., Tan, C. W., Bottasso, C. L., Paek, I., ... Kim, K. (2016). Wind tunnel testing of power maximization control strategies applied to a multi-turbine floating wind power platform. In *Isope international ocean and polar engineering conference* (pp. ISOPE–I).

Carlson, D. W., & Modarres-Sadeghi, Y. (2018). Vortex-induced vibration of spar platforms for floating offshore wind turbines. *Wind Energy*, *21*(11), 1169–1176.

Chai, W., & Leira, B. J. (2018). Environmental contours based on inverse sorm. *Marine Structures*, *60*, 34–51.

Chakrabarti. (1987). Wave force on small structures. *Hydrodynamics of offshore structures, Computational Mechanics Publications, Southampton*, 168–170.

Chakrabarti, & Tam, W. A. (1975). Interaction of waves with large vertical cylinder. *Journal of Ship Research*, *19*(01), 23–33.

Chakrabarti, S. K. (1984). Steady drift force on vertical cylinder-viscous vs. potential. *Applied ocean research*, *6*(2), 73–82.

Chakrabarti, S. K. (1996). Discussion: Equilibrium-range spectrum of waves propagating on currents. *Journal of Waterway, Port, Coastal, and Ocean Engineering*, *122*(6), 302–303.

Chaviaropoulos, P. K., Natarajan, A., & Jensen, P. H. (2014). Key performance indicators and target values for multi-megawatt offshore turbines. In *European wind energy conference.*

Chawla, A., & Kirby, J. T. (1998). Experimental study of wave breaking and blocking on opposing currents. In *Coastal engineering 1998* (pp. 759–772).

Chen, L., & Basu, B. (2018). Fatigue load estimation of a spar-type floating offshore wind turbine considering wave-current interactions. *International Journal of Fatigue*, *116*, 421–428.

Chen, L., & Basu, B. (2019). Wave-current interaction effects on structural responses of floating offshore wind turbines. *Wind Energy*, *22*(2), 327–339.

Chen, L., Basu, B., & Nielsen, S. R. (2018). A coupled finite difference mooring dynamics model for floating offshore wind turbine analysis. *Ocean Engineering*, *162*, 304–315.

Chen, L., Zhai, H., Wang, P., Zhang, Q., Wang, S., Duan, L., & Jeng, D.-S. (2022). Experimental study on the irregular wave (current)-induced pore-water pressures around a monopile. *Journal of Coastal Research*, *38*(1), 114–132.

Chen, Q., Kirby, J. T., Dalrymple, R. A., Shi, F., & Thornton, E. B. (2003). Boussinesq modeling of longshore currents. *Journal of Geophysical Research: Oceans*, *108*(C11).

Chen, W., Guo, S., Li, Y., & Shen, Y. (2021). Impacts of mooring-lines hysteresis on dynamic response of spar floating wind turbine. *Energies*, *14*(8), 2109.

Chen, X., Li, J., & Chen, J. (2014). Nonlinear wave and currents loads analysis of offshore wind turbines. *KSCE Journal of Civil Engineering*, *18*, 1877–1883.

Clemens, S. C., Prell, W. L., Sun, Y., Liu, Z., & Chen, G. (2008). Southern hemisphere forcing of pliocene δ18o and the evolution of indo-asian monsoons. *Paleoceanography*, *23*(4).

Coulling, A. J., Goupee, A. J., Robertson, A. N., Jonkman, J. M., & Dagher, H. J. (2013). Validation of a fast semi-submersible floating wind turbine numerical model with deepcwind test data. *Journal of Renewable and Sustainable Energy*, *5*(2).

Cummins, W., et al. (1962). The impulse response function and ship motions.

Dai, J., Abrahamsen, B. C., Viuff, T., & Leira, B. J. (2022). Effect of wave-current interaction on a long fjord-crossing floating pontoon bridge. *Engineering Structures*, *266*, 114549.

Dalrymple, R. A. (1973). Water wave models and wave forces with shear currents. *COASTAL AND OCEANOGRAPHIC ENGINEERING LABORATORY University of Florida Gainesvilie, Florida Technical Report No. 20*.

Dalrymple, R. A. (1977). A numerical model for periodic finite amplitude waves on a rotational fluid. *Journal of Computational Physics*, *24*(1), 29–42.

Davidson, J., & Ringwood, J. V. (2017). Mathematical modelling of mooring systems for wave energy converters—a review. *Energies*, *10*(5), 666.

Davies, A. G., Soulsby, R. L., & King, H. (1988). A numerical model of the combined wave and current bottom boundary layer. *Journal of Geophysical Research: Oceans*, *93*(C1), 491–508.

De Graaff, D. B., & Eaton, J. K. (2000). Reynolds-number scaling of the flat-plate turbulent boundary layer. *Journal of Fluid Mechanics*, *422*, 319–346.

de Jesus Henriques, T., Tedds, S., Botsari, A., Najafian, G., Hedges, T., Sutcliffe, C., ... Poole, R. (2014). The effects of wave-current interaction on the performance of a model horizontal axis tidal turbine. *International Journal of Marine Energy*, *8*, 17–35.

Devolder, B., Stratigaki, V., Troch, P., & Rauwoens, P. (2018). Cfd simulations of floating point absorber wave energy converter arrays subjected to regular waves. *Energies*, *11*(3), 641.

Diep Nguyen, T. T., Nguyen, V. M., & Yoon, H. K. (2021). Experimental and numerical simulation on dynamics of a moored semi-submersible in various wave directions. *Science Progress*, *104*(4_suppl), 00368504221096003.

DNV-OS-E301. (2010). Offshore standard dnv-os-e301 position mooring. *Det Norske Veritas: Høvik, Norway*.

DNV-RP-C205. (2017). 'dnv-rp-c205: Environmental conditions and environmental loads. *Det Norske Veritas: Høvik, Norway*.

DNV-RP-C205. (2019). *Dnv-rp-c205: Environmental conditions and environmental loads*. Det Norske Veritas: Høvik, Norway.

Draycott, S., Noble, D., Davey, T., Bruce, T., Ingram, D., Johanning, L., ... Kaklis, P. (2018). Re-creation of site-specific multi-directional waves with non-collinear current. *Ocean Engineering*, *152*, 391–403.

Draycott, S., Pillai, A., Gabl, R., Stansby, P., & Davey, T. (2022). An experimental assessment of the effect of current on wave buoy measurements. *Coastal Engineering*, *174*, 104114.

Draycott, S., Pillai, A. C., Gabl, R., & Davey, T. (2021). Wave buoys in current-experimental results and observations. *Proc. European Wave and Tidal Energy Conference, Plymouth, UK*.

Draycott, S., Sellar, B., Davey, T., Noble, D., Venugopal, V., & Ingram, D. (2019). Capture and simulation of the ocean environment for offshore renewable energy. *Renewable and Sustainable Energy Reviews*, *104*, 15–29.

Draycott, S., Steynor, J., Davey, T., & Ingram, D. M. (2018). Isolating incident and reflected wave spectra in the presence of current. *Coastal Engineering Journal*, *60*(1), 39–50.

Draycott, S. T. (2017a). On the re-creation of site-specific directional wave conditions.

Draycott, S. T. (2017b). *On the re-creation of site-specific directional wave conditions* (Unpublished doctoral dissertation). Engineering.

Dresselhaus, E., & Tabor, M. (1992). The kinematics of stretching and alignment of material elements in general flow fields. *Journal of Fluid Mechanics*, *236*, 415–444.

Duan, F., Hu, Z., & Wang, J. (2016). Investigation of the vims of a spar-type fowt using a model test method. *Journal of renewable and sustainable energy*, *8*(6).

Duarte, T., Price, S., Peiffer, A., & Pinheiro, J. M. (2022). Windfloat atlantic project: Technology development towards commercial wind farms. In *Offshore technology conference.*

Durakovic, A. (2021). *World's largest floating wind farm takes final shape.* SCHIEDAM, South Holland: OffshoreWIND.biz. Retrieved from https://www.offshorewind.biz/2021/07/05/worlds-largest-floating-wind-farm-takes-final-shape/ (July 5)

Edition, F., Journée, J., & Massie, W. (2001). Offshore hydromechanics. In *Delft university of technology.*

Edwards, E. C., Holcombe, A., Brown, S., Ransley, E., Hann, M., & Greaves, D. (2023). Evolution of floating offshore wind platforms: A review of at-sea devices. *Renewable and Sustainable Energy Reviews*, *183*, 113416.

Elobeid, M., Tao, L., Ingram, D., Pillai, A. C., Mayorga, P., & Hanssen, J. E. (2022). Hydrodynamic performance of an innovative semisubmersible platform with twin wind turbines. In *International conference on offshore mechanics and arctic engineering* (Vol. 85932, p. V008T09A032).

EnerOcean S.L. (2007). *SME Marine Energy Engineering.* Málaga, Spain.

Enerocean-S.L. and Pelagic-Power. (2015). *Marine Renewables Infrastructure Network for emerging Energy Technologies (MARINET): W2P TRL 5 Validation - Hybrid Floating Platforms in Deep Waters (Phase IV).* Europe.

EOLINK. (2023). *Eolink: Floating wind turbine concepts.* France. Retrieved from http://eolink.fr/en/ (Accessed: September 14, 2023)

Equinor. (2023). *Equinor marks operational landmark at Hywind Scotland wind farm.* Houston, Texas: Offshore magazine. Retrieved from https://www.offshore-mag.com/renewable-energy/article/14287752/equinor-marks-operational-landmark-at-hywind-scotland-wind-farm (Jan 3)

Faltinsen, O. M. (1993). *Sea loads on ships and offshore structures* (Vol. 1). Cambridge University Press.

Faraci, C., Musumeci, R. E., Marino, M., Ruggeri, A., Carlo, L., Jensen, B., ... Elsaßer, B. (2021). Wave-and current-dominated combined orthogonal flows over fixed rough beds. *Continental Shelf Research*, *220*, 104403.

Faraci, C., Scandura, P., Musumeci, R., & Foti, E. (2018). Waves plus currents crossing at a right angle: near-bed velocity statistics. *Journal of Hydraulic Research*, *56*(4), 464–481.

Fenton, J. D., & McKee, W. (1990). On calculating the lengths of water waves. *Coastal Engineering*, *14*(6), 499–513.

Fernando, P. C., Guo, J., & Lin, P. (2011). Wave–current interaction at an angle 1: experiment. *Journal of hydraulic research*, *49*(4), 424–436.

Finne, S., & Grue, J. (1998). On the complete radiation-diffraction problem and wave-drift damping of marine bodies in the yaw mode of motion. *Journal of Fluid Mechanics*, *357*, 289–320.

Finne, S., Grue, J., & Nestegård, A. (2000). Prediction of the complete second order wave drift damping force for offshore structures. In *Isope international ocean and polar engineering conference* (pp. ISOPE–I).

FloWave. (2014). *Flowave ocean energy research facility.* The University of Edinburgh, Edinburgh, UK. Retrieved from www.flowavett.co.uk

Fonseca, N., Nybø, S., Rodrigues, J. M., Gallego, A., & Garrido, C. (2022). Identification of wave drift forces on a floating wind turbine sub-structure with heave plates and comparison with predictions. In *International conference on offshore mechanics and arctic engineering* (Vol. 85932, p. V008T09A063).

FPP. (2023). *Floating power plant: a combined wind and wave device.* Bandholm, Denmark. Retrieved from https://www.floatingpowerplant.com/

Fredsøe, J. (1984). Turbulent boundary layer in wave-current motion. *Journal of Hydraulic Engineering*, *110*(8), 1103–1120.

Fritts, D. C., & Alexander, M. J. (2003). Gravity wave dynamics and effects in the middle atmosphere. *Reviews of geophysics*, *41*(1).

Froude, W. (1868). Observations and suggestions on the subject of determining by experiment the resistance of ships. *Correspondence with the Admiralty, Chelston Cross, December*, 120–128.

Froude, W. (1920). *On the elementary relation between pitch, slip, and propulsive efficiency* (Tech. Rep.).

Gabl, R., Davey, T., Nixon, E., Steynor, J., & Ingram, D. M. (2019). Experimental data of a floating cylinder in a wave tank: Comparison solid and water ballast. *Data*, *4*(4), 146.

Gabl, R., Draycott, S., Pillai, A. C., & Davey, T. (2021). Experimental data of bottom pressure and free surface elevation including wave and current interactions. *Data*, *6*(10), 103.

Gabl, R., Steynor, J., Forehand, D. I., Davey, T., Bruce, T., & Ingram, D. M. (2018). Capturing the motion of the free surface of a fluid stored within a floating structure. *Water*, *11*(1), 50.

GeinE. (2020). Sesam-genie manual. *Det Norske Veritas (DNV), Oslo, Norway*. Retrieved from www.dnv.com

Global Wind Atlas. (2021). *The global wind atlas: Gwa 3.1.* Europe. Retrieved from www.globalwindatlas.info

Gon†calves, R. T., Chame, M. E., Silva, L. S., Koop, A., Hirabayashi, S., & Suzuki, H. (2021). Experimental flow-induced motions of a fowt semi-submersible type (oc4 phase ii floater). *Journal of Offshore Mechanics and Arctic Engineering*, *143*(1), 012004.

Gon†calves, R. T., Pinto, L. A., & Fujarra, A. L. (2020). Experimental study on vortex-induced motions of a semi-submersible platform with four square columns, part iii: Effects of the collinear irregular and regular wave incidence and current. *Ocean Engineering*, *217*, 107585.

Gon†calves, R. T., Rosetti, G. F., Fujarra, A. L., & Oliveira, A. C. (2013). Experimental study on vortex-induced motions of a semi-submersible platform with four square columns, part ii: Effects of surface waves, external damping and draft condition. *Ocean engineering*, *62*, 10–24.

Goupee, A. J., Koo, B. J., Kimball, R. W., Lambrakos, K. F., & Dagher, H. J. (2014). Experimental comparison of three floating wind turbine concepts. *Journal of Offshore Mechanics and Arctic Engineering*, *136*(2), 020906.

Grant, W. D., & Madsen, O. S. (1979). Combined wave and current interaction with a rough bottom. *Journal of Geophysical Research: Oceans*, *84*(C4), 1797–1808.

Gueydon, S., Judge, F. M., O'shea, M., Lyden, E., Le Boulluec, M., Caverne, J., ... others (2021). Round robin laboratory testing of a scaled 10 mw floating horizontal axis wind turbine. *Journal of Marine Science and Engineering*, *9*(9), 988.

GWEC. (2022). Global wind report 2022. *Global Wind Energy Council: Brussels, Belgium*.

Hall, M., Buckham, B., & Crawford, C. (2014). Evaluating the importance of mooring line model fidelity in floating offshore wind turbine simulations. *Wind energy*, *17*(12), 1835–1853.

Hall, M., & Goupee, A. (2015). Validation of a lumped-mass mooring line model with deepcwind semisubmersible model test data. *Ocean Engineering*, *104*, 590–603.

Hanssen, J. E. (2023). *Floating wind power: Multi-use at sea using the w2power platform as an innovation tool.* Congleton, Cheshire: Innovation News Network - Energy. Retrieved from https://www.innovationnewsnetwork.com/floating-wind-power-multi-use-at-sea-using-w2power-platform-innovation-tool/35889/ (12th September)

Hanssen, J. E., Margheritini, L., Mayorga, P., Hezari, R., O'Sullivan, K., Martinez, I., ... Ingram, D. (2015). Design and performance validation of a hybrid offshore renewable energy platform: A path to cost-efficient development of deepwater marine energy resources. *the10th International Conference on Ecological Vehicles and Renewable Energies, EVER 2015*.

Haselsteiner, A. F., Lehmkuhl, J., Pape, T., Windmeier, K.-L., & Thoben, K.-D. (2019). Virocon: A software to compute multivariate extremes using the environmental contour method. *SoftwareX*, *9*, 95–101.

Hashemi, M. R., Grilli, S. T., & Neill, S. P. (2016). A simplified method to estimate tidal current effects on the ocean wave power resource. *Renewable energy*, *96*, 257–269.

Hassan, A. M., Downie, M. J., Incecik, A., Baarholm, R., Berthelsen, P., Pakozdi, C., & Stansberg, C. (2009). Contribution of the mooring system to the low-frequency motions of a semisubmersible in combined wave and current. In *International conference on offshore mechanics and arctic engineering* (Vol. 43413, pp. 55–62).

Hasselmann, K., Barnett, T. P., Bouws, E., Carlson, H., Cartwright, D. E., Enke, K., ... others (1973). Measurements of wind-wave growth and swell decay during the joint north sea wave project (jonswap). *Ergaenzungsheft zur Deutschen Hydrographischen Zeitschrift, Reihe A*.

Hedges, & Lee. (1992). The equivalent uniform current in wave-current computations. *Coastal engineering*, *16*(3), 301–311.

Hedges, T. (1981). Some effects of currents on wave spectra. In *Proceedings of the first indian conference in ocean engineering* (Vol. 1, pp. 30–35).

Hedges, T. (1987). Combinations of waves and currents: an introduction. *Proceedings of the Institution of Civil Engineers*, *82*(3), 567–585.

Hedges, T. S., Anastasiou, K., & Gabriel, D. (1985). Interaction of random waves and currents. *Journal of waterway, port, coastal, and ocean engineering*, *111*(2), 275–288.

Henderson, A., Leutz, R., & Fujii, T. (2002). Potential for floating offshore wind energy in japanese waters. *The Twelfth (2002) International Offshore and Polar Engineering Conference*.

Henderson, A., Watson, G. M., Patel, M. H., & Halliday, J. A. (2000). Floating offshore wind farms—an option. *Proceedings of the offshore wind energy in mediterranean and other European seas, Siracusa, Sicilia, Italy*.

Henderson, A. R. (2000). *Analysis tools for large floating offshore wind farms*. University of London, University College London (United Kingdom).

Hintze, J. L., & Nelson, R. D. (1998). Violin plots: a box plot-density trace synergism. *The American Statistician*, *52*(2), 181–184.

Hocking, G., & Forbes, L. (1992). Subcritical free-surface flow caused by a line source in a fluid of finite depth. *Journal of engineering mathematics*, *26*(4), 455–466.

Hsu, W.-Y., Yang, R.-Y., Chang, F.-N., Wu, H.-T., & Chen, H.-H. (2016). Experimental study of floating offshore platform in combined wind/wave/current environment. *International Journal of Offshore and Polar Engineering*, *26*(02), 125–131.

Hu, C., Sueyoshi, M., Liu, C., Kyozuka, Y., & Ohya, Y. (2013). Numerical and experimental study on a floating platform for offshore renewable energy. In *International conference on offshore mechanics and arctic engineering* (Vol. 55423, p. V008T09A069).

Hu, Y., Yang, J., Baniotopoulos, C., Wang, X., & Deng, X. (2020). Dynamic analysis of offshore steel wind turbine towers subjected to wind, wave and current loading during construction. *Ocean Engineering*, *216*, 108084.

Huang, H., & Chen, H.-C. (2020). Investigation of mooring damping effects on vortex-induced motion of a deep draft semi-submersible by coupled cfd-fem analysis. *Ocean Engineering*, *210*, 107418.

Huang, N. E., Chen, D. T., Tung, C.-C., & Smith, J. R. (1972). Interactions between steady won-uniform currents and gravity waves with applications for current measurements. *Journal of Physical Oceanography*, *2*(4), 420–431.

Huo, F., Xu, J., Yang, H., Yuan, Z., & Shen, Z. (2023). Study on characteristics of mooring system of a new floating offshore wind turbine in shallow water by experiment. *Frontiers in Energy Research*, *10*, 1007996.

IEC-61400-3. (2009). International electrotechnical committee iec 61400-3: Wind turbines part 3: Design requirements for offshore wind turbines. *Proceedings of the IEC, Geneva*.

Iijima, K., Kim, J., & Fujikubo, M. (2010). Coupled aerodynamic and hydroelastic analysis of an offshore floating wind turbine system under wind and wave loads. In *International conference on offshore mechanics and arctic engineering* (Vol. 49118, pp. 241–248).

Ingram, D., Wallace, R., Robinson, A., & Bryden, I. (2014). The design and commissioning of the first, circular, combined current and wave test basin. In *Proceedings of the oceans.*

Ingram, D. M. (2011). *Protocols for the equitable assessment of marine energy converters*. Lulu. com.

INNWIND.EU. (2020). *Innovative wind conversion systems (10-20mw) for offshore applications.* Retrieved from http://www.innwind.eu/

IPCC. (2023). *Urgent climate action can secure a liveable future for all* (Tech. Rep. No. March). Interlaken, Switzerland: Intergovernmental panel on climate change.

IRENA, I. (2019). Future of wind: Deployment, investment, technology, grid integration and socio-economic aspects. *Abu Dhabii*.

Isaacson, M., & Cheung, K. F. (1993). Time-domain solution for wave—current interactions with a two-dimensional body. *Applied Ocean Research*, *15*(1), 39–52.

Ishihara, Phuc, P., & Sukegawa, H. (2007). A numerical study on the dynamic response of a floating offshore wind turbine system due to resonance and nonlinear wave. In *Proceedings of the european offshore wind conference (eow2007), berlin, germany* (pp. 4–6).

Ishihara, T., & Liu, Y. (2020). Dynamic response analysis of a semi-submersible floating wind turbine in combined wave and current conditions using advanced hydrodynamic models. *Energies*, *13*(21), 5820.

Ishihara, T., Phuc, P. V., Sukegawa, H., Shimada, K., & Ohyama, T. (2007). A study on the dynamic response of a semi-submersible floating offshore wind turbine system part 1: A water tank test. In *Proceedings of the 12th international conference on wind engineering* (pp. 2511–2518).

Ismail, N. M. (1984). Wave-current models for design of marine structures. *Journal of waterway, port, coastal, and ocean engineering*, *110*(4), 432–447.

Iwagaki, Y., & Asano, T. (1984). Hydrodynamic forces on a circular cylinder due to combined wave and current loading. *Coastal Engineering Proceedings*(19), 191–191.

Iyer, S., Thomson, J., Thompson, E., & Drushka, K. (2022). Variations in wave slope and momentum flux from wave-current interactions in the tropical trade winds. *Journal of Geophysical Research: Oceans*, *127*(3), e2021JC018003.

Jang, H., Kim, H., Kim, M., & Kim, K. (2015). Coupled dynamic analysis for multi-unit floating offshore wind turbine in maximum operational and survival conditions. In *International conference on offshore mechanics and arctic engineering* (Vol. 56574, p. V009T09A070).

Jang, H.-K., Park, S., Kim, M.-H., Kim, K.-H., & Hong, K. (2019). Effects of heave plates on the global performance of a multi-unit floating offshore wind turbine. *Renewable energy*, *134*, 526–537.

Janssen, P. A. (1989). Wave-induced stress and the drag of air flow over sea waves. *Journal of Physical Oceanography*, *19*(6), 745–754.

Jian, Y., Zhan, J., & Zhu, Q. (2008). Short crested wave–current forces around a large vertical circular cylinder. *European Journal of Mechanics-B/Fluids*, *27*(3), 346–360.

Jin, S., Brown, S. A., Tosdevin, T., Hann, M., & Greaves, D. (2022). Laboratory investigation on short design wave extreme responses for floating hinged-raft wave energy converters. *Frontiers in Energy Research*, *10*, 1069108.

Jonkman, & Buhl, J. (2007). Loads analysis of a floating offshore wind turbine using fully coupled simulation. In *Proceedings of the windpower conference & exhibition.* Los Angeles, California, USA.

Jonkman, B., & Kilcher, L. (2012). Turbsim user's guide: version 1.06. 00. *National Renewable Energy Laboratory: Golden, CO, USA*.

Jonkman, J. (2010a). *Definition of the floating system for phase iv of oc3* (Tech. Rep.). Golden, Colorado, USA: National Renewable Energy Lab.(NREL).

Jonkman, J. (2010b). *Definition of the floating system for phase iv of oc3* (Tech. Rep.). National Renewable Energy Lab.(NREL), Golden, CO (United States).

Jonkman, J., Butterfield, S., Musial, W., & Scott, G. (2009). *Definition of a 5-mw reference wind turbine for offshore system development* (Tech. Rep.). National Renewable Energy Lab.(NREL), Golden, CO (United States).

Jonkman, J. M. (2007). *Dynamics modeling and loads analysis of an offshore floating wind turbine*. University of Colorado at Boulder.

Jonkman, J. M., & Jonkman, B. J. (2016). Fast modularization framework for wind turbine simulation: full-system linearization. In *Journal of physics: Conference series* (Vol. 753, p. 082010).

Jonkman, J. M., & Matha, D. (2011). Dynamics of offshore floating wind turbines—analysis of three concepts. *Wind Energy*, *14*(4), 557–569.

Jonsson, I. G. (1966). *The friction factor for a current superimposed by waves*. Coastal engineering laboratory, hydraulic laboratory, technical University ....

Jonsson, I. G. (1990). Wave-current interactions. *The Sea, A*, *9*, 65–120.

Jonsson, I. G., & Carlsen, N. A. (1976). Experimental and theoretical investigations in an oscillatory turbulent boundary layer. *Journal of Hydraulic Research*, *14*(1), 45–60.

Jonsson, I. G., Skougaard, C., & Wang, J. D. (1970). Interaction between waves and currents. In *Coastal engineering 1970* (pp. 489–507).

Ju, X., Amaechi, C. V., Dong, B., Meng, X., & Li, J. (2023). Numerical analysis of fishtailing motion, buoy kissing and pullback force in a catenary anchor leg mooring (calm) moored tanker system. *Ocean Engineering*, *278*, 114236.

Kallesoe, B., Paulson, U., Køhler, A., & Hansen, H. (2011). Aero-hydro-elastic response of a floating platform supporting several wind turbines. In *49th aiaa aerospace sciences meeting including the new horizons forum and aerospace exposition* (p. 721).

Kane, T. R. (1961). Dynamics of nonholonomic systems. *Journal of Applied Mechanics*, *28*(4), 574–578.

Kang, H., Kim, M.-H., Kim, K.-H., & Hong, K. (2017). Hydroelastic analysis of multi-unit floating offshore wind turbine platform (mufowt). In *Isope international ocean and polar engineering conference* (pp. ISOPE–I).

Karimirad, M., & Collu, M. (2020). *Assessment and nonlinear modeling of wave, tidal and wind energy converters and turbines*. MDPI AG.

Kemp, P., & Simons, R. (1982). The interaction between waves and a turbulent current: waves propagating with the current. *Journal of Fluid Mechanics*, *116*, 227–250.

Kemp, P., & Simons, R. (1983). The interaction of waves and a turbulent current: waves propagating against the current. *Journal of fluid mechanics*, *130*, 73–89.

Kim, D., & Kim, M. (1997). Wave-current interaction with a large three-dimensional body by thobem. *Journal of ship research*, *41*(04), 273–285.

Kim, H. (2018). *Global performances and structural health monitoring method of single unit or multi units floating offshore wind turbines* (Unpublished doctoral dissertation). Department of Civil Engineering.

Kim, H., O'Connor, B. A., Park, I., & Lee, Y. (2001). Modeling effect of intersection angle on near-bed flows for waves and currents. *Journal of waterway, port, coastal, and ocean engineering*, *127*(6), 308–318.

Kim, H.-C., Kim, K.-H., Kim, M.-H., & Hong, K. (2017). Global performance of a kriso semisubmersible multiunit floating offshore wind turbine: Numerical simulation vs. model test. *International Journal of Offshore and Polar Engineering*, *27*(01), 70–81.

Kim, K. H., Hong, J. P., Park, S., Lee, K., & Hong, K. (2016). An experimental study on dynamic performance of large floating wave-offshore hybrid power generation platform in extreme conditions. *Journal of the Korean Society for Marine Environment & Energy*, *19*(1), 7–17.

Kim, S.-J., & Kim, M. (2022). The nonlinear wave and current effects on fixed and floating bodies by a three-dimensional fully-nonlinear numerical wave tank. *Ocean Engineering*, *245*, 110458.

Kim, S.-Y., Kim, K.-M., Park, J.-C., Jeon, G.-M., & Chun, H.-H. (2016). Numerical simulation of wave and current interaction with a fixed offshore substructure. *International Journal of naval Architecture and ocean engineering*, *8*(2), 188–197.

Kinoshita, T., & Bao, W. (1996). Hydrodynamic forces acting on a circular cylinder oscillating in waves and a small current. *Journal of marine science and technology*, *1*, 155–173.

Kristiansen, T., & Faltinsen, O. M. (2015). Experimental and numerical study of an aquaculture net cage with floater in waves and current. *Journal of Fluids and Structures*, *54*, 1–26.

Lamb, H. (1932). *Hydrodynamics* (6th ed., Vol. 1-8). Cambridge , United Kingdom: Cambridge University Press.

Lamei, A., Hayatdavoodi, M., & Riggs, H. R. (2023). Motion and elastic response of wind-tracing floating offshore wind turbines. *Journal of Ocean Engineering and Marine Energy*, *9*(1), 43–67.

Latheef, M., Abdulla, N., & Jupri, M. F. M. (2018). Wave current interaction: Effect on force prediction for fixed offshore structures. In *Matec web of conferences* (Vol. 203, p. 01011).

Legaz, M. J., Coronil, D., Mayorga, P., & Fernández, J. (2018). Study of a hybrid renewable energy platform: W2power. In *International conference on offshore mechanics and arctic engineering* (Vol. 51326, p. V11AT12A040).

Li, S., Lamei, A., Hayatdavoodi, M., & Wong, C. (2019). Concept design and analysis of wind-tracing floating offshore wind turbines. In *International conference on offshore mechanics and arctic engineering* (Vol. 59353, p. V001T01A014).

Li, X., Xiao, Q., Gon†calves, R. T., & Peyrard, C. (2022). A coupled wave-current-structure study for a floating offshore wind turbine platform. In *International conference on offshore mechanics and arctic engineering* (Vol. 85925, p. V007T08A027).

Li, X., Xiao, Q., Wang, E., Peyrard, C., & Gon†calves, R. T. (2023). The dynamic response of floating offshore wind turbine platform in wave-current condition. *Physics of Fluids*, *35*(8).

Li, Y., Liu, L., Zhu, Q., Guo, Y., Hu, Z., & Tang, Y. (2018). Influence of vortex-induced loads on the motion of spar-type wind turbine: A coupled aero-hydro-vortex-mooring investigation. *Journal of Offshore Mechanics and Arctic Engineering*, *140*(5), 051903.

Liang, F., Jia, X., Zhang, H., Wang, C., & Shen, P. (n.d.). Seismic responses of offshore wind turbines based on a lumped parameter model subjected to complex marine loads at scoured sites. *Available at SSRN 4573135*.

Liang, F., Yuan, Z., Liang, X., & Zhang, H. (2022). Seismic response of monopile-supported offshore wind turbines under combined wind, wave and hydrodynamic loads at scoured sites. *Computers and Geotechnics*, *144*, 104640.

Lim, K. Y., & Madsen, O. S. (2016). An experimental study on near-orthogonal wave–current interaction over smooth and uniform fixed roughness beds. *Coastal Engineering*, *116*, 258–274.

Lin, J., Jeng, D.-S., Zhao, H., Gao, Y., Liu, J., & Guo, Y. (2023). Recent advances of seabed liquefaction around the vicinity of marine structures. *Ocean Engineering*, *280*, 114660.

Lir NOTF. (2009). *Lir national ocean test facility.* MaREI Centre at University College Cork, Cork, Ireland. Retrieved from www.lir-notf.com

Liu, A. Y., Su, Z., Chen, J., Yu, H., Duggal, A., & Kolb, J. A. (2023). Evaluation of a 15 mw turret moored floating offshore wind turbine. In *Offshore technology conference* (p. D011S012R002).

Liu, B., & Yu, J. (2022). Effect of mooring parameters on dynamic responses of a semi-submersible floating offshore wind turbine. *Sustainability*, *14*(21), 14012.

Liu, M., Xiao, L., Liang, Y., & Tao, L. (2017). Experimental and numerical studies of the pontoon effect on vortex-induced motions of deep-draft semi-submersibles. *Journal of Fluids and Structures*, *72*, 59–79.

Liu, Y., Ge, D., Bai, X., & Li, L. (2023). A cfd study of vortex-induced motions of a semi-submersible floating offshore wind turbine. *Energies*, *16*(2), 698.

Liu, Y., Xiao, Q., Incecik, A., & Peyrard, C. (2019). Aeroelastic analysis of a floating offshore wind turbine in platform-induced surge motion using a fully coupled cfd-mbd method. *Wind Energy*, *22*(1), 1–20.

Liu, Z., Lin, Z., Tao, L., & Lan, J. (2016). Nonlinear wave–current interaction in water of finite depth. *Journal of Waterway, Port, Coastal, and Ocean Engineering*, *142*(6), 04016009.

Liu, Z., Tu, Y., Wang, W., & Qian, G. (2019). Numerical analysis of a catenary mooring system attached by clump masses for improving the wave-resistance ability of a spar buoy-type floating offshore wind turbine. *Applied Sciences*, *9*(6), 1075.

Longuet-Higgins, M. S., & Stewart, R. (1961). The changes in amplitude of short gravity waves on steady non-uniform currents. *Journal of fluid mechanics*, *10*(4), 529–549.

Longuet-Higgins, M. S., & Stewart, R. (1964). Radiation stresses in water waves; a physical discussion, with applications. In *Deep sea research and oceanographic abstracts* (Vol. 11, pp. 529–562).

Longuet-Higgins, M. S., & Stewart, R. W. (1960, Sep). Changes in the form of short gravity waves on long waves and tidal currents. *Journal of Fluid Mechanics*, *8*(04), 565.

MARINA. (2010). *Marina platform (marine renewable integrated application platform).* Europe. Retrieved from https://cordis.europa.eu/project/id/241402 (Jan 2010 - Jun 2014)

Martín San Román, R. (2022). *Coupled dynamics of multi wind turbine floating platforms* (Unpublished doctoral dissertation). Espacio.

Massel, S. R. (1996). *Ocean surface waves: their physics and prediction* (Vol. 11). World scientific.

Masson, D. (1996). A case study of wave–current interaction in a strong tidal current. *Journal of physical oceanography*, *26*(3), 359–372.

Matha, D., Schlipf, M., Pereira, R., & Jonkman, J. (2011). Challenges in simulation of aerodynamics, hydrodynamics, and mooring-line dynamics of floating offshore wind turbines. In *Isope international ocean and polar engineering conference* (pp. ISOPE–I).

Maximiano, A., Koop, A., de Wilde, J., & Gon†calves, R. T. (2017). Experimental study on the vortex-induced motions (vim) of a semi-submersible floater in waves. In *International conference on offshore mechanics and arctic engineering* (Vol. 57748, p. V07BT06A016).

Mayorga, P. (2016). Experimental validation of the w2power hybrid floating platform. In *13th deep sea offshore wind r&d conference, trondheim (norway)* (pp. ISOPE–I).

Mehernosh, I., & Lyle, F. (2005). Improved strake design for vortex induced motions of spar platforms. In *Proceedings of the 24th international conference on offshore mechanics and arctic engineering.*

Mei, X., & Xiong, M. (2021). Effects of second-order hydrodynamics on the dynamic responses and fatigue damage of a 15 mw floating offshore wind turbine. *Journal of Marine Science and Engineering*, *9*(11), 1232.

Meinshausen, M., Lewis, J., McGlade, C., Gütschow, J., Nicholls, Z., Burdon, R., ... Hackmann, B. (2022). Realization of paris agreement pledges may limit warming just below 2 c. *Nature*, *604*(7905), 304–309.

Mekias, H., & Vanden-Broeck, J.-M. (1989). Supercritical free-surface flow with a stagnation point due to a submerged source. *Physics of Fluids A: Fluid Dynamics*, *1*(10), 1694–1697.

Mekias, H., & Vanden-Broeck, J.-M. (1991). Subcritical flow with a stagnation point due to a source beneath a free surface. *Physics of Fluids A: Fluid Dynamics*, *3*(11), 2652–2658.

Meng, L., He, Y., Zhou, T., Zhao, Y., & Liu, Y. (2018). Research on dynamic response characteristics of 6mw spar-type floating offshore wind turbine. *Journal of Shanghai Jiaotong University (Science)*, *23*, 505–514.

Miloh, T., & Tyvand, P. A. (1993). Nonlinear transient free-surface flow and dip formation due to a point sink. *Physics of Fluids A: Fluid Dynamics*, *5*(6), 1368–1375.

Moës, N., Cloirec, M., Cartraud, P., & Remacle, J.-F. (2003). A computational approach to handle complex microstructure geometries. *Computer methods in applied mechanics and engineering*, *192*(28-30), 3163–3177.

Mohamed, H. (2011). *Hydrodynamic loading and responses of semisubmersibles* (Unpublished doctoral dissertation). University of Newcastle Upon Tyne.

Moreira. (2001). *Nonlinear interactions between water waves, free surface flows and singularities* (Unpublished doctoral dissertation). University of Bristol.

Moreira, & Peregrine, D. (2012). Nonlinear interactions between deep-water waves and currents. *Journal of Fluid Mechanics*, *691*, 1–25.

Moreira, & Peregrine, D. H. (2010). Nonlinear interactions between a free-surface flow with surface tension and a submerged cylinder. *Journal of fluid mechanics*, *648*, 485–507.

Morison, J., Johnson, J. W., & Schaaf, S. A. (1950). The force exerted by surface waves on piles. *Journal of Petroleum Technology*, *2*(05), 149–154.

Moulas, D., Shafiee, M., & Mehmanparast, A. (2017). Damage analysis of ship collisions with offshore wind turbine foundations. *Ocean Engineering*, *143*, 149–162.

Murfet, T., & Abdussamie, N. (2019). Loads and response of a tension leg platform wind turbine with non-rotating blades: An experimental study. *Journal of Marine Science and Engineering*, *7*(3), 56.

Myhr, A., Bjerkseter, C., Ågotnes, A., & Nygaard, T. A. (2014). Levelised cost of energy for offshore floating wind turbines in a life cycle perspective. *Renewable energy*, *66*, 714–728.

Myrhaug, D. (1995). Bottom friction beneath random waves. *Coastal Engineering*, *24*(3-4), 259–273.

Myrhaug, D., Holmedal, L. E., Simons, R. R., & MacIver, R. D. (2001). Bottom friction in random waves plus current flow. *Coastal engineering*, *43*(2), 75–92.

Natarajan, A., Jensen, P., Rasmussen, F., & Chaviaropoulos, P. (2014). Innovative wind conversion systems (10-20 mw) for offshore applications. *In: Proceedings of EWEA. Vienna, Austria*.

Nestegård, A., Ronæss, M., Hagen, Ø., Ronold, K., & Bitner-Gregersen, E. M. (2019). Recommended practice dnv-rp-c205: On environmental conditions and environmental loads.

Netzband, S., Schulz, C., & Abdel-Maksoud, M. (2020). Passive self-aligning of a floating offshore wind turbine. In *Journal of physics: Conference series* (Vol. 1618, p. 052027).

Nguyen, H. X. (2022). *Dynamic response of spar-type floating offshore wind turbines: Eulerian and lagrangian approaches* (Unpublished doctoral dissertation). Trinity College Dublin. School of Engineering.

Nguyen, P. T., Manuel, L., & Coe, R. G. (2019). On the development of an efficient surrogate model for predicting long-term extreme loads on a wave energy converter. *Journal of Offshore Mechanics and Arctic Engineering*, *141*(6), 061103.

NKUA-AM&WFG. (2021). *Long-term hincast data from: Atmospheric modeling and weather forecasting group (am&wfg).* National & Kapodistrian University of Athens, Athens, Greece. Retrieved from https://forecast.uoa.gr/en/group

NMRI. (2006). *National maritime research institute (nmri).* National Maritime Research Institute, Tokyo, Japan. Retrieved from www.nmri.go.jp

Noble, D. R. (2018). *Combined wave-current scale model testing at flowave* (Unpublished doctoral dissertation). Engineering.

Noble, D. R., Davey, T., Smith, H. C., Kaklis, P., Robinson, A., & Bruce, T. (2015). Spatial variation in currents generated in the flowave ocean energy research facility. In *Proceedings of the 11th european wave and tidal energy conference (ewtec2015)* (pp. 1–8).

Noble, D. R., Draycott, S., Nambiar, A., Sellar, B. G., Steynor, J., & Kiprakis, A. (2020). Experimental assessment of flow, performance, and loads for tidal turbines in a closely-spaced array. *Energies*, *13*(8), 1977.

Nossen, J., Grue, J., & Palm, E. (1991). Wave forces on three-dimensional floating bodies with small forward speed. *Journal of Fluid Mechanics*, *227*, 135–160.

Nwogu, O. (1993). Effect of steady currents on directional wave spectra. *Proc.12th Intl Conf on Offshore Mechanics & Arctic Engng, Glasgow, UK*.

OrcaFlex. (2023). Orcaflex manual. *Orcina Ltd, Cumbria, UK*. Retrieved from www.orcina.com

OrcaWave. (2023). Orcawave manual. *Orcina Ltd, Cumbria, UK*. Retrieved from www.orcina.com

OrcFxAPI. (2024). Orcfxapi: Orcaflex python interface. *Orcina Ltd, Cumbria, UK*. Retrieved from www.orcina.com

Otter, A., Desmond, C., Flannery, B., & Murphy, J. (2022). Combined current and wind simulation for floating offshore wind turbines. In *Journal of physics: Conference series* (Vol. 2362, p. 012028).

Otter, A., Flannery, B., Murphy, J., & Desmond, C. (2022). Current simulation with software in the loop for floating offshore wind turbines. In *Journal of physics: Conference series* (Vol. 2265, p. 042028).

Palm, J., Eskilsson, C., Paredes, G. M., & Bergdahl, L. (2016). Coupled mooring analysis for floating wave energy converters using cfd: Formulation and validation. *International Journal of Marine Energy*, *16*, 83–99.

Pan, Z., Vada, T., Finne, S., Nestegård, A., Hoff, J. R., Hermundstad, E. M., & Stansberg, C. T. (2016). Benchmark study of numerical approaches for wave-current interaction problem of offshore floaters. In *International conference on offshore mechanics and arctic engineering* (Vol. 49927, p. V001T01A024).

Papandroulakis, N., Thomsen, C., Mintenbeck, K., Mayorga, P., & Hernández-Brito, J. J. (2017). The eu-project 'tropos'. In B. H. Buck & R. Langan (Eds.), *Aquaculture perspective of multi-use sites in the open ocean: The untapped potential for marine resources in the anthropocene* (pp. 355–374). Springer Nature.

Pascal, R., Lucas, J., Ingram, D., & Bryden, I. (2009). Assessing and improving the edinburgh curved wave tank. In *Isope international ocean and polar engineering conference* (pp. ISOPE–I).

Peeringa, J. M. (2014). Fatigue loading on a 5mw offshore wind turbine due to the combined action of waves and current. In *Journal of physics: Conference series* (Vol. 524, p. 012093).

Pegalajar-Jurado, A., Borg, M., & Bredmose, H. (2018). An efficient frequency-domain model for quick load analysis of floating offshore wind turbines. *Wind Energy Science*, *3*(2), 693–712.

Peregrine, D. H. (1976). Interaction of water waves and currents. *Advances in applied mechanics*, *16*, 9–117.

Peters, H., & Boonstra, H. (1988). Fatigue loading on a single pile platform due to combined action of waves and currents. In *Intl. conference on behaviour of offshore structures (boss '88), vol. 3: Structures* (Vol. 3, p. 1015). Trondheim, Norway. (21 pp., 6 ref., 10 fig.)

Phillips, . M. (1977). The dynamics of the upper ocean. *Journal of Fluid Mechanics*, *88*(4), 793–796.

Pierson Jr, W. J., & Moskowitz, L. (1964). A proposed spectral form for fully developed wind seas based on the similarity theory of sa kitaigorodskii. *Journal of geophysical research*, *69*(24), 5181–5190.

Pillai, Gordelier, T., Thies, P., Cuthill, D., & Johanning, L. (2022). Anchor loads for shallow water mooring of a 15 MW floating wind turbine—Part II: Synthetic and novel mooring systems. *Ocean Engineering*, *266*, 112619.

Pillai, Gordelier, T., Thies, P., Dormenval, C., Wray, B., Parkinson, R., & Johanning, L. (2022b). Anchor loads for shallow water mooring of a 15 MW floating wind turbine—Part I: Chain catenary moorings for single and shared anchor scenarios. *Ocean Engineering*, *266*, 111816.

Pillai, A. C., Davey, T., & Draycott, S. (2021). A framework for processing wave buoy measurements in the presence of current. *Applied Ocean Research*, *106*, 102420.

Pillai, A. C., Thies, P. R., & Johanning, L. (2018a). Mooring system design optimization using a surrogate assisted multi-objective genetic algorithm. *Engineering Optimization*.

Pillai, A. C., Thies, P. R., & Johanning, L. (2018b). Optimization of mooring line axial stiffness characteristics for offshore renewable energy applications. In *Isope international ocean and polar engineering conference* (pp. ISOPE–I).

Pillai, A. C., Thies, P. R., & Johanning, L. (2019). Impact of simulation duration for offshore floating wind turbine analysis using a coupled fast-orcaflex model. In *International conference on offshore mechanics and arctic engineering* (Vol. 58899, p. V010T09A063).

Prandle, D. (1982). The vertical structure of tidal currents. *Geophysical & astrophysical fluid dynamics*, *22*(1-2), 29–49.

Qu, X., Li, Y., Tang, Y., Hu, Z., Zhang, P., & Yin, T. (2020). Dynamic response of spar-type floating offshore wind turbine in freak wave considering the wave-current interaction effect. *Applied Ocean Research*, *100*, 102178.

Ranasoma, K. M., & Sleath, J. F. (1994). Combined oscillatory and steady flow over ripples. *Journal of waterway, port, coastal, and ocean engineering*, *120*(4), 331–346.

Recharge. (Jan 12, 2024). *World's first floating wind farm Hywind Scotland faces shutdown for 'heavy maintenance.* Oslo (Norway), London (UK): Recharge Magazine. Retrieved from https://www.rechargenews.com/wind/worlds-first-floating-wind-farm-hywind-scotland-faces-shutdown-for-heavy-maintenance/2-1-1582273

Ren, N., Li, Y., & Ou, J. (2010). The motion performance of two offshore wind turbine floating platforms with combined tension leg-mooring line system. In *Isope pacific/asia offshore mechanics symposium* (pp. ISOPE–P).

Robertson, A. N., & Jonkman, J. M. (2011). Loads analysis of several offshore floating wind turbine concepts. *International Ocean and Polar Engineering Conference (ISOPE-I-11-204)*.

Robertson, A. N., Jonkman, J. M., Goupee, A. J., Coulling, A. J., Prowell, I., Browning, J., ... Molta, P. (2013). Summary of conclusions and recommendations drawn from the deepcwind scaled floating offshore wind system test campaign. In *International conference on offshore mechanics and arctic engineering* (Vol. 55423, p. V008T09A053).

Robinson, A., Ingram, D., Bryden, I., & Bruce, T. (2015a). The effect of inlet design on the flow within a combined waves and current flumes, test tank and basins. *Coastal Engineering*, *95*, 117–129.

Robinson, A., Ingram, D., Bryden, I., & Bruce, T. (2015b). The generation of 3d flows in a combined current and wave tank. *Ocean Engineering*, *93*, 1–10.

Roddier, D., Finnigan, T., & Liapis, S. (2009). Influence of the reynolds number on spar vortex induced motions (vim): multiple scale model test comparisons. In *International conference on offshore mechanics and arctic engineering* (Vol. 43451, pp. 797–806).

Rogers, N., & Still, D. (1999). Structural dynamics of offshore wind turbines subject to extreme wave loading. In *Ewec-conference-* (pp. 369–374).

Rognebakke, O. (2002). Sloshing in rectangular tanks and interaction with ship motions.

Rotor, M. A. (2023). *Multidisciplinary design optimization of horizontal-axis tidal turbine blades for tropical site conditions in a shear-flow environment with wave-current interaction* (Unpublished doctoral dissertation). State University of New York at Stony Brook.

Rusu, L., & Guedes Soares, C. (2007). Modelling of the wave-current interactions in tagus estuary. *Maritime industry, ocean engineering and coastal resources*, *2*, 801–810.

Rusu, L., & Soares, C. G. (2011). Modelling the wave–current interactions in an offshore basin using the swan model. *Ocean Engineering*, *38*(1), 63–76.

Ryu, S., Kim, M., & Lynett, P. J. (2003). Fully nonlinear wave-current interactions and kinematics by a bem-based numerical wave tank. *Computational mechanics*, *32*, 336–346.

SAITEC. (2023). *Demosath - rwe: Saitec.* Bilbao, Spain. Retrieved from https://www.rwe.com/en/our-energy/discover-renewables/floating-offshore-wind/demosath/ (Accessed: September 14, 2023)

Sandner, F., Wie, Y., Matha, D., Grela, E., Azcona, J., Munduate, X., ... Natarajan, A. (2015). *Innwind.eu deliverable 4.3.3 - innovative concepts for floating structures* (Tech. Rep.). INNWIND.EU: Partners WP4 Task 4.3: USTUTT, DTU, CENER, NTUA.

Santo, H., Stagonas, D., Buldakov, E., & Taylor, P. (2017). Current blockage in sheared flow: Experiments and numerical modelling of regular waves and strongly sheared current through a space-frame structure. *Journal of Fluids and Structures*, *70*, 374-389.

Santo, H., Taylor, P. H., Bai, W., & Choo, Y. S. (2015). Current blockage in a numerical wave tank: 3d simulations of regular waves and current through a porous tower. *Computers & Fluids*, *115*, 256–269.

Sarkar, S., Chen, L., Fitzgerald, B., & Basu, B. (2020). Multi-resolution wavelet pitch controller for spar-type floating offshore wind turbines including wave-current interactions. *Journal of Sound and Vibration*, *470*, 115170.

Saruwatari, A., Ingram, D. M., & Cradden, L. (2013). Wave–current interaction effects on marine energy converters. *Ocean Engineering*, *73*, 106–118.

SCD-Nezzy^2. (2014). *aerodyn engineering gmbh.* Büdelsdorf, Germany. Retrieved from http://www.scd-technology.com/scd-technology-scd-nezzy/

Schnepf, A. (2019). *New technology demonstration project for a floating offshore wind turbine foundation with guy wire supported tower* (MSc Thesis). Université de Liège, Liège, Belgique.

Scotstream Generation Limited. (2023). *Marine energy technology: Weathervaning floating structure.* Brechin, Angus, UK. Retrieved from https://scotstream.scot/ (Accessed: October 2023)

Sellar, B. G., Sutherland, D. R., Ingram, D. M., & Venugopal, V. (2017). Measuring waves and currents at the european marine energy centre tidal energy test site: Campaign specification, measurement methodologies and data exploitation. In *Oceans 2017-aberdeen* (pp. 1–7).

Seo, M. G., Ha, Y. J., Nam, B. W., & Kim, Y. (2021). Experimental and numerical analysis of wave drift force on kvlcc2 moving in oblique waves. *Journal of Marine Science and Engineering*, *9*(2), 136.

Shen, Y., Greco, M., Faltinsen, O. M., & Nygaard, I. (2018). Numerical and experimental investigations on mooring loads of a marine fish farm in waves and current. *Journal of Fluids and Structures*, *79*, 115–136.

Shin, H. (2011). Model test of the oc3-hywind floating offshore wind turbine. In *The twenty-first international offshore and polar engineering conference.*

Shittu, A. A., Mehmanparast, A., Wang, L., Salonitis, K., & Kolios, A. (2020). Comparative study of structural reliability assessment methods for offshore wind turbine jacket support structures. *Applied Sciences*, *10*(3), 860.

Silva, L., Cazzolato, B., Sergiienko, N., & Ding, B. (2021). Nonlinear dynamics of a floating offshore wind turbine platform via statistical quadratization—mooring, wave and current interaction. *Ocean Engineering*, *236*, 109471.

Silva, M., Vitola, M., Esperanca, P., Sphaier, S., & Levi, C. (2016). Numerical simulations of wave–current flow in an ocean basin. *Applied Ocean Research*, *61*, 32–41.

Sima. (2023). Sima: Marine operations and mooring analysis software. *Det Norske Veritas (DNV), Oslo, Norway*. Retrieved from www.dnv.com

Simons, R. R., MacIver, R. D., & Saleh, W. M. (1997). Kinematics and shear stresses from combined waves and longshore currents in the uk coastal research facility. In *Coastal engineering 1996* (pp. 3481–3494).

Simons, R. R., Whitehouse, R. J., MacIver, R. D., Pearson, J., Sayers, P. B., Zhao, Y., & Channell, A. R. (1995). Evaluation of the uk coastal research facility. In *Coastal dynamics' 95* (pp. 161–172).

Singh, S. K., & Debnath, K. (2016). Combined effects of wave and current in free surface turbulent flow. *Ocean Engineering*, *127*, 170–189.

Skaare, B. (2017). Development of the hywind concept. In *International conference on offshore mechanics and arctic engineering* (Vol. 57779, p. V009T12A050).

Slade, W. H., & Boss, E. (2015). Spectral attenuation and backscattering as indicators of average particle size. *Applied optics*, *54*(24), 7264–7277.

Sleath, J. (1993). Velocities and bed friction in combined flows. In *Coastal engineering 1990* (pp. 450–463).

Sloan, C., Hall, M., Housner, S., Lozon, E., & Sirnivas, S. (2022). *Shared mooring systems for deep-water floating wind farms* (Tech. Rep.). Los Angeles, California, USA: National Renewable Energy Laboratory (NREL).

Smith, E., & Klick, H. (2007). Explaining nimby opposition to wind power. In *Annual meeting of the american political science association* (pp. 1–19).

Smith, J. (1997). *One-dimensional wave-current interaction* (Technical note). Engineer Research and Development Center (ERDC), Coastal and Hydraulics Laboratory (CHL). Retrieved from http://hdl.handle.net/11681/2219

Soares, C. G., & De Pablo, H. (2006). Experimental study of the transformation of wave spectra by a uniform current. *Ocean engineering*, *33*(3-4), 293–310.

Solidworks. (2021). Solidworks manual. *Dassault Systèmes SOLIDWORKS Corp, Waltham, Massachusetts, USA*. Retrieved from www.solidworks.com

Soulsby, R. L., Hamm, L., Klopman, G., Myrhaug, D., Simons, R., & Thomas, G. (1993). Wave-current interaction within and outside the bottom boundary layer. *Coastal engineering*, *21*(1-3), 41–69.

Spraul, C., Pham, H.-D., Arnal, V., & Marine, R. (2017). Effect of marine growth on floating wind turbines mooring lines responses. In *23e congrès fran†cais de mécanique.*

Stansberg, C. T., Hoff, J. R., Hermundstad, E. M., & Baarholm, R. (2013). Wave drift forces and responses in current. In *International conference on offshore mechanics and arctic engineering* (Vol. 55317, p. V001T01A071).

Stokes, Hocking, G., & Forbes, L. (2003). Unsteady free-surface flow induced by a line sink. *Journal of engineering mathematics*, *47*, 137–160.

Stokes, Hocking, G. C., & Forbes, L. K. (2008). Unsteady free surface flow induced by a line sink in a fluid of finite depth. *Computers & fluids*, *37*(3), 236–249.

Suastika, & Battjes, J. (2009). A model for blocking of periodic waves. *Coastal Engineering Journal*, *51*(02), 81–99.

Suastika, Jong, M. d., & Battjes, J. (2001). Experimental study of wave blocking. In *Coastal engineering 2000* (pp. 227–240).

Suh, K. D., Kim, Y.-Y., & Lee, D. Y. (1994). Equilibrium-range spectrum of waves propagating on currents. *Journal of waterway, port, coastal, and ocean engineering*, *120*(5), 434–450.

Sutherland, D. R., Noble, D. R., Steynor, J., Davey, T., & Bruce, T. (2017). Characterisation of current and turbulence in the flowave ocean energy research facility. *Ocean Engineering*, *139*, 103–115.

Tang, H.-J., Yang, R.-Y., & Yao, H.-C. (2023). Experimental and numerical study on the hydrodynamic behaviors of mooring line failure on a net cage in irregular waves and currents. *Frontiers in Marine Science*, *10*, 1122855.

Tao, L., & Thiagarajan, K. (2003). Low kc flow regimes of oscillating sharp edges i. vortex shedding observation. *Applied ocean research*, *25*(1), 21–35.

Tarrant, K., & Meskell, C. (2016). Investigation on parametrically excited motions of point absorbers in regular waves. *Ocean Engineering*, *111*, 67–81.

Tatum, S., Frost, C., Allmark, M., O'doherty, D., Mason-Jones, A., Prickett, P., ... O'Doherty, T. (2016). Wave–current interaction effects on tidal stream turbine performance and loading characteristics. *International Journal of Marine Energy*, *14*, 161–179.

Tayfun, M., Dalrymple, R., & Yang, C. (1976). Random wave-current interactions in water of varying depth. *Ocean Engineering*, *3*(6), 403–420.

Taylor, P., Santo, H., & Choo, Y. (2013a). Current blockage: Reduced morison forces on space frame structures with high hydrodynamic area, and in regular waves and current. *Ocean Engineering*, *57*, 11-24.

Taylor, P., Santo, H., & Choo, Y. (2013b). Current blockage: reduced morison forces on space frame structures with high hydrodynamic area, and in regular waves and current. *Ocean Engineering*, *57*, 11–24.

TetraFloat. (2014). *Marinet infrastructure access report infrastructure: Ifremer deep seawater wave tank performance of a free-yawing tetrahedral floating platform for offshore wind turbines in wind and wave conditions.* Brussels, Belgium. Retrieved from https://www.tetrafloat.com/

Thomas, G. (1979). Water wave-current interactions: a review. *Editor TL Shaw, University of Bristol, Pitman Publishing Ltd, London, Printed in England, ISBN: 0 273 08433 X*.

Thomas, G. (1981). Wave-current interactions: an experimental and numerical study. part 1. linear waves. *Journal of Fluid Mechanics*, *110*, 457–474.

Thomas, G. (1990). Wave–current interactions: an experimental and numerical study. part 2. nonlinear waves. *Journal of Fluid Mechanics*, *216*, 505–536.

Tian, Z., Perlin, M., & Choi, W. (2011). Frequency spectra evolution of two-dimensional focusing wave groups in finite depth water. *Journal of fluid mechanics*, *688*, 169–194.

Tolman, H. L. (1990). The influence of unsteady depths and currents of tides on wind-wave propagation in shelf seas. *Journal of Physical Oceanography*, *20*(8), 1166–1174.

Tolman, H. L. (1991a). Effects of tides and storm surges on north sea wind waves. *Journal of physical oceanography*, *21*(6), 766–781.

Tolman, H. L. (1991b). A third-generation model for wind waves on slowly varying, unsteady, and inhomogeneous depths and currents. *Journal of Physical Oceanography*, *21*(6), 782–797.

Touzon, I., de Miguel, B., Nava, V., Petuya, V., Mendikoa, I., & Boscolo, F. (2018). Mooring system design approach: a case study for marmok-a floating owc wave energy converter. In *International conference on offshore mechanics and arctic engineering* (Vol. 51319, p. V010T09A025).

Touzon, I., Nava, V., de Miguel, B., & Petuya, V. (2020). A comparison of numerical approaches for the design of mooring systems for wave energy converters. *Journal of Marine Science and Engineering*, *8*(7), 523.

Touzon, I., Nava, V., Gao, Z., Mendikoa, I., & Petuya, V. (2020). Small scale experimental validation of a numerical model of the harshlab2. 0 floating platform coupled with a non-linear lumped mass catenary mooring system. *Ocean Engineering*, *200*, 107036.

TROPOS. (2012). *Modular multi-use deep water offshore platform harnessing and servicing mediterranean, subtropical and tropical marine and maritime resources.* Europe. Retrieved from https://cordis.europa.eu/project/id/288192

Tuck, E., & Vanden-Broeck, J.-M. (1984). A cusp-like free-surface flow due to a submerged source or sink. *The ANZIAM Journal*, *25*(4), 443–450.

Tung, C. C., & Huang, N. E. (1973). Influence of wave-current interactions on fluid force. *Ocean Engineering*, *2*(5), 207–218.

Tung, C. C., & Huang, N. E. (1974). Influence of current on statistical properties of waves. *Journal of the Waterways, Harbors and Coastal Engineering Division*, *100*(4), 267–278.

Tyvand, P. A. (1991). Motion of a vortex near a free surface. *Journal of fluid mechanics*, *225*, 673–686.

Tyvand, P. A. (1992). Unsteady free-surface flow due to a line source. *Physics of Fluids A: Fluid Dynamics*, *4*(4), 671–676.

Udoh, I. E., & Zou, J. (2020). Optimizing floating offshore multi-wind-turbine design: A parametric study on tower inclination and column spacing. In *Offshore technology conference* (p. D021S019R003).

UK-DBT. (2023, Jan). *UK Offshore Wind.* United Kingdom: The Department for Business and Trade (DBT). Retrieved from https://www.great.gov.uk/international/content/investment/sectors/offshore-wind/

Umeyama, M. (2005). Reynolds stresses and velocity distributions in a wave-current coexisting environment. *Journal of waterway, port, coastal, and ocean engineering*, *131*(5), 203–212.

Umeyama, M. (2009). Changes in turbulent flow structure under combined wave-current motions. *Journal of waterway, port, coastal, and ocean engineering*, *135*(5), 213–227.

Umeyama, M. (2011). Coupled piv and ptv measurements of particle velocities and trajectories for surface waves following a steady current. *Journal of waterway, port, coastal, and ocean engineering*, *137*(2), 85–94.

Utsunomiya, T., Sato, T., Matsukuma, H., & Yago, K. (2009). Experimental validation for motion of a spar-type floating offshore wind turbine using 1/22.5 scale model. In *International conference on offshore mechanics and arctic engineering* (Vol. 43444, pp. 951–959).

Utsunomiya, T., Yoshida, S., Ookubo, H., Sato, I., & Ishida, S. (2014). Dynamic analysis of a floating offshore wind turbine under extreme environmental conditions. *Journal of Offshore Mechanics and Arctic Engineering*, *136*(2), 020904.

Van den Boom, H. (1985). Dynamic behaviour of mooring lines. In *Boss conference* (Vol. 1, pp. 359–368).

Vanden-Broeck, J.-M., & Keller, J. B. (1987). Free surface flow due to a sink. *Journal of Fluid Mechanics*, *175*, 109–117.

Van Der Tempel, J., Diepeveen, N., De Vries, W., & Salzmann, D. C. (2011). Offshore environmental loads and wind turbine design: impact of wind, wave, currents and ice. In *Wind energy systems* (pp. 463–478). Elsevier.

Van Hoften, J., & Karaki, S. (1976). Interaction of waves and a turbulent current. In *Coastal engineering 1976* (pp. 404–422).

Van Kessel, J. L. F. (2010). *Aircushion supported mega-floaters* (Unpublished doctoral dissertation). Mechanical, Maritime and Materials Engineering.

Van Phuc, P., & Ishihara, T. (2007). A study on the dynamic response of a semi-submersible floating offshore wind turbine system part 2: numerical simulation. *ICWE12. Cairns, Australia*, 959–966.

Van Rossum, G., Drake, F. L., et al. (1995). *Python reference manual* (Vol. 111). Centrum voor Wiskunde en Informatica Amsterdam.

W2Power. (2010). *W2power: A twin-turbine floating solution being developed by enerocean s.l.* Málaga & Canary Islands, Spain. Retrieved from https://enerocean.com/w2power/

Wang, C., Utsunomiya, T., Wee, S., & Choo, Y. (2010). Research on floating wind turbines: a literature survey. *The IES Journal Part A: Civil & Structural Engineering*, *3*(4), 267–277.

Wang, H.-Y., Fang, H.-M., & Chiang, Y.-C. (2021). Study on the coexistence of offshore wind farms and cage culture. *Water*, *13*(14), 1960.

Wang, P., Wang, H., Guo, Y., Yang, X., Ye, F., Yang, Y., & Lian, J. (2021). The influence of wave-current on the motion response of air-floating structure. *Journal of Renewable and Sustainable Energy*, *13*(6).

Wang, P., Zhao, M., & Du, X. (2019). Short-crested wave-current forces on composite bucket foundation for an offshore wind turbine. *Mathematical Problems in Engineering*, *2019*.

Watanabe, R. K. (1982). *The effect of wave-current interactions on the hydrodynamic loading of large offshore structures*. Texas A&M University.

Wayman, E. N., Sclavounos, P., Butterfield, S., Jonkman, J., & Musial, W. (2006). Coupled dynamic modeling of floating wind turbine systems. In *Offshore technology conference* (pp. OTC–18287).

Wei, S.-x., Liang, Z.-d., Cui, L., Zhai, H.-l., & Jeng, D.-s. (2022). Numerical study of seabed response and liquefaction around a jacket support offshore wind turbine foundation under combined wave and current loading. *Water Science and Engineering*, *15*(1), 78–88.

White, B. S. (1999). Wave action on currents with vorticity. *Journal of Fluid Mechanics*, *386*, 329–344.

WILSON, A. B. (2020). *Offshore wind energy in europe.* EPRS: European Parliamentary Research Service.

WindEurope. (2018, November). *Floating offshore wind energy: A policy blueprint for europe.* Etterbeek, Brussels. Retrieved from www.windeurope.org

Winterstein, S. R., Ude, T. C., Cornell, C. A., Bjerager, P., & Haver, S. (1993). Environmental parameters for extreme response: Inverse form with omission factors. *Proceedings of the ICOSSAR-93, Innsbruck, Austria*, 551–557.

Wiser, R., Rand, J., Seel, J., Beiter, P., Baker, E., Lantz, E., & Giman, P. (2021). *Expert elicitation survey predicts 37% to 49% declines in wind energy costs by 2050. nature energy, 6, 555–565.*

Wolf, J., & Prandle, D. (1999). Some observations of wave-current interaction. *Coastal Engineering*, *37*(3-4), 471–485.

Wong, C. (2015). Wind tracing rotational semi-submerged raft for multi-turbine wind power generation. In *European wind energy association offshore 2015 conference, mar* (pp. 10–12).

Wright, C., Murphy, J., & Pakrashi, V. (2016). The dynamic effects of marine growth on a tension moored floating wind turbine. *Guedes Soares, C.(ed.). Progress in Renewable Energies Offshore*.

Wu, S. C. (1976). The effects of current on dynamic response of offshore platforms. In *Offshore technology conference.*

Wyatt, L., Gurgel, K., Peters, H., Prandle, D., Krogstad, H., Haug, O., ... Wensink, G. (1998). The scawvex project. In *Ocean wave measurement and analysis* (pp. 1457–1467).

X1-Wind. (2023). *X1 wind - innovative floating wind turbine technology.* Barcelona, Spain. Retrieved from https://www.x1wind.com/

Xiang, G., & Guedes Soares, C. (2020). Incorporating irregular nonlinear waves in simulation of dropped cylindrical objects. *Proceedings of the Institution of Mechanical Engineers, Part M: Journal of Engineering for the Maritime Environment*, *234*(1), 272–283.

Xiao, L., Tao, L., Yang, J., & Li, X. (2014). An experimental investigation on wave runup along the broadside of a single point moored fpso exposed to oblique waves. *Ocean Engineering*, *88*, 81–90.

Xu, X., Xing, Y., Gaidai, O., Wang, K., Patel, K. S., Dou, P., & Zhang, Z. (2022). A novel multi-dimensional reliability approach for floating wind turbines under power production conditions. *Frontiers in Marine Science*, *9*.

Xue, M., & Yue, D. K. (1998). Nonlinear free-surface flow due to an impulsively started submerged point sink. *Journal of Fluid Mechanics*, *364*, 325–347.

YAGO, K., OHKAWA, Y., HINENO, M., TAKANO, O., & SUNAHARA, S. (2006). An experimental study of floating wind power system. In *Proceedings of civil engineering in the ocean* (Vol. 22, pp. 863–868).

Yang, H., Zhao, Y.-P., Bi, C.-W., & Cui, Y. (2020). Numerical study on hydrodynamic responses of floating rope enclosure in waves and currents. *Journal of Marine Science and Engineering*, *8*(2), 82.

Yang, M., Teng, B., Ning, D., & Shi, Z. (2012). Coupled dynamic analysis for wave interaction with a truss spar and its mooring line/riser system in time domain. *Ocean Engineering*, *39*, 72–87.

Yang, Q., & Liu, H. (2018). Dynamic response of multilayered silty seabeds under wave-current action in the yellow river estuary. *International Journal of Geomechanics*, *18*(6), 04018031.

Yang, S.-H., Ringsberg, J. W., Johnson, E., Hu, Z., & Palm, J. (2016). A comparison of coupled and de-coupled simulation procedures for the fatigue analysis of wave energy converter mooring lines. *Ocean Engineering*, *117*, 332–345.

Yde, A., Pedersen, M. M., Bellew, S. B., Køhler, A., Clausen, R. S., & Nielsen, A. W. (2014). *Experimental and theoretical analysis of a combined floating wave and wind energy conversion platform* (Tech. Rep.). Denmark: Technical University of Denmark.

Yin, D., Passano, E., Jiang, F., Lie, H., Wu, J., Ye, N., ... Leira, B. J. (2022). State-of-the-art review of vortex-induced motions of floating offshore wind turbine structures. *Journal of Marine Science and Engineering*, *10*(8), 1021.

Youngworth, R. N., Gallagher, B. B., & Stamper, B. L. (2005). An overview of power spectral density (psd) calculations. *Optical manufacturing and testing VI*, *5869*, 206–216.

Zanganeh, R., & Thiagarajan, K. (2018). Prediction of the mean heading of a turret moored fpso in bi-modal and bi-directional sea states. *Applied Ocean Research*, *78*, 156–166.

Zhai, Y., Zhao, H., Li, X., & Shi, W. (2022). Hydrodynamic responses of a barge-type floating offshore wind turbine integrated with an aquaculture cage. *Journal of Marine Science and Engineering*, *10*(7), 854.

Zhang, H., Wang, H., Cai, X., Xie, J., Wang, Y., & Zhang, N. (2022). Research on the dynamic performance of a novel floating offshore wind turbine considering the fully-coupled-effect of the system. *Journal of Marine Science and Engineering*, *10*(3), 341.

Zhang, J., Zeng, Y., Tang, Y., Guo, W., & Wang, Z. (2021). Numerical and experimental research on the effect of platform heave motion on vortex-induced vibration of deep sea top-tensioned riser. *Shock and Vibration*, *2021*, 1–13.

Zhang, L., Shi, W., Karimirad, M., Michailides, C., & Jiang, Z. (2020). Second-order hydrodynamic effects on the response of three semisubmersible floating offshore wind turbines. *Ocean Engineering*, *207*, 107371.

Zhang, X., Ni, W., & Sun, L. (2022). Fatigue analysis of the oil offloading lines in fpso system under wave and current loads. *Journal of Marine Science and Engineering*, *10*(2), 225.

Zhang, X., Simons, R., Zheng, J., & Zhang, C. (2022). A review of the state of research on wave-current interaction in nearshore areas. *Ocean Engineering*, *243*, 110202.

Zhao, R., & Faltinsen, O. M. (1988). Interaction between waves and current on a two-dimensional body in the free surface. *Applied Ocean Research*, *10*(2), 87–99.

Zhao, R., & Faltinsen, O. M. (1989). Interaction between current, waves and marine structures. In *International conference on numerical ship hydrodynamics, 5th.*

Zhao, R., Faltinsen, O. M., Krokstad, J., & Aanesland, V. (1988). Wave-current interaction effects on large-volume structures. *BOSS'88*, 623–638.

Zhao, Y., Guan, C., Bi, C., Liu, H., & Cui, Y. (2019). Experimental investigations on hydrodynamic responses of a semi-submersible offshore fish farm in waves. *Journal of Marine Science and Engineering*, *7*(7), 238.

Zhao, Y.-s., She, X.-h., He, Y.-p., Yang, J.-m., Peng, T., & Kou, Y.-f. (2018). Experimental study on new multi-column tension-leg-type floating wind turbine. *China Ocean Engineering*, *32*, 123–131.

Zhen, L., Bin, T., Ning, D.-z., & Ying, G. (2010). Wave-current interactions with three-dimensional floating bodies. *Journal of Hydrodynamics, Ser. B*, *22*(2), 229–240.

Zheng, Z., Chen, J., Liang, H., Zhao, Y., & Shao, Y. (2020). Hydrodynamic responses of a 6 mw spar-type floating offshore wind turbine in regular waves and uniform current. *Fluids*, *5*(4), 187.

Appendix A

W2Power Floating Platform

A.1 Development Trajectory

Since its introduction in 2009, W2Power has undergone extensive research and tests. It benefited from investigations performed by Acciona Energia, the Norwegian University of Science and Technology, and the University of Edinburgh as part of the European MARINA Platform project (MARINA, 2010). In the subsequent European TROPOS project (which considered multi-use platforms), it was selected as an energy-producing "satellite unit" (TROPOS, 2012; Papandroulakis et al., 2017). It has successfully passed several tests on its path to the TRL of 6. These tests are summarised in Table A.1 and depicted in Figure A.1.

A.1.1 Innovative Multi-Use Solutions

Multi-Use Power Solutions: W2Power can harness wave energy, aligning with its initial design objective (i.e. hybrid wind/wave concept). It can effectively harness wave energy, aligning with its original design purpose, see Figure A.1.(a, c). Engineering assessments conducted across various locations have demonstrated that, under optimal wave conditions, W2Power could generate an additional 3 MW from waves in conjunction with its existing industry-leading wind power capacity of 20 MW (Hanssen, 2023).

Furthermore, EnerOcean's design investigations indicate the potential to produce 350-375 kW of photovoltaic (PV) electricity using the current W2Power configuration; see Figure A.2.(a). The platform is also adaptable for power conditioning and export, as design studies have revealed that lightweight, flexible modular substations can be integrated into the bow column without requiring substantial floater reinforcement; see Figure A.2.(b). This innovative approach enables uninterrupted wind power generation from the W2Power-substation solution (Hanssen, 2023).

Versatility Beyond Power Generation: Aside from energy production, W2Power offers the potential for energy storage and seawater desalination, further enhancing its utility in the maritime sector. EnerOcean has developed a compressed air-based energy storage system tailored for offshore applications. EnerOcean has also invented a technology for anchoring large fish cages to floating platforms, significantly reducing costs. Utilising this innovative

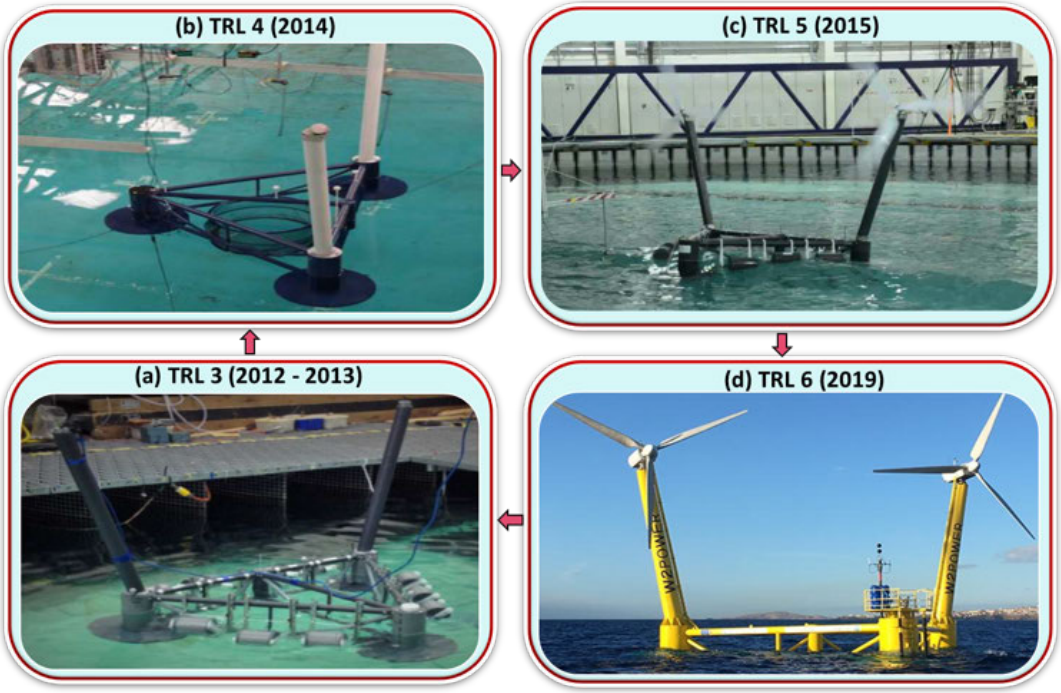

Figure A.1: Artistic depictions of various W2Power scale models during its TRL development tests. Clockwise from bottom left: (a) A photograph of a 1:100 scale model of the hybrid wind/wave W2Power with WEC arrays at the Curved tank, University of Edinburgh; (b) W2Power at a 1:100 scale at UCC-Beaufort (HMRC) tank, Cork, to test its aquaculture compatibility; (c) A 1:40 scale model examined during tests at FloWave, Edinburgh; (d) W2Power prototype (1:6) during its first deployment in the open sea near the PLOCAN, Spain. EnerOcean S.L. (2007).

anchoring solution, W2Power becomes the world's first floating wind platform to integrate a fully functional fish cage (Figure A.2.(c). This achievement was demonstrated during the second deployment of its 1:6 prototype as part of the AquaWind project (EnerOcean S.L., 2007; AquaWind, 2022; Hanssen, 2023).

A.2 Subsystems Assembly and Model Setup

Prior to conducting the tests, several essential steps were undertaken, as visualised in Figure A.3. These tasks include:

- **Assemble the model:** this involved bringing together the platform, towers, and wind turbines to form a coupled FOWT system.
- **Instrumentation Calibration and Installation:** calibration and installation of instrumentation, including MoCap Qualisys, load cells, wave gauges, and reflective balls and markers for Qualisys, were carried out.

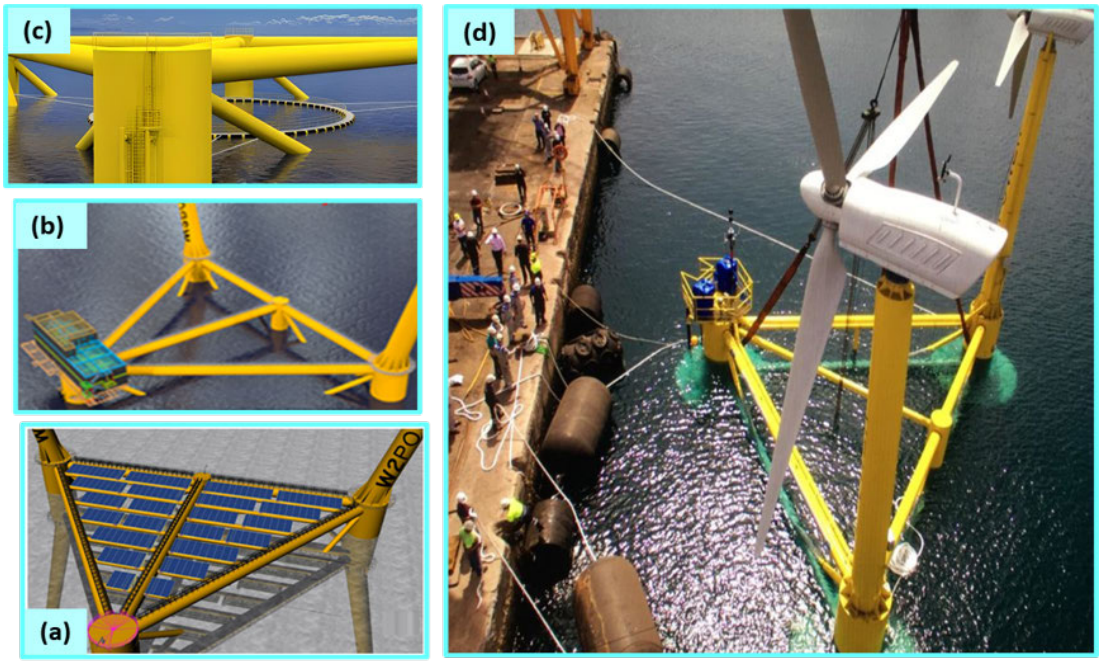

Figure A.2: Artistic illustrations of the W2Power with its wind and multi-use applications. Clockwise from bottom left: Rendered images of full-size W2Power equipped with (a) solar PV arrays, (b) a compact substation, and (c) an innovative finfish aquaculture solution; (d) W2Power prototype with two nacelles mounted being prepared for towing from ASTICAN shipyard, Canary Islands, to its sea moorings, eliminating jack-up crane costs. After Ener-Ocean S.L. (2007), Hanssen (2023) and AquaWind (2022).

- **Mooring design and preparation:** the mooring system, comprising three lines at 120 degrees with a weight of approximately 760 g/m, was designed and prepared.
- **Model positioning:** the scale model was precisely positioned at the centre of the tank.
- **Installation of mooring lines:** the mooring lines were attached to station-keep the model. This involved attaching the necessary pretension and stiffness, replicating the down-scaled characteristics of the full-scale mooring system.
- **Adjustment for operational water draft:** systematic ballasting was executed to attain the desired operational water draft of 0.375 m (15 m at full scale). Herein, the required masses were calculated and weighted using sensitive mass scales to ensure accurate scaling of the necessary weights for insertion into predefined locations in the hull. Subsequently, the scaled weights (i.e. steel bars and chains) were added to the three main corner columns to set the correct draft.

Overall, this assembly and setup process ensured the model's readiness for testing and met the specified conditions and configurations (see Figure 4.8).

Figure A.3: Artistic depictions illustrating the assembly and configuration of the floating system. Proceeding clockwise from the bottom left: (a) depiction of the W2Power hull being transit via crane, (b) assembled towers with turbines being affixed, (c) attachment of mooring lines to fairleads under the bow column, (d) the assembled model floating with the crane partially released, accompanied by ballasting using mass pieces on the scaler (small photo outlined in red).

A.3 Potential Sources of Inconsistency in Measurements

The potential sources of inconsistency in measurements, particularly in mooring line loads, stem from various factors related to the experimental setup and environmental conditions. One notable discrepancy arises from the expectation that mooring lines would experience lower loads under crossing wave conditions compared to following or opposing loading conditions (see Figures A.4 and A.6. This expectation is based on the mooring configuration and loading conditions; however, empirical observations from irregular load cases (A, D, and E) contradict this anticipation. The unexpected higher loads under crossing wave conditions can be attributed to wave reflections in the tank, which are influenced by factors such as frequency, flow velocity, and angle.

Figure A.5 illustrates how waves accumulate towards positive sway and reflect back, indicating the presence of reflections that could arise from imperfect absorption by absorbing paddles or reflections from physical models in the tank. Any imperfections in maintaining the model's position at the centre of the test can exacerbate these reflections, underscoring the need to measure and understand them to accurately assess dynamic responses and performance, especially for FOWTs.

Moreover, the presence of currents introduces further inconsistencies in mooring line tensions, deviating from expected behaviours. The altered tension behaviours, particularly on LineB and LineC, highlight the complex interplay between wave-current interaction and mooring line dynamics. Furthermore, sufficient time is required between wave tests for reflections to dissipate and the tank to return to a quiescent state, a process influenced by the frequency and energy of the sea state. Currents can exacerbate reflection levels and alter perceived phases, especially when reflections do not oppose incident components. This phenomenon is evident in time series plots, where currents impact the dissipation time of reflections, with following currents sweeping reflected waves away and reducing settling time, while crossing wave-current interactions prolong settling time.

Overall, these factors contribute to increased loads in mooring lines and sway and roll motion responses, highlighting the intricate dynamics and challenges inherent in experimental testing of offshore structures under varying environmental conditions.

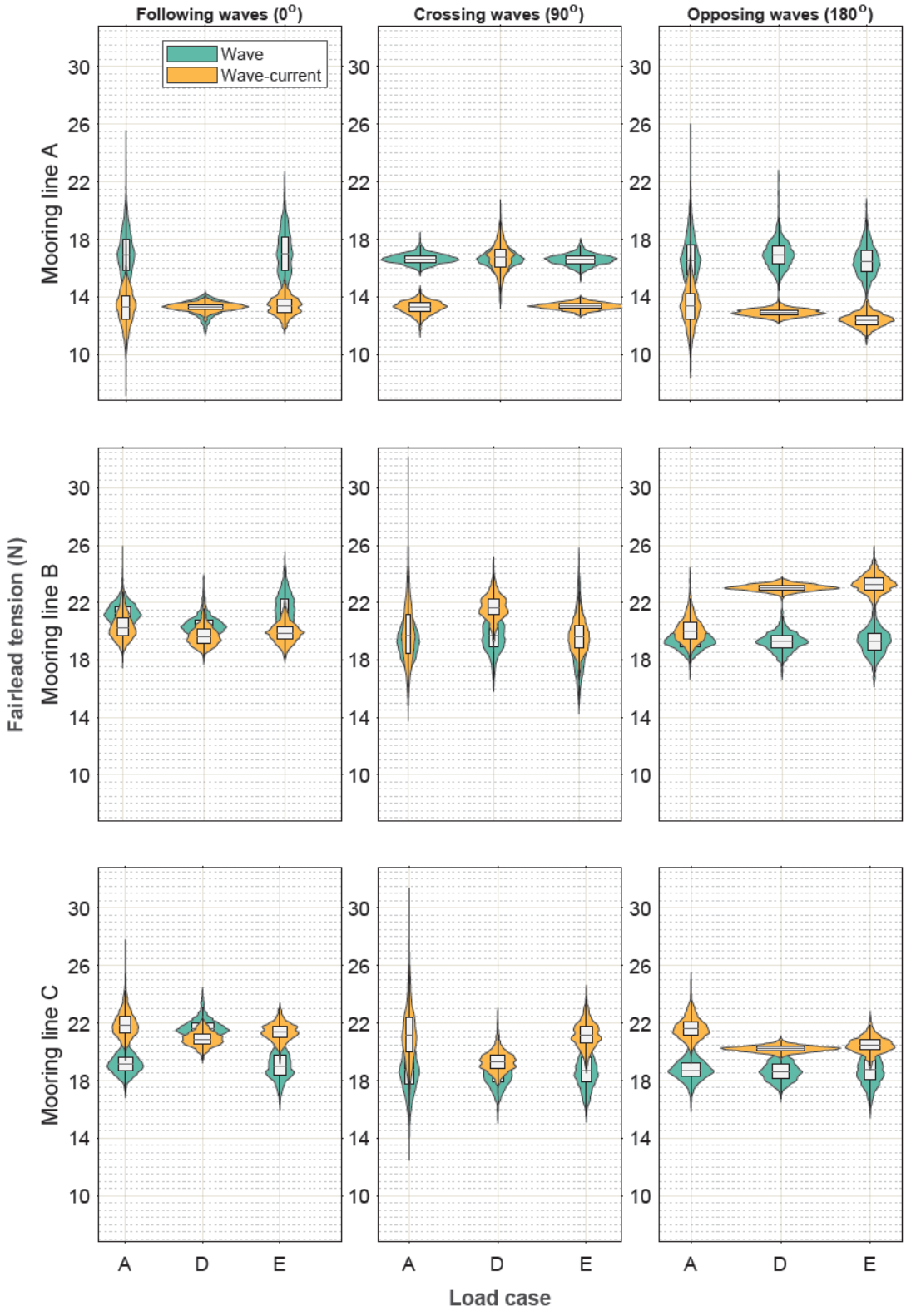

Figure A.4: Effects of irregular waves and combined wave-current loads on mooring loads. Showing the interaction of a current from 0° with (left) following, (middle) crossing, and (right) opposing. Horizontal panels also show tensions at fairleads of the mooring lines: (top) line A, (middle) line B, and (bottom) line C.

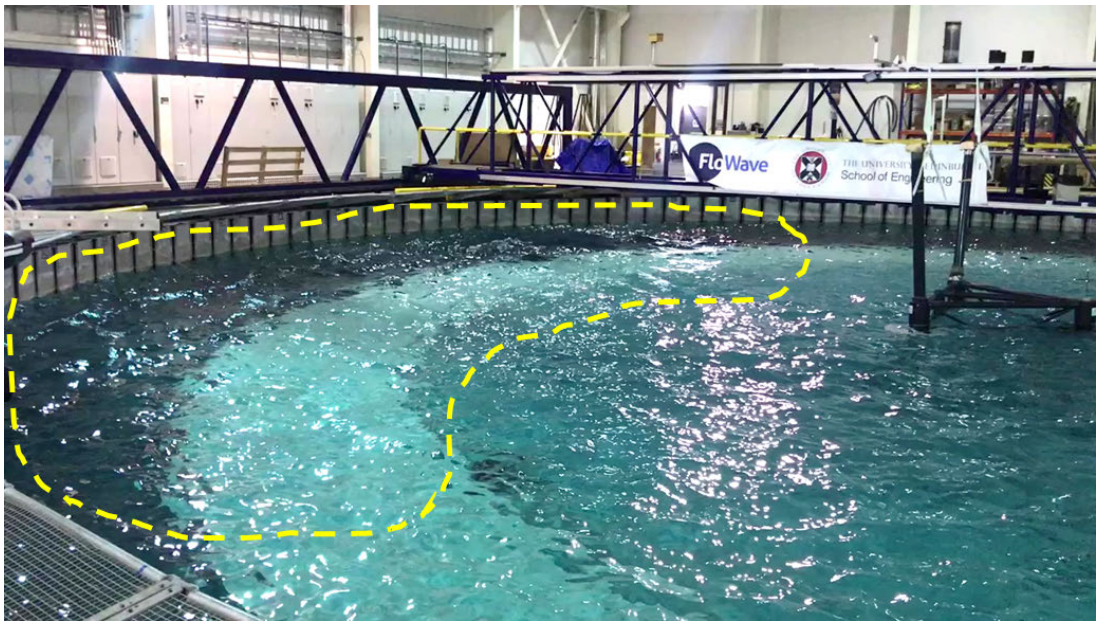

Figure A.5: Visualisation of potential reflections of waves in FloWave.

Table A.1: Chronological progression of technology readiness levels for the W2Power technology development (EnerOcean S.L., 2007; Hanssen et al., 2015; Mayorga, 2016; Papandroulakis et al., 2017; Legaz et al., 2018).

Year	Testing facility	TRL	Model scale	Description and testing scope
2012 - 2013	Curved Wave Tank, University of Edinburgh, UK	3	1:100	Multi-directional sea states generated (i.e., operational and survival conditions) for: - Design verification - WECs characterisation - System's global behaviour
2014	UCC-Beaufort (HMRC), Cork, Ireland	4	1:100	Multi-directional sea states generated (i.e., operational and survival conditions) to validate: - Wind forces - Mooring loads - System performance - Cage culture compatibility - System's components individually
			1:30	- Innovative control system - WECs characteristics
2015	FloWave Ocean Energy Research Facility, University of Edinburgh, UK	5	1:40	- Mooring design fully validated - Wind load simulations (i.e., thrust forces and gyroscopic effects) - Validation of WECs' impact on the platform in the worst scenarios (operational and survival modes)
2019	PLOCAN site, Canary Islands, Spain	6	1:6	- Two 100 kW turbines Field deployment for four months, without any operational disruptions, involved seven storms with wave heights equivalent to 24 m (of three storms have maximum wave heights equivalent to more than 30 m) demonstrated: - Platform stability - Mooring survivability - Main subsystems functionality
2022				- Optimisation of marine space through the development of wind-aquaculture systems - Validation of wave forecasting algorithms with added instruments - Validation of control strategies for wind-aquaculture platforms - Assessment of environmental impacts of wind-aquaculture systems (AquaWind, 2022)

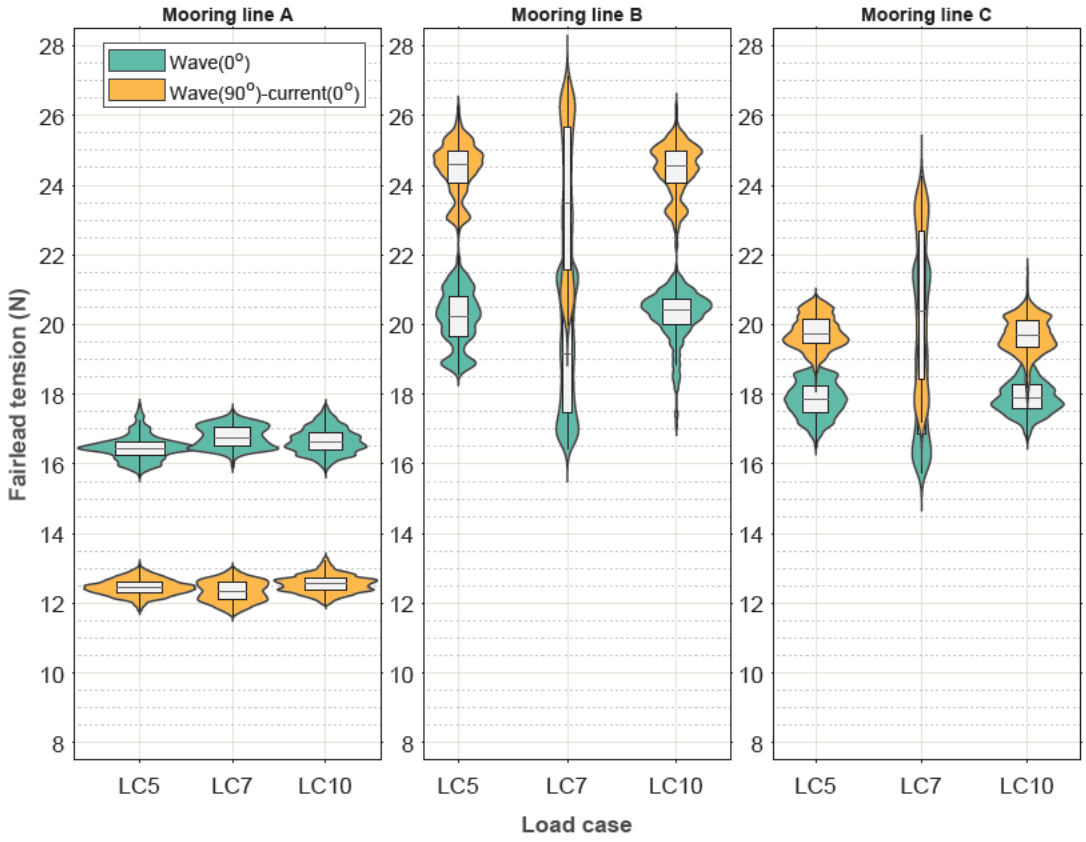

Figure A.6: Effects of waves and combined wave-current loads on mooring loads. Showing load cases of following regular waves (propagating from 90°) and their interaction with a current from 0°. Panels differentiate tensions at fairleads of mooring lines: (left) line A, (middle) line B, and (right) line C.

Appendix B

Convergence and Survivability Analyses

B.1 Panel Size Convergence Analysis

The panel size convergence analysis aimed at identifying the proper sizes of panel elements required for the findings to converge satisfactorily. To do this convergence study, the following steps were undertaken:

1. A panel model was created using a conservative yet practical number of elements, as shown in Figure 1. Subsequent analysis is conducted using this initial model.
2. The panel model was re-meshed with a denser distribution of elements. The recalculated results are then compared to those obtained from the previous model.
3. The process was repeated, systematically increasing the number of panel elements (mesh density) until satisfactory convergence was achieved.

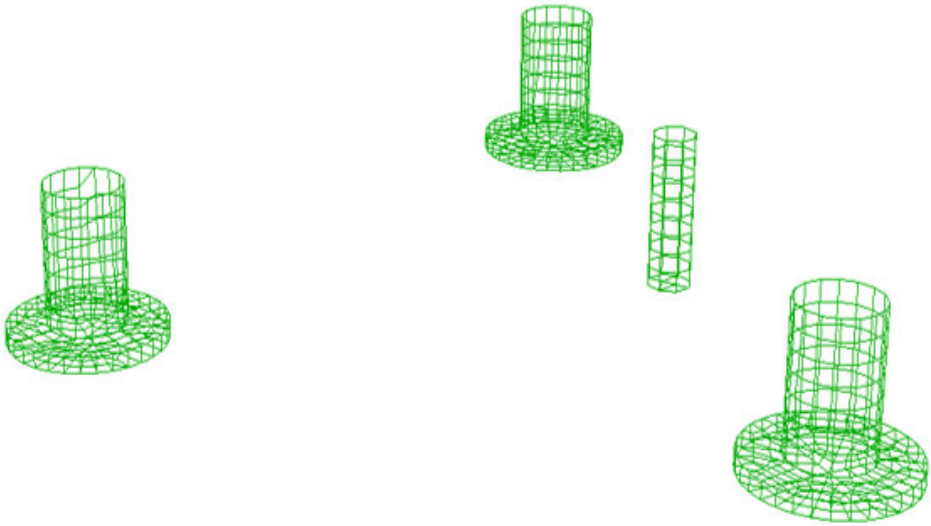

Figure B.1: A GeniE sketch of the entire panel model for the coarsest mesh of a panel size $(\Delta x) = 0.05$ m.

The present study examined four different panel models (see Figure 6.3). Key geometric characteristics of the panel models and assessments with analytical values are summarised in Table 6.1. Comparisons of the amplitudes of load RAOs for the surge, sway, heave, roll, pitch, and yaw modes computed using various panel models are given in Figure B.2.

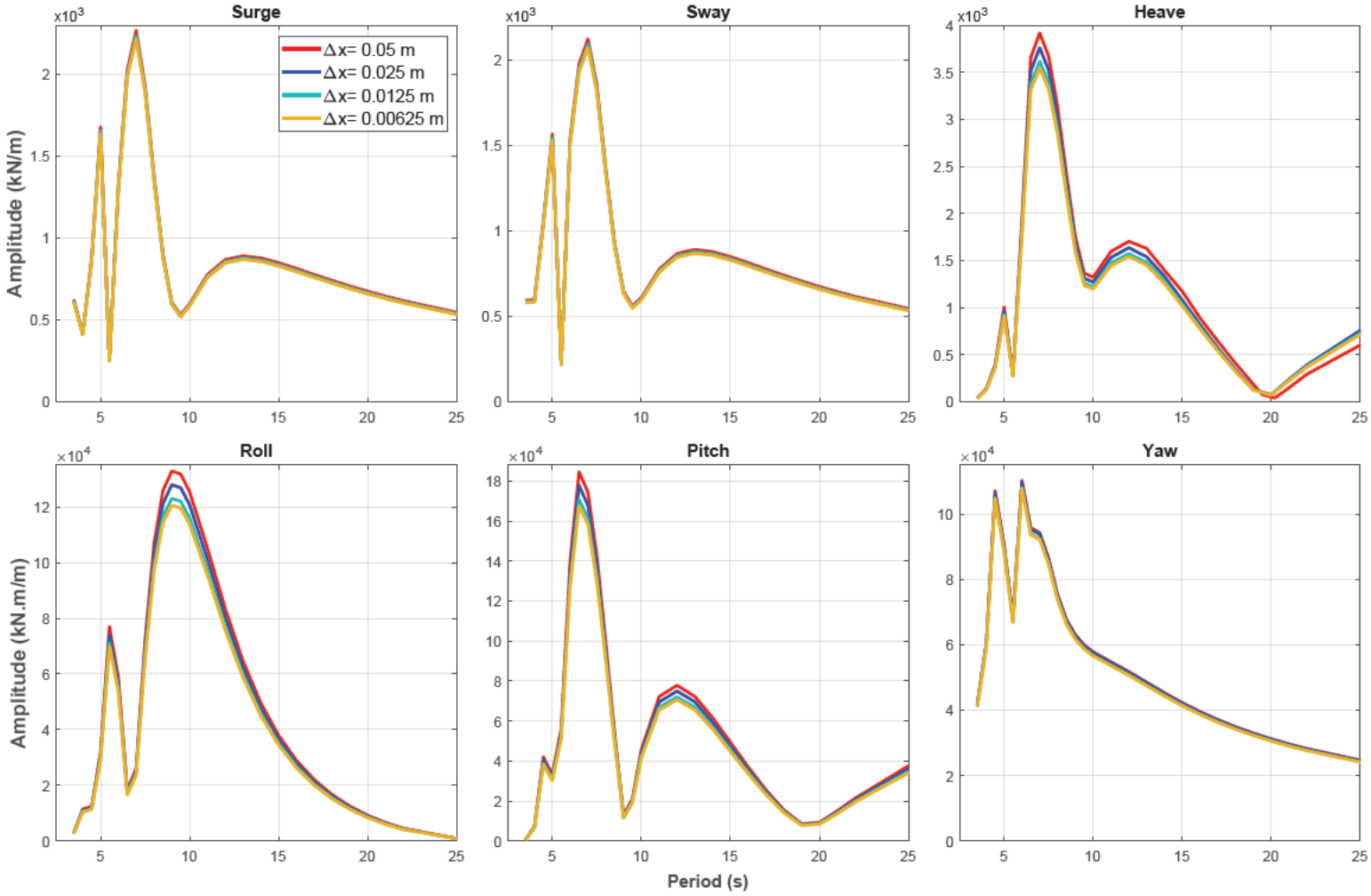

Figure B.2: Load RAO amplitudes in 6 DoFs for different mesh densities for sensitivity analysis, for a wave heading of 4°.

B.2 Survivability Analysis of Mooring System

From the contour surface in Figure 4.12 and as recommended by DNV (DNV-OS-E301, 2010; DNV-RP-C205, 2019), four extreme load cases are defined with six different wave seeds for each. These load conditions are represented by the JONSWAP spectrum of γ of 3.3 (Hasselmann et al., 1973) and summarised in Table B.1.

Table B.1: Environmental conditions for the mooring survivability analysis.

Load case (LC)	**Significant wave height (H_S) [m]**	**Peak wave period (T_P) [s]**
LC1	4	16.5
LC2	4.1	13.5
LC3	3.8	8
LC4	4	10

Employing Equations (6.43) and (6.44), the survivability analyses for the proposed mooring systems, both at full and 1:40 scales, have been carried out under extreme conditions. The results of the Ultimate Limit State (ULS) analyses are summarised in Table B.2. For the defined load cases, the utilisation factors (UF) for all lines were found to be quite conservative (i.e. UF < 1). Thereby indicating that the mooring lines are sufficiently strong to withstand the extreme waves at the Canari-I reference site (Figure 4.9).

Table B.2: ULS results for the mooring survivability analysis.

LC	**Mooring line**	**Mean tension (T_{mean})**		**Dynamic tension (T_{dyn})**		**Utilisation factor** (UF)
		Full scale [kN]	1:40 scale [N]	Full scale [kN]	1:40 scale [N]	
LC1	line A	825.90	12.59	808.56	13.85	1.98×10^{-3}
	line B	572.03	8.72	173.18	2.64	7.74×10^{-4}
	line C	571.38	8.71	171.87	2.62	7.71×10^{-4}
LC2	line A	870.51	13.27	1468.78	22.39	2.75×10^{-3}
	line B	564.16	8.6	213.20	3.25	8.18×10^{-4}
	line C	561.54	8.56	210.58	3.21	8.13×10^{-4}
LC3	line A	1148.66	17.51	13362.06	203.69	1.85×10^{-2}
	line B	532.67	8.12	610.74	9.31	1.31×10^{-3}
	line C	533.33	8.13	837.06	12.76	1.60×10^{-3}
LC4	line A	1003.02	15.29	54812.74	835.56	7.25×10^{-2}
	line B	545.79	8.32	367.36	5.6	1.00×10^{-3}
	line C	547.10	8.34	727.50	11.09	1.47×10^{-3}

Appendix C

Decay and Static Pull-Out Tests

C.1 Static Pull-Out Tests

Static pull-out tests were conducted to identify and verify the characteristics of the proposed mooring system. The tests were attempted by imposing forced offsets in the surge direction to ascertain the stiffness of mooring line A. This aimed at establishing a relationship between the surge displacement of the platform and the tension in line A. Various surge offsets were applied, and the resulting tensions were measured. Figure C.1 compares the experimental and numerical mooring line tensions in the surge direction for a pull-out case.

From Figure C.1, it is evident that the numerical predictions align with the test data, demonstrating good agreement. The behaviour of the system and its decay towards the line pretension can be clearly observed.

For instance, line A gradually decays to the precalculated line pretension of approximately 1153 kN. However, the test matrices were not as successful as initially planned. This was primarily due to time constraints for testing and the high demand for the FloWave tank during the test time. Therefore, these challenges highlight important considerations for future research endeavours.

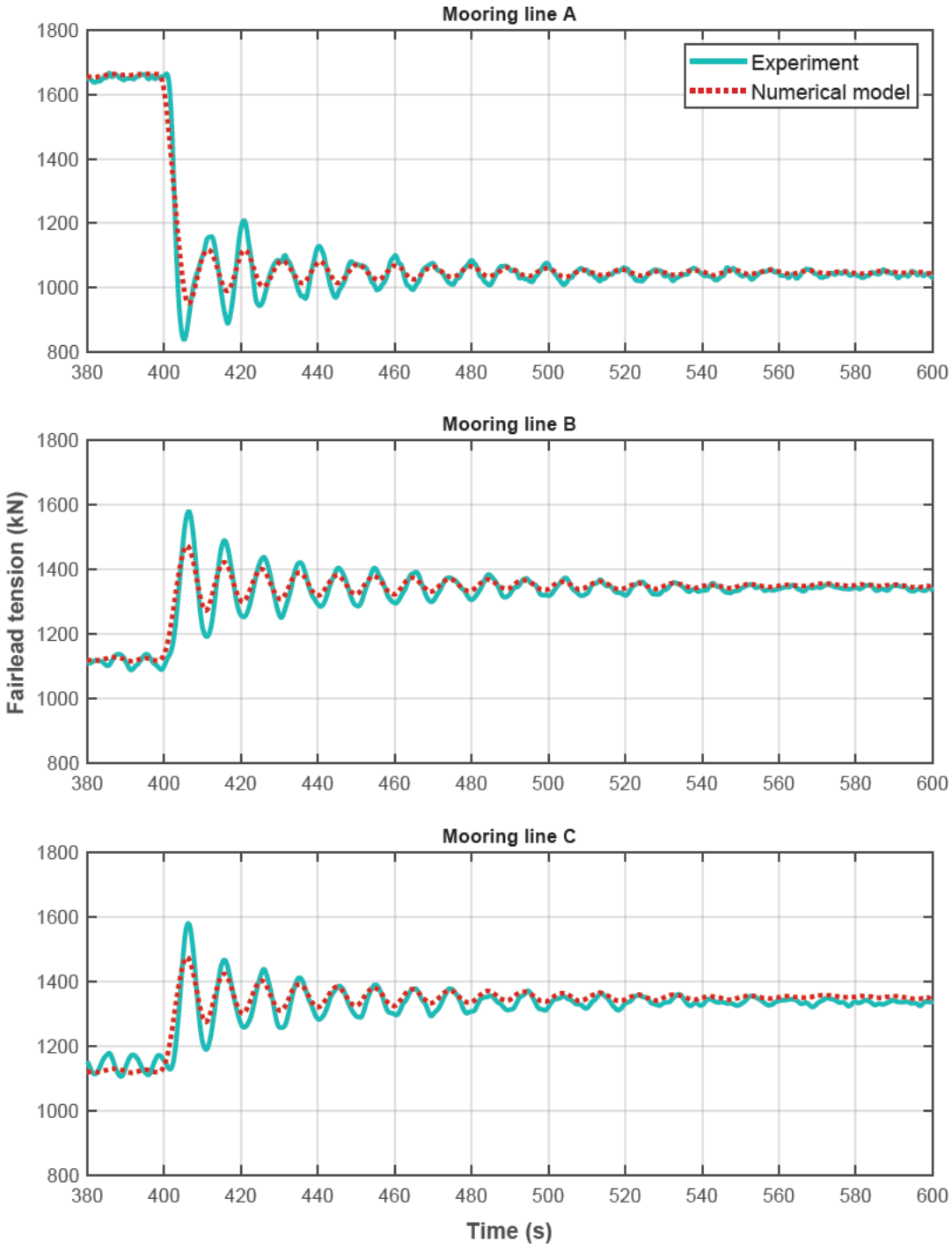

Figure C.1: Time histories of static pull-out tests in still water. Validation of measurements against numerical simulations for the mooring line tension at the fairlead.

Appendix D

Publications and Conferences

Conference and journal publications resulting from this EngD research project are included and appended in chronological order as follows:

- Elobeid, M., Tao, L., Ingram, D., Pillai, A.C., Mayorga, P. and Hanssen, J.E., (2022), June. Hydrodynamic performance of an innovative semi-submersible platform with twin wind turbines. In International Conference on Offshore Mechanics and Arctic Engineering (Vol. 85932, p. V008T09A032). American Society of Mechanical Engineers.
- Elobeid, M., Pillai, A.C., Tao, L., Ingram, D., Hanssen, J.E. and Mayorga, P., (2024). Implications of wave-current interaction on the dynamic responses of a floating offshore wind turbine. Ocean Engineering Journal, 292, p.116571.
- **Technical Conferences:**
  - ◇ Poster presented. “Hydrodynamic Performance of a Floating Offshore Wind Turbine under Combined Wave and Current”. The International Network on Offshore Renewable Energy (INORE) European Symposium 2022. Zarautz, Spain (October 2022).
  - ◇ Poster presented. "PO084: Coupled Analysis of a Floating Offshore Wind Turbine under Combined Wave and Current”. WindEurope Annual Event 2023. Copenhagen, Denmark (April 2023).
  - ◇ Poster presented. “Experimental Investigations on the Dynamic Responses of a Floating Offshore Wind Turbine in Combined Wave-Current Environments”. Seanergy 2023. Paris, France (June 2023).

Proceedings of the ASME 2022 41st International Conference on Ocean, Offshore and Arctic Engineering
OMAE2022
June 5-10, 2022, Hamburg, Germany

OMAE2022-79248

HYDRODYNAMIC PERFORMANCE OF AN INNOVATIVE SEMISUBMERSIBLE PLATFORM WITH TWIN WIND TURBINES

Mujahid Elobeid
School of Engineering, The University of Edinburgh
Edinburgh, UK

Longbin Tao
Department of Naval Architecture, Ocean & Marine Engineering, University of Strathclyde
Glasgow, UK

David Ingram
School of Engineering, The University of Edinburgh
Edinburgh, UK

Ajit C. Pillai
College of Engineering, Mathematics and Physical Sciences, University of Exeter Penryn, UK

Pedro Mayorga
EnerOcean S.L
Málaga, Spain

Jan Erik Hanssen
EnerOcean S.L
Málaga, Spain

ABSTRACT

The deployment of offshore wind turbines has focused primarily on shallow seas (such as the North Sea, Chinese coastal waters, and the New England coast) using bottom fixed foundations. However, much of the world's offshore wind resource lies in deeper waters where bottom-fixed foundations are not suitable, and floating platforms must be utilised. To date, the majority of floating concepts have been developed to support a single wind turbine. This leads to a high capital cost for each individual platform and consequently a high levelised cost of energy.

The W2Power platform (developed by EnerOcean S.L, Spain) currently supports a pair of 6 MW wind turbines on outward-leaning towers. The design significantly reduces the cost per installed MW, increases the structure's natural period, added mass, and radiation damping. The platform, patented in 2009, was the world's first twin-turbine platform and the first to be demonstrated at sea (2019).

This paper presents the hydrodynamics of a 1:40 scale model of the W2Power platform using the well-known OrcaFlex software. The analysis has been carried out under extreme and operational conditions, and the resulting hydrodynamic loads and motion response are presented.

The mooring system was found to be sensitive to wave direction, particularly when propagating along the current direction. Furthermore, the results showed advantages in the hydrodynamic responses for the W2Power platform as an innovative floating system.

Keywords: MUFOP, FOWT, semisubmersible, coupled analysis, mooring dynamics.

NOMENCLATURE

ρ_w	water density
γ	gamma
θ	theta
Lat	latitude
Lon	longitude
DoF	degree of freedom
RAO	response amplitude operator
WD	water depth
ML	mooring line
MBL	minimum breaking load

1. INTRODUCTION

Climate change is a critical issue, and wind energy is widely considered a valuable renewable energy source for decarbonising electricity generation and mitigating greenhouse gas emissions. As a result, significant effort is being made to design wind turbines that capture energy at sea. These turbines can be installed on bottom-fixed or floating foundations connected to the seabed by mooring lines. Furthermore, 80% of the offshore wind potential is in waters deeper than 60 m [1], making bottom-fixed installations challenging, whereas floating installations would be feasible.

The offshore wind industry has grown tremendously in the last decade due to recent technological advances and policy encouragement worldwide. Offshore market trends indicate that floating offshore wind turbines (FOWTs) of 10-20 MW will be operational [2]. Deploying such large turbines at commercial

scales using conventional single platforms is both technically challenging and, so far, has proven very expensive.

Consequently, multi-unit floating offshore platforms (MUFOPs) are being developed as viable innovations for higher installed wind capacity. Baltrop [3] highlighted the significant benefits and drawbacks of MUFOPs. Since the introduction of W2Power in 2009 [4], twin-turbine floating platforms, where two turbines use the same platform and mooring system to save installation and mooring expenses, have emerged as lower cost per MW power production systems suitable for deep-water use. Twin turbines allow more cost-efficient wind energy capture since the platform's height and loads are lower than single-turbine floaters of comparable power [5].

Such platforms are distinguished by heave plates that reduce heave and pitch motions, thereby shifting their natural frequencies towards the lower frequency region with minimum added mass and ultimately improving their hydrodynamic performance [6]. Henderson et al. [7] developed analytical tools for assessing the performance of wind farms with MUFOPs and their anticipated costs and feasible locations, particularly in the UK waters. For one specific hull shape and design configuration, the effect of columns spacing and towers inclination on the performance has been investigated by Udoh and Zou [8].

1.1 W2Power Platform

1.1.1 Development Trajectory

This paper presents the innovative W2Power twin-turbine concept currently developed by EnerOcean S.L (Spain). The platform was introduced by Pelagic Power from Norway as a novel hybrid wind-wave power concept for the offshore market in 2009. Since 2012, it has been developed primarily as a floating wind platform with multi-use capabilities (not limited to wave power). W2Power benefited from extensive preliminary research performed by Acciona Energia, NTNU and the University of Edinburgh as part of the European MARINA Platform project [9]. In the subsequent European TROPOS project (which considered multi-use platforms), it was selected as an energy-producing "satellite unit" [10].

W2Power has successfully passed five laboratory testing campaigns on a 1:100 scale model in the Curved Wave Tank at the University of Edinburgh, UK (2012–2013) and the UCC-Beaufort tank (HMRC) in Cork, Ireland (2014), and these tests have resulted in the following:

- Demonstration of concept and improvement of the platform's design.
- Appraisal of the platform's effectiveness upon two aquaculture systems
- Investigation of RAOs, moorings and forces determination of a preliminary mooring system
- Picking the appropriate wave energy converters (WECs) and their impacts on the platform dynamics, in particular, a 1:30 model of a three-WECs array and innovative control system was built and tank-tested.

Following individual validation of the key components, the Technology Readiness Level (TRL) of W2Power has been upgraded from 3 to 4.

In 2015, W2Power completed a series of validation trials at the FloWave Ocean Energy Research Facility at the University of Edinburgh. Precise sea states based on measured met-ocean conditions at EMEC, Scotland, and Cabo Silleiro, Spain, were used with a 1:40 scale model, achieving a TRL of 5.

Subsequently, W2Power has gone through several design iterations, becoming the world's first twin wind turbine platform tested at sea, achieving a TRL of 6. It should be noted that the current design omits WECs; interested readers are referred to earlier studies by Hanssen et al. [11] and Legaz et al. [12]. Figure 1 shows the 1:6 W2Power scale prototype tested in open sea near the PLOCAN platform, Canary Islands, Spain.

The current W2Power design is engineered to support a pair of original equipment manufacturers (OEMs) wind turbines on out-leaning towers, as studied here with two "generic" 6 MW turbines and giving each platform 12 MW rated power. The platform is anchored to the seabed by a single point mooring system comprising three lines.

FIGURE 1: W2POWER PLATFORM PROTOTYPE DURING 2019 SEA TESTS. PHOTO COURTESY OF ENEROCEAN.

1.1.2 Wind Farm Scale Advantages

EnerOcean has proposed two wind farms with a total capacity of 180 MW, and up to 15 floating platforms are likely to be deployed. W2Power is the most cost-effective technology at the wind farm scale in terms of cost-effectiveness [13 - 14], and provides the following:

- Maximisation of power generation due to its weathervaning system that allows the platform to align with the predominant wind direction and eliminates conventional yaw
- W2Power, with its light-weight but stable design, offers up to twice the rated capacity of a single turbine floater while using less material (saving up greater than 25% of steel weight)
- Assembling two turbines on a single platform can be done in a dry dock or a load-out quay, which keeps time and installation costs down since fewer tows and moorings are required

- A W2Power wind farm reduces inter-array cabling and mooring requirements by increasing turbines density in the array, thus improving seabed space management.

1.1.3 Model Design Description

This study considers a 1:40 scale model of the W2Power platform, which is a triangular semi-submersible structure that supports a pair of OEM wind turbines mounted on outward-leaning towers at columns A and C.

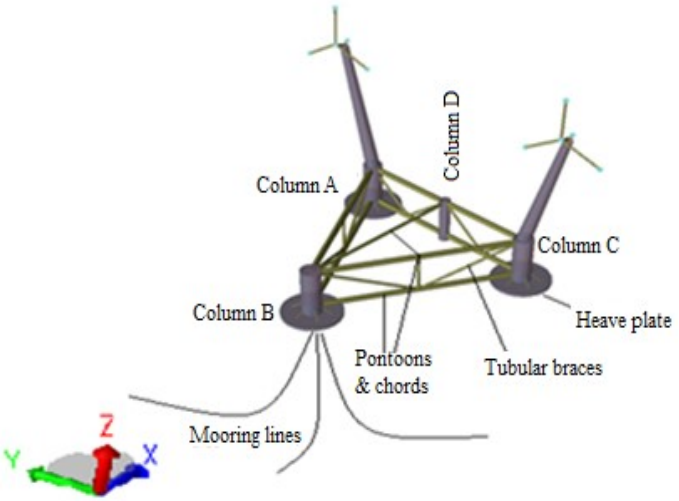

FIGURE 2: SCHEMATIC REPRESENTATION OF THE MODEL'S COMPONENTS.

The platform will be anchored to the seabed by a single point mooring system comprising three lines and attached to column B. Horizontal pontoons and chords link all columns to form a triangle and tubular braces (slender elements) are attached between the columns and the pontoons. In order to prevent excessive heave, the platform is passively ballasted by water in three heave plates attached to the base of the corner columns A, B, and C. The dimensions of the W2Power's main constituents at full scale are listed in Table 1.

TABLE 1: MAIN PARTICULARS OF THE FULL-SCALE W2POWER PLATFORM.

Description, unit	Prototype
Draft, m	15
Water depth, m	200
Outward leaning angle, °	15
Corner columns diameter, m	9
Column D diameter, m	5
Columns heights, m	25
Towers bases separation, m	90

2. ANALYSIS METHODS

The floating system here consists of two components:

1) the floater, modelled as a large rigid body with six DOFs
2) the mooring lines, modelled as slender bodies using the Morison equation

The hydrodynamic loads on these components are evaluated by employing different theories since their dimensions differ. A fully coupled analysis is used to evaluate the system's performance. The non-linear interactions between hydro- and mooring- dynamics are captured by solving the governing equations in the time domain:

$$([M] + [A])\ddot{X} + [B]\dot{X} + [C]X = F_{wave} + F_{moor} \quad (1)$$

Where, [M] is the 6×6 structural mass (dry mass + inertia) matrix, which includes platform, towers, nacelles, and rotors as superstructures. [A] is the 6×6 frequency-dependent added mass, B is the 6×6 potential damping matrix, and C is the 6×6 hydrostatic stiffness matrix. F_{wave} is the 6-DOF wave forces (excitation, viscous and drift forces) in which the Newman approximation was utilised to account for wave drift loads [15], and F_{moor} is the mooring force.

2.1 Numerical Model Setup

The numerical model is built at a scale of 1:40, and its properties are listed in Table 2. Then numerical simulations were performed using the SESAM (GeniE) software developed by DNV [16] and Orcina Ltd's packages (OrcaWave and OrcaFlex) [17 - 18].

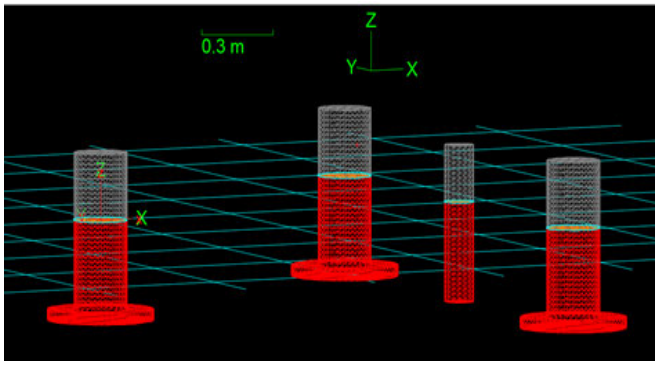

FIGURE 3: PANEL MODEL IN ORCAWAVE, WET SURFACES (IN RED) BELOW THE LOADING CONDITION.

GeniE was utilised to construct and generate FEM models of the platform's substructures: the panel model including the four columns (A, B, C, and D) and the Morison model represented by the pontoons and braces. Then OrcaWave was used to perform the hydrodynamic study based on the 3D potential theory. As a result, the hydrostatic stiffness coefficients were obtained, along with the frequency-dependent hydrodynamic added mass and damping.

TABLE 2: SCALE MODEL PROPERTIES.

Mass, kg	122.087		
Centre of mass (x, y, z), m	1.2E+00	-3.3E+-05	1.9E-01
Centre of buoyancy (x, y, z), m	1.2E+00	1.6E-07	-2.3E-01
Waterplane area, m^2	1.3E-01		
Mass moments of inertia, $kg.m^2$	4.0E+05	6.7E-03	-4.1E+01
	6.7E-03	4.0E+05	1.9E-15
	-4.1E+01	0.0E+00	4.0E+05

After obtaining the platform's hydrodynamic characteristics (i.e. RAOs), all substructures were imported into the OrcaFlex to analyse the floater and mooring coupled system in the time domain. The coupled analysis model setup is depicted in Figure 3.

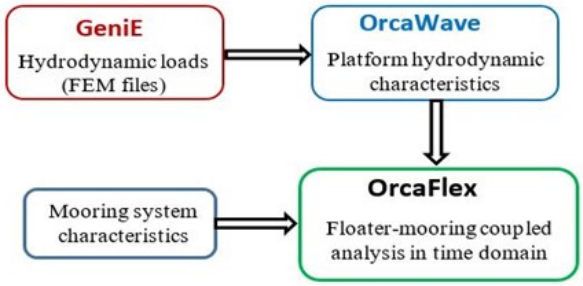

FIGURE 3: MODEL SETUP FOR COUPLED ANALYSIS.

2.2 Environmental Conditions

The environmental data considered here are for a potential deployment site off the island of Gran Canaria in the Atlantic Ocean, as shown in Figure 4. The National and Kapodistrian University of Athens provided wind and wave hindcast data from 2001 to 2010 [19].

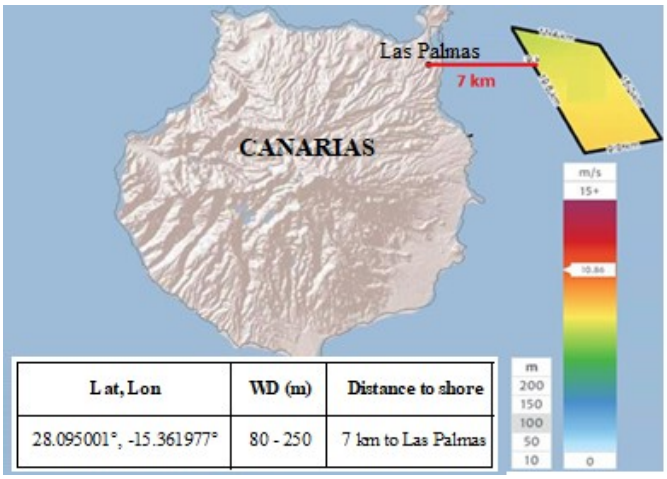

FIGURE 4: REFERENCE SITE (GLOBAL WIND ATLAS) [20].

Figure 5 shows the distribution of significant wave height (Hs) and peak wave period (Tp) by sector. As can be seen, the dominant sector is East-North-East, with the majority of long-period waves (mostly between 6 and 15s) and large significant wave height emanating from that direction.

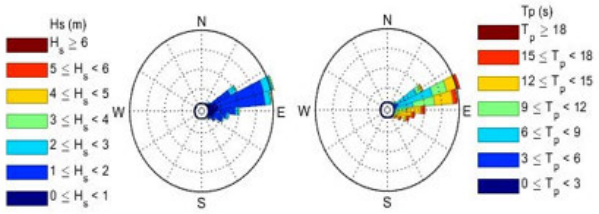

FIGURE 5: DIRECTIONAL WAVE ROSE: (LEFT) HS AND (RIGHT) TP.

Accordingly, neglecting aerodynamic loads and considering both waves and current conditions, operational load cases for two wave directions are simulated, as described in Table 3.

TABLE 3: PARTICULARS FOR OPERATIONAL LOAD CASES SIMULATIONS.

Description	**Full Scale**	**Model Scale**
Water depth (m)	80	2
	200	5
Current conditions		
Speed (m/s)	1	0.158
Direction (°)	180	180
Wave conditions (JONSWAP spectrum)		
Hs (m)	1.5	0.0375
Tp (s)	8	1.265
γ	2	2
Directions (°)	180	180
	210	210

2.3 Frequency-domain Hydrodynamic Analysis

2.3.1 Eigenfrequency Analysis

Due to the floater's symmetry, pitch and roll motions are nearly identical, and the mooring system significantly influences horizontal motions. Therefore, only heave and pitch motions are of interest. When the platform is analysed without a mooring system, the restoring force is generated mainly by the large waterplane area, which remains unchanged for the two water depth conditions due to the use of the same floater, and also the body mass remains unchanged. However, only the added mass term varies in response to the dynamic pressure generated by the platform's motion.

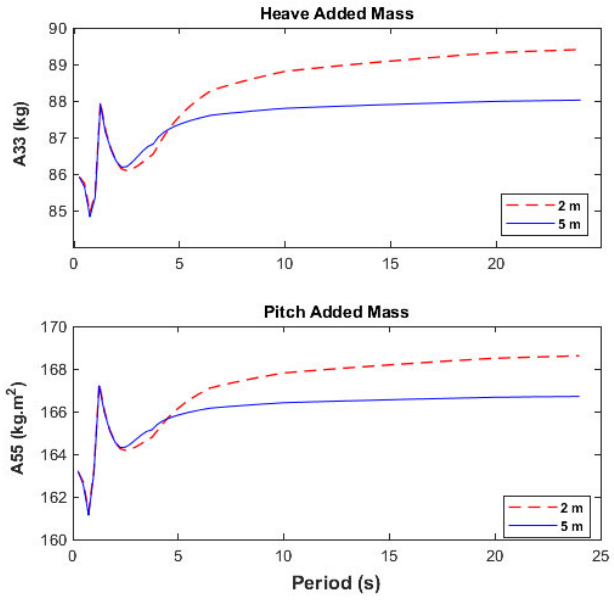

FIGURE 6: ADDED MASS OF HEAVE (A33) AND PITCH (A55) MOTIONS IN A 0º WAVE HEADING FOR WATER DEPTHS OF 5 AND 2 M.

The added mass is dependent on the period of the excitation wave and converges towards a constant value for both heave and pitch, as illustrated in Figure 6. Then the natural periods, T_{Ni}, for the heave and pitch responses can be calculated by Eq (2), and Table 4 summarises the results.

$$T_{Ni} = 2\pi \left(\frac{M+A_{ii}}{C_{ii}}\right)^{0.5} \quad (2)$$

Where, M is the body mass, A_{ii} and C_{ii} are the added mass and restoring stiffness in the *i*th DoF, respectively.

TABLE 4: EIGENFREQUENCY CALCULATION FOR WATER DEPTH 5 AND 2 M.

Description	DoF			
	Heave		Pitch	
Water depth (m)	5	2	5	2
Body mass (kg, kg.m^2)	122.087	122.087	180.189	180.189
Added mass (kg, kg.m^2)	87.887	89.326	166.342	167.330
Restoring (N/m, N.m)	1311.923	1311.523	2178.313	2178.313
Natural period (s)	2.514	2.523	2.506	2.510

2.3.2 Platform RAOs Motion

Figure 7 compares the response amplitude operators (RAOs) for heave and pitch motions. The RAOs reveal that the resonance occurs at a wave period of approximately 2 to 3 s, which is consistent with the eigenfrequency calculations in Table 4, especially in the heave response. Furthermore, as the water depth decreases, there is a significant rise in pitch response, particularly at low frequencies. However, this is not seen in the heave RAO; hence, more illustrations (i.e. excitation forces) might be presented that are not shown in this study. Following that, the hydrodynamic characteristics of the platform were determined for each water depth in preparation for time-domain analysis of the floater-mooring coupling.

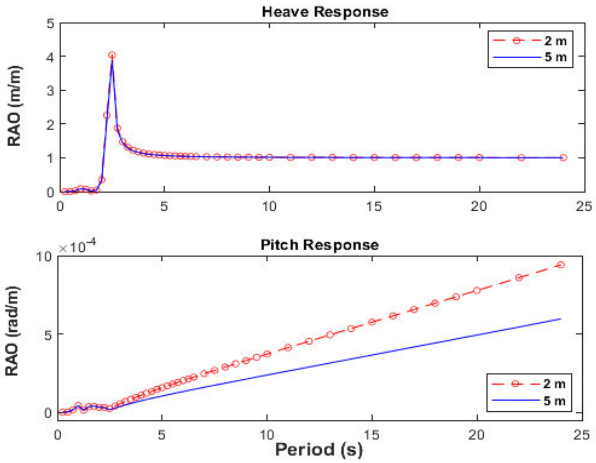

FIGURE 7: HEAVE AND PITCH RAOS IN A 0º WAVE HEADING FOR WATER DEPTHS OF 5 AND 2 M.

2.4 Time-domain Hydrodynamic Analysis

To more accurately model drag loadings on submerged parts of the hull, large members (i.e. columns and heave plates) and cross members (i.e. pontoons, chords, and tubular braces) were modelled in OrcaFlex as Morison elements. Furthermore, all columns and the three heave plates are equipped with Morison elements. In accordance with [21] and [22], the drag coefficients used in the analysis are listed in Table 5, with colour coding consistent with that in Figure 8.

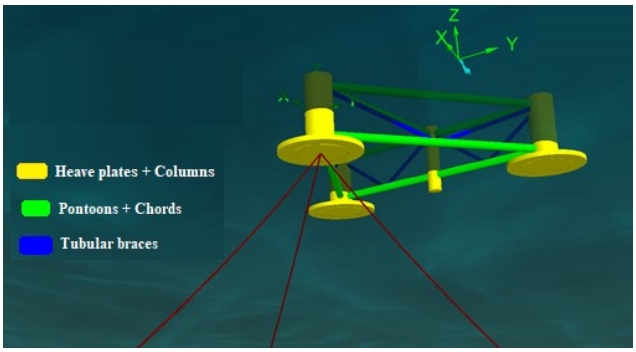

FIGURE 8: MORISON DRAG ELEMENTS RENDERING AND THEIR COLOUR CODES IN ORCAFLEX.

TABLE 5: DRAG COEFFICIENTS FOR MORISON ELEMENTS.

Hull component	Drag Coefficient (Cd)
Corner columns (A, B & C)	0.61
Middle column (D)	0.56
Heave plates	0.68 4.8 in z-direction
Pontoons and chords	1
Tubular braces	0.63

2.5 Mooring System

Three catenary lines (A, B and C) are placed symmetrically along the platform's Z-axis and spread by 120° to anchor it to the seabed, as seen in Figure 9. According to DNV guidelines [23], stud-less chains of a drag coefficient of 2.4 were selected; the characteristics of the mooring system are listed in Table 6.

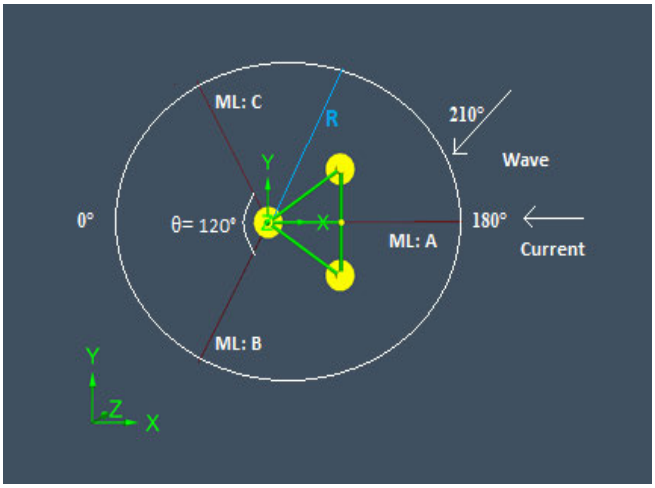

FIGURE 9: TOP VIEW OF MOORING LINES ARRANGEMENT AND ENVIRONMENTAL LOADING DIRECTIONS.

TABLE 6: CHARACTERISTICS OF THE MOORING SYSTEM MODELLED.

Description, unit	Water depth	
	5 m	2 m
Line grade and type	R4 - studless chains	
Dry-line weight, N/m	3.01	
Wet-line weight, N/m	2.61	
Nominal chain diameter, mm	8.00	
Minimum breaking load (MBL), N	31.38E+03	
Axial stiffness, N	1.32E+06	
Fairlead pretension, N	33.37	11.71
Line unstretched length, m	22.93	9.17
Fairlead depth, m	0.375	0.375
Anchor radius (R), m	21.35	8.54
Anchor depth, m	5	2

2.6 System Survivability Analysis

To check the system survivability, contour surfaces for joint wind and wave parameters are constructed based on long-term joint distributions of mean wind speed at 100 m height (Uw), significant wave height (Hs) and spectral peak period (Tp), with the probability of exceeding corresponding to a 50-year return period. The contour surfaces shown in Figures 10 and 11 were produced using the ViroCon, Python-based, software [24]. The zero-crossing period (Tz) was estimated using the relationship Tp = 1.2859 Tz, and as recommended by DNV [22], the duration of each sea state is 3600 s. Accordingly, four extreme load cases (LCs) are defined with six different wave seeds for each and summarised in Table 7. Likewise, the load cases in Table 3 are considered to analyse the performance of the floater-mooring system under operational conditions.

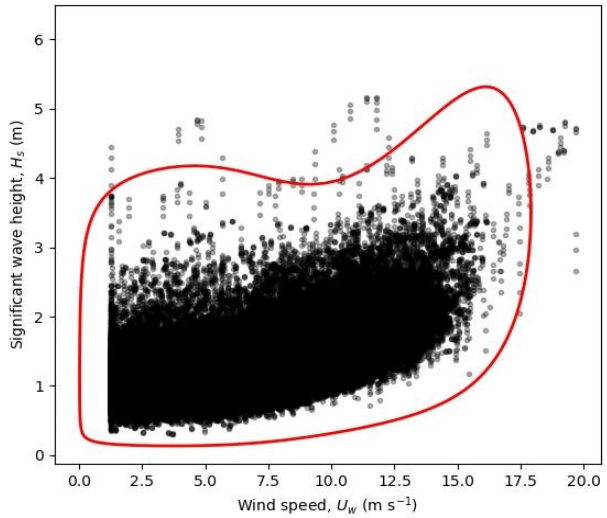

FIGURE 10: 50-YEAR ENVIRONMENTAL CONTOURS FOR UW AND HS.

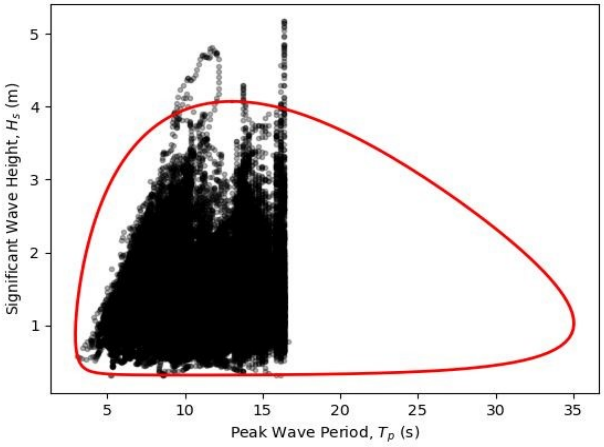

FIGURE 11: 50-YEAR ENVIRONMENTAL CONTOURS FOR TP AND HS.

TABLE 7: PARTICULARS FOR SURVIVABILITY ANALYSIS.

Description		Full Scale	Model Scale
		80	2
Water depth (m)		200	5
Simulation time (s)		3600	
Wave conditions (JONSWAP spectrum)			
LC 1	Hs (m)	4	0.100
	Tp (s)	16.5	2.609
LC 2	Hs (m)	4.1	0.103
	Tp (s)	13.5	2.135
LC 3	Hs (m)	3.8	0.095
	Tp (s)	8	1.265
LC 4	Hs (m)	4	0.100
	Tp (s)	10	1.581
γ		3.3	
Direction (°)		180	

2.7 Simulation Setup

Regarding the simulation settings, the platform is positioned, as seen in Figure 9. Since no wind is considered, both waves and currents propagate in the x-direction (at 180°). While the current direction remains unchanged, waves hit the floater at 210°, which leads to a 30° misalignment between the wave and current directions.

3. RESULTS AND DISCUSSION

3.1 Extreme Condition Results

The ultimate limit state (ULS) check is performed to ensure that individual mooring lines are strong enough to withstand the loads imposed by extreme environmental conditions. According to standard DNV-OS-E301 [23], the design equation in the form of a utilisation factor (UF) can be expressed as follows:

$$UF = \frac{T_d}{S_c} < 1 \qquad (3)$$

$$T_d = (\gamma_{mean} * T_{mean}) + (\gamma_{dyn} * T_{dyn}) \qquad (4)$$

Where, S_C is the characteristic mooring line strength and was obtained from the minimum breaking strength ($Sc = 0.95 \times S_{MBS}$). T_d is the design tension, γ_{mean} and γ_{dyn} are partial safety factors for the mooring line's mean (T_{mean}) and dynamic (T_{dyn}) tensions, respectively, which have been determined in accordance with a consequence class 1, see Table 8.

TABLE 8: PARTIAL SAFETY FACTORS FOR ULS.

Consequence class	Safety factor for mean tension (γ_{mean})	Safety factor for dynamic tension (γ_{dyn})
1	1.10	1.50
2	1.40	2.10

Matlab was utilised for post-processing. The results of the ULS analysis are summarised in Table 9. In all loading cases, the utilisation factors for all lines were found to be quite conservative, indicating that the mooring lines are sufficiently strong to withstand the extreme waves in that location. However, mooring line A showed a higher utilisation factor than the other two lines due to its alignment with the incoming waves.

TABLE 9: ULS RESULTS FOR THE MOORING LINES.

LC	ML	T_{mean} (N)		T_{dyn} (N)		UF	
		2 m	5 m	2 m	5 m	2 m	5 m
LC1	A	13	35	14	13	1.98E-03	3.28E-03
	B	9	30	3	8	7.74E-04	2.56E-03
	C	9	30	3	8	7.71E-04	2.58E-03
LC2	A	13	35	22	29	2.75E-03	4.68E-03
	B	9	30	3	11	8.18E-04	2.78E-03
	C	9	30	3	11	8.13E-04	2.84E-03
LC3	A	18	39	204	84	1.85E-02	9.64E-03
	B	8	29	9	15	1.31E-03	3.11E-03
	C	8	29	13	20	1.60E-03	3.48E-03
LC4	A	15	37	836	68	7.25E-02	8.17E-03
	B	8	29	6	13	1.00E-03	2.90E-03
	C	8	29	11	19	1.47E-03	3.49E-03

The maximum mooring line tension and floater surge and heave movements are some of the most critical design criteria for semisubmersibles. Figure 12 illustrates the surge and heave motions of the platform under extreme conditions, whereas Figure 13 depicts the maximum tension in the three lines. As can be observed, the three parameters are controlled by the significant wave height (Hs) and peak period (Tp). The heave response reduces as the wave period decreases, whereas the surge response increases.

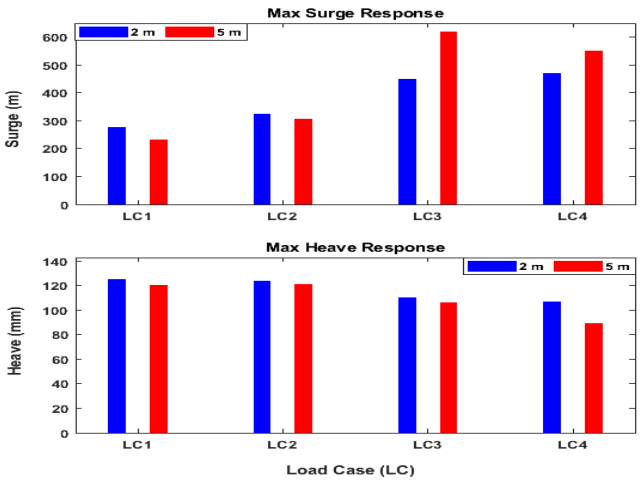

FIGURE 12: MAXIMUM SURGE AND HEAVE MOTIONS FOR EACH EXTREME LOAD CASE AND TWO DEPTHS.

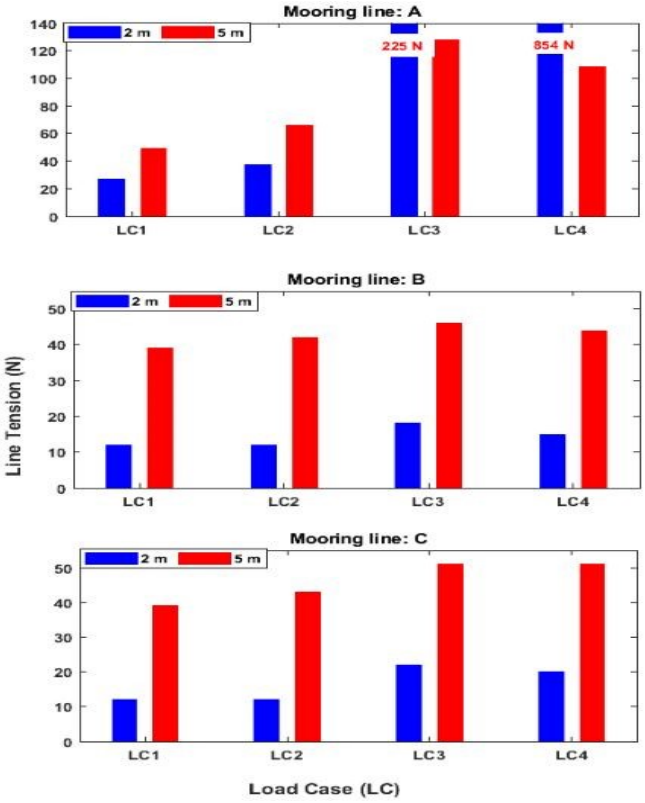

FIGURE 13: MAXIMUM MOORING LINE TENSIONS FOR EACH EXTREME LOAD CASE AND TWO DEPTHS.

At a water depth of 2 m, mooring line A experienced extremely high tensions of 225 N and 854 N during the most severe wave circumstances due to the line's direction of collinear waves and currents (180°), but these tensions are still less than the line MBL. The surge follows a similar pattern, and it is interesting to note that the maximum tension and surge do not coincide. One of these values (both T_{max}= 225 N and $Surge_{max}$= 450 mm) occurred while the wave height (Hs= 0.095 m) was less than the maximum, emphasising the significance of modelling different realisations (i.e. random seeds) and employing a focused-wave technique to reproduce an extreme wave condition the sea state of interest, particularly for single mooring systems. This argument is consistent with the findings of Hann et al. [25] and Coe et al. [26], who concluded that a single focused wave was insufficient to accurately quantify the extreme loads encountered by a single taut moored wave energy converter. On the other hand, the heave response was found to have values relatively close to those observed at 5 m water depth, averaging about 0.11 m.

3.2 Operational Condition Results

3.2.1 Mooring Line Tension

This section discusses the platform's performance under the operational load case defined in Table 3. The effective tensions at the fairleads of three mooring lines are shown in Figure 14 for an operational load case and two water depths. The coexistence of waves and currents causes the most substantial tensions in line A. The average tension at a depth of 2 m is around 12.7 N, while at a depth of 5 m, it is approximately 35 N. As can be seen, the tension at 5 m water depth is approximately 1.7 times that at 2m. This is due to the increased tension associated with the deeper water level caused by the long line suspended and laid at the seabed.

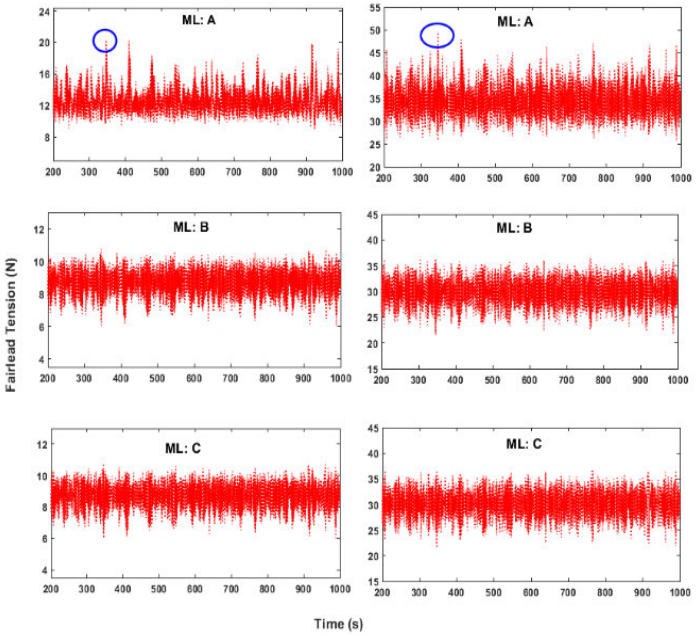

FIGURE 14: TIME-SERIES RESULTS OF THE MOORING LINES TENSION AT WAVE HEADING 180° AND WATER DEPTH 2 M (LEFT) AND 5 M (RIGHT).

The tensions on the other leeward mooring cables (B and C) are comparable as they are misaligned with the incoming waves and current. The maximum tensions are measured at mooring line A at water depths of 2 and 5 m (circled in blue) with approximate values of 22 and 50 N, respectively.

3.2.2 Platform Motion

This section reports the findings of platform responses, in which surge, sway and heave time series have been compared for a 180º wave direction and the two water depths. The response is obtained from the floater-mooring coupled responses from 200 to 1000 seconds by omitting the transient period. According to Figure 15, the platform appears to respond similarly in the surge motion at 2 and 5 m water depth, with corresponding maximum displacements of 0.2 and 0.15 m (circled in red).

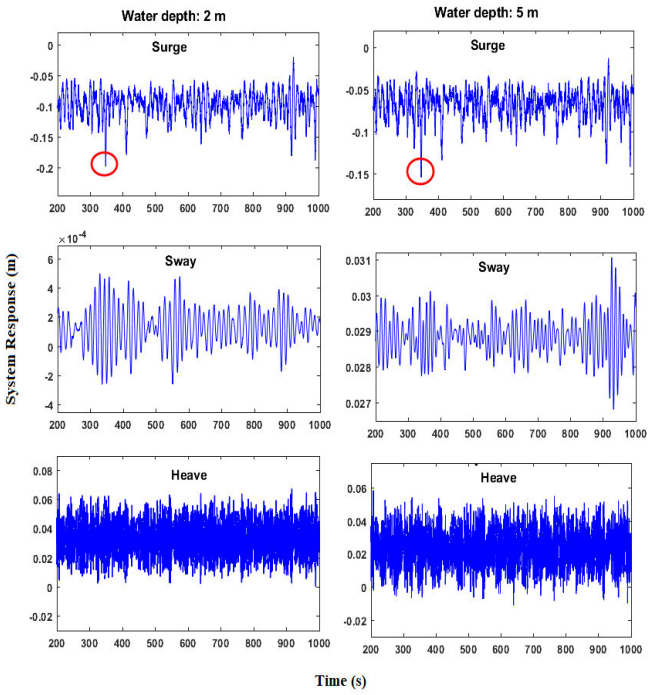

FIGURE 15: TIME-SERIES RESULTS OF THE PLATFORM MOTIONS AT WAVE HEADING 180° AND TWO WATER DEPTHS.

3.2.3 Effect of Wave Directionality

Taking advantage of the platform's capability to weathervane, it is crucial to investigate the consequence of the incoming wave heading on the mooring floater reactions. Thus, a single mooring line's tension and the pitch response are analysed under the most wave-dominated headings in the proposed deployment site, 180º and 210º. As shown in Figure 16, the wave direction does not affect the platform pitch motion.

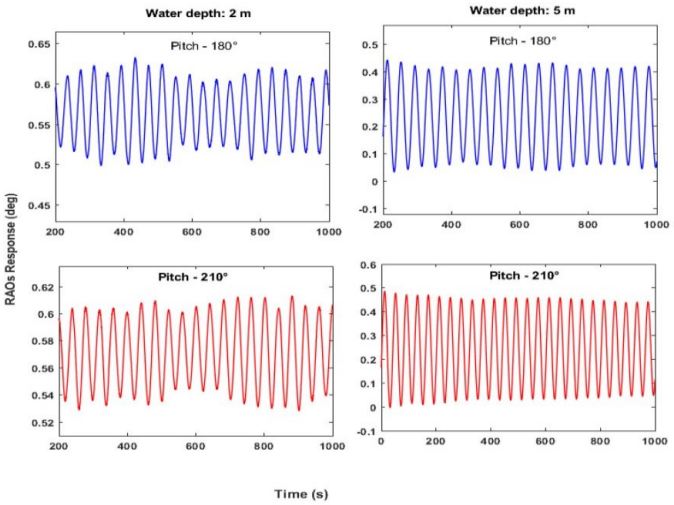

FIGURE 16: TIME-SERIES RESULTS OF THE PITCH RESPONSE AT DIFFERENT WAVE HEADINGS AND WATER DEPTHS.

However, as seen in Figure 17, the wave direction strongly impacts the mooring line tension at both water depths. When a wave with a 180º hits the platform, it tends to severely drift the floater from its initial position, aided by currents from the same direction. On the other hand, when waves attack the platform at a 210º, they lack that significant drift force due to the mooring lines being out of phase with both current and waves, which is clearly seen in the figure.

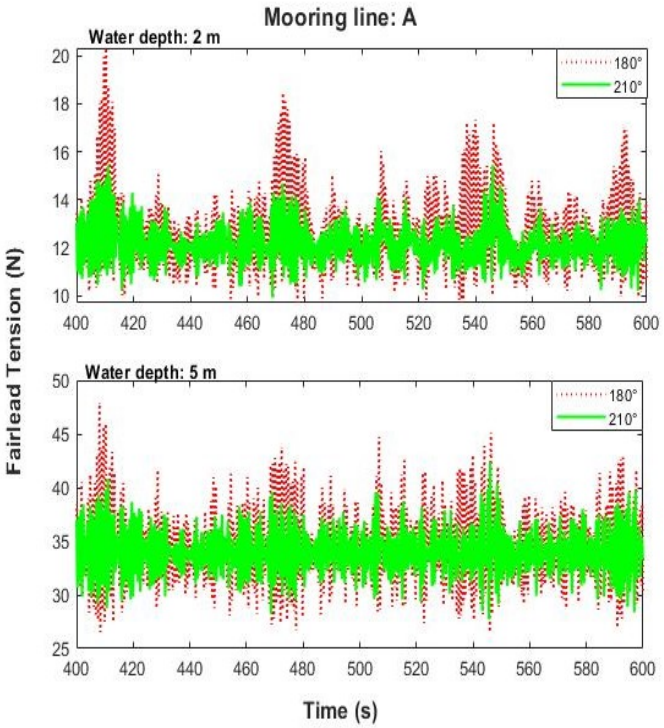

FIGURE 17: TIME-SERIES RESULTS OF A MOORING LINE AT TWO WAVE HEADINGS AND TWO WATER DEPTHS.

3.2.4 Sensitivity of Drag Coefficients

To demonstrate the influence of drag coefficients on the study, the numerical simulations were performed using pontoons of drag coefficients ranging from 0.70 to 1.05; the results reveal that the numerical simulations are insensitive to pontoons Cd values, as illustrated in Figure 18.

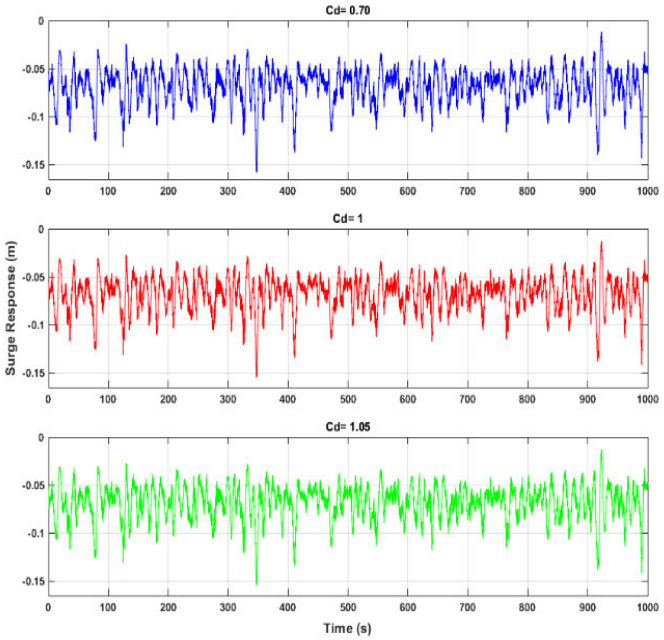

FIGURE 18: TIME-SERIES RESULTS OF THE PLATFORM SURGE MOTION WITH PONTOONS OF DIFFERENT CD VALUES, WAVE HEADING 180° AND WATER DEPTH 5 M.

4 CONCLUSION

The purpose of this study was to assess the hydrodynamic performance for a 1:40 scale model of the W2Power twin-turbine floating platform. Investigations were conducted under survival and operating conditions considering long-term hindcast marine data. Two scaled mooring systems were proposed for moderated and deep waters of depths of 2 and 5 m, respectively.

Eigenfrequency analysis has been carried out; accordingly, the natural periods of floater motions in both heave and pitch have been calculated in detail and presented. The pitch response increased with decreasing water depth, especially at low frequencies, so for a more accurate coupling analysis, it is necessary to obtain the platform's hydrodynamic characteristics for each water depth separately.

In extreme analysis, the significant wave height (Hs) and peak period (Tp) affect both the maximum line tension and platform surge, such that increasing the significant wave height and peak period tends to increase the maximum tension and surge.

The mooring system performs effectively at a water depth of 2 m without requiring as much tension as at a water depth of 5 m, which is a vital sign that the degree of tightness of the smaller water depth is accurately approximated.

The numerical simulations were found to be insensitive to the pontoons' drag coefficient values. The mooring system was found to be sensitive to wave direction, particularly when wave and current directions coincide, even though the aerodynamic loads were not considered. This indicates that waves and current loading and their interaction are crucial in simulations of FOWTs, particularly when the FOWTs are to be deployed in locations where currents may travel in the opposite direction of the surface wave directions.

Since the platform weathervanes in response to both applied current and wind direction, further work is needed to investigate the impact on either platform stability or power production. Also, future work will explore the wave-current interaction using tank testing experiments in the FloWave Ocean Energy Research Facility to provide validation data for the present simulations and the aerodynamic loads that will be incorporated.

ACKNOWLEDGEMENTS

The authors would like to express their gratitude for funding from the EPSRC and NERC for the Industrial CDT in Offshore Renewable Energy (EP/S023933/1). We are also grateful to Prof. George Kallos and Dr. Christina Kalogeri of the National and Kapodistrian University of Athens for providing the site's hindcast data.

REFERENCES

[1] The European Parliament and the Council of the European Union, “Offshore Wind Energy in Europe,” Brussels, Belgium. pp. 1–6, October 2020: (www.europarl.europa.eu).

[2] Wind Energy Newsletter, Illustrated by Josh Bauer, NREL, April 2020: (www.nrel.gov).

[3] N. Barltrop, “Multiple unit floating offshore wind farm (MUFOW),” Wind Eng., vol. 17, no. 4, pp. 183–188, 1993.

[4] Dagfinn Røyseth, Reza Hezari, Jan Erik Hanssen, W2Power: Combining wind and waves, Proc. 2009 All-Energy Conference & Exhibition, Aberdeen, Scotland, 17 May 2009.

[5] S. Bashetty and S. Ozcelik, “Design and Stability Analysis of an Offshore Floating Multi-Turbine Platform,” in 2020 IEEE Green Technologies Conference (GreenTech), 2020, pp. 184–189.

[6] H. K. Jang, S. Park, M. H. Kim, K. H. Kim, and K. Hong, “Effects of heave plates on the global performance of a multi-unit floating offshore wind turbine,” Renew. Energy, vol. 134, pp. 526–537, 2019.

[7] A. Henderson and M. Patel, “Floating Offshore Wind Farms – an Option ?”, 2000.

[8] I. E. Udoh and J. Zou, “Optimizing Floating Offshore Multi-Wind-Turbine Design: A Parametric Study on Tower Inclination and Column Spacing,” pp. 1–19, 2020.

[9] The MARINA Platform project (Jan. 2010 - Jun. 2014), full title Marine Renewable Integration Application Platform, public site: (www.marina-platform.info).

[10] N. Papandroulakis, C. Thomsen, K. Mintenbeck, P. Mayorga, and J. J. Hernández-Brito, The EU-Project "TROPOS", in Aquaculture Perspective of Multi-Use Sites in the Open Ocean: The Untapped Potential for Marine Resources in the Anthropocene, B. H. Buck and R. Langan, Eds. Cham, Switzerland: Springer International Publishing, 2017, pp. 355–374.

[11] J. E. Hanssen et al., “Design and performance validation of a hybrid offshore renewable energy platform: A path to cost-efficient development of deepwater marine energy resources,” the 10th Int. Conf. Ecol. Veh. Renew. Energies, EVER 2015, 2015.
[12] M. J. Legaz, D. Coronil, P. Mayorga, and J. Fernández, “STUDY OF A HYBRID RENEWABLE ENERGY PLATFORM: W2POWER,” in the ASME - the 37th International Conference on Ocean, Offshore and Arctic Engineering OMAE2018, 2018, pp. 1–9.
[13] J. Parfitt, “SPAIN’S FIRST TWO-HEADED FLOATING WIND TURBINE EXPECTED TO BECOME ‘LOWEST COST SOLUTION’ FOR RENEWABLE ENERGY FAR FROM COASTLINE”, The Olive Press, 2019: (The OLIVE PRESS).
[14] J. E. Hanssen, Consultation response from 1-Tech SPRL, Brussels (Belgium) - DemoWind Cost modelling: ‘Costing and economic performance of the W2Power floating wind energy technology’, 2019: (Demo Wind Cost Modelling Report).
[15] NEWMAN and J.N., “Second-Order, Slowly-Varying Forces on Vessels in Irregular Waves.,” no. 1, pp. 1–4, 1974.
[16] SESAM-GeniE by DNV, 2021: (www.dnv.com).
[17] Orcina Ltd., OrcaWave User Manual, (version 11.a), 2021: (www.orcina.com).
[18] Orcina Ltd., OrcaFlex User Manual, (version 11.a), 2021: (www.orcina.com).
[19] Atmospheric Modeling and Weather Forecasting Group (AM&WFG), National & Kapodistrian University of Athens, Athens, Greece, 2021: (www.forecast.uoa.gr).
[20] Global Wind Atlas: (www.globalwindatlas.info), accessed in October 2021.
[21] A. Robertson, J. Jonkman, M. Masciola, and H. Song, “Definition of the Semisubmersible Floating System for Phase II of OC4,” 2014.
[22] DNV-RP-C205: Environmental Conditions and Environmental Loads - Recommended Practice.
[23] DNV-OS-E301: Position Mooring.
[24] A. F. Haselsteiner, J. Lehmkuhl, T. Pape, K. L. Windmeier, and K. D. Thoben, “ViroCon: A software to compute multivariate extremes using the environmental contour method,” SoftwareX, vol. 9, pp. 95–101, 2019.
[25] M. Hann, D. Greaves, and A. Raby, “Snatch loading of a single taut moored floating wave energy converter due to focussed wave groups,” Ocean Eng., vol. 96, pp. 258–271, 2015.
[26] R. G. Coe, V. S. Neary, M. J. Lawson, Y. Yu, and J. Weber, Extreme Conditions Modeling Workshop Report, no. July. 2014.

Ocean Engineering 292 (2024) 116571

Contents lists available at ScienceDirect

Ocean Engineering

journal homepage: www.elsevier.com/locate/oceaneng

Implications of wave–current interaction on the dynamic responses of a floating offshore wind turbine☆

Mujahid Elobeid [a,b,*], Ajit C. Pillai [a,c], Longbin Tao [a,b], David Ingram [a,d], Jan Erik Hanssen [e], Pedro Mayorga [e]

[a] EPSRC and NERC Industrial Centre for Doctoral Training in Offshore Renewable Energy (IDCORE), The University of Edinburgh, King's Buildings, Edinburgh EH9 3FB, UK
[b] Department of Naval Architecture, Ocean and Marine Engineering, University of Strathclyde, Glasgow G4 0LZ, UK
[c] Renewable Energy Group, Engineering Discipline, Faculty of Environment, Science, and Economy, University of Exeter, Penryn Campus, Penryn TR10 9FE, UK
[d] Institute for Energy Systems, School of Engineering, The University of Edinburgh, King's Buildings, Edinburgh EH9 3FB, UK
[e] EnerOcean S.L., Bulevar Louis Pasteur, n° 5, of.321, 29010 Málaga, Spain

ARTICLE INFO

Keywords:
Floating offshore wind turbines (FOWTs)
Wave–current interaction (WCI)
Nonlinear mooring dynamics
Combined wave and current
Dispersion relation
Semisubmersible
W2Power

ABSTRACT

This study investigates the implications of wave–current interaction on the dynamic responses of the W2Power semisubmersible platform for floating offshore wind turbines under operational and extreme conditions. Firstly, two analytical models based on Airy wave theory are developed to analyse the effects of current interaction with regular and irregular waves. Then, these models are integrated with the well-known engineering tool OrcaFlex for the coupled aero-hydro-servo-elastic analysis. The presence of current was found to significantly modify the wave profiles and influence the static equilibrium, mooring system, and motion dynamics of the FOWT.

The results reveal that the translational motion responses, such as surge and heave, are affected by wave–current interaction, with mean and maximum values decreasing under a following current and increasing under an opposing current. However, rotational motion responses are minimally affected. Wave–current interaction also notably affects maximum mooring tensions, with variations of up to ±22% depending on the current direction and mooring layout. Furthermore, reductions in maximum longitudinal acceleration are observed due to such interaction. Incorporating wave–current interaction in simulations enhances our understanding of FOWT dynamics and allows for more reliable estimations of system behaviour, emphasising the importance of ensuring safe operating conditions, particularly in sites with opposing currents.

1. Introduction

Offshore wind is widely regarded as a significant renewable energy source for decarbonising power production and decreasing greenhouse gas emissions. Thus, substantial efforts are being made to design wind turbines capable of capturing energy at sea. These turbines can be installed on bottom-fixed or floating foundations anchored to the seabed by mooring lines. When it comes to the shallow water (e.g. the North Sea, Chinese coastal waters, and the New England coast) of soft seabeds (i.e. made of sand, gravel or mud), the deployment of bottom-fixed foundations is the most cost-effective and optimal option. However, some regions (e.g. the Mediterranean Sea) lack favourable seabed conditions for bottom-fixed foundations. Moreover, 80% of offshore wind potential is in waters deeper than 60 m, thereby bottom-fixed foundations are problematic (WindEurope, 2018). Hence, floating offshore foundations are emerging as potential revolutionary solutions that offer broader wind resource exploitation and alleviate problems associated with bottom-fixed designs.

These floating offshore wind turbines (FOWTs) are subjected to various environmental loads, such as wind, waves, and currents (see Fig. 1). For their design and lifetime safety, the dynamic response in storm conditions, as well as the static stability and coupled dynamic response under operation conditions, are of paramount importance and, hence, have been an ongoing research focus. The hydrodynamic

☆ This work was funded by the EPSRC and NERC Industrial Centre for Doctoral Training in Offshore Renewable Energy (EP/S023933/1). The authors are also grateful to the National and Kapodistrian University of Athens for providing the hindcast data.

* Corresponding author at: EPSRC and NERC Industrial Centre for Doctoral Training in Offshore Renewable Energy (IDCORE), The University of Edinburgh, King's Buildings, Edinburgh EH9 3FB, UK.
E-mail address: (M. Elobeid).
URL: https://www.idcore.ac.uk (M. Elobeid).

https://doi.org/10.1016/j.oceaneng.2023.116571
Received 5 June 2023; Received in revised form 25 November 2023; Accepted 11 December 2023
Available online 16 December 2023

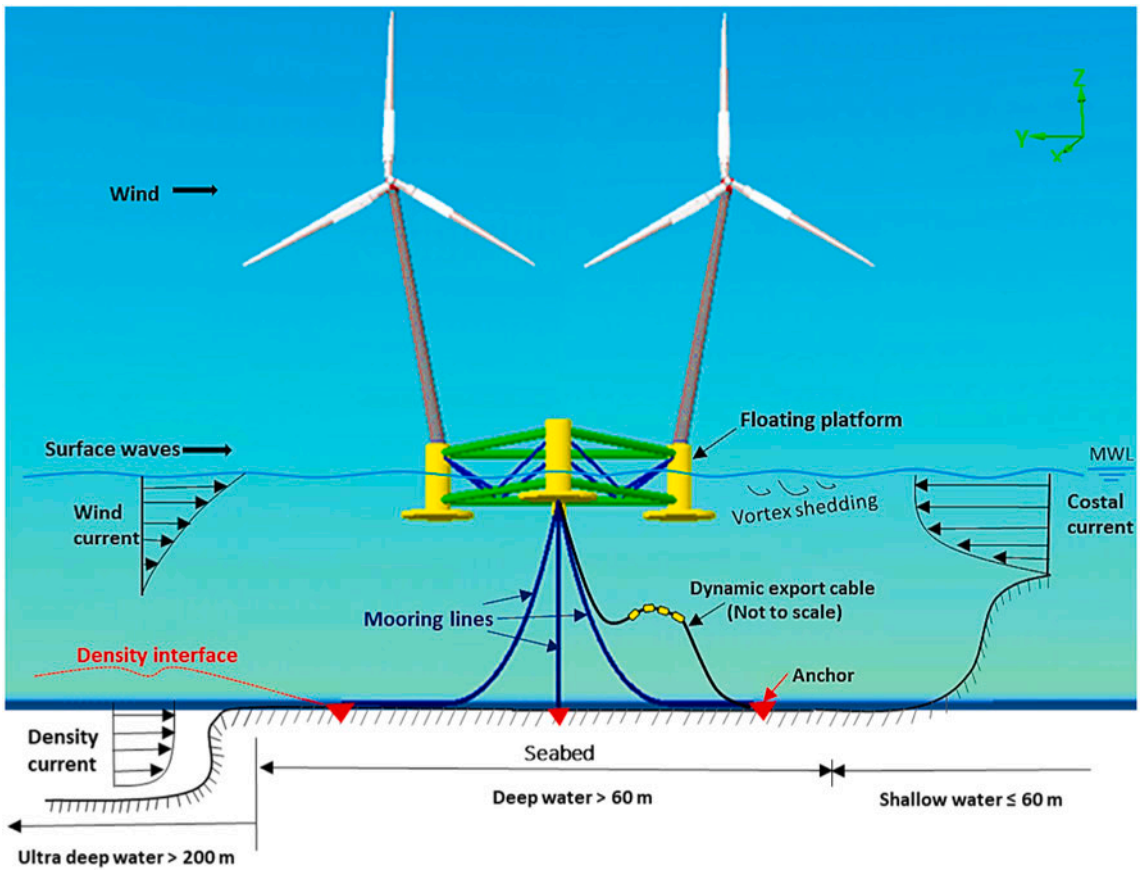

Fig. 1. Schematic showing the influence of wind-driven and near-shore currents on a floating platform moored in deep water.

loads due to the waves applied to the structure's large and slender elements are usually estimated using potential flow theory and Morison's formula, respectively (Morison et al., 1950). These hydrodynamic loads are composed of two components: (i) the drag force, which is proportional to the fluid particle velocity, and (ii) the inertia force, which is proportionate to fluid particle acceleration.

Sea currents are a potentially significant loading source for FOWTs that act as a constant lateral drag force on the platform, dynamic export cables, and mooring lines, and the DNV offshore standard recommends that they should be accounted for in mooring simulations (DNV, 2010). Nevertheless, previous investigations that utilised linearised or quasi-static cable models disregarded the current effects on mooring lines (Jonkman, 2007). These currents affect the operating point of the mooring system of FOWTs and result in the mooring lines' static, dynamic, and damping responses (Hall et al., 2014). Moreover, for the overall floating system, currents can cause floater vortex-induced motion (VIM), static offset, and augmented wave drift forces (Gonçalves et al., 2021). These currents may be triggered by winds, tides, or density changes, as illustrated in Fig. 1.

When waves propagate on a current, the interaction between the current and the waves results in frequency shifts (i.e. Doppler effect) and changes to the wave parameters (i.e. wavelength, amplitude, and spectral energy density); thus, a higher-velocity current substantially impacts the wave field through such interaction (Jonsson, 1990; Masson, 1996; Smith, 1997; Moreira and Peregrine, 2012). In shallow and intermediate water depths, the potential impacts of wave–current interaction (WCI) on fatigue loading for a single pile platform were identified physically i.e., using in-situ measurements (Peters and Boonstra, 1988) and emphasised numerically by methods of spectral fatigue analysis (Peeringa, 2014). Pillai et al. (2021) developed a framework to calculate current and current-modified wave parameters, showcasing the influence of WCI on fatigue loading of floating structures. Experiments further demonstrated the effects of WCI on both structural loads and VIM of these floating structures (Draycott et al., 2021).

In deep waters, where FOWTs are deployed and WCI coexist, this interaction impacts the dynamic responses of FOWTs during operational and extreme conditions. As a consequence, they might increase the platform's mean surge wave-drift force (Zhao et al., 1988) and lead to fatigue in the system's superstructures (e.g. mooring lines and towers) (Chen and Basu, 2018; Qu et al., 2020; Silva et al., 2021). However, the interaction of waves with an underlying current was found to have no significant impact on the performance of the system's pitch controller (Sarkar et al., 2020).

WCI has not yet been addressed extensively in the coupled analysis of FOWTs, and that is due to two key challenges that must be handled: a fully nonlinear mooring model capable of incorporating current and an appropriate WCI model. The recent development of nonlinear mooring models has addressed the first challenge; interested readers are referred to previous studies (Palm et al., 2016; Davidson and Ringwood, 2017; Pillai et al., 2018). However, the latter has not yet been overcome and is still an ongoing research topic. Moreover, most commercial engineering tools (e.g. FAST, Sima, OrcaFlex) employ the conventional superposition of waves and currents when defining the properties of waves, such as JONSWAP waves (Hasselmann et al., 1973). What is missing is the Doppler shift modification of the linear dispersion relationship that accounts for the effect of the current (Azcona et al., 2017). To overcome this limitation, new formulations and derivations for the total fluid particle velocity, the vector sum of the current velocity and wave-induced fluid particle velocity, are needed to incorporate Doppler shift appropriately. Subsequently, custom analytical models must be developed to account for the interaction between currents and waves (both regular and irregular) and then analyse the dynamic behaviours of FOWTs appropriately.

The well-known model for the interaction of regular waves and currents is based on the Airy wave theory, in which the current effects alter the wave frequency and dispersion relation (Thomas, 1981). For irregular waves, Huang et al. (1972) and Tung and Huang (1974) proposed analytical spectral models based on the solution of the regular wave model, and these models account for the impacts of the current on the wave spectrum (Huang et al., 1972; Tung and Huang, 1974). Hedges (1981) then extended these models to account for wave breaking driven by opposing or unfavourable currents (Hedges, 1981; Hedges et al., 1985). These models were verified and validated using numerical simulations and tests, respectively, and demonstrated sufficient accuracy for waves with small amplitudes (Thomas, 1981; Lai et al., 1989; Soares and De Pablo, 2006). They have been used in the design and structural response assessment of offshore structures, such as floating bridges and marine platforms (Ismail, 1984; Dai et al., 2022).

In offshore renewable energy applications, these models have been utilised to investigate the performance of marine tidal turbines and the fatigue loading of a bottom-fixed wind turbine (Barltrop et al., 2007; de Jesus Henriques et al., 2014; Peeringa, 2014). Recently, they were employed to assess the impact of WCI on the fatigue life and dynamic structural responses of a Spar FOWT. Quantitatively, the incorporation of wave–current interaction resulted in up to 10% differences in the dynamic responses of this FOWT and up to 15% increases in its cable fairlead tension (Chen and Basu, 2018, 2019). Additionally, Nguyen (2022) looked into the interaction effect of long-amplitude waves and currents on the same FOWT, finding that the FOWT drifted 15 m downstream in the presence of a favourable current. In contrast, when the current opposes the waves, the line fairlead tension can increase by up to 20% (Nguyen, 2022). Yet, the effects of WCI on single-point-mooring FOWTs have not been investigated. Yet, the effects of WCI on semisubmersible FOWTs that utilise single-point-mooring (SPM) systems have not been investigated.

Consequently, this paper looks into the effect of wave and current interaction on the mooring loads of an SPM system of a semisubmersible FOWT and explores how this interaction impacts the dynamic behaviour of the entire floating system under realistic environmental conditions. To achieve this, a nonlinear hydrodynamic model of the mooring system and analytical wave–current models are incorporated into a coupled analysis of the FOWT to account for the interaction. Following the introduction, the remainder of the paper is structured as follows: Section 2 presents the wave–current interaction models. Section 3 describes a coupled model for the numerical modelling of the W2Power floating wind turbine, focusing on the mooring system's hydrodynamic loading and nonlinear dynamics. The effects of wave–current interaction are then investigated numerically and discussed in Section 4. The results of the study are presented in Section 5 before the conclusions are discussed in Section 6.

2. Mathematical models of wave–current interaction

2.1. Governing equations

When wave and current fields coexist, the velocity potential can be divided into a steady current potential and an unsteady wave potential. Then, the water surface elevation surrounding the structure can be calculated by plugging both the unstable wave potential and the current velocity into the first-order dynamic surface boundary condition (Isaacson and Cheung, 1993). The following coordinate system (x, z), shown in Fig. 2, is defined to introduce the models for the wave–current flows. The origin, $O_{(0,0)}$, is assumed to be the mean water level (MWL), with the positive X-axis aligned horizontally in the direction of wave propagation, whereas the z-axis points vertically upward.

The continuity equation and momentum (Euler) equations governing the rotational flow of an inviscid and incompressible fluid are as follows:

$$\frac{\partial u}{\partial x} + \frac{\partial w}{\partial z} = 0 \tag{1}$$

$$\frac{\partial u}{\partial t} + u\frac{\partial u}{\partial x} + w\frac{\partial u}{\partial z} = -\frac{1}{\rho}\frac{\partial p}{\partial x} \tag{2}$$

$$\frac{\partial w}{\partial t} + u\frac{\partial w}{\partial x} + w\frac{\partial w}{\partial z} = -\frac{1}{\rho}\frac{\partial p}{\partial x} - g \tag{3}$$

where, u and w represent the horizontal and vertical components of fluid velocity, p, g, and ρ are the pressure, the gravitational acceleration and water density, respectively.

2.2. Regular wave–current mathematical model

For regular wave–current interaction, the model formulations given in Thomas (1981) and Silva et al. (2016) are roughly adopted, and the following flow assumptions are made:

- The flow field is irrotational,
- Waves are of small amplitudes and propagate on currents,
- No flow fluctuations exist perpendicular to the O_{xz} plane, and the waves undergo no refraction,
- The time and length scales of the current are relatively larger than the waves' period and wavelength.

Therefore, the resulting velocities (u_T and w_T) and pressure (p_T) fields are represented by the sum of the flow due to currents and waves:

$$u_T(x, z, t) = U(z) + u(z)\cos(\kappa x - \omega t) \tag{4}$$

$$w_T(x, z, t) = w(z)\sin(\kappa x - \omega t) \tag{5}$$

$$p_T(x, z, t) = -\rho g z + p\cos(\kappa x - \omega t) \tag{6}$$

where u, w, and p denote the magnitude of the perturbation caused by the wave, κ denotes the wave number in the direction of wave propagation (i.e. $\kappa = 2\pi/L$, L is the wavelength), and $U(z)$ is the current velocity profile as a function of water depth (h_w) in the absence of waves. ω is the wave's "apparent" angular frequency, and for an observer in a fixed reference system is the sum of the relative or intrinsic frequency in quiescent water (ω_r) and the Doppler frequencies (White, 1999) and can be written as:

$$\omega = \omega_r + \vec{\kappa} \cdot \vec{U} \tag{7}$$

in which, $\vec{\kappa}$ and $\vec{U}$ are, respectively, the vectors of the current velocity and wave number. In the linear Airy wave theory, the water surface elevation $\eta(x, t)$ is sinusoidal and can be expressed as:

$$\eta(x, t) = A\cos(\kappa x - \omega t) \tag{8}$$

in which A is the current-altered wave amplitude. Substituting the formulae of the resulting fields of velocities and pressure, Eq. (4)–(6), into the continuity, Eq. (1), and momentum equations, Eq. (2) and (3), gives:

$$\frac{\partial w}{\partial z} = \kappa u \tag{9}$$

$$p = \frac{\rho}{\kappa^2}\left[\frac{\partial w}{\partial z}(\omega - U(z)\kappa) + w(\kappa\frac{\partial U(z)}{\partial z})\right] \tag{10}$$

$$\frac{\partial p}{\partial z} = \rho w(\omega - U(z)\kappa) \tag{11}$$

After straightforward elimination of variables and some manipulation, Eq. (9)–(11) yield an alternate equation for vertical velocity, written as:

$$\frac{\partial^2 w}{\partial z^2} - \left[\kappa^2 - \frac{\kappa}{\omega - U(z)\kappa}\frac{\partial^2 U(z)}{\partial z^2}\right] w = 0 \tag{12}$$

Eq. (12) is known as the "inviscid Orr–Sommerfeld" or "Rayleigh" equation of classical hydrodynamic stability theory in the flow domain $-h_w < z < 0$, which must be solved in accordance with the rigid bottom boundary condition:

$$w_T = w(z) = 0 \quad \text{on } z = -h_w \tag{13}$$

and the mean free surface linearised boundary conditions:

$$w(z) = A(\omega - \kappa U(z)) \quad \text{on } z = 0 \tag{14}$$

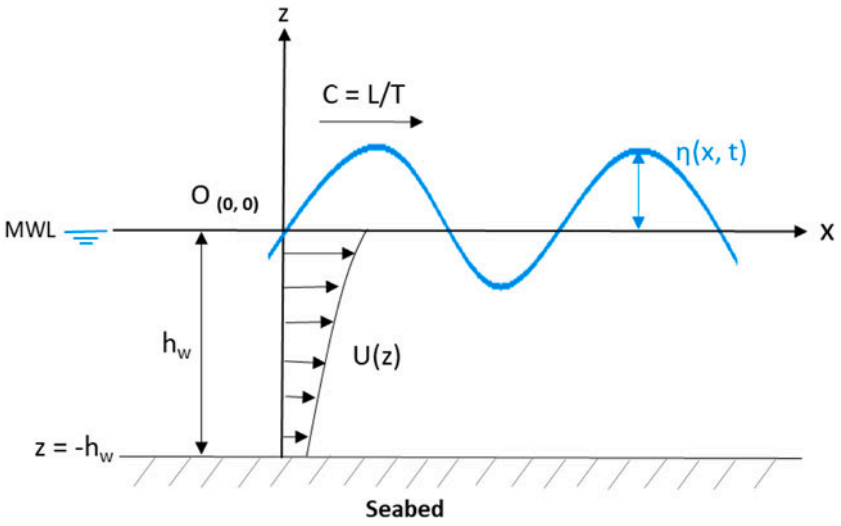

Fig. 2. Definition of the coordinate system for wave–current interaction of a finite depth.

$$p = \rho g A \quad \text{on } z = 0 \tag{15}$$

Substituting the boundary conditions on $z = 0$, Eq. (14) and (15), into the pressure field equation, Eq. (10), gives the current-affected dispersion relation.

$$(\omega - \kappa U(z))^2 \frac{\partial w}{\partial z} + \left[\kappa(\omega - \kappa U(z)) \frac{\partial U(z)}{\partial z} - g\kappa^2\right] w = 0 \tag{16}$$

If the parameters A, ω, and h_w, alongside $U(z)$, can be treated as known values in advance from experimental specifications or measurements, then the system of Eqs. (12)–(14) can be solved for the wavenumber κ and the vertical velocity $w(z)$. Accordingly, once these unknowns have been determined, the depth-varying component of the horizontal velocity $u(z)$ can be derived from the continuity equation, Eq. (1), as:

$$u(z) = \frac{1}{\kappa} \frac{\partial w}{\partial z} \tag{17}$$

However, the system is defined by the set of equations, Eq. (12), (13) and (16), cannot be solved analytically for general wavenumbers and frequencies unless the second derivative of the current velocity profile is equal to zero ($\frac{\partial^2 U(z)}{\partial z^2} = 0$), which corresponds to a depth-independent current or a current that changes linearly with depth. The Rayleigh equation, Eq. (12), can thus be rewritten as:

$$\frac{\partial^2 w}{\partial z^2} - \kappa^2 w = 0 \tag{18}$$

this Rayleigh equation, Eq. (18), depends on the vertical velocity $w(z)$ and the current velocity profile $U(z)$, and its solution for the wavelike horizontal velocity u(z) can be given by:

$$u(z) = A(\omega - U_0\kappa) \frac{\cosh[\kappa(z + h_w)]}{\sinh(\kappa h_w)}; \tag{19}$$

for $w(z)$ by:

$$w(z) = A(\omega - U_0\kappa) \frac{\sinh[\kappa(z + h_w)]}{\sinh(\kappa h_w)}; \tag{20}$$

and for $p(z)$ by:

$$p(z) = \rho A(\omega - \kappa U_0) \frac{1}{\kappa \sinh(\kappa h_w)} \times \left[(\omega - \kappa U(z)) \cosh[\kappa(z + h_w)] + \frac{dU(z)}{dz} \sinh[\kappa(z + h_w)]\right] \tag{21}$$

Substitution of Eqs. (19)–(21) in the resultant velocity and pressure fields, Eq. (4)–(6), yields:

$$u_T(x, z, t) = U(z) + A(\omega - U_0\kappa) \frac{\cosh[\kappa(z + h_w)]}{\sinh(\kappa h_w)} \cos(\kappa x - \omega t) \tag{22}$$

$$w_T(x, z, t) = A(\omega - \kappa U_0) \frac{\sinh[\kappa(z + h_w)]}{\sinh(\kappa h_w)} \sin(\kappa x - \omega t) \tag{23}$$

$$p_T(x, z, t) = -\rho g z + \frac{\rho A(\omega - \kappa U_0)}{\kappa \sinh(\kappa h_w)} \left([\omega - \kappa U(z)] \cosh(\kappa(z + h_w)) + \frac{\partial U(z)}{\partial z} \sinh(\kappa(z + h_w)) \right) \cos(\kappa x - \omega t) \tag{24}$$

U_0 denotes the current velocity at $z = 0$. Substituting Eq. (20) into Eq. (16) gives the modified dispersion relation as:

$$(\omega - \kappa U_0)^2 = [g\kappa - (\omega - \kappa U_0) \frac{\partial U(z = 0)}{\partial z}] \tanh(\kappa h_w) \tag{25}$$

This equation is only valid for both uniform and linear shear current profiles (i.e. when $\frac{\partial^2 U(z)}{\partial z^2} = 0$). For the former, it can thus be simplified to the convenient form of the dispersion relation:

$$(\omega - \kappa U_0)^2 = g\kappa \tanh(\kappa h_w) \tag{26}$$

For a linear shear current profile that can be expressed by:

$$U(z) = U_0 + Bz \tag{27}$$

then the modified dispersion relation can be represented as:

$$(\omega - \kappa U_0)^2 = [g\kappa - (\omega - \kappa U_0) B] \tanh(\kappa h_w) \tag{28}$$

where B is the current slope, and Eq. (28) is true for $B = 0$ (i.e. uniform profile), and $B \neq 0$ (i.e. linear shear profile).

Based on the principle of 'wave-action' conservation (Bretherton and Garret, 1970), the modified wave amplitude of Eq. (8) in the presence of a current, (A), can be expressed as follows (Smith, 1997; Draycott et al., 2018):

$$A = A_a \left[\frac{C_{g,a}}{C_g} \cdot \frac{1}{1 + \frac{U \cos\alpha}{C_g}}\right]^{\frac{1}{2}}; \tag{29}$$

the subscript 'a' indicates a region with the absence of current, and α is the angle between the propagation directions of the wave and current, and C_g is the velocity of the wave group and is given as:

$$C_g = \frac{1}{2} C \left(1 + \frac{2\kappa h_w}{\sinh(2\kappa h_w)}\right); \tag{30}$$

where C is the wave apparent celerity, which is the sum of the wave celerity in the moving reference frame (C_a) and the current velocity

(U), and can be expressed by the wavelength (L) and the corresponding period (T) as:

$$C = C_a + U; \quad = \frac{L}{T} \tag{31}$$

2.3. Stochastic wave–current mathematical model

Under the wave and current assumptions described in Section 2.2, a stochastic wave–current interaction model can be established by coupling the spectral representation of irregular waves with the equations of the regular wave–current model (Huang et al., 1972) Consequently, the spectral density of surface waves in the presence of the current, $S(\omega, U)$, is given by:

$$S(\omega, U) = \frac{4S(\omega)}{\left[1 + \frac{4U\omega}{g}\right]^{1/2}\left[1 + \left(1 + \frac{4U\omega}{g}\right)^{1/2}\right]^2} \tag{32}$$

in which $S(\omega)$ spectral density of waves without the influence of current; U, ω, and g are the current speed, frequency, and gravitational acceleration, respectively. In this paper, the JONSWAP (Joint North Sea Wave Project) spectrum was selected to generate the irregular waves (Hasselmann et al., 1973), whose expression is:

$$S(\omega) = \frac{\alpha g^2}{\omega^5}\exp\left[-\frac{4}{5}\left[\frac{\omega_p}{\omega}\right]^4\right]\gamma^{\alpha} \tag{33}$$

where ω_p is the peak frequency, γ is the peak enhancement factor, and parameters α and σ are

$$\alpha = \exp\left[\left[-\frac{(\omega-\omega_p)^2}{2\omega_p^2\sigma^2}\right]\right], \quad \sigma = \begin{cases} 0.07 & \text{if } \omega < \omega_p \\ 0.09 & \text{if } \omega \geq \omega_p \end{cases}, \text{ respectively.}$$

From Eq. (32), waves tend to shorten and become steeper when they encounter an opposing current (i.e. when the current speed is negative), and vice versa for waves travelling with a following current. Thus, it is worth mentioning that when the current speed is negative, there is a cut-off frequency that can be determined using the following formula:

$$1 + \frac{4U\omega}{g} \geq 0 \tag{34}$$

Before this critical frequency ($\omega = -\frac{g}{4U}$), surface waves with frequencies close to it become extremely steep, and theoretically, beyond this frequency, no waves can exist. In reality, wave breaking will occur at the current threshold, and since the wave amplitude at this critical speed would be infinite; thus the waves break a long time before they reach this limit. However, breaking still impacts wave components that propagate onto the current, so there is a limit to how big waves can develop over a certain frequency range (Phillips, 1977). In order to address this issue, Hedges (1981) derived the following "equilibrium range limit" for deep water (Hedges, 1981; Hedges et al., 1985):

$$S_{ER}(\omega, U) = \frac{A^* g^2}{(\omega - \kappa U)^5}\frac{1}{1 + \frac{2U(\omega - \kappa U)}{g}} \tag{35}$$

in which "ER" denotes the equilibrium range, and A^* is a numerical (Phillips-like) constant for the waves generated on currents, its values provided by Phillips in the range $0.008 - 0.015$ (Phillips, 1977).

Given that the equilibrium range of the spectrum is associated with deep water, the preceding equation, Eq. (35), can be used to predict spectral densities for the current region whenever $S_{\mathrm{ER}}(\omega, U)$ is smaller than $S(\omega, U)$. Following that, alterations in the spectra corresponding to flow velocity and acceleration driven by the subsurface current can be estimated (Hedges et al., 1985; Soares and De Pablo, 2006; Peeringa, 2014). By employing these spectral representations, the sinusoidal water surface elevation $\eta(x, t)$ for ith wave components can be written as:

$$\eta(x, t) = \sum_{i=1}^{N} A_i \cos(\kappa_i x - \omega_i t + \phi_i) \tag{36}$$

in which ϕ is the random phase angle spread evenly between 0 and 2π, and N refers to the total number of wave components. In this stochastic model, the amplitude of the ith wave component with frequency interval $\Delta\omega$ is given by:

$$A_i = \left[2S(\omega_i, U)\Delta\omega\right]^{1/2} \tag{37}$$

The corresponding formulae for the resultant horizontal and vertical velocities and pressure fields are:

$$u_T(x, z, t) = U(z) + \sum_{i=1}^{N} A_i(\omega_i - \kappa_i U)\frac{\cosh[\kappa_i(z + h_w)]}{\sinh(\kappa_i h_w)}\cos(\kappa_i x - \omega_i t + \phi_i), \tag{38}$$

$$w_T(x, z, t) = \sum_{i=1}^{N} A_i(\omega_i - \kappa_i U)\frac{\sinh[\kappa_i(z + h_w)]}{\sinh(\kappa_i h_w)}\sin(\kappa_i x - \omega_i t + \phi_i), \tag{39}$$

$$p_T(x, z, t) = -\rho g z + \sum_{i=1}^{N} \frac{\rho A_i(\omega_i - \kappa_i U)^2 \cosh[\kappa_i(z + h_w)]}{\kappa_i \sinh(\kappa_i h_w)} \times \cos(\kappa_i x - \omega_i t + \phi_i), \tag{40}$$

respectively. Differentiating the velocity fields equations, Eq. (38) and (39), with regard to time yields the corresponding resultant accelerations (i.e. the horizontal and vertical) as:

$$\dot{u}_T(x, z, t) = \sum_{i=1}^{N} A_i\omega_i(\omega_i - \kappa_i U)\frac{\cosh[\kappa_i(z + h_w)]}{\sinh(\kappa_i h_w)}\sin(\kappa_i x - \omega_i t + \phi_i), \tag{41}$$

$$\dot{w}_T(x, z, t) = \sum_{i=1}^{N} A_i\omega_i(\omega_i - \kappa_i U)\frac{\sinh[\kappa_i(z + h_w)]}{\sinh(\kappa_i h_w)}\cos(\kappa_i x - \omega_i t + \phi_i), \tag{42}$$

in which the wavenumber k_i will be obtained from the modified dispersion relation, Eq. (26), for each wave component. Although this model is stochastic, it cannot capture the nonlinear effects of wave and wave–current interaction because it relies on the linear wave theory. However, some nonlinear effects (e.g. fluid velocity and acceleration) can be captured by employing kinematic stretching techniques (e.g. vertical, extrapolation, and Wheeler) (Faltinsen, 1993; Nestegård et al., 2019; OrcaFlex, 2023).

3. W2Power floating offshore wind turbine model

3.1. Platform model description

In order to investigate the effects of wave–current interaction on the dynamic responses of FOWTs, this paper employs an innovative floating wind turbine model called W2Power as a case study. This model was developed by EnearOcean S.L. (2007), Spain, in 2015 and does not represent the current design of the platform (Hanssen et al., 2015). It is a triangular semisubmersible structure that houses a pair of wind turbines mounted on out-leaning towers. The platform is moored to the seabed via a single-point mooring system, whose lines are attached to the bottom of the front column (B). The main particulars of the platform are given in Table 1. The towers are conical tubular steel structures that are cantilevered at 15° on the top of the floater's stern columns (A and C) (Elobeid et al., 2022), with tower data adopted from the OC3-Hywind spar FOWT (Jonkman, 2010).

3.2. Mooring system characteristics

The configuration of the single-point mooring system is a typical catenary that comprises three lines placed symmetrically along the platform's Z-axis and spread by 120°, and these individual lines are made of stud-less chains. The W2Power is designed for water depths of 200 m, whilst this study focuses on a prospective deployment site of 80 m water depth. The scaled mooring system proposed by Elobeid et al. (2022) has been up-scaled, optimised and employed in the current study; its properties are given in Table 2.

Table 1
Main parameters of the W2Power platform.

Parameter	Value (unit)	Parameter	Value (unit)
Draft	15 m	Braces diameter	1.32 m
Water depth	80 m	Pontoons diameters	3 m
Column D height	25 m	Heave plates height	1.5 m
Column D diameter	5 m	Heave plates diameter	27 m
Corner columns height	25 m	Towers bases separation	90 m
Corner columns diameter	9 m	Towers' out-leaning angle	15°

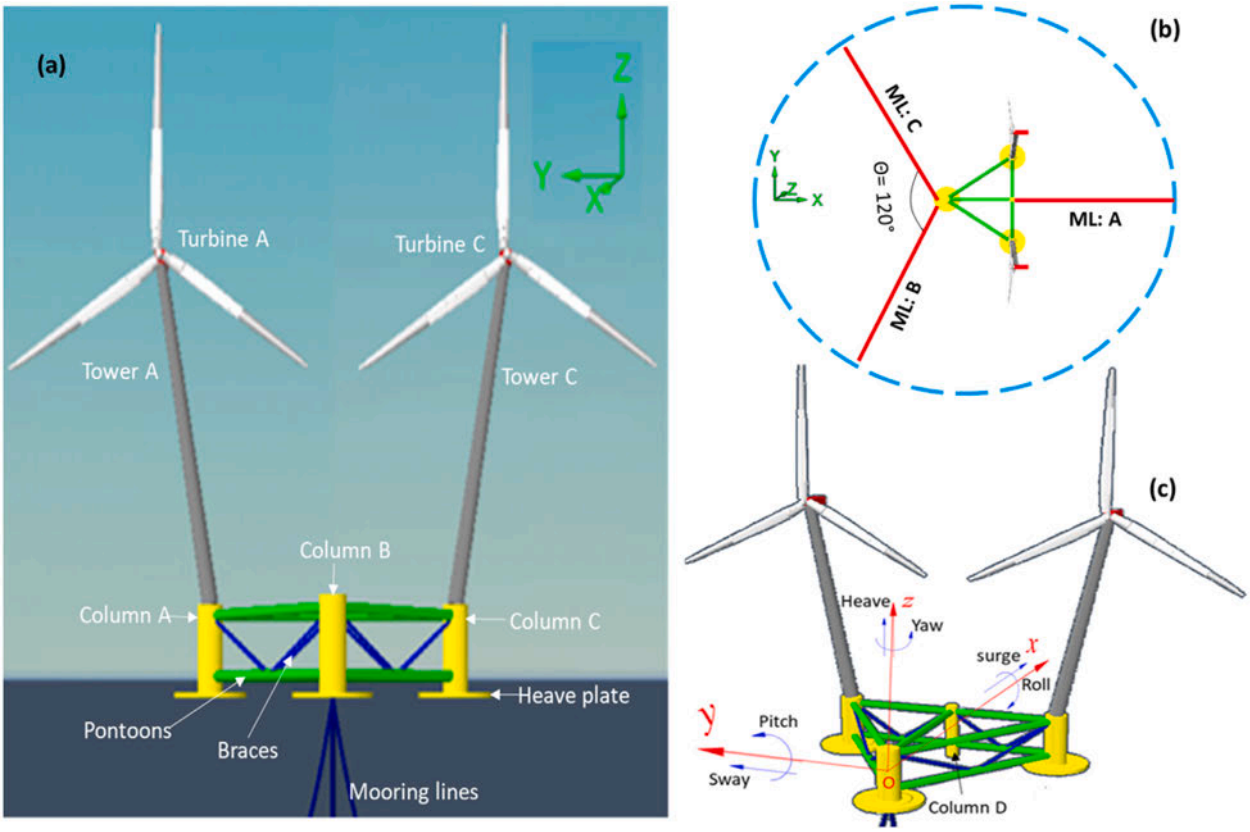

Fig. 3. Description of the W2Power FOWT: (a) the system's main particulars; (b) the mooring system configuration; (c) the 6 degrees-of-freedom of the system.

Table 2
Characteristics of the mooring system.

Parameter	Value (unit)	Parameter	Value (unit)
Fairlead depth	15 m	Line length	398.3 m
Number of lines	3	Axial stiffness	252.5E03 kN
Anchor depth, radius	80, 382.24 m	Line dry, wet weight	537, 466.4 kN/m
Line type (grade)	Chains (R4–Studless)	Fairlead pretension	1153 kN
Nominal chain diameter	157 mm	Minimum breaking load (MBL)	21235 kN

3.3. Floater-towers-nacelles-rotors model

The platform is engineered to accommodate two 6 MW wind turbines (WTs). Due to a lack of data on this WT, it is, therefore, analysed with a pair of the well-documented and publicly accessible NREL-5MW WT (Jonkman et al., 2009). The towers are conical tubular steel structures of a height of 77.6 m and base (platform top) and top diameters of 6.5 m and 3.87 m, respectively. They are cantilevered at an outward 15°atop the floater's stern columns (A and C). Towers' data are adopted from the OC3-Hywind spar FOWT (Shin, 2011), see Table 3.

The converging equation is established to calculate the displacement, velocity, and acceleration of the FOWT, as well as the mooring dynamics. It considers the effects of wind, wave, cable forces, and wave–current interaction, and is written to be solved for the 6 degrees-of-freedom (DoF) motions as follows:

$$(\mathbf{M}+\mathbf{A}_{\infty})\ddot{x}(t)+\int_0^t \mathbf{K}(t-\tau)\dot{x}(\tau)d\tau+\mathbf{B}\dot{x}(t)+\mathbf{C}x(t) = F_m(t)+F_h(t)+F_a(t) \quad (43)$$

this equation is known as Cummins equation, in which, **M** is the mass matrix of the entire FOWT including ballast, $\mathbf{A}_{\infty}$ is the added mass matrix at infinite frequency, and **K**(t) is the retardation function matrix (impulse response), which was calculated by the Cummins model (Cummins et al., 1962). The convolution integral handles the 'memory' effect of past motions (Rognebakke, 2002), whose τ is a 'time' variable ranging from 0 to t. **B** is the nonlinear damping matrix, and **C** is the stiffness matrix that comprises both the hydrostatic stiffness provided by buoyancy and the mooring stiffness, $\mathbf{C} = (\mathbf{C_h} + \mathbf{C_m})$. The displacement, velocity, and acceleration vectors of the body are, respectively, denoted by x, $\dot{x}$, and $\ddot{x}$. On the right side, F_m is the mooring

Table 3
Specifications of the NREL 5MW baseline wind turbine.

Parameter	Value (unit)	Parameter	Value (unit)
Rated power	5 MW	Rotor configuration	Upwind
Number of blades	3	Hub, rotor diameter	3, 126 m
Cut-in, rated rotor speed	6.9, 12.1 RPM	Drivetrain, control	Geared, pitch regulated
Cut-in, rated, cut-out wind speed	3, 11.4, 25 m/s	Rotor, nacelle, tower mass	110, 240, 249.7 tonne

fairlead tensions, F_h is the hydrodynamic loads (first- and second-order wave forces, and current drag force), and F_a is the aerodynamic loads on the two rotors.

4. Model setup for the implications of wave–current interaction

4.1. Platform-mooring modelling

The numerical modelling tools used are SolidWorks, DNV's Sesam-GeniE, and Orcina Ltd's OrcaWave and OrcaFlex (Solidworks, 2021; GeinE, 2020; OrcaWave, 2023; OrcaFlex, 2023). The floater's geometry was developed using SolidWorks, and its mass and inertia matrices were obtained. The hull's panel model (i.e. heave plates and columns) was meshed using GeniE, and a finite element file was subsequently generated. OrcaWave was then used to perform the diffraction analysis for the ballasted floater in the absence of the mooring system and superstructures (e.g. turbines, towers, nacelles). This yielded the floater's RAOs (response amplitude operator) and other hydrodynamic parameters such as the hydrostatic stiffness coefficients, the frequency-dependent hydrodynamic added mass and radiation damping, the first-and second-order wave forces, and difference-frequency quadratic transfer functions (QTFs). The OrcaWave-generated model was loaded as a vessel object into OrcaFlex to model the floater as a rigid body, whose motion is defined by three translations displacements (surge, sway, and heave) and three rotational displacements (roll, pitch, and yaw) at the body origin $(0, 0, 0)$ (see Fig. 3).

Then, three mooring lines were added between the platform's fairleads and the seafloor. Based on the properties listed in Table 2, the mooring cables were simulated using OrcaFlex's finite-element-method (FEM) model. Each line was discretised into segments, which were then modelled by straight massless model segments with a node at each end (Van den Boom, 1985). The model segments only capture the line's axial and torsional properties, whereas the other properties, like mass, weight, and buoyancy, were all lumped into the nodes (OrcaFlex, 2023). The seabed was assumed to be horizontal and on a rigid plane.

To account for the contribution of current-induced drag loads on viscous damping and mean platform offsets, the analysis considered drag loads on the submerged superstructures (mooring lines, heave plates, columns, pontoons, and braces). Thereby, an extended form of Morison's formula was employed to calculate the hydrodynamic loads on the mooring lines and platform (Morison et al., 1950; OrcaFlex, 2023), whose can be expressed as follows:

$$f = \overbrace{(C_m \Delta a_f - C_a \Delta a_b)}^{\text{Inertia}} + \overbrace{\left(\frac{1}{2}\rho C_d A |v_f| v_f\right)}^{\text{Drag}} \tag{44}$$

in which, f is the fluid force per unit length exerted on the body. C_m and C_a are, respectively, the inertia and added mass coefficients for the body, and the value of C_m was taken to be $1+C_a$. Δ denotes the mass of the fluid displaced by the body, and a_f is the fluid acceleration relative to the earth. ρ represents the density of water, C_d is the drag coefficient for the body, A is the drag area, and v_f is the fluid velocity relative to the earth.

4.2. Superstructures modelling

The superstructures (e.g. towers, heavy topsides) are modelled explicitly to include the rotors' rotation and flexing of the towers and blades in the OrcaFlex model. The towers are modelled as profiled cylinders via line objects that utilise homogeneous pipe attributes, which enable the modelling of variable outer and inner diameter profiles and their corresponding physical properties (e.g. mass and inertia). The rotors are then connected to the towers via nacelles that are modelled as lumped 6D buoys with their respective properties, and to increase blade-to-tower clearances, the rotors and nacelles are tilted by 5° (Jonkman et al., 2009). The blade structural model closely resembles a line model, with segmented blades and nodes at the ends of each segment. The blade discretisation and segment lengths were meticulously adjusted to be consistent with the overall length of the NREL-5MW turbine (Jonkman et al., 2009). At each node, the mass and inertia properties are appropriately grouped. Blade element momentum (BEM) theory is utilised to capture aerodynamic loads (Froude, 1920).

4.3. Modelling of wave–current interaction

Wave–current interaction is modelled in the Python programme to solve the linear dispersion relation, Eq. (26), and obtain the current-included wavenumber. It is not possible to solve Eq. (26) analytically; therefore, it is solved using the physical approximations by Fenton and McKee (1990). The presence of current slightly modifies the solution method; therefore, the well-known Newton–Raphson's method is used to refine the approximation. It is tailored to attain arbitrary customisable accuracy (Ben-Israel, 1966). Subsequently, these custom analytical models that account for the interaction between currents and waves (regular and irregular) are compiled as dynamic link libraries (DLLs) utilising the OrcaFlex Python API (i.e. Application Programming Interface), OrcFxAPI. The developed model incorporates two key aspects: the current effect on the mooring lines and the incorporation of WCI in hydrodynamic loading estimation on the FOWT. The coupled analysis model setup is shown in Fig. 4.

4.4. Environmental loads and simulation setup

This study investigates the performance of the W2Power platform at a reference site, Canari-I, off the coast of Gran Canaria in the Atlantic Ocean, whose environmental contours are constructed with a 50-year return period based on long-term hindcast data (wind, wave and current) (NKUA-AM&WFG, 2021). Different sea conditions are subsequently defined to represent both the "survival" and "operational" conditions. In extreme sea states, the turbines' rotors are parked. When the rotor is parked, the turbine blades are feathered to minimise the aerodynamic loads. This allows us to focus on the effects of WCI on the dynamic responses of the platform and mooring lines under such loading conditions. Whilst the aerodynamic loads and wind drag forces act on the wind turbine systems are included in the operational conditions. The rated wind speed (U_w) at the top of the towers is assumed to be 11.4 m/s, corresponding to the mean wind speed at 100 m hub height at the Canari-I site, and it is assumed to be in the same direction as the axes of the rotor and is modelled using the NPD (Norwegian Petroleum Directorate) spectrum with full field turbulent winds (Jonkman and Kilcher, 2012).

Different sea states are picked from the environmental contour, whose regular wave trains are defined by linear Airy types of height (H) and period (T). While the irregular ones are represented by the JONSWAP spectrum using a peak factor (γ), significant heights (H_s), and peak period (T_p). The Canari-I site has maximal and average

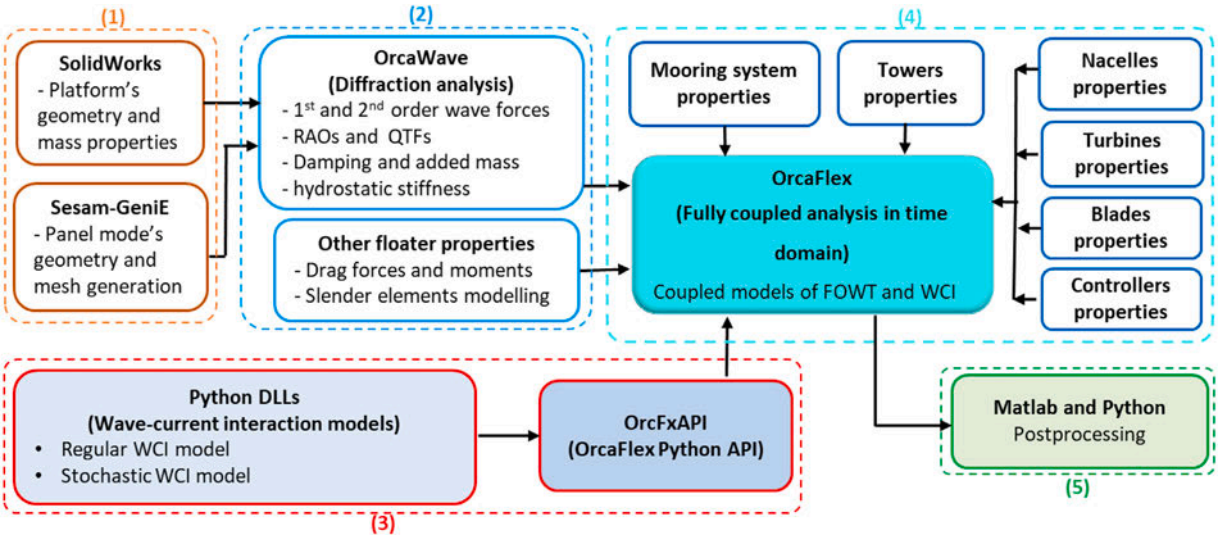

Fig. 4. Schematic flow chart of the coupled model setup and numerical modelling analysis.

Table 4
Load case parameters for coupled-analysis simulations of wave–current interaction.

LC No.	Wave model	H/H_s (m)	T/T_p (s)	γ	U_c (m/s)	Direction	U_w (m/s)
			Extreme sea states				
1	Regular	4.63	16	–	0.8	Following	0
2	Regular	4.63	16	–	0.8	Opposing	0
3	Regular	3.85	8	–	0.8	Following	0
4	Regular	3.85	8	–	0.8	Opposing	0
5	Irregular	4.63	16.4	3.3	0.8	Following	0
6	Irregular	4.63	16.4	3.3	0.8	Opposing	0
7	Irregular	3.85	9	3.3	0.8	Following	0
8	Irregular	3.85	9	3.3	0.8	Opposing	0
			Operational sea states				
9	Regular	1.4	7.4	–	0.3	Following	11.4
10	Regular	1.4	7.4	–	0.3	Opposing	11.4
11	Irregular	1.4	7.4	2	0.3	Following	11.4
12	Irregular	1.4	7.4	2	0.3	Opposing	11.4

current speeds (U_c) of 0.8 m/s and 0.3 m/s, respectively, whose profiles are characterised within OrcaFlex environment data.

In the simulations, the direction of the waves is fixed at 180°, and the current hits the platform from two directions, 180° and 0°, creating two current scenarios when interacting with waves, following and opposing, respectively. To assess the effect of current and the inclusion of wave–current interaction on the dynamic responses of the FOWT, the simulated scenarios are: (i) currents only; (ii) waves only; (iii) straightforward superposition of wave–current effects without considering any interaction; (iv) and incorporation of the wave–current interaction effects. Accordingly, the environmental conditions and identification numbers for all the load cases (LCs) considered are presented in Table 4.

5. Results and discussion

5.1. Current effects on wave fields

Wave–current interaction models established in Section 2 are used to examine the influence of current on regular and irregular waves. Two current velocities are considered: 0.3 and 0.8 m/s. For regular waves and utilising Eq. (8) and (29), current alters both the mean value and the amplitude of the wave free-surface elevation (η), whether the current is following or opposing, as shown in the left panel of Fig. 5. For clarity, a following current refers to a flow with a velocity in the same direction of wave propagation. In contrast, an opposing current propagates in the opposite direction as the waves, resulting in a negative velocity. Furthermore, frequency shifts were observed, as evident at the peaks of both the crests and troughs of the wave.

Eq. (32) and (35) are executed to generate the energy spectrum for stochastic waves with a JONSWAP spectrum of $\gamma = 1$, which reduces to the Pierson–Moskowitz (PM) spectrum (Pierson, Jr. and Moskowitz, 1964). In turn, the spectra are obtained for four different current velocities and shown on the right side of Fig. 5. The presence of current significantly modifies the peak value of the wave spectra. For opposing currents of speeds of −0.3 and −0.8 m/s, the peak spectral amplitude increases by 5% and 14.2%, respectively, while it decreases by 5% and 11.2% when the currents are following. The peak frequency is also shifted, as observed in the inset plots. Increasing the absolute value of the current speed results in a more significant alteration of the peak value and changes the shape of the wave spectrum. Furthermore, for opposite currents, the high-frequency tails of the spectra are adjusted using Eq. (35) with a Phillips's constant, A^*, of 0.015. Accordingly, the wave spectra are truncated beyond the cutoff frequency, and the cutoff frequency (i.e. ω_{cutoff} = 0.244 Hz, 1.532 rad/s) is chosen to be four times the peak spectral frequency (i.e. ω_{peak} = 0.061 Hz, 0.383 rad/s) (Jonkman, 2007). The results in Fig. 5 shed light on the fundamental physics of wave–current interaction in extreme and operational conditions at the reference site, Gran Canaria. The following subsections demonstrate the implications of these findings on the dynamic responses of the W2Power FOWT.

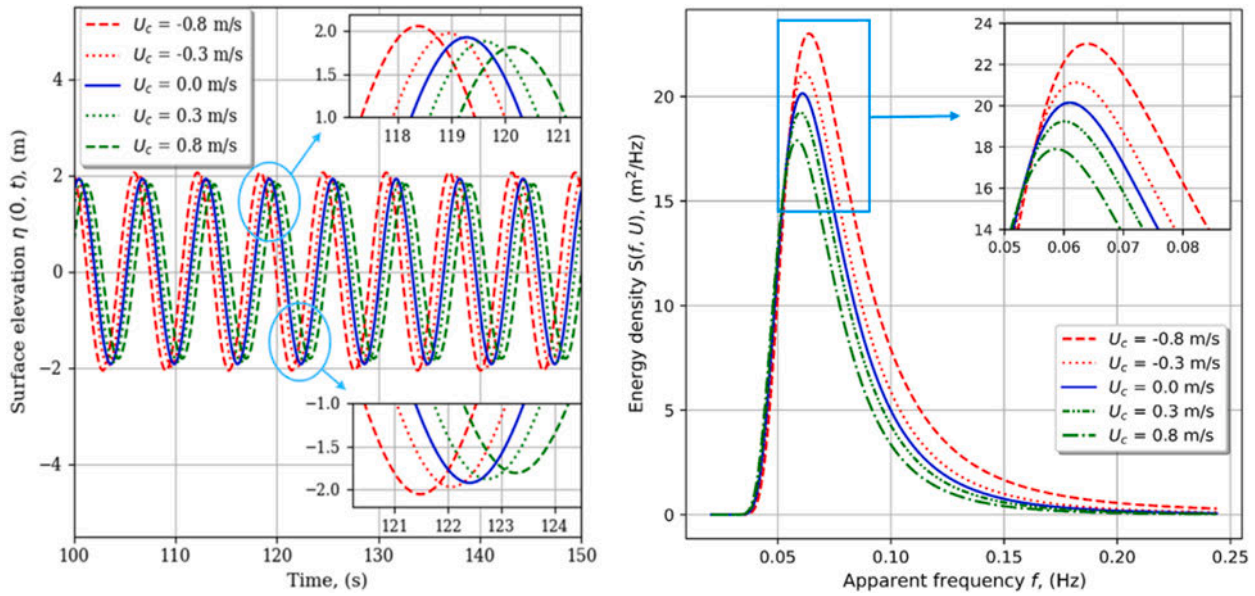

Fig. 5. Current effect on (left) the free surface elevation, $\eta(0,t)$, for a regular wave of H = 3.85 m and T = 6.2 s; and (right) the reduced JONSWAP spectrum of H_s = 4.63 m and T_p = 16.4 s.

5.2. Effect of wave–current interaction on motion dynamics

The simulation results for the FOWT system's motion responses under an operational load case (LC11) of an irregular wave with uniform current are shown in Fig. 6. The presence of the current induces offsets in the FOWT's structural responses and alters the system's equilibrium position; thereby, the current influences both the static and dynamic responses. To account for the current effect in simulating WCI load cases in OrcaFlex, the platform was first subjected to a pure current until it reached its static position. This new static position was then implemented in OrcaFlex, and the floater object's DoFs were deliberately deselected; by doing so, the current-modified wave file's effect on the platform's static analysis was incorporated. The simulations were run for 3800 s, with 200 s allotted for wave build-up and transient effect elimination. Thus, each load case analysis is an hour (3600 s) coupled simulation, which is enough for identifying the characteristics of the system dynamics according to the standards (DNV, 2019).

Fig. 6 illustrates the effect of wave–current interaction on the translational and rotational DoFs of the platform. Note that, herein, the mean values have been omitted to focus on the dynamic behaviour of the motion responses. Surge and heave DoFs were the most affected, while the pitch was moderately impacted, and the rest were less influenced. Despite wind damping the effect of WCI, there were slight changes in the mean values of surge, heave and pitch due to this interaction with a current speed of 0.3 m/s. Hypothetically, the interaction's effect should be more pronounced in the absence of wind, which is demonstrated in Fig. 7 for an extreme case of a current speed of 0.8 m/s. As can be seen, the mean values of the surge and heave decrease in the presence of the following current and increase with the opposing current due to the current drag force. Moreover, the relative maximum and minimum values are amplified by an opposing current, whereas a following current attenuates them.

The mean, maximum, and standard deviation of the surge, heave, and pitch motion responses are provided in Table 5. It can be seen that an opposing current increases the mean values of the three motion responses while a following current decreases them. In the absence of wind, the opposing current can increase the maximum surge and heave responses by up to 40% when interacting with regular waves (i.e. LC2 and LC4). On the other hand, when interacting with irregular waves (i.e. LC6 and LC8), the opposing current can increase surge motion by up to 26% and heave motion by up to 30%, while the following current decreases both surge and heave motions (i.e. LC1, LC3, LC5 and LC7). The interaction has minimally affected the pitch motion, even though this can induce an extra restoring force in the negative heave direction. Accordingly, the heave response has experienced alterations when considering the nonlinear coupling effect of heave and pitch responses, particularly for a single-point mooring system (Li et al., 2018; Qu et al., 2020).

The inclusion of wind speed in operational load cases induced stronger responses of surge, heave, and pitch in operational sea states compared to extreme sea states, as highlighted in Table 5. This observation is attributed to the significant impact of wind on FOWTs, even when parked under extreme sea conditions. The aerodynamics of wind are expected to be the dominant loading in extreme wind events, potentially diminishing the comparative impact of WCI on the floating system. The deliberate exclusion of wind in extreme sea states aligns with the rationale of highlighting the impact of WCI during conditions where it might be more pronounced. Nevertheless, it is imperative to acknowledge the significant impact of wind on the twin-turbine system and the importance of including it in the operational conditions. Thus, these load cases (LC9–LC12) were selected to mirror the environmental conditions of the reference site, providing additional insights into the system's behaviour under realistic scenarios (Chen and Basu, 2018). These findings underline the significance of simulating holistic environmental conditions, encompassing both wind and WCI dynamics, to comprehensively estimate the dynamics of FOWTs. Hence, it is crucial to understand the intricate interaction between wind and wave–current dynamics and their combined implications.

5.3. Effect of wave–current interaction on mooring dynamics

The effect of WCI on mooring dynamics is studied by analysing the effective tension at each line's fairlead. Figs. 8 and 9 show the statistical results of the mooring tension's time series. The configuration of the three mooring lines is depicted in Fig. 3.b, with mooring line A aligned along the positive X-axis. Given the mooring system's symmetry with respect to the X-axis, the responses of mooring lines B and C are identical. The emphasis is, therefore, on presenting the outcomes of lines A and B. In order to provide a clearer illustration of the effect of WCI, the results are presented separately for extreme load cases (LC1–LC8) and operational load cases (LC9–LC12) under favourable and adverse current scenarios. WCI was found to impact the mooring lines' mean and

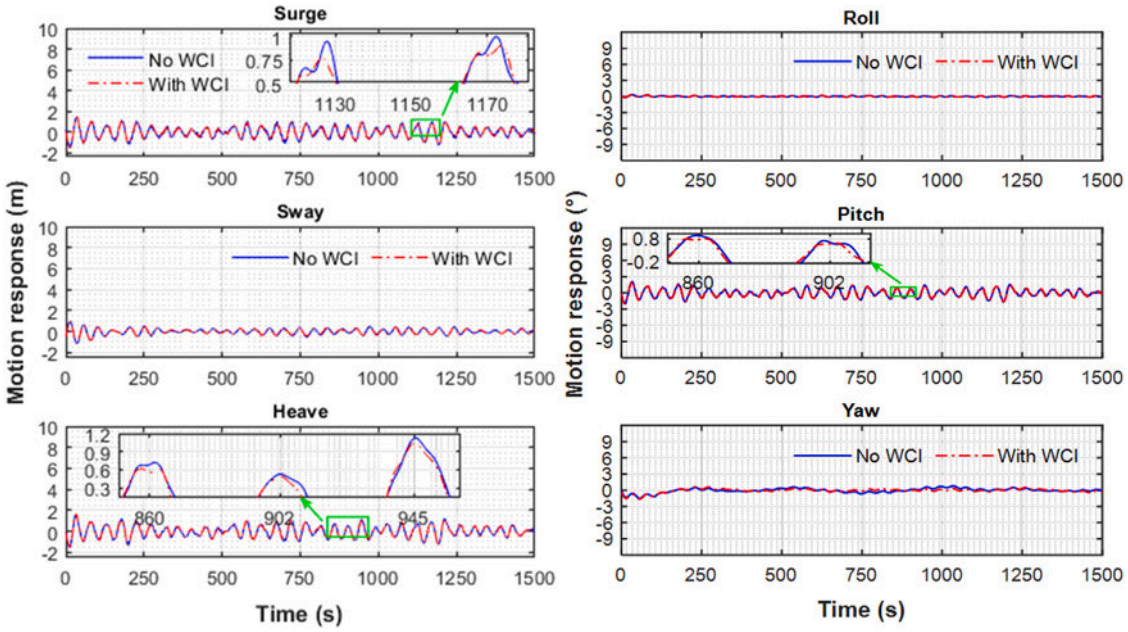

Fig. 6. Time histories of the FOWT motion responses considering wave–current interaction for the operation load case of a favourable current, LC11: (left) translational; (right) rotational.

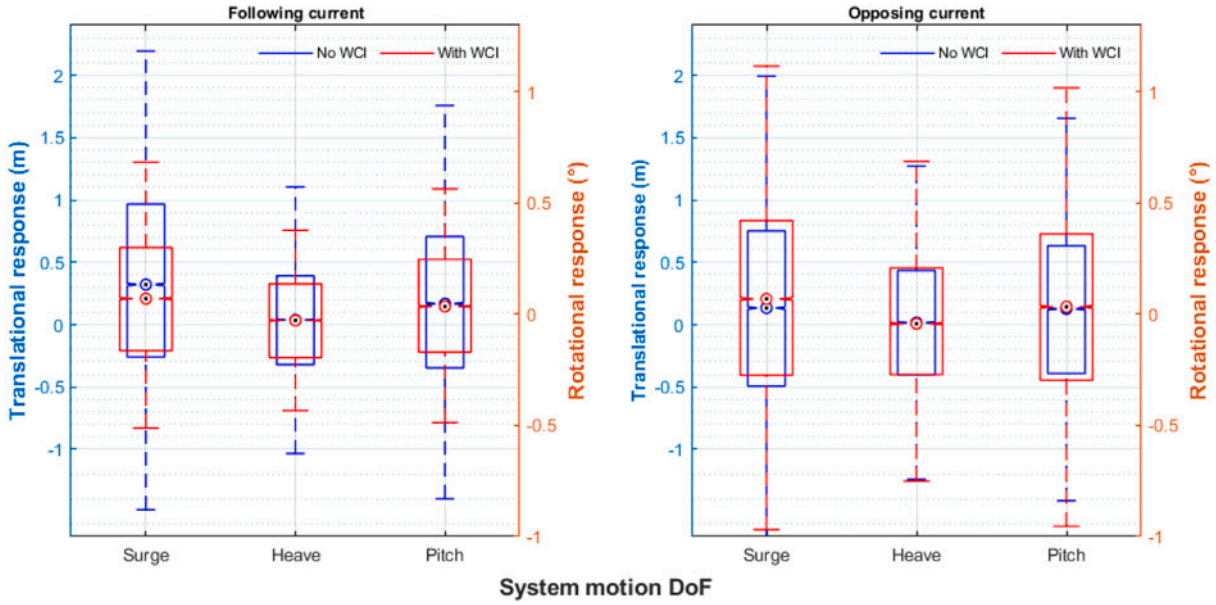

Fig. 7. Statistical distributions of the FOWT motion responses for irregular waves considering wave–current interaction: (left) LC5 with a following current; (right) LC6 with an opposing current.

maximum fairlead tension; in particular, the interaction significantly impacts the maximum tension, while their effect on the mean tension is insignificant, see Figs. 8 and 9. For mooring line A, as depicted in Fig. 8, when regular waves (extreme cases: LC1–LC4) interact with a following current, the maximum tension increases, whereas the opposite effect is observed for an opposing current, with a difference of up to 22%. In the worst-case modelled scenario (LC10), incorporating interaction resulted in a maximum fairlead tension increase of up to 3000 kN, compared to approximately 2450 kN without interaction, indicating a significant 23% increase. The changed surge brought on by WCI may account for these tension load differences. Hence, this highlights the importance of properly handling the increased fairlead tension in mooring design. Therefore, WCI should be included in mooring standards since they partially minimise the uncertainty of the estimated loads, thereby reducing the substantial safety factors that mooring systems are conventionally designed with.

Conversely, line B exhibits the opposite behaviour of the mooring load. Furthermore, despite the negligible effect of interaction on mean line tension for regular waves, an apparent impact was seen in the sea states of the short periods (LC3 and LC4; LC9 and LC10). This can be ascribed to the nonlinearity inherent in the stiffness of the catenary mooring system. Additionally, the dynamics of FOWT in regular seas depend not solely on the effect of current on the wave amplitude but also on the wave frequency due to the resonance effect. On the other hand, differences of up to ±10% have been recorded due to the accounting of such interaction, which is mainly dependent on the arrangement of the mooring cables in relation to the loading conditions. Furthermore, it is important to note that the tension of mooring lines

Table 5
Statistical comparison of FOWT motion responses considering wave–current interaction.

LC	Coupled model	Surge (m)			Heave (m)			Pitch (°)		
No.	With/No WCI	Mean	Max	StdDev	Mean	Max	StdDev	Mean	Max	StdDev
1	No WCI	0.404	2.139	1.231	0.065	1.068	0.910	0.084	0.910	0.583
	With WCI	0.229	3.612	2.347	0.037	3.725	2.520	0.036	0.885	0.591
2	No WCI	0.043	2.978	1.289	0.097	1.312	0.741	0.008	0.963	0.435
	With WCI	0.072	3.606	2.544	0.050	4.792	3.371	0.031	0.512	0.333
3	No WCI	1.529	2.076	0.381	0.069	0.320	0.172	0.096	0.526	0.298
	With WCI	0.155	2.952	1.953	0.024	3.200	2.126	0.023	0.709	0.472
4	No WCI	0.720	1.093	0.435	0.123	0.688	0.240	0.031	0.799	0.180
	With WCI	0.129	5.070	2.174	0.097	4.406	2.815	0.006	0.956	0.400
5	No WCI	0.385	3.481	0.873	0.045	1.743	0.519	0.057	1.540	0.436
	With WCI	0.282	3.937	0.843	0.033	1.811	0.514	0.043	1.589	0.394
6	No WCI	0.136	2.944	0.872	0.017	1.821	0.603	0.025	1.447	0.423
	With WCI	0.212	2.964	0.912	0.025	1.952	0.622	0.037	1.739	0.483
7	No WCI	0.781	3.225	0.600	0.045	0.836	0.196	0.062	1.260	0.306
	With WCI	0.512	2.527	0.493	0.035	0.712	0.186	0.047	1.098	0.293
8	No WCI	0.327	1.146	0.403	0.138	0.985	0.235	0.012	0.825	0.169
	With WCI	0.692	2.225	0.400	0.050	1.128	0.217	0.069	1.291	0.307
9	No WCI	2.587	4.113	0.466	2.488	4.182	0.483	3.223	5.435	0.635
	With WCI	2.581	4.952	1.099	2.496	5.398	1.091	3.240	5.529	0.636
10	No WCI	2.652	4.155	0.417	2.490	4.257	0.473	3.229	5.552	0.622
	With WCI	2.527	5.090	1.087	2.481	5.481	1.257	3.222	5.265	0.635
11	No WCI	2.626	4.168	0.485	2.494	4.219	0.517	3.230	5.528	0.682
	With WCI	2.638	4.192	0.485	2.496	4.253	0.521	3.232	5.512	0.687
12	No WCI	2.627	4.056	0.435	2.491	4.287	0.505	3.230	5.621	0.667
	With WCI	2.628	4.060	0.431	2.491	4.277	0.500	3.231	5.639	0.661

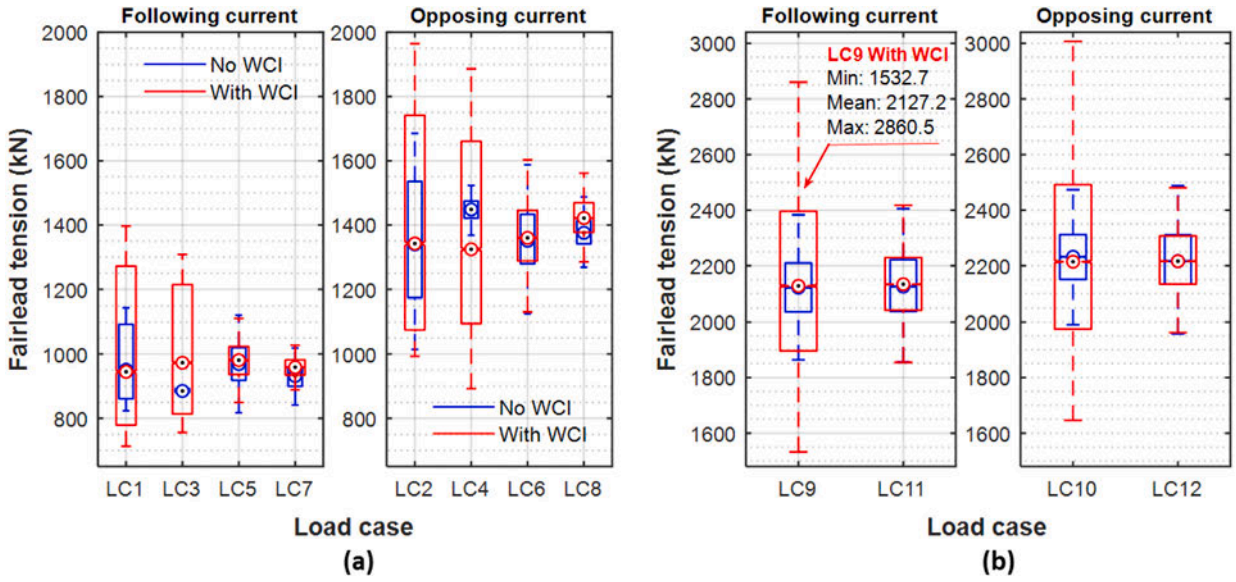

Fig. 8. Effect of wave–current interaction on the mooring tension of line A for different load cases: (a) extreme; (b) operational.

is intricately connected to the surge motion, which is prominently influenced by the presence of the current (Pillai et al., 2018).

5.4. Effect of wave–current interaction on nacelles dynamics

Ensuring the nacelle accelerations of a FOWT system remain within acceptable limits is crucial for its safe operation in a specific location. Thus, the impact of wave–current interaction on the magnitudes of nacelle accelerations (G) and their longitudinal (surge), transverse (sway), and vertical (heave) components, denoted as G_x, G_y, and G_z, respectively, are analysed for four operational load cases. The findings are presented in Figs. 10 and 11; and Table 6. Fig. 10.a demonstrates that incorporating interaction reduces the maximal longitudinal acceleration, G_x. This reduction is particularly pronounced for regular waves (i.e. LC9 and LC10), where a decrease of up to 48% is observed, whereas irregular waves (LC11, LC12) experienced a drop of up to 22%. Consequently, these reductions notably influence the mean values of acceleration magnitudes, which decrease by approximately 50% and 10% when considering the current interaction with regular and irregular waves, respectively (Fig. 10.b). Since WCI was not relevant for the operational cases and as well as the pitch response was found to be less impacted by such interaction. Thus, the significant changes observed in the G_x could be attributed to the WCI-altered surge.

Furthermore, Table 6 summarises the statistics for nacelles accelerations. Notably, incorporating wave–current interaction reduces the minimum, mean, maximum, and standard deviation values, further emphasising the impact of WCI on the nacelle dynamics. On the contrary, the statistical distribution presented in Fig. 11 reveals minor differences in the transverse (G_y) and vertical (G_z) accelerations when considering the interaction effect. These subtle variations can be attributed to the collinearity of the environmental conditions. It is worth noting that the wind, with a speed of 11.4 m/s, opposes the direction of the waves. Given the dominance of these loads (wind and wave), distinguishing

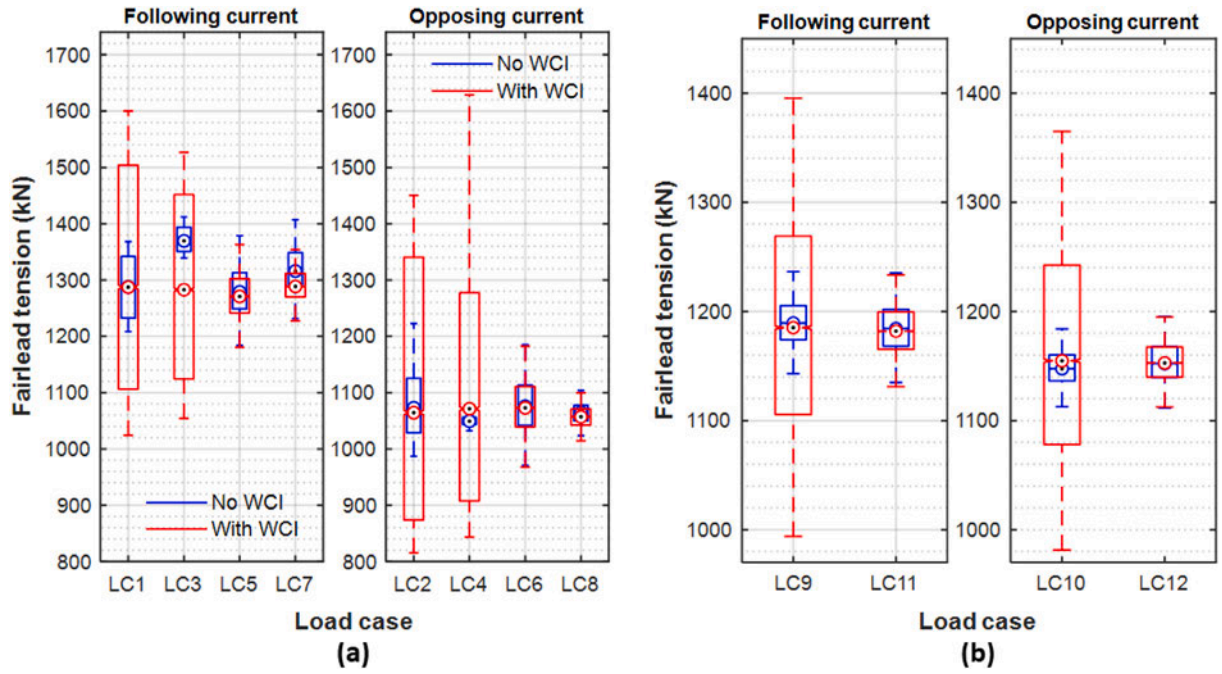

Fig. 9. Effect of wave–current interaction on the mooring tension of line B for different load cases: (a) extreme; (b) operational.

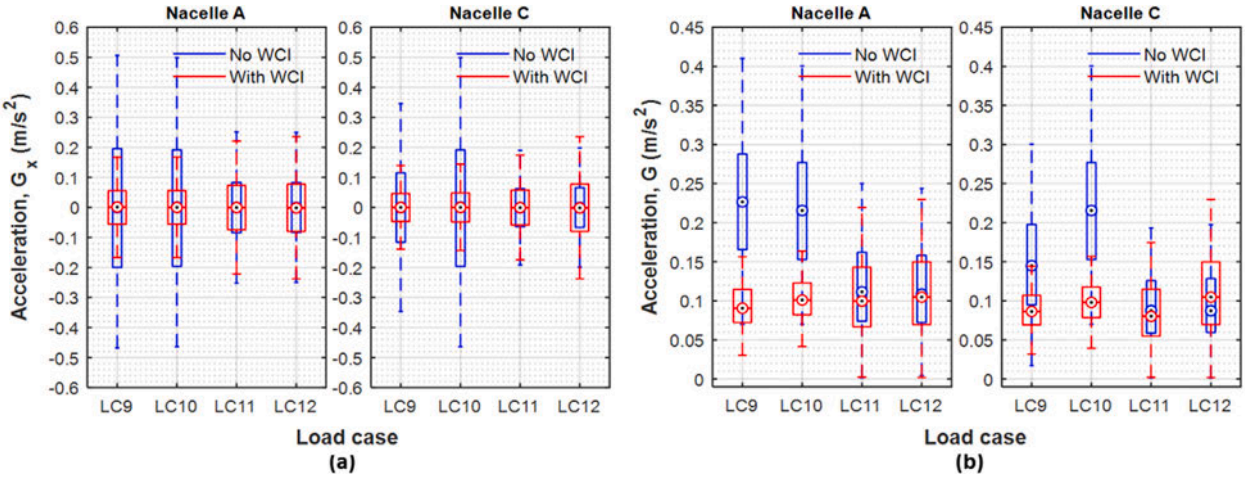

Fig. 10. Effect of wave–current interaction on nacelles accelerations under operational conditions: (a) longitudinal component (G_x); (b) total acceleration (G).

Table 6
Statistical comparison of nacelles' accelerations under operational conditions considering wave–current interaction.

LC	Coupled model	Nacelle A acceleration, G (m^2/s)				Nacelle C acceleration, G (m^2/s)			
No.	With/No WCI	Min	Max	Mean	StdDev	Min	Max	Mean	StdDev
9	No WCI	7.01E−2	5.19E−1	2.30E−1	7.87E−2	1.71E−2	3.97E−1	1.50E−1	6.58E−2
	With WCI	3.84E−3	2.83E−1	9.57E−2	3.47E−2	1.88E−3	2.57E−1	8.96E−2	3.12E−2
10	No WCI	7.01E−2	5.09E−1	2.19E−1	7.84E−2	1.97E−2	4.18E−1	1.62E−1	6.80E−2
	With WCI	4.44E−3	2.64E−1	1.04E−1	3.45E−2	5.65E−3	2.53E−1	9.90E−2	3.23E−2
11	No WCI	1.71E−3	5.14E−1	1.25E−1	6.72E−2	1.45E−3	4.01E−1	9.744E−2	5.23E−2
	With WCI	2.34E−3	3.92E−1	1.11E−1	5.90E−2	2.08E−3	3.26E−1	8.91E−2	4.67E−2
12	No WCI	4.58E−3	4.94E−1	1.21E−1	6.60E−2	1.45E−3	3.97E−1	9.90E−2	5.35E−2
	With WCI	1.89E−3	4.83E−1	1.17E−1	6.33E−2	1.86E−3	4.01E−1	9.63E−2	5.18E−2

the specific influence of the current, with a speed of 0.3 m/s, becomes challenging when it is either following or opposing.

To delve further into the impact of WCI on nacelle structural responses, time series for regular waves and power spectral density (PSD) for irregular waves are depicted in Figs. 12 and 13, respectively. These plots are generated from 0 to 3600 s after excluding the 200-second transient phase during wave build-up. Mean values have been removed for the time series plot, and data has been smoothed to emphasise the dynamics of nacelles' accelerations. As shown in Fig. 12, the consideration of WCI effectively reduces nacelle accelerations. Fig. 13 illustrates the impact of irregular waves, indicating an apparent reduction in acceleration PSDs under the influence of WCI, particularly within the

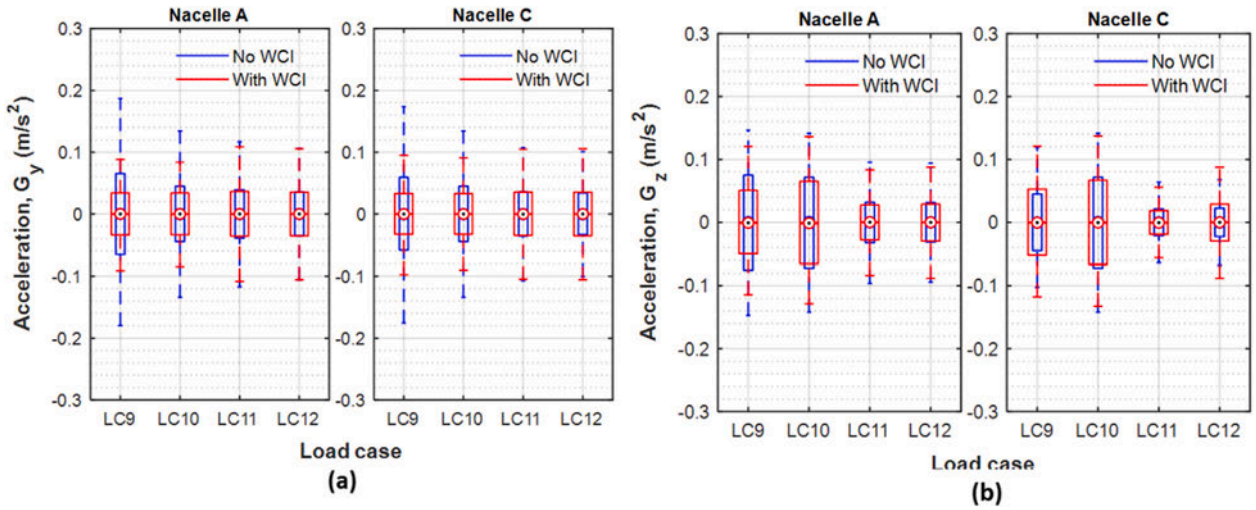

Fig. 11. Effect of wave–current interaction on translational accelerations of the nacelles under operational conditions: (a) transverse component (G_y); (b) vertical component (G_z).

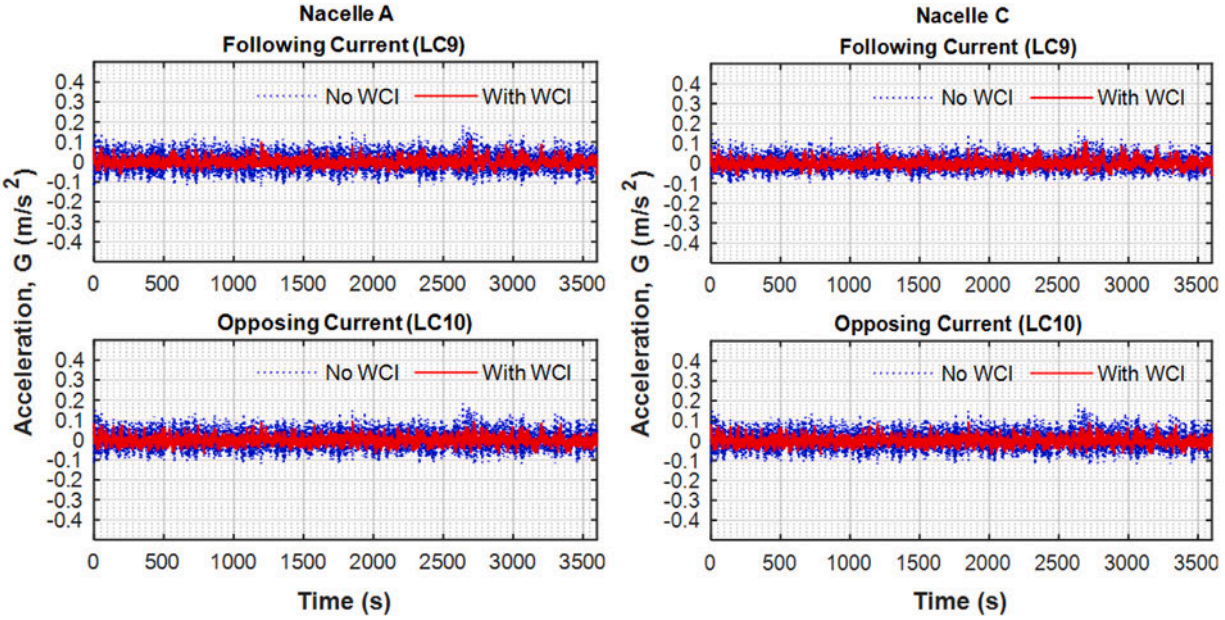

Fig. 12. Time histories of nacelles' accelerations considering wave–current interaction under operational conditions for regular waves: (left) Nacelle A and (right) Nacelle C.

frequency range of 0 to 0.25 Hz, irrespective of the current direction. Interestingly, nacelle A exhibited higher acceleration than nacelle C at very low frequencies.

The observed reductions in nacelles' accelerations when incorporating WCI can be attributed to the complex hydrodynamic interaction caused by the coupling of waves and currents. The intricate WCI introduces additional forces and moments, thereby modifying the flow conditions around the entire floating system. These altered flow fields influence the inertia of the system, which, in turn, contributes to the system's dampening response (Goupee et al., 2014). Furthermore, twin FOWTs add another level of complexity due to the wake interaction between the rotors, which is not considered in this study. Therefore, the assessment of their aerodynamics is a topic of ongoing research (Martín San Román, 2022).

Commonly, the interaction of the current with the incoming waves results in a larger excitation force in surge and excitation moment in pitch. The surge drift force also changes with the current-altered wave height (Chakrabarti, 1984). Unlike conventional offshore structures, FOWTs are distinguished by their towering superstructures. These towers lead to a significant rotor displacement from even a minor pitch motion of the floating platform. Moreover, in this peculiar FOWT design with a single-point mooring system, the presence of wind could potentially tilt the platform, inducing pitch motion and vibrations in the tower fore-aft that could affect nacelle acceleration (Antonutti et al., 2016). Consequently, it impacts the generated power efficiency and contributes to the accumulation of fatigue loads. Therefore, the inclusion of WCI is considerably effective for capturing more accurate wind-wave effects. Then, a trade-off between vibration reduction and rotor speed enhancement could be advantageous for extending the operational life of wind turbine components.

6. Conclusions

This study investigates wave–current interaction effects on the W2Power FOWT, which is equipped with a pair of NREL 5MW wind turbines and moored to the seabed using a single-point mooring system of conventional catenary configuration with three lines made of studless chains. Two analytical models were developed to analyse current interaction with regular and irregular waves. The effects of following and

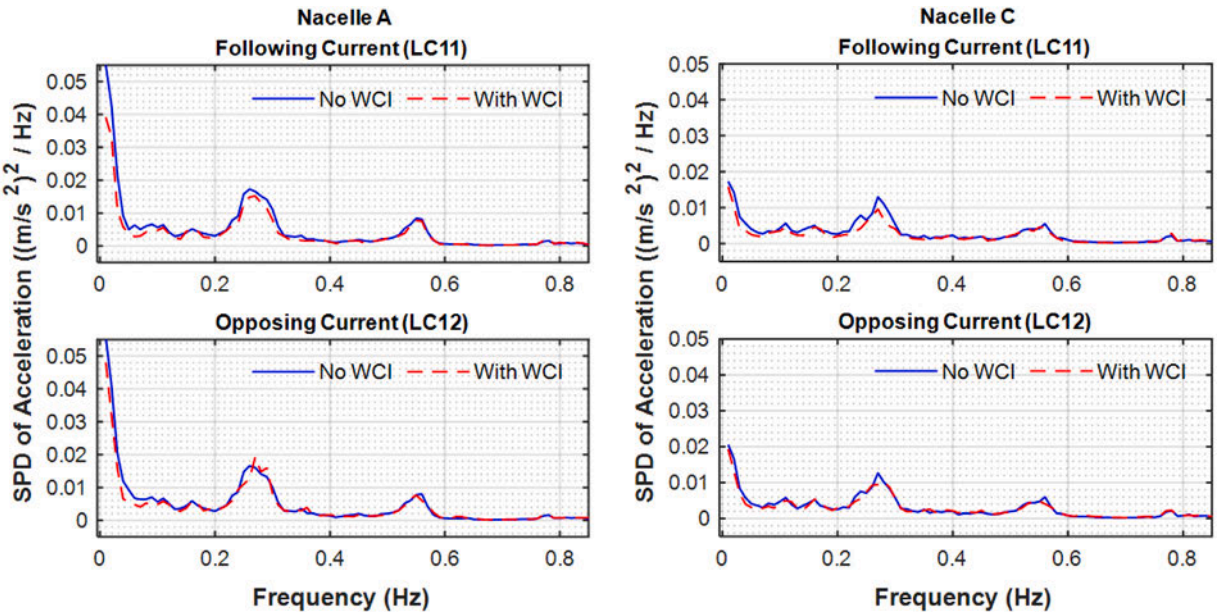

Fig. 13. Power spectral densities of nacelles' accelerations considering wave–current interaction under operational conditions for irregular waves: (left) Nacelle A and (right) Nacelle C.

opposing currents on wave characteristics were investigated, revealing alterations in the regular and stochastic wave fields. WCI models are then integrated with the OrcaFlex programme to analyse the dynamic responses of the floating system. The simulations involved various loading scenarios, including current-only, wave-only, and wave–current with and without interaction. The key findings are as follows:

- The presence of current significantly impacts the FOWT's static equilibrium and, consequently, its mooring system's operational point and motion dynamics.
- WCI significantly affects the translational motion response of the FOWT system, while rotational motion is relatively unaffected. The mean values of surge and heave decreased with a following current and increased with an opposing current, resulting in differences of up to ±26% and ±30%, respectively.
- WCI impacted the mooring system's dynamics, with notable effects observed on the maximum tension at the fairlead, while the mean tension was insignificantly affected. For regular seas, the interaction can lead to differences of up to ±22.5% in the maximum tension, depending on the current direction and mooring layout. For irregular seas, the differences were up to ±10%.
- WCI was found to minimise maximum longitudinal acceleration (G_x) substantially. G_x has experienced a notable decrease of up to 48% in regular seas, while a drop of up to 22% in irregular ones. Transverse and vertical accelerations showed slight variations due to the collinearity of environmental conditions along the X-axis.

The analysis highlights the significance of incorporating WCI to accurately simulate the dynamic responses of FOWTs and ensure operational safety. The current framework and results of the parametric studies presented in this paper can be the basis for the applications of advanced wave–current interaction models in future studies. For instance, nonlinear WCI models, such as those developed by Moreira and Peregrine (2012), can be established to account for more nonlinear effects of such interaction and their implications on the structural responses of FOWTs. Future work will involve the validation of the developed numerical models through tank testing experiments conducted at the Facility (Ingram et al., 2014). This study rigorously examines the FOWT dynamics under extreme sea states and operational conditions, adopting a simplified rigid body approach for the floater subjected to environmental loads. Thus, future research should also consider incorporating floater flexibility in numerical modelling.

CRediT authorship contribution statement

Mujahid Elobeid: Conceptualization, Data curation, Formal analysis, Investigation, Methodology, Software, Validation, Visualization, Writing – original draft, Writing – review & editing. **Ajit C. Pillai:** Conceptualization, Methodology, Writing – review & editing, Project administration, Resources, Supervision. **Longbin Tao:** Conceptualization, Methodology, Project administration, Resources, Supervision, Writing – review & editing. **David Ingram:** Conceptualization, Funding acquisition, Methodology, Project administration, Resources, Supervision, Writing – review & editing. **Jan Erik Hanssen:** Project administration, Resources, Writing – review & editing. **Pedro Mayorga:** Project administration, Resources.

Declaration of competing interest

The authors declare that they have no known competing financial interests or personal relationships that could have appeared to influence the work reported in this paper.

Data availability

The data that has been used is confidential.

References

Antonutti, R., Peyrard, C., Johanning, L., Incecik, A., Ingram, D., 2016. The effects of wind-induced inclination on the dynamics of semi-submersible floating wind turbines in the time domain. Renew. Energy 88, 83–94.

Azcona, J., Palacio, D., Munduate, X., Gonzalez, L., Nygaard, T.A., 2017. Impact of mooring lines dynamics on the fatigue and ultimate loads of three offshore floating wind turbines computed with IEC 61400-3 guideline. Wind Energy 20 (5), 797–813.

Barltrop, N., Varyani, K., Grant, A., Clelland, D., Pham, X., 2007. Investigation into wave—current interactions in marine current turbines. Proc. Inst. Mech. Eng., Part A: J. Power Energy 221 (2), 233–242.

Ben-Israel, A., 1966. A Newton-Raphson method for the solution of systems of equations. J. Math. Anal. Appl. 15 (2), 243–252.

Bretherton, F.P., Garret, C., 1970. Wavetrains in inhomogeneous moving media. Hyperbol. Equ. Waves: Battelle Seattle 1968 Recontres 211–236.

Chakrabarti, S.K., 1984. Steady drift force on vertical cylinder-viscous vs. potential. Appl. Ocean Res. 6 (2), 73–82.

Chen, L., Basu, B., 2018. Fatigue load estimation of a spar-type floating offshore wind turbine considering wave-current interactions. Int. J. Fatigue 116, 421–428.

Chen, L., Basu, B., 2019. Wave-current interaction effects on structural responses of floating offshore wind turbines. Wind Energy 22 (2), 327–339.
Cummins, W., et al., 1962. The Impulse Response Function and Ship Motions. Department of the Navy, David Taylor Model Basin Bethesda, MD, USA.
Dai, J., Abrahamsen, B.C., Viuff, T., Leira, B.J., 2022. Effect of wave-current interaction on a long fjord-crossing floating pontoon bridge. Eng. Struct. 266, 114549.
Davidson, J., Ringwood, J.V., 2017. Mathematical modelling of mooring systems for wave energy converters—A review. Energies 10 (5), 666.
de Jesus Henriques, T., Tedds, S., Botsari, A., Najafian, G., Hedges, T., Sutcliffe, C., Owen, I., Poole, R., 2014. The effects of wave–current interaction on the performance of a model horizontal axis tidal turbine. Int. J. Mar. Energy 8, 17–35.
DNV, 2010. Offshore Standard DNV-OS-E301 Position Mooring. Det Norske Veritas, Høvik, Norway.
DNV, 2019. Environmental Conditions and Environmental Loads. Oslo, Norway, Det Norske Veritas.
Draycott, S., Noble, D., Davey, T., Bruce, T., Ingram, D., Johanning, L., Smith, H., Day, A., Kaklis, P., 2018. Re-creation of site-specific multi-directional waves with non-collinear current. Ocean Eng. 152, 391–403.
Draycott, S., Pillai, A.C., Gabl, R., Davey, T., 2021. Wave buoys in current-experimental results and observations. In: European Wave and Tidal Energy Conference. EWTEC.
Elobeid, M., Tao, L., Ingram, D., Pillai, A.C., Mayorga, P., Hanssen, J.E., 2022. Hydrodynamic performance of an innovative semisubmersible platform with twin wind turbines. In: International Conference on Offshore Mechanics and Arctic Engineering, Vol. 85932. American Society of Mechanical Engineers, V008T09A032.
EnearOcean S.L., 2007. SME marine energy engineering SME, Málaga, Spain. SME Mar. Energy Eng. SME URL https://enerocean.com/.
Facility, F.O.E.R., 2013. FloWave Ocean Energy Research Facility. The University of Edinburgh, Edinburgh, UK, URL www.flowavett.co.uk.
Faltinsen, O., 1993. Sea Loads on Ships and Offshore Structures, Vol. 1. Cambridge University Press.
Fenton, J.D., McKee, W., 1990. On calculating the lengths of water waves. Coast. Eng. 14 (6), 499–513.
Froude, W., 1920. On the Elementary Relation Between Pitch, Slip, and Propulsive Efficiency. Technical Report.
GeinE, 2020. SESAM-GeniE Manual. Det Norske Veritas (DNV), Oslo, Norway, URL www.dnv.com.
Gonçalves, R.T., Chame, M.E., Silva, L.S., Koop, A., Hirabayashi, S., Suzuki, H., 2021. Experimental flow-induced motions of a FOWT semi-submersible type (OC4 phase II floater). J. Offshore Mech. Arct. Eng. 143 (1).
Goupee, A.J., Koo, B.J., Kimball, R.W., Lambrakos, K.F., Dagher, H.J., 2014. Experimental comparison of three floating wind turbine concepts. J. Offshore Mech. Arct. Eng. 136 (2), 020906.
Hall, M., Buckham, B., Crawford, C., 2014. Evaluating the importance of mooring line model fidelity in floating offshore wind turbine simulations. Wind Energy 17 (12), 1835–1853.
Hanssen, J.E., Margheritini, L., Mayorga, P., Hezari, R., O'Sullivan, K., Martinez, I., Arriaga, A., Agos, I., Todalshaug, J.H., Steynor, J., Ingram, D., 2015. Design and performance validation of a hybrid offshore renewable energy platform: A path to cost-efficient development of deepwater marine energy resources. In: The 10th International Conference on Ecological Vehicles and Renewable Energies, EVER 2015.
Hasselmann, K., Barnett, T.P., Bouws, E., Carlson, H., Cartwright, D.E., Enke, K., Ewing, J., Gienapp, A., Hasselmann, D., Kruseman, P., et al., 1973. Measurements of wind-wave growth and swell decay during the joint north sea wave project (JONSWAP). Ergaenzungsheft Deutschen Hydrographischen Z., Reihe A.
Hedges, T., 1981. Some effects of currents on wave spectra. In: Proceedings of the First Indian Conference in Ocean Engineering, Vol. 1. pp. 30–35.
Hedges, T.S., Anastasiou, K., Gabriel, D., 1985. Interaction of random waves and currents. J. Waterw., Port, Coastal, Ocean Eng. 111 (2), 275–288.
Huang, N.E., Chen, D.T., Tung, C.C., Smith, J.R., 1972. Interactions between steady won-uniform currents and gravity waves with applications for current measurements. J. Phys. Oceanogr. 2 (4), 420–431.
Ingram, D., Wallace, R., Robinson, A., Bryden, I., 2014. The design and commissioning of the first, circular, combined current and wave test basin. In: Proceedings of the Oceans.
Isaacson, M., Cheung, K.F., 1993. Time-domain solution for wave—current interactions with a two-dimensional body. Appl. Ocean Res. 15 (1), 39–52.
Ismail, N.M., 1984. Wave-current models for design of marine structures. J. Waterw., Port, Coastal, Ocean Eng. 110 (4), 432–447.
Jonkman, J.M., 2007. Dynamics Modeling and Loads Analysis of an Offshore Floating Wind Turbine. University of Colorado at Boulder.
Jonkman, J., 2010. Definition of the Floating System for Phase IV of OC3. Technical Report, National Renewable Energy Lab.(NREL), Golden, CO (United States).
Jonkman, J., Butterfield, S., Musial, W., Scott, G., 2009. Definition of a 5-MW Reference Wind Turbine for Offshore System Development. Technical Report, National Renewable Energy Lab.(NREL), Golden, CO (United States).
Jonkman, B., Kilcher, L., 2012. TurbSim User's Guide: Version 1.06. 00. National Renewable Energy Laboratory, Golden, CO, USA.
Jonsson, I.G., 1990. Wave-current interactions. Sea, A 9, 65–120.
Lai, R.J., Long, S.R., Huang, N.E., 1989. Laboratory studies of wave-current interaction: Kinematics of the strong interaction. J. Geophys. Res.: Oceans 94 (C11), 16201–16214.
Li, Y., Liu, L., Zhu, Q., Guo, Y., Hu, Z., Tang, Y., 2018. Influence of vortex-induced loads on the motion of SPAR-type wind turbine: A coupled aero-hydro-vortex-mooring investigation. J. Offshore Mech. Arct. Eng. 140 (5).
Martín San Román, R., 2022. Coupled Dynamics of Multi Wind Turbine Floating Platforms (Ph.D. thesis). Espacio.
Masson, D., 1996. A case study of wave–current interaction in a strong tidal current. J. Phys. Oceanogr. 26 (3), 359–372.
Moreira, R., Peregrine, D., 2012. Nonlinear interactions between deep-water waves and currents. J. Fluid Mech. 691, 1–25.
Morison, J., Johnson, J.W., Schaaf, S.A., 1950. The force exerted by surface waves on piles. J. Pet. Technol. 2 (05), 149–154.
Nestegård, A., Ronæss, M., Hagen, Ø., Ronold, K., Bitner-Gregersen, E.M., 2019. Recommended Practice DNV-RP-C205: On Environmental Conditions and Environmental Loads. Det Norske Veritas (DNV), Oslo, Norway.
Nguyen, H.X., 2022. Dynamic Response of Spar-Type Floating Offshore Wind (Ph.D. thesis). Trinity College Dublin. School of Engineering. Disc of Civil Structural ....
NKUA-AM&WFG, 2021. Long-term Hincast Data from: Atmospheric Modeling and Weather Forecasting Group (AM&WFG). National & Kapodistrian University of Athens, Athens, Greece, URL https://forecast.uoa.gr/en/group.
OrcaFlex, 2023. Orcaflex Manual. Orcina Ltd, Cumbria, UK, URL www.orcina.com.
OrcaWave, 2023. OrcaWave Manual. Orcina Ltd, Cumbria, UK, URL www.orcina.com.
Palm, J., Eskilsson, C., Paredes, G.M., Bergdahl, L., 2016. Coupled mooring analysis for floating wave energy converters using CFD: Formulation and validation. Int. J. Mar. Energy 16, 83–99.
Peeringa, J.M., 2014. Fatigue loading on a 5MW offshore wind turbine due to the combined action of waves and current. J. Phys.: Conf. Ser. 524 (1), 012093.
Peters, H., Boonstra, H., 1988. Fatigue loading on a single pile platform due to combined action of waves and currents.
Phillips, .M., 1977. The dynamics of the upper ocean. J. Fluid Mech. 88 (4), 793–794.
Pierson, Jr., W.J., Moskowitz, L., 1964. A proposed spectral form for fully developed wind seas based on the similarity theory of SA kitaigorodskii. J. Geophys. Res. 69 (24), 5181–5190.
Pillai, A.C., Davey, T., Draycott, S., 2021. A framework for processing wave buoy measurements in the presence of current. Appl. Ocean Res. 106, 102420.
Pillai, A.C., Thies, P.R., Johanning, L., 2018. Optimization of mooring line axial stiffness characteristics for offshore renewable energy applications. In: ISOPE International Ocean and Polar Engineering Conference. ISOPE, ISOPE–I.
Qu, X., Li, Y., Tang, Y., Hu, Z., Zhang, P., Yin, T., 2020. Dynamic response of spar-type floating offshore wind turbine in freak wave considering the wave-current interaction effect. Appl. Ocean Res. 100, 102178.
Rognebakke, O., 2002. Sloshing in Rectangular Tanks and Interaction with Ship Motions. Fakultet for ingeniørvitenskap og teknologi.
Sarkar, S., Chen, L., Fitzgerald, B., Basu, B., 2020. Multi-resolution wavelet pitch controller for spar-type floating offshore wind turbines including wave-current interactions. J. Sound Vib. 470, 115170.
Shin, H., 2011. Model test of the OC3-hywind floating offshore wind turbine. In: The Twenty-First International Offshore and Polar Engineering Conference. OnePetro.
Silva, L., Cazzolato, B., Sergiienko, N., Ding, B., 2021. Nonlinear dynamics of a floating offshore wind turbine platform via statistical quadratization—Mooring, wave and current interaction. Ocean Eng. 236, 109471.
Silva, M., Vitola, M., Esperança, P., Sphaier, S., Levi, C., 2016. Numerical simulations of wave–current flow in an ocean basin. Appl. Ocean Res. 61, 32–41.
Smith, J.M., 1997. One-Dimensional Wave-Current Interaction. Technical Report, Engineer Research and Development Center Vicksburg Ms Coastal and Hydraulics Lab.
Soares, C.G., De Pablo, H., 2006. Experimental study of the transformation of wave spectra by a uniform current. Ocean Eng. 33 (3–4), 293–310.
Solidworks, 2021. Solidworks Manual. Dassault Systèmes SOLIDWORKS Corp, Waltham, Massachusetts, USA, URL www.solidworks.com.
Thomas, G., 1981. Wave-current interactions: an experimental and numerical study. Part 1. linear waves. J. Fluid Mech. 110, 457–474.
Tung, C.C., Huang, N.E., 1974. Influence of current on statistical properties of waves. J. Waterw., Harbors Coastal Eng. Div. 100 (4), 267–278.
Van den Boom, H., 1985. Dynamic behaviour of mooring lines. In: BOSS Conference, Vol. 1. pp. 359–368.
White, B.S., 1999. Wave action on currents with vorticity. J. Fluid Mech. 386, 329–344.
WindEurope, 2018. Floating offshore wind energy: A policy blueprint for europe. pp. 2–3, URL www.windeurope.org.
Zhao, R., Faltinsen, O.M., Krokstad, J., Aanesland, V., 1988. Wave-current interaction effects on large-volume structures. In: BOSS'88. pp. 623–638.